Opis rozprawy doktorskiej:

Imię i nazwisko autora pracy	Krzysztof Wojciech Sobucki
Adres e-mail, telefon autora pracy	krzsob@amu.edu.pl, 518 665 653
Imię i nazwisko promotora lub promotorów pracy	dr hab. Paweł Gruszecki
Wydział	Wydział Fizyki i Astronomii
Instytut/Zakład	Instytut Spintroniki i Informacji Kwantowej, Zakład Fizyki Nanometeriałów
Tytuł pracy w jęz. polskim	Efekty rezonansowe w liniowej i nieliniowej dynamice fal spinowych do kontroli biegnących fal spinowych
Tytuł pracy w jęz. angielskim	Resonance effects in linear and nonlinear spin wave dynamics for control of propagating spin waves
Język pracy	angielski
Słowa kluczowe w jęz. polskim (max 5)	Magnonika, symulacje mikromagnetyczne, interferometry magnoniczne, efekt Goosa-Hänchen, nieliniowa dynamika fal spinowych
Słowa kluczowe w jęz. angielskim (max 5)	Magnonics, micromagnetic simulations, magnonic interferometers, Goos-Hänchen effect, nonlinear spin-wave dynamics
Streszczenie pracy w jęz. polskim (max 1400 znaków)	Fale spinowe są oscylacjami magnetycznymi, którymi zajmuje się dział fizyki zwany magnoniką. Z powodu swoich właściwości fale spinowe są uważane za obiecującą bazę pod nowe technologie przetwarzania informacji. Wynika to z faktu, iż są one niskoenergetycznymi oscylacjami, nie doznają rozpraszania ciepła Joula oraz mają znacznie mniejsze długości fal w porównaniu do mikrofal. Wykorzystanie fal spinowych jest hamowane przez ich wysokie tłumienie oraz czułości na fluktuacje termiczne. Dodatkowo, wciąż potrzebne jest opracowywanie nowych metod kontroli propagowania się fal. W tej dysertacji przedstawione są nowe metody kontroli propagowania się fal spinowych bazujące na liniowych i nieliniowych efektach rezonansowych w dynamice fal spinowych. Liniowe efekty rezonansowe, zapewniają kontrolę nad fazą fal spinowych oraz zmianą kierunku ich propagowania. Efekty nieliniowe zostały zaobserwowane podczas nieelastycznego rozpraszania wiązek fal spinowych. Następstwem ich jest powstanie nowych wiązek o zmienionej

	częstotliwości, które propagują się pod innymi kątami oraz doznają przesunięcia przestrzennego na interfejsie. Dodatkowo, gdy odpowiednie warunki są spełnione, w układzie zaobserwowano występowanie kaskady efektów nieliniowych, których jednym z rezultatów jest powstanie płaskich fal spinowych propagujących się w układzie. Badania stanowiące rdzeń dysertacji są zawarte w pięciu publikacjach naukowych. Przedstawione publikacje są poprzedzone opisem magnoniki i teorii symulacji numerycznych. Dysertacja jest zakończona krótkim podsumowaniem badań oraz wykazem osiągnięć Autora.
Streszczenie pracy w jęz. angielskim (max 1400 znaków)	Spin waves are coherent magnetic oscillations, the field of physics describing them is called magnonics. Spin waves are considered a promising replacement for, or addition to, current electronic technologies. This potential is due the fact that spin waves represent low-energy oscillations, lack of Joule heating, and wavelengths smaller in comparison to microwaves. However, to fully exploit the potential of spin waves, several obstacles must be overcome, including high magnetic damping, sensitivity to thermal fluctuations, the limited number of methods for spin-wave excitation, and new methods for spin-wave propagation control. This thesis addresses the last of mentioned challenges. New spin-wave propagation control methods have been developed by investigations of linear and nonlinear resonance effects in spin-wave dynamics. Linear resonance effects, demonstrated in magnonic interferometers, provide control over the spin-wave. Nonlinear effects were observed during the inelastic scattering of spin waves, producing new spin waves with altered frequencies that propagate at different angles and experience lateral shifts. Moreover, under specific conditions, a cascade of nonlinear effects is triggered, resulting in the generation of plane spin waves. The findings are presented across five publications that constitute the core of the thesis. The publications are preceded by descriptions of magnonics and micromagnetic employed in the investigations. The thesis concludes with a summary offering an outlook for future investigations and a list of the author's achievements.
liczba stron	172

Abstract

Spin waves are coherent magnetic oscillations whose quanta are called magnons; thus, the field of physics describing spin waves is known as magnonics. Spin waves are considered to be a promising replacement for, or addition to, current electronic technologies. This potential stems from the fact that spin waves represent low-energy oscillations, they do not cause heat dissipation due to Joule heating, and their wavelengths are smaller compared to microwaves of the same frequency. However, to fully exploit the potential of spin waves, several obstacles must be overcome, including high magnetic damping in most magnetic media, sensitivity of low-energy oscillations to thermal fluctuations, the limited number of reliable methods for spin-wave excitation and detection, and new methods for spin-wave propagation control.

This thesis addresses the last of these challenges by presenting new methods for controlling spin-wave propagation. These methods have been developed through investigations of linear and non-linear resonance effects in spin-wave dynamics. Linear resonance effects, demonstrated in magnonic interferometers, provide control over the spin-wave phase and enable redirection of spin waves by exciting an interferometer's eigenmode by the obliquely incident spin wave. Non-linear effects were observed during the inelastic scattering of spin waves on a localized edge mode, producing new spin waves with altered frequencies that propagate at different angles, experience lateral shifts analogous to the Goos-Hänchen effect and amplitude change analogous to Wood's anomaly. Moreover, under specific conditions, a cascade of non-linear effects is triggered, resulting in the generation of plane spin waves at the system's edge.

The findings are presented across five publications that constitute the core of this thesis. Additionally, two other publications concerning spin waves, which do not directly address the primary research question, are also briefly discussed. The publications are preceded by synthetic descriptions of magnonics and micromagnetic simulations necessary for a full understanding of the presented results. The thesis concludes with a brief summary offering an outlook for future investigations and a list of Author's achievements.

Streszczenie

Fale spinowe są koherentnymi oscylacjami namagnesowania, których kwanty nazywane są magnonami. Stąd pochodzi nazwa magnonika, która odnosi się do działu fizyki zajmującego się falami spinowymi. Fale spinowe, z powodu swoich właściwości, są uważane za obiecujący nośnik informacji w nowych technologiach komunikacji i przetwarzania danych, które mogą wyprzeć technologie bazujące na elektronach bądź też wspomóc starsze technologie. Wynika to z faktu, iż fale spinowe są niskoenergetycznymi oscylacjami, nie powodują rozpraszania energii w postaci ciepła Joula oraz cechują się znacznie krótszymi długościami fal dla częstotliwości mikrofalowych od fal elektromagnetycznych. Jednakże wykorzystanie potencjału fal spinowych jest hamowane przez ich wysokie tłumienie w większości znanych materiałów magnetycznych, ich czułości na fluktuacje termiczne medium w którym się przemieszczają oraz ograniczonej liczbie metod na efektywne wzbudzenie i detekcję fal spinowych. Dodatkowo, wciąż potrzebne jest opracowywanie nowych metod kontroli propagowania się fal spinowych bazujących na geometrii elementów układów magnonicznych lub zmianie zewnętrznych parametrów układu.

W tej dysertacji są przedstawione nowe metody kontroli propagowania się fal spinowych, które bazują na liniowych i nieliniowych efektach rezonansowych w dynamice fal spinowych. Liniowe efekty rezonansowe, zademonstrowane za pomocą magnonicznych interferometrów, zapewniają kontrolę nad fazą fal spinowych oraz zmianą kierunku ich propagowania się poprzez wzbudzanie stanów własnych interferometrów przy ukośnym padaniu fal spinowych. Efekty nieliniowe zostały zaobserwowane podczas nieelastycznego rozpraszania wiązki fal spinowych na modzie zlokalizowanym na krawędzi układu magnonicznego. Następstwem tychże efektów nieliniowych jest powstanie nowych wiązek o zmienionej częstotliwości, które propagują się pod innymi kątami, doznają przesunięcia przestrzennego na krawędzi układu, co jest magnonicznym analogiem efektu Goosa-Hänchen, oraz dochodzi do obniżenia amplitudy odbitych wiązek co jest magnonicznym odpowiednikiem anomalii Wooda. Wielkości rezultatów tych efektów zależą od częstotliwości i wektora falowego zlokalizowanego modu na którym następuje rozproszenie wiązek padających. Dodatkowo, gdy odpowiednie warunki opisane w dysertacji są spełnione w układzie zaobserwowano występowanie kaskady efektów nieliniowych, których jednym z wyników jest powstanie w układzie płaskich fal spinowych propagujących się od krawędzi układu.

Badania stanowiące rdzeń tej dysertacji są zawarte w pięciu publikacjach naukowych załączonych w niniejszej pracy. Dodatkowe dwie publikacje z zakresu badań nad innymi aspektami fal spinowych są również krótko przedstawione, nie należą one jednak do głównych badań w ramach tej dysertacji. Przedstawione publikacje są poprzedzone syntetycznym wstępem do magnoniki i teorii symulacji numerycznych potrzebnym do zrozumienia metodologii i wyników. Dysertacja jest zakończona krótkim podsumowaniem badań, planami na przyszłość oraz wykazem osiągnięć Autora podczas studiów doktorskich.

Adam Mickiewicz University, Poznań
Faculty of Physics and Astronomy
Institute of Spintronics and Quantum Information

DOCTORAL THESIS

Resonance effects in linear and nonlinear spin wave dynamics for control of propagating spin waves

Krzysztof Wojciech Sobucki

Supervisor: **dr hab. Paweł Guszecki, prof. UAM**

Poznań 2025

I would like to dedicate this thesis to my loving parents
Marzanna and Czesław.

Declaration

Declaration of the author of this dissertation

I hereby declare that except where specific reference is made to the work of others, the contents of this dissertation are original and have not been submitted in whole or in part for consideration for any other degree or qualification in this, or any other university. This dissertation is my own work and all the contents of the dissertation have been obtained by legal means.

....
mgr Krzysztof Sobucki

Declaration of the thesis Supervisor

This dissertation is ready to be reviewed.

....
dr hab. Paweł Gruszecki

Acknowledgments

family-like atmosphere in the high school, thanks to which I have only good memories of that time.

Now, I would like to thank my parents, Marzanna and Czesław, for their unwavering love, encouragement, and support throughout my life and during my time at university. I also wish to thank my sister, Natalia, for her constant support. And last but not least, I am deeply grateful to my best friend, Mikołaj, who was always there whenever I needed help, and who helped me stay (relatively) sane during my PhD journey.

Abstract

Spin waves are coherent magnetic oscillations whose quanta are called magnons; thus, the field of physics describing spin waves is known as magnonics. Spin waves are considered to be a promising replacement for, or addition to, current electronic technologies. This potential stems from the fact that spin waves represent low-energy oscillations, they do not cause heat dissipation due to Joule heating, and their wavelengths are smaller compared to microwaves of the same frequency. However, to fully exploit the potential of spin waves, several obstacles must be overcome, including high magnetic damping in most magnetic media, sensitivity of low-energy oscillations to thermal fluctuations, the limited number of reliable methods for spin-wave excitation and detection, and new methods for spin-wave propagation control.

This thesis addresses the last of these challenges by presenting new methods for controlling spin-wave propagation. These methods have been developed through investigations of linear and non-linear resonance effects in spin-wave dynamics. Linear resonance effects, demonstrated in magnonic interferometers, provide control over the spin-wave phase and enable redirection of spin waves by exciting an interferometer's eigenmode by the obliquely incident spin wave. Non-linear effects were observed during the inelastic scattering of spin waves on a localised edge mode, producing new spin waves with altered frequencies that propagate at different angles, experience lateral shifts analogous to the Goos-Hänchen effect and amplitude change analogous to Wood's anomaly. Moreover, under specific conditions, a cascade of non-linear effects is triggered, resulting in the generation of plane spin waves at the system's edge.

The findings are presented across five publications that constitute the core of this thesis. Additionally, two other publications concerning spin waves, which do not directly address the primary research question, are also briefly discussed. The publications are preceded by synthetic descriptions of magnonics and micromagnetic simulations necessary for a full understanding of the presented results. The thesis concludes with a brief summary offering an outlook for future investigations and a list of Author's achievements.

Streszczenie

Fale spinowe są koherentnymi oscylacjami namagnesowania, których kwanty nazywane są magnonami. Stąd pochodzi nazwa magnonika, która odnosi się do działu fizyki zajmującego się falami spinowymi. Fale spinowe, z powodu swoich właściwości, są uważane za obiecujący nośnik informacji w nowych technologiach komunikacji i przetwarzania danych, które mogą wyprzeć technologie bazujące na elektronach bądź też wspomóc starsze technologie. Wynika to z faktu, iż fale spinowe są niskoenergetycznymi oscylacjami, nie powodują rozpraszania energii w postaci ciepła Joula oraz cechują się znacznie krótszymi długościami fal dla częstotliwości mikrofalowych od fal elektromagnetycznych. Jednakże wykorzystanie potencjału fal spinowych jest hamowane przez ich wysokie tłumienie w większości znanych materiałów magnetycznych, ich czułości na fluktuacje termiczne medium w którym się przemieszczają oraz ograniczonej liczbie metod na efektywne wzbudzenie i detekcję fal spinowych. Dodatkowo, wciąż potrzebne jest opracowywanie nowych metod kontroli propagowania się fal spinowych bazujących na geometrii elementów układów magnonicznych lub zmianie zewnętrznych parametrów układu.

W tej dysertacji są przedstawione nowe metody kontroli propagowania się fal spinowych, które bazują na liniowych i nieliniowych efektach rezonansowych w dynamice fal spinowych. Liniowe efekty rezonansowe, zademonstrowane za pomocą magnonicznych interferometrów, zapewniają kontrolę nad fazą fal spinowych oraz zmianą kierunku ich propagowania się poprzez wzbudzanie stanów własnych interferometrów przy ukośnym padaniu fal spinowych. Efekty nieliniowe zostały zaobserwowane podczas nieelastycznego rozpraszania wiązki fal spinowych na modzie zlokalizowanym na krawędzi układu magnonicznego. Następstwem tychże efektów nieliniowych jest powstanie nowych wiązek o zmienionej częstotliwości, które propagują się pod innymi kątami, doznają przesunięcia przestrzennego na krawędzi układu, co jest magnonicznym analogiem efektu Goosa-Hänchen, oraz dochodzi do obniżenia amplitudy odbitych wiązek co jest magnonicznym odpowiednikiem anomalii Wooda. Wielkości rezultatów tych efektów zależą od częstotliwości i wektora falowego zlokalizowanego modu na którym następuje rozproszenie wiązek padających. Dodatkowo, gdy odpowiednie warunki opisane w dysertacji są spełnione w układzie zaobserwowano występowanie kaskady efektów nieliniowych, których jednym z wyników jest powstanie w układzie płaskich fal spinowych propagujących się od krawędzi układu.

Badania stanowiące rdzeń tej dysertacji są zawarte w pięciu publikacjach naukowych załączonych w niniejszej pracy. Dodatkowe dwie publikacje z zakresu badań nad innymi aspektami fal spinowych są również krótko przedstawione, nie należą one jednak do głównych badań w ramach

tej dysertacji. Przedstawione publikacje są poprzedzone syntetycznym wstępem do magnoniki i teorii symulacji numerycznych potrzebnym do zrozumienia metodologii i wyników. Dysertacja jest zakończona krótkim podsumowaniem badań, planami na przyszłość oraz wykazem osiągnięć Autora podczas studiów doktorskich.

Contents

Chapter 1

Introduction to magnetism and magnonics

Magnetic interactions were known to the humankind from the dawn of time. The tales of stones that attract one other via an unknown force come from the antiquity and can be found in the texts of ancient philosophers such as Plato and Aristotle. As there was no explanation on the nature of magnets many, as it is usual among people, attributed magical properties to them. Thus magnetism for a long time remained shrouded in mystery with notable exceptions of medieval physicist Petrus Peregrinus and renaissance physicist William Gilbert who left behind extensive descriptions of their experiments with magnets. Later, in the time of Scientific Revolution and Enlightenment, magnetism or more precisely electromagnetism became one of the primary topic of investigations for many physicists whose name become etched in history such as Gauss, Coulomb, Ampère, Oersted, Faraday, Maxwell. However, the proper explanation of the nature of magnetism came from quantum physics and can be found in works of Pauli, Hund, Ising, Lenz, Weiss, Curie, Néel to name a few. Modern investigations on magnetism focus heavily on magnetisation precession as a new mean for data transmission and processing. The basis of these investigations come from seminal works of von Neumann, Landau, Lifshitz, Gilbert, Aharoni, Thiele, Slonczewski and many more.

This Chapter starts with a compact introduction to the concept of magnetism with its origin. Then the description of magnetic wave propagation is provided with its properties. The Chapter ends with a brief presentation of certain non-linear processes observed in magnetic wave motion.

1.1   Origin of magnetism

The source of magnetism lies in the structure of an atom. To be more precise, the dual angular momentum of electrons which are one of the atom's building elements. The electrons, bonded with the atom's nucleus primarily by the electromagnetic interaction display total angular momentum $\mathbf{J}$, Fig. 1.1, which consists of two components [1][p. 10]

$$\mathbf{J} = \mathbf{L} + \mathbf{S}, \tag{1.1}$$

where $\mathbf{L}$ describes the orbital angular momentum of electron and $\mathbf{S}$ stands for electron's intrinsic angular momentum called **spin**. The name 'spin' is problematic as it may invoke a picture of spinning subatomic particle. Such an image is incorrect when taking into account the uncertainty principle of quantum mechanics [2]. Nevertheless, for the historical and practical reasons, the name spin is widely used in science and will be used in this thesis as well.

The spin creates around itself a dipole-like magnetic field as sketched in Fig. 1.3. The arrows indicate the field's flow from the 'South' pole to the 'North' pole of the spin. In quantum physics the spin is described by the spin quantum number which takes integer or half-integer values. The particles with integer spin quantum number are called bosons and obey Bose-Einstein statistics [3], while the particles with half-integer spin quantum number are called fermions which obey Fermi-Dirac statistics [4, 5]. The electrons display spin quantum number $s = \pm\frac{1}{2}$ what was shown in the famous Stern–Gerlach experiment [6]. The quantum nature of spin also manifest
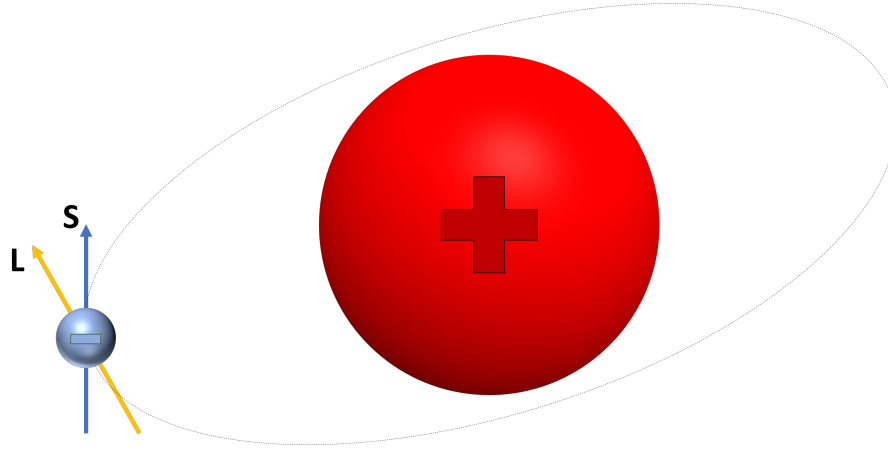
Figure 1.1 Rutherford model of an atom. The electron, depicted with the green sphere, has two types of angular momenta. The orbital angular momentum **L** is related to electron's orbital movement around the nuclei. The intrinsic angular momentum **S** is an inherent property of electrons. The main contribution to magnetic properties of a body comes from **S** as the average orbital angular momenta in a system consisting of may atoms is close to zero because of so called quenching phenomenon.

itself also in the uncertainty principle for angular momentum. In this case of spin the uncertainty principle states that only one of its spatial components can be measured at a given time.

The angular momentum of the electrons gives rise to the magnetic moment defined as

$$\mu = \gamma \mathbf{J},\tag{1.2}$$

where to proportionality factor γ, which later will be called the gyromagnetic ratio, is defined as

$$\gamma = g\frac{q}{2m_q}.\tag{1.3}$$

The charge and mass of the electron are represented by q and m_q respectively, g stands for so called Landé factor which provides the information on the contributions to the angular momentum [1][p. 12]. The numerical value of Landé factor is in range between 1 and 2, where 1 means contribution from the orbital angular momentum only and 2 indicates a sole contribution from the spins. In the majority of magnetic materials the main contribution to magnetic moments comes from the spins. This situation is a result of phenomenon known as quenching of orbital angular momentum caused by self-cancelling of electric fields generated by the periodic arrangement of ions in magnetic materials [7]. In this thesis the value of gyromagnetic ratio $|\gamma|$ is assumed as 176 radGHz/T in the International System of Units (SI), which corresponds to pure spin contribution to the magnetic moment.

The magnetisation of a given material is the space average of all its magnetic moments. The overall vector of net magnetisation **M** can be defined in a discreet approach as a sum of magnetic moments per unit volume

$$\mathbf{M} = \frac{1}{V}\sum_{\mathbf{i}}\mu(\rho_{\mathbf{i}})\tag{1.4}$$

where ρ_i is vector of a particular atom position in the magnetic body and V is the volume of magnetic body. In SI units magnetisation is defined as ampere per metre (A/m). The magnetisation is of great importance as it is a quantity that can be relatively easily measured in experiments. As stated in the previous paragraph the spins of electrons give rise to the magnetism. Thus, the order of spins determines the magnetic character of a given material. The magnetic order in turn depends on number of factors such as the interactions among the spins, the applied external magnetic field, the temperature, and the internal structure of material. The following sections of this Chapter are devoted to the description of the most prevalent interactions between spins and most common types of magnetic materials.

1.2   Types of magnetic interactions

In this section chosen types of interactions between spins will be described. The focus will be on the interactions encountered in the main part of the research presented in this thesis. Also a smaller list of other interactions will be presented shortly. These interactions were either used in the auxiliary studies carried out in parallel to the main research or will be used in the future investigations.

1.2.1   Zeeman interaction

The spin can be imagined as the smallest possible magnet unit with two magnetic poles, North (N) and South (S). When placed in an external magnetic field $\mathbf{H}_{\text{ext}}$, as shown in Fig. 1.2, a torque τ acts on the spin that try to align it with the field's direction. Such a situation occurs to minimise the potential energy of the spin submerged in $\mathbf{H}_{\text{ext}}$. The strength of magnetic field has SI unit of (A/m). In terms of energy density the interaction between spin and external magnetic field can be written as [1][p. 37]

$$E_{\text{Zeeman}} = -\mu_0 \mathbf{H}_{\text{ext}} \cdot \mathbf{M}, \tag{1.5}$$

where μ_0 is the permeability of vacuum which numerical value is $\mu_0 = 1.26\ \mu\text{H/m}$ in SI units. The interaction, named after the Dutch physicist Pieter Zeeman who first described it, favours then a parallel alignment of the magnetisation vector to the applied external magnetic field.

1.2.2   Dipolar interaction

A spin can be associated with a magnetic dipole moment, analogous to an electric dipole in electrostatics. This magnetic dipole moment generates a dipolar field through which the spin interacts with other nearby spins. If we define the distance between two spins as a vector $\mathbf{r}$, Fig. 1.3, we can describe the energy of dipole-dipole interaction as

$$E_{\text{dip}} = -\mathbf{B_1}(\mathbf{r}) \cdot \mu_2, \tag{1.6}$$
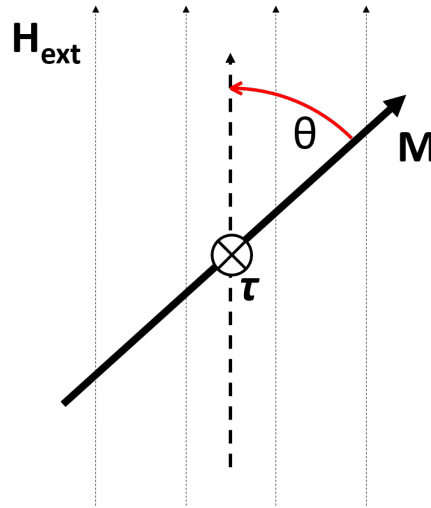
Figure 1.2 Illustration of Zeeman interaction. When magnetisation vector **M** is placed in the external magnetic field **H**ext a torque τ appears that aligns **M** parallel with the direction of **H**ext. The energy associated with this interaction scales as a negative scalar product of **M** and **H**ext.

where μ_2 is magnetic moment of a second spin and $\mathbf{B_1}(\mathbf{r})$ is magnetic flux density, which SI unit is Tesla (T), created by the first spin of magnetic moment μ_1. The relation between magnetic flux density and magnetic field intensity may be described with a formula [8][p. 35], [9][p. 280]

$$\mathbf{B} = \mu_0 \left(\mathbf{H} + \mathbf{M} \right). \tag{1.7}$$

The field $\mathbf{B_1}(\mathbf{r})$ is given as [10][p. 148]

$$\mathbf{B_1}(\mathbf{r}) = \frac{\mu_0}{2\pi} \frac{3(\mu_1 \cdot \mathbf{r})\mathbf{r} - r^2\mu_1}{r^5}. \tag{1.8}$$

The dipolar interaction, as evident in Eq. 1.6, favours the anti-parallel alignment of spins. However, its energy is relatively low. In typical magnetic materials, the dipolar interaction between two spins involves energies on the order of $\sim 10^{-21}$ J [8][p. 50] [11][p. 7]. Comparing this with the energy of thermal fluctuations given by the Boltzmann formula, $E_{th} = k_b T$, where k_b is the Boltzmann constant, it is evident that the dipolar interaction corresponds to temperatures only slightly above the absolute zero. Because of this, one might expect its influence on spin ordering in magnetic materials to be negligible. However, as it will be demonstrated later in this dissertation, the dipolar interaction plays a crucial role in long-range spin ordering despite its seemingly weak nature.

When considering a mesoscopic description of a magnetic material, the anti-parallel alignment of spins within a given volume leads to a vanishing net magnetisation. However, at the boundaries of a uniformly magnetised body, there are not enough opposing dipoles to cancel the magnetic field produced by the surface dipoles. These uncompensated dipoles are referred to as magnetic surface charges, and the magnetic field they generate is described in two ways: as the demagnetising field **H**demag inside the magnetic body, and as the stray field **H**stray outside it.
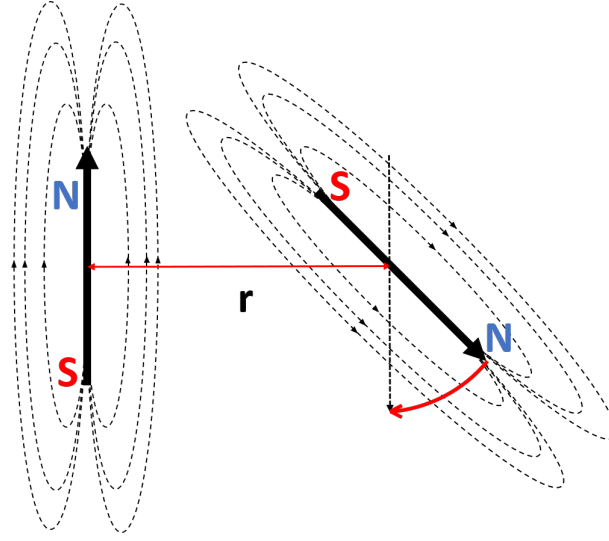
Figure 1.3 Illustration of magnetic dipole-dipole interactions. Two spins generate around themselves dipolar fields through which they interact with each other. Dipolar interaction favours anti-parallel configuration of spins, the opposite poles of spins are attracted to one another. The strength of interaction scales as r^{-3} thus it can be regarded as long ranged interaction.

The demagnetising field always opposes the magnetisation inside the sample, as indicated by the formula [12, 13]

$$\mathbf{H}_{\text{demag}} = -\bar{N} \cdot \mathbf{M}, \tag{1.9}$$

where $\bar{N}$ is the demagnetising tensor which depends on the shape of magnetic sample and may be defined as

$$\bar{N} = \begin{pmatrix} N_{xx} & 0 & 0 \\ 0 & N_{yy} & 0 \\ 0 & 0 & N_{zz} \end{pmatrix}, \tag{1.10}$$

where N_{xx}, N_{yy}, N_{zz} are called demagnetisation factors [14][p. 380]. Then the internal field experienced by a magnetic body in the presence of external magnetic field can be written as $\mathbf{H}_{\text{int}} = \mathbf{H}_{\text{ext}} - \mathbf{H}_{\text{demag}}$. The calculation of the demagnetising field is, in most cases, complex as the dipolar interactions are anisotropic and long-range in nature. Nonetheless, for the simple geometries such as thin films, spheres, or ellipsoids the demagnetising field can be derived relatively easy because of the shape symmetries. In other cases the demagnetising field has to be calculated numerically with some degree of error. The importance of demagnetising field lies in its alteration of parameters of the magnetic body at its boundaries, what was exploited in the investigations presented in Section 5.6.

Outside of the magnetic material Gauss equation for the magnetism states that $\nabla \cdot \mathbf{B} = 0$. The magnetic flux is defined as [8][p. 33]

$$\mathbf{B} = \mu_0(\mathbf{H}_{\text{stray}} + \mathbf{M}). \tag{1.11}$$

For the purpose of this derivation it is assumed that the magnetic body which creates the stray field is placed in a vacuum where there are no magnetic particles and no electric currents. Then, according to Ampère's law, the rotation of stray field should be zero,

$$\nabla \times \mathbf{H}_{\text{stray}} = 0. \tag{1.12}$$

Solving this equation yields an expression for $\mathbf{H}_{\text{stray}}$ in the terms of a scalar potential field [8][p. 46]

$$\mathbf{H}_{\text{stray}} = -\nabla\phi. \tag{1.13}$$

The potential ϕ, known as the magnetostatic potential, extends throughout the magnetic body and into the surrounding space. Its presence enables interactions between magnetic bodies that are not in direct physical contact. This long-range character of the magnetostatic potential gives rise to rich physical phenomena, particularly in magnetic interferometers, which are explored in detail later in this dissertation, especially in Sections 5.2, 5.3, 5.4 and 5.5.

1.2.3　Exchange interaction

The exchange interaction originates from the Pauli exclusion principle and electrostatic Coulomb interaction. Heisenberg [15] and Dirac [5] developed the theoretical framework for this interaction to explain the spontaneous order of magnetisation observed in certain metals and their alloys (the types of magnetisation ordering will be described in Section 1.3). This interaction depends on the spatial overlap of adjacent electrons' wave-functions. The mathematical description of the exchange interaction energy can be written as a Hamiltonian [1][p. 46]

$$\mathcal{H}_{\text{ex}} = -\frac{2}{\hbar^2} \sum_{i \neq j} \mathcal{J}_{ij} \mathbf{S_i} \cdot \mathbf{S_j}, \tag{1.14}$$

where $\mathcal{J}_{ij}$ is the exchange integral that depends on the energy difference between parallel and antiparallel spin configurations, and $\mathbf{S}$ is the spin operator. The exchange interaction is typically short-ranged, as $\mathcal{J}_{ij}$ is significant for nearest-neighbour spins only. Additionally, the sign of $\mathcal{J}_{ij}$ determines the type of spin ordering in magnetic materials. A positive $\mathcal{J}_{ij}$ favours parallel spin alignment, while a negative $\mathcal{J}_{ij}$ favours antiparallel alignment.

To simplify the derivation it can be assumed that $\mathcal{J}_{ij}$ has a constant value for all spins in the system and that only interaction with the nearest neighbours provides a substantial input to the exchange energy, then

$$E_{\text{ex}} = -2\mathcal{J}\mathbf{S_i} \cdot \sum_{\text{n.n}} \mathbf{S_j}, \tag{1.15}$$

in discreet notation, where $n.n.$ expression means "nearest neighbours". Defining the magnetic moment in term of spin $\mu = -g\mu_B \mathbf{S}$, where $\mu_B = \frac{e\hbar}{2m_e}$ is Bohr magneton, the magnetic field

created by the exchange interaction can be written as

$$\mathbf{H_{ex}} = \frac{2\mathcal{J}}{g\mu_0\mu_B} \sum_{n.n} \mathbf{S_j}. \tag{1.16}$$

In the case of magnetic materials regarded in this thesis it can be assumed that the materials exhibit cubic lattice and non-uniform magnetisation. Then the effective magnetic field related to the exchange interaction is defined as

$$\mathbf{H_{ex}} = \lambda_{ex}^2 \nabla^2 \mathbf{M}, \tag{1.17}$$

where λ_{ex} is the exchange length which characterises magnetic materials and is defined as [16, 17]

$$\lambda_{ex} = \sqrt{\frac{2A_{ex}}{\mu_0 M_S^2}}. \tag{1.18}$$

The new parameter A_{ex} is called the exchange stiffness constant, has an SI unit (J/m) and depends on the material's atomic structure as $A_{ex} = \frac{nS^2\mathcal{J}}{a}$ where n is number of the nearest neighbouring spins and a is the lattice constant. The parameter M_S is called magnetisation saturation and describes the magnetisation of a magnetic body with all spins aligned in one direction. The Laplacian operator ∇^2 in Eq. 1.17 is introduced by using an approximation of $\mathbf{S_j}$ regarded as $\mathbf{S}(\mathbf{r}_i)$ shifted by an infinitesimal distance $d\mathbf{r}_i$ [1][p. 83]

$$\mathbf{S_j} = \mathbf{S}(\mathbf{r}_i + d\mathbf{r}_i) \approx a^2 \nabla^2 \mathbf{S}(\mathbf{r_i}) + 6\mathbf{S}(\mathbf{r_i}). \tag{1.19}$$

The term $6\mathbf{S}(\mathbf{r_i})$ can be omitted as contribution from the magnetisation non-uniformities is mainly responsible for exchange interaction. In the end the magnetisation vector can be introduced using a formula

$$\mathbf{M} = g\mu_B \langle \mathbf{S} \rangle_V, \tag{1.20}$$

where $\langle \mathbf{S} \rangle_V$ is an average of spins over a space.

The magnetic interactions presented in this Section were the cornerstone of the main investigations shown in this thesis which are described in Chapter 5.

1.2.4 Other components of effective magnetic field

1.2.4.1 Magnetocrystalline anisotropy

The crystallographic lattice of magnetic materials may favour certain directions along which the magnetisation vector $\mathbf{M}$ aligns spontaneously. These directions are known as easy axes. Conversely, there are directions along which a strong external magnetic field is required to align $\mathbf{M}$; these are referred to as hard axes. The existence of such energetically favourable and unfavourable directions of magnetisation is known as magnetocrystalline anisotropy. Its

origin lies in the symmetry breaking of electron orbitals within periodic lattices. As mentioned, anisotropy depends on the crystallographic structure of the magnetic body, but it can also be influenced by lattice imperfections, the shape of a magnetic sample, or externally applied conditions such as strain or temperature [18].

In the case of uniaxial magnetocrystalline anisotropy the energy density can be described with a formula [1][p. 84]

$$E_{\text{ua}} = K_{\text{u1}}\sin^2(\theta) + K_{\text{u2}}\sin^4(\theta) + ...,\tag{1.21}$$

where K_{ui} are anisotropy constants (unit J/m^3), θ is a polar angle with regard to the anisotropy easy axis direction and $\sin(\theta)$ functions raised to even powers assure symmetry of the anisotropy. The ellipsis in Eq. 1.21 indicates that for better accuracy of anisotropy calculations higher order components can be added to the expression. The positive value of K_{ui} parameter indicates the easy-axis in the system and the negative value indicates the hard-axis.
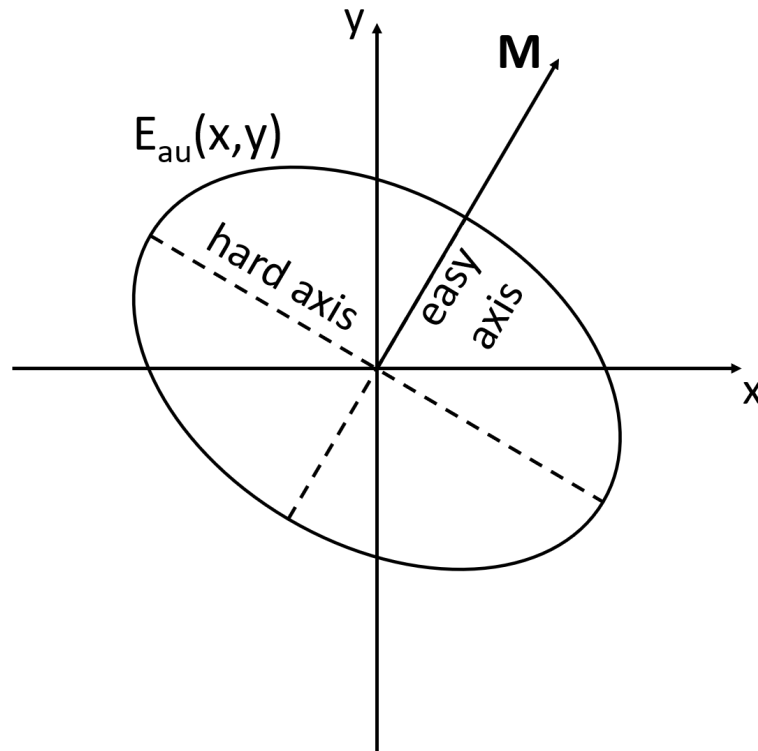
Figure 1.4 Anisotropy energy as a function of direction in (x, y) plane. The function is described by an ellipse which minor axis represents system's easy axis and major axis represents the hard axis. The energetically favourable magnetic configuration will align with the easy axis in the absence of the external magnetic field as it is shown.

The effective magnetic field created by the anisotropy in a magnetic material can be expressed as a variation of anisotropy energy functional with respect to the magnetisation vector [11][p. 37], [1][p. 85].

$$\mathbf{H}_a = -\frac{1}{\mu_0}\frac{\delta E_{ua}}{\delta \mathbf{M}}. \tag{1.22}$$

To derive the effective magnetic field in the case of a material with uniaxial anisotropy along its z-axis we can simplify the expression Eq. 1.21 by using the trigonometric unity formula $\sin^2(\theta) = 1 - \cos^2(\theta)$ and by approximating $\cos(\theta)$ by an expression m_z/M_S. This approximation is done with an assumption of small angle θ ($\theta \ll 5°$). Then, by taking into account only contribution from K_{u1} the expression for the anisotropy energy density is

$$E_{ua} \approx K_{u1}\left(1 - \frac{m_z^2}{M_S^2}\right). \tag{1.23}$$

After using expression Eq. 1.23 in Eq. 1.22 the effective uniaxial anisotropy field takes the from of

$$\mathbf{H}_a = \frac{K_{u1}}{\frac{1}{2}\mu_0 M_S^2}m_z\hat{z}, \tag{1.24}$$

where $\hat{z}$ is a unit vector pointing along the z-axis.

1.2.4.2   Shape anisotropy

The anisotropy can also be induced in the magnetic body by its shape [19][p. 88], [8][p. 168]. It is a results of the dipolar interaction that creates the demagnetising field at the magnetic bodies' surfaces along which magnetic charges align. This phenomenon is especially prevalent in the thin magnetic bodies where there is not enough magnetic dipoles in the bulk of the magnetic body to separate demagnetising fields induced at the layer's surfaces. In the thin layers the shape anisotropy favours in-plane (IP) spin alignment which requires application of a strong external magnetic field to change the spins alignment to out-of-plane (OOP) configuration.

1.2.4.3   Dzialoshinskii-Moriya interaction

Due to spin-orbit coupling and broken inversion symmetry, Dzialoshinskii-Moriya interaction (DMI) introduces an antisymmetric exchange interaction that favours a canted or chiral spin arrangement, leading to non-collinear magnetic structures [20–22]. This interaction can be described with a following Hamiltonian [8][p. 139]

$$\mathcal{H}_{DMI} = -\mathbf{D}\cdot(\mathbf{S}_i \times \mathbf{S}_j), \tag{1.25}$$

where $\mathbf{D}$ is the Dzyaloshinskii-Moriya vector. This form of interaction is antisymmetric, as it arises from the cross product of neighbouring spins, leading to a preferred chirality in spin alignment. Opposite to the other mentioned interactions DMI does not favour either parallel or anti-parallel alignment of the neighbouring spins but an orthogonal one. Additionally, DMI also introduces chirality to the spin ordering (whether spins are aligned counter- or clockwise), what is indicated by the negative sign in Eq. 1.25. Thus when DMI appears in a magnetic system it

allows for more complex magnetic textures such as skyrmions, hopfions, etc. DMI can occur in two distinct forms: bulk DMI, which arises in magnetic materials with non-centrosymmetric crystal structures [23]; and interfacial DMI, observed at interfaces between thin films when one of the materials exhibits strong spin–orbit coupling [24].

Both magnetocrystalline anisotropy and DMI have been taken into account in additional studies presented in Chapter 6.

1.3   Classification of magnetic materials

1.3.1   Diamagnets

Diamagnets constitute a class of materials with zero net magnetic moment. When placed in an external magnetic field the electrons in diamagnetic atoms start to rotate in such a way that their orbits induce their own magnetic field which is opposite to the applied one. This phenomenon is the result of Lenz's law [1][p. 3]. Hence diamagnets weaken locally the magnetic field in which they are placed [19][p. 10].

The relation between magnetisation vector and the external magnetic field can be expressed as [1][p. 1]

$$\mathbf{M} = \mathbf{M}_0 + \bar{\chi}\mathbf{H}, \tag{1.26}$$

where $\mathbf{M}_0$ is the spontaneous magnetisation vector (magnetisation which is present in the absence of the applied external magnetic field) and $\bar{\chi}$ is the susceptibility tensor. In the case of isotropic diamagnets $\bar{\chi}$ is a scalar of negative value which can be calculated with so-called Langevin formula of diamagnetism [1][p. 69].

It is also important to note that all materials possessing magnetic moments exhibit diamagnetic behaviour to some extent [25][p. 459]. However, in many materials, other magnetic phenomena—such as paramagnetism, ferromagnetism, or antiferromagnetism—dominate the overall magnetic response, effectively overshadowing the underlying diamagnetism. Some of these magnetic behaviours will be discussed in the following subsections. Nonetheless, diamagnetism remains a universal and intrinsic property of all matter in the presence of the external magnetic field.

1.3.2   Paramagnets

The next class of magnetic materials is known as paramagnets. These materials contain atoms or ions with intrinsic magnetic moments due to unpaired electrons. However, in the absence of external magnetic field, thermal fluctuations prevent long-range magnetic order in paramagnets. When an external magnetic field is applied, the magnetic moments of paramagnet tend to align with the field. This occurs because aligning with the external field lowers Zeeman energy. However, due to persistent thermal agitation, full alignment is not achieved, resulting in only

a weak net magnetisation [19][p. 12]. The partial alignment of magnetic moments slightly enhances the external magnetic field, although the effect is relatively weak. For isotropic paramagnets, the magnetic susceptibility tensor $\bar{\chi}$, Eq.1.26 , reduces to a positive scalar quantity [1][p. 72].

1.3.3 Ferromagnets
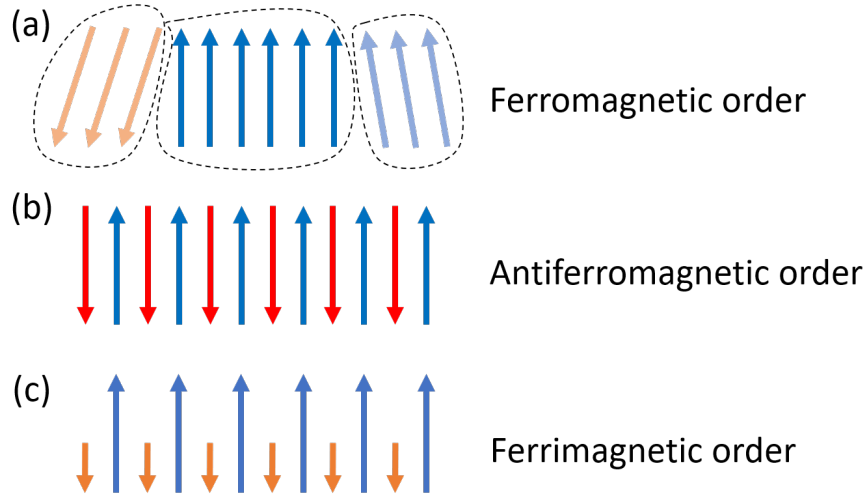
Figure 1.5 Examples of magnetic configuration order in different magnetic materials. (a) presents the ferromagnetic order where all spins within one domain point to the same direction. Such a system appears when the exchange integral $\mathcal{J}$ is positive. (b) shows the antiferromagnetic order, the spins are arranged alternatively and can be regarded as two sublattices. The antiferromagnetic order occurs when $\mathcal{J}$ is negative. (c) displays the ferrimagnetic order, which resembles antiferromagnetic but one of the sublattices has smaller magnetisation magnitude, thus system in total has non-zero net magnetisation.

Ferromagnets, similarly as paramagnets, are made of intrinsic magnetic moments. The permanent magnetic moments come from the unfilled electron shells of certain atoms [25][p. 435]. According to the Hund's rule, electron shells are filled with electrons in such a way to assure the lowest possible energy state of an atom [26][p. 765]. In the case of most atoms it means that each shell is filled by a pair of electrons with different spin numbers with zero net angular momentum. However, for certain elements Hund's rule actually favours leaving some inner shells unfilled. The ramification of this fact is that these elements have non-zero angular momentum which is unaffected even when these elements create bonding with other elements. These few elements and their alloys have ferromagnetic or ferrimagnetic (this class of materials will be the topic of one of the next subsections) nature. The notable representants of these elements are Fe, Co, Ni and rare earth metals such as Nd [8][p. 375]. Examples of widely used alloys with ferromagnetic nature are Permalloy (Py, an alloy made of Fe and Ni in different proportions) and CoFeB.

The key difference between ferromagnets and paramagnets is that ferromagnets exhibit spontaneous magnetisation. When no external magnetic field is applied, the magnetisation in
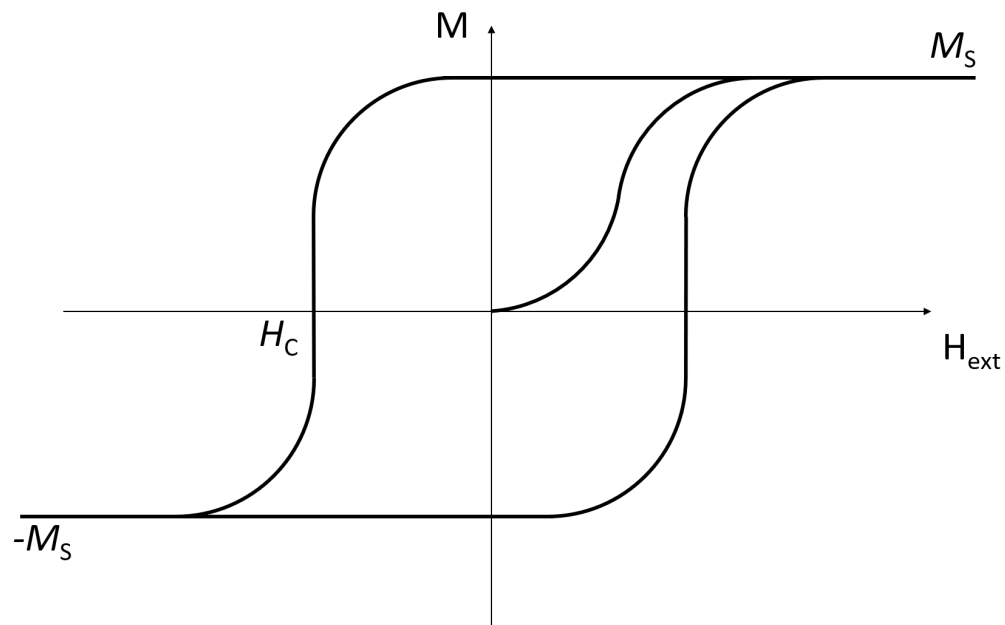
Figure 1.6 A scheme of hysteresis loop of a ferromagnet that is obtained by measuring system's magnetisation vector in changing external magnetic field. The relation starts with so called initial magnetisation curve at point $(0,0)$ with refers to non-magnetised state. Then with an increase of the external magnetic field the order of spins appears which causes an increase of magnetisation vector magnitude up to certain value called magnetisation saturation, M_S. For higher applied magnetic fields changing the magnitude and direction of the external magnetic field does not affects the order of spins in ferromagnetic, only their direction. The crucial property of $M(H_{ext})$ is the fact that it depends on the previous magnetic configuration of the system. Because of that $M(H_{ext})$ dependency resembles a loop. The value of field needed to reset system's magnetic order is called coercive field and is marked with H_c. The area enclosed by a loop contains information on the energy needed to change the direction of system's magnetisation.

a ferromagnet consists of multiple magnetic domains. Within each magnetic domain, spins are aligned in parallel due to the strong exchange interaction among them [19][p. 16]. The division into multiple magnetic domains is favoured due to dipole interactions, cf. Section 1.2.2. If a ferromagnet consisted of only one large domain, the dipole interaction energy would be substantial. To minimise the dipolar energy, the system naturally breaks into microscopic domains with lower energy [14][p. 352], [19][p. 120]. Even though the domains themselves are not exactly parallel to one another, the ferromagnet may still exhibit a net magnetic moment in the absence of an external field. This net magnetic moment is called remanence.

When an external magnetic field is applied the magnetic domains start to align with the field. At a certain value of the magnetic field all of the domains align with the field and the ferromagnet reaches the state of saturation, cf. Section 1.2.3. When the value of external magnetic field is decreased the magnetisation does not take the same values as during increasing of the field. This phenomenon is called hysteresis and is typical for the ferromagnetic materials, because their magnetisation at a given value of $\mathbf{H}_{ext}$ depends also on the previous magnetic state $\mathbf{M}_0$. When dependency $M(H_{ext})$[1] is plotted as in Fig. 1.6 it it a closed curve, which is called a hysteresis loop [27]. The shape and features of hysteresis loop provides significant amount of information about the ferromagnetic material. For instance, they reveal the coercive field, H_C, the magnitude of the external magnetic field that must be applied in the opposite direction to reduce the remanent magnetisation to zero. Furthermore, the area enclosed by the hysteresis loop provides insight into the ease of re-magnetisation. A small area indicates a soft ferromagnet, whose magnetisation can be readily reoriented, while a large area signifies a hard ferromagnet, requiring much stronger fields for magnetisation reversal [8][p. 8].

The magnetisation order in a ferromagnet depends also on temperature. The long-range order of ferromagnet's exists only when thermal fluctuations of spins are relatively small. It means that above certain temperature the energy of random thermal fluctuations is high enough to destroy the magnetic order. This temperature is called Curie temperature (T_C) and differs for particular ferromagnets [1][p. 73]. At T_C ferromagnets undergo a phase transition to paramagnet state [11][p. 7]. A sketch of $M(T)$ dependency with marked T_C temperature is shown in Fig. 1.7.

1.3.4 Antiferromagnets

For certain magnetic materials the exchange integral $\mathcal{J}$ from Eq. 1.15 takes negative values [19][p. 20]. It means that the exchange interaction in this case favours the anti-parallel configuration of spins, see Fig. 1.5(b). Such a configuration can be regarded as two sublattices of spins with opposite magnetisations. When the magnitudes of magnetisation in these sublattices are equal, the material is referred to as an antiferromagnet. Antiferromagnets display only a small net magnetisation if temperature is above the absolute zero. Only then the thermal fluctuations disturb the ordering of spins in both sublattices and the net magnetisation can differ from zero [1][p. 5]. When antiferromagnet is placed in an external magnetic field parallel to the plane

---

[1]Mark here that, the dependency $M(H_{ext})$ operates on scalars and not on the vectors. In measurements of the hysteresis usually only one of the field and one of magnetisation components are measured.
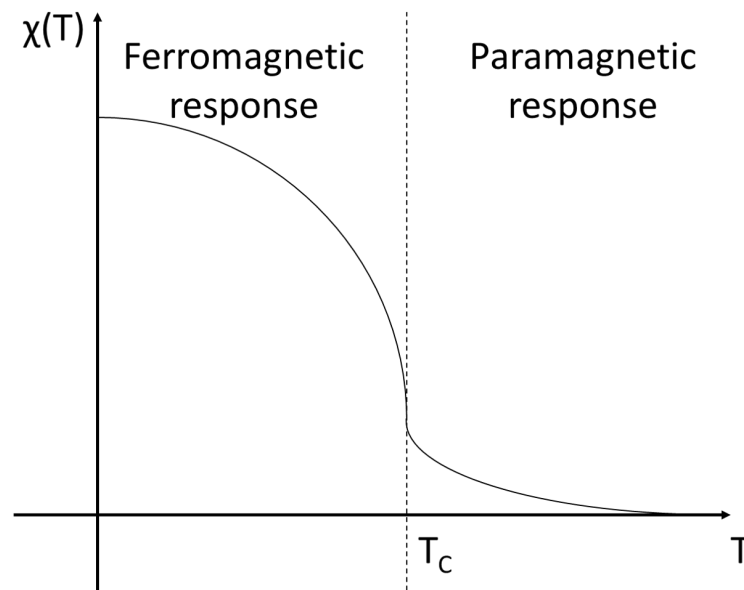
Figure 1.7 Magnetic susceptibility χ of a ferromagnetic as a function of temperature. At certain value of temperature, called Curie temperature T_C, phase transition happens when ferromagnetic looses its magnetic ordering due to strong thermal fluctuations. In the temperatures above T_C systems resembles a paramagnetic.

of spin ordering small or no torque can be measured as two opposite sublattices create opposite torques which cancel each other. When a perpendicular magnetic field above certain threshold is applied to the antiferromagnet its spins align with the field. Such a phenomenon is called spin flop transition [28–30].

Similarly as in the case of ferromagnets, thermal fluctuations also can destroy the spin order in antiferromagnets when the temperature is too high. The critical temperature below which antiferromagnetic ordering appears is called Néel temperature [1][p. 79] and it is a direct analogue to the Curie temperature for ferromagnets. When temperature is higher than Néel temperature antiferromagnets behave like paramagnets.

1.3.5 Ferrimagnets

Ferrimagnets display two sublattices ordering of spins as antiferromagnets. Unlike for the antiferromagnets however, two sublattices in ferrimagnets differ in their net magnetisation, as shown in Fig. 1.5(c) [19][p. 27]. Because of that ferrimagnets have an uncompensated net magnetisation and for low frequencies (for microwaves and lower) they behave like ferromagnets [1][p. 4]. A ferrimagnet of particular interest in magnetic investigations is yttrium iron garnet (YIG), $Y_3Fe_5O_{12}$ [8][p. 201]. In this material five iron atoms provide the ferromagnetic nature in YIG, where three atoms belong to one lattice and two to the other. Thus in YIG effectively only one atom of iron provides an input to the net magnetisation. The most important property of YIG is its low magnetic damping (magnetic damping will be described in the next Section) what makes

it a very promising material for applications. Additionally, YIG exhibit relatively low M_S what makes easier to excite magnetic precession in this material [1][p. 333].

1.4   Dynamics of magnetic moment

1.4.1   Magnetisation equation of precession

The precession of the angular momentum Eq. 1.2 placed in an effective magnetic field $\mathbf{H}_{\text{eff}}$ is defined as [1][p. 91]

$$\frac{d\mathbf{J}}{dt} = \gamma\mu_0\mathbf{J} \times \mathbf{H}_{\text{eff}}. \tag{1.27}$$

This equation can be rewritten in terms of magnetisation vector by using formula $\mathbf{M} = \gamma N \mathbf{J}$, where N is number of the magnetic moments under consideration. Then Eq. 1.27 takes form of

$$\frac{d\mathbf{M}}{dt} = \gamma_G\mathbf{M} \times \mathbf{H}_{\text{eff}}. \tag{1.28}$$

The equation Eq. 1.28 is called the Landau-Lifshitz (LL) equation and it is the cornerstone of investigations on magnetisation dynamics [31]. The new parameter γ_G is defined as $\gamma_G = \gamma\mu_0$. The LL equation preserves the magnitude of magnetisation vector $\|\mathbf{M}\|$ in time. The effective magnetic field, $\mathbf{H}_{\text{eff}}$, is a sum of magnetic fields derived from the dipole interaction $\mathbf{H}_{\text{demag}}$ (Eqs. 1.9, 1.13), the exchange interaction $\mathbf{H}_{\text{ex}}$ (Eq. 1.17), magnetocrystalline anisotropy $\mathbf{H}_a$ (Eq. 1.24), external magnetic field $\mathbf{H}_{\text{ext}}$, DMI interaction, ect...

In the simplified approach where the only contribution of effective magnetic field comes from the external magnetic field $\mathbf{H}_{\text{eff}} = \mathbf{H}_{\text{ext}}$ it is possible to describe the precession of the magnetisation vector as a sum of the saturation magnetisation vector M_S pointing in the direction of effective magnetic field and a dynamic magnetisation vector $\mathbf{m}(t)$ [2]

$$\mathbf{M}(t) = M_S\hat{z} + \mathbf{m}(t). \tag{1.29}$$

After introduction of this expression to the Eq. 1.28 the equation of precession takes form

$$\frac{d\mathbf{m}}{dt} = \gamma_G\mathbf{m} \times \mathbf{H}_{\text{ext}}, \tag{1.30}$$

because $\frac{dM_S}{dt} = 0$ and $M_S \times \mathbf{H}_{\text{ext}} = 0$. Assuming that the precession of magnetisation vector is harmonic, $\mathbf{m}(t) = m_0 e^{i\omega t}$, the solution of Eq. 1.30 in the frequency domain is

$$\omega = \omega_L = \gamma_G H_{\text{ext}}. \tag{1.31}$$

---

[2]with an assumption that $M_S \gg \|\mathbf{m}\|$

This solution is called the Larmor frequency ω_{L} and it is the frequency of harmonic precession of magnetisation vector in the presence of external magnetic field. This precession is schematically presented in the Fig. 1.8.
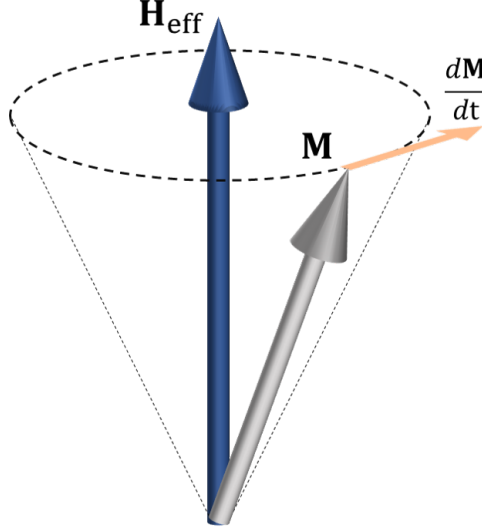
Figure 1.8 Scheme of magnetisation vector $\mathbf{M}$ precession around the effective magnetic field $\mathbf{H}_{\mathrm{eff}}$. The vector $\mathbf{M}$ precesses around $\mathbf{H}_{\mathrm{eff}}$ with $\mathbf{M} \times \mathbf{H}_{\mathrm{eff}}$ tangential to the precession orbit being traced. In isotropic materials $\mathbf{M}$ draws circle around $\mathbf{H}_{\mathrm{eff}}$, in the case of anisotropic materials $\mathbf{M}$ trajectory is elliptical.

However, in more general approach, where additional contributions to the effective magnetic field are included, the precession of magnetisation vector becomes more complex as it changes dynamically the magnetic field around it. Additionally, in real magnetic bodies also their shape anisotropy plays a significant role in influencing the precession of magnetisation. To make the derivation Eq. 1.30 more general also the vector of effective magnetic field has to be separated into the static and dynamic parts

$$\mathbf{H}_{\mathrm{eff}}(t) = \mathbf{H}_{\mathrm{ext}} + \mathbf{H}_{\mathrm{demag}} + \mathbf{h}(t), \tag{1.32}$$

$$\mathbf{M}(t) = M_{\mathrm{S}}\hat{z} + \mathbf{m}(t). \tag{1.33}$$

With this generalisation Eq. 1.28 can be rewritten as

$$\frac{d\mathbf{m}}{dt} = \gamma_G[\mathbf{m} \times (\mathbf{H}_{\mathrm{ext}} + \mathbf{H}_{\mathrm{demag}}) + M_{\mathrm{S}}\hat{z} \times \mathbf{h} + \mathbf{m} \times \mathbf{h}]. \tag{1.34}$$

The last term in Eq. 1.34 can be discarded as it is a multiplication of two small fields[3], therefore it can be neglected. Thus Eq. 1.34 simplifies to the form

$$\frac{d\mathbf{m}}{dt} = \gamma_G[\mathbf{m} \times (\mathbf{H}_{\mathrm{ext}} + \mathbf{H}_{\mathrm{demag}}) + M_{\mathrm{S}}\hat{z} \times \mathbf{h}]. \tag{1.35}$$

---

[3] $\|\mathbf{H}_{\mathrm{eff}}^{(\mathrm{stat})}\| \gg \|\mathbf{h}\|$ and $M_{\mathrm{S}} \gg \|\mathbf{m}\|$

Further calculations demand proper assumptions of dipolar interaction in the system. This leads to the determination of demagnetising tensor in Eq. 1.9.

For the purpose of this derivation a popular in the magnetisation investigations thin film shape is selected. Additionally, similarly as in the case of Larmor frequency, the harmonic oscillation of the magnetisation is chosen $\mathbf{m}(t) = m_0 e^{i\omega t}$. This means that the frequency of derived precession will describe a uniform magnetic mode of a thin magnetic layer with zero momentum. Such a mode is called ferromagnetic resonance (FMR) mode and was theoretically described by Kittel after its experimental observation by Griffiths [32, 33].
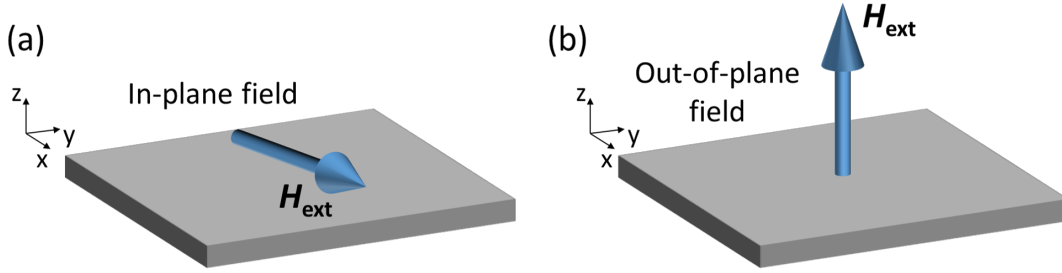
Figure 1.9 Illustration of external magnetic field configurations used in derivation FMR frequencies of thin ferromagnetic layers, (a) the field is directed IP, (b) the field is directed OOP.

In the case of the thin film two distinctly different magnetisation configurations are possible. In the first configuration the external magnetic field is applied IP to the film, as presented in Fig. 1.9(a). Then the static component of the effective magnetic film is $\mathbf{H}_{\text{ext}}$ and magnetisation saturation M_S are directed along the x axis, $\mathbf{H}_{\text{ext}} = [H_{\text{ext}}, 0, 0]^T$, $\mathbf{M} = [M_S, m_y, m_z]^T$. Additionally, in this configuration the elements of demagnetisation tensor of Eq. 1.10 are as follows $N_{xx} = N_{yy} = 0$ and $N_{zz} = 1$. Then the demagnetising field, according to Eq. 1.9 is $\mathbf{H}_{\text{demag}} = [0, 0, -m_z]^T$. In such a case the Eq. 1.35 yields

$$\omega = \omega_{\text{FMR}}^{(\text{IP})} = \gamma_G \sqrt{H_{\text{ext}}(H_{\text{ext}} + M_S)}. \tag{1.36}$$

For the second configuration the external magnetic field is applied OOP, Fig. 1.9(b). Then the parameters of the system are $\mathbf{H}_{\text{ext}} = [0, 0, H_{\text{ext}}]^T$ and $\mathbf{M} = [m_x, m_y, M_S]^T$. The demagnetising tensor is the same in this configuration as it only depends on the shape of magnetic body. The demagnetising field is $\mathbf{H}_{\text{demag}} = [0, 0, -M_S]^T$. With the new parameters the frequency of FMR is

$$\omega = \omega_{\text{FMR}}^{(\text{OOP})} = \gamma_G (H_{\text{ext}} - M_S). \tag{1.37}$$

In both configuration the component $M_S \hat{z} \times \mathbf{h}$ in Eq. 1.35 is omitted as it is assumed that $h = 0$ [1][p.145,146].

The presented results derived by solving LL equation for the uniform modes provide important information about the magnetic materials. They are the base on which more complex behaviour of magnetisation precession will be described in the following Section 1.5.

1.4.2   Introduction of damping in magnetisation precession equation

The precession of magnetisation vector described by Eq. 1.28 is endless contrary to the experimental results which show that magnetisation vectors eventually align with the direction of the effective magnetic field. This is due to the presence of damping in real systems, which causes the energy dissipation of precessing magnetisation vector. The process in which the magnetisation vector loses its energy to reach the equilibrium state is called relaxation. The phenomenological addition of damping to the equation of magnetisation vector precession proposed by Gilbert [34, 35] takes form of [4]

$$\frac{d\mathbf{M}}{dt} = \gamma_G \mathbf{M} \times \mathbf{H}_{\text{eff}} - \frac{\alpha}{M_S} \left(\mathbf{M} \times \frac{d\mathbf{M}}{dt} \right),\tag{1.38}$$

where α is Gilbert damping parameter. In this form the equation of magnetisation precession is called Landau-Lifshitz-Gilbert (LLG) equation and is used in the numerical simulations of magnetic precession [37]. The precession of magnetisation vector governed by the LLG equation is presented in Fig. 1.10. After the introduction of damping the tip of magnetisation vector draws a spiral path on a surface of a virtual sphere of radius $\|M_S\|$ with the spiral ending spot in space that aligns with the effective magnetic field vector direction.
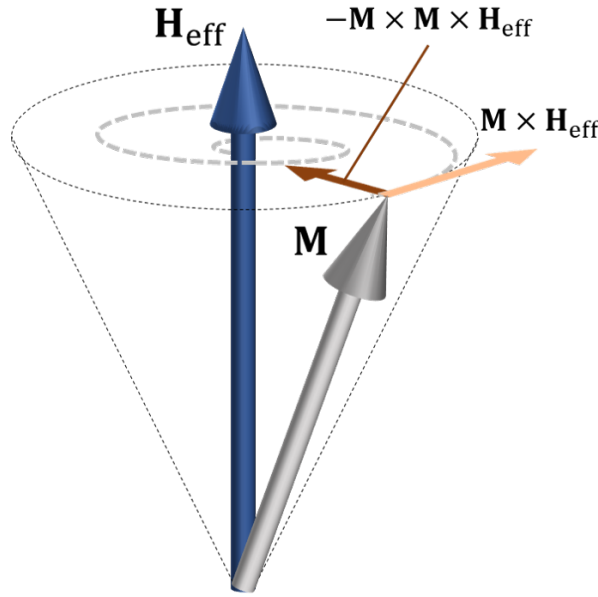
Figure 1.10 The movement of magnetisation vector $\mathbf{M}$ around the effective magnetic field $\mathbf{H}_{\text{eff}}$ in a material with magnetic damping. $\mathbf{M}$ is pulled towards the direction of $\mathbf{H}_{\text{eff}}$ by a torque proportional to $-\mathbf{M} \times \mathbf{M} \times \mathbf{H}_{\text{eff}}$ and is rotated by an another torque proportional to $\mathbf{M} \times \mathbf{H}_{\text{eff}}$. In result $\mathbf{M}$ moves on spiral trajectory to its equilibrium position which is aligned with $\mathbf{H}_{\text{eff}}$ direction.

---

[4]Thomas L. Gilbert first proposed his formulation of damping in LL equation in his PhD thesis in 1956 when he worked in Illinois Institute of Technology. However, this thesis was not openly available thus, over the years citing his contribution was difficult. For that reason he decided to publish a paper dedicated to his implementation of magnetic precession damping almost 50 years after publishing his thesis [36].

As both of Eq. 1.28 and Eq. 1.38 preserve the magnitude of the magnetisation vector $\|\mathbf{M}\|$ and are equivalent it is possible to transform Eq. 1.38 to the form

$$\frac{d\mathbf{M}}{dt} = \gamma[\mathbf{M} \times \mathbf{H}_{\text{eff}} - \frac{\alpha}{M_{\text{S}}}(\mathbf{M} \times (\mathbf{M} \times \mathbf{H}_{\text{eff}}))],\qquad(1.39)$$

which is the original formulation of LL equation with damping which is widely used in numerical calculations of magnetic precession [37]. In this form it is evident that the second component of Eq. 1.39 is a vector directed towards the effective magnetic field vector and is perpendicular to the rotational precession of the magnetisation vector. Thus, it causes the magnetisation vector to align with the direction of the effective magnetic field vector.

1.5   Spin waves

In the previous Section a special type of magnetisation precession was described. Both LL and LLG equations, respectively Eqs. 1.28 and 1.39, allow a uniform, in-phase oscillations of all spins within a magnetic body[5]. What is more important, both equations also provide the description of a more complex and coherent spin precession with phase varying over space and time. Such a precession resembles a wave and thus is called spin wave (SW). A quantum of SW is called a magnon, thus the study on SWs if often referred to as magnonics [14][p. 330]. The parameters of the SWs depend strongly on the magnetic interactions among spins that create the waves, the external magnetic field strength and the magnetic configuration of the system. This Section outlines the mathematical description of these dependencies.

1.5.1   Dispersion relation

The dispersion relation is a dependency between the wavelength and the frequency of waves. Usually, the dispersion relation is presented in a form of $\omega(k)$, where k is the wavenumber defined as $k = 2\pi/\lambda$, λ being the wavelength of SW, and ω is the angular frequency of SW. Depending on the wavelengths of the SWs there is a possibility to distinguish two main regimes of SWs. In the regime of small wavenumber k SWs have long wavelengths thus, the impact of the exchange interaction is significantly smaller than the long-range dipole interaction. For the spins with short wavelengths and big k values the situation is reversed and the short-ranged exchange interaction plays the main role in interactions among spins.

The derivation of the SWs dispersion relation can be done by using LL equation, Eq. 1.28. Similarly like in the case of deriving FMR frequencies the vectors of effective magnetic field and magnetisation can be split into static and dynamic parts. However to derive dispersion relation the dynamical parts of these vectors have to vary both in time and space. Assuming harmonic

---

[5]Eq. 1.39 allows such a precession only where there is an additional source of energy involved which compensates the dissipation of energy due to damping.

oscillations of the magnetic field and magnetisation

$$\mathbf{h}_{\text{eff},i}(\mathbf{r},t) = h_i e^{i(\mathbf{k}\cdot\mathbf{r}-\omega t)}, \tag{1.40}$$

$$\mathbf{m}_i(\mathbf{r},t) = m_i e^{i(\mathbf{k}\cdot\mathbf{r}-\omega t)}, \tag{1.41}$$

where h_i and m_i are the amplitudes and $\mathbf{k}$ is the wavevector.
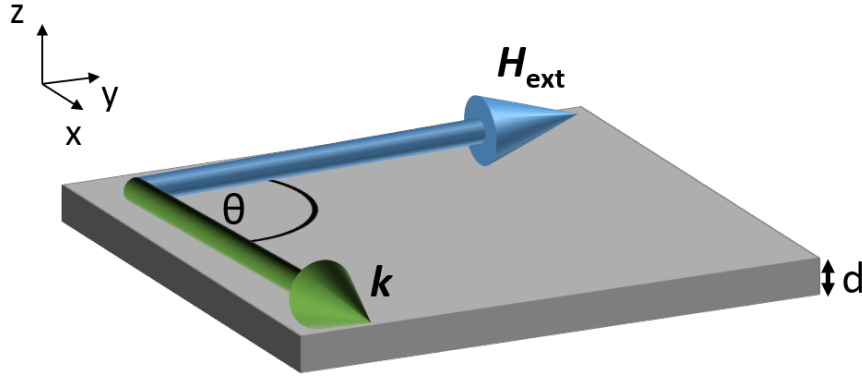
Figure 1.11 The geometry of thin Py layer used in SW dispersion relation derivation. The external magnetic field $\mu_0\mathbf{H}_{\text{ext}}$ is marked with a blue arrow. SWs propagate under angle θ to the external magnetic field. The thickness of Py layer is d.

In this example the system under consideration is a thin magnetic film with thickness d, magnetised IP along its y axis, Fig. 1.11. The effective magnetic field consists of the exchange, dipole and external fields. The dynamic exchange field will be introduced using formula Eq. 1.17. The dynamic dipole field is approximated by the formula $\mathbf{h}_{\text{dip}} = [-\sin^2(\theta)\xi(kd)m_x, 0, -(1-\xi(kd))m_z]^{\text{T}}$ valid for small d, where $\xi(x) = 1 - (1-e^{-|x|})/|x|$ and θ is an angle between SW propagation and the external magnetic field direction [38, 39]. The effective magnetic field can be written in a matrix form as

$$\mathbf{H}_{\text{eff}} = \begin{pmatrix} \lambda_{\text{ex}}^2\partial^2 m_x - \sin^2(\theta)\xi(kd)m_x \\ H_{\text{ext}} \\ \lambda_{\text{ex}}^2\partial^2 m_z - (1-\xi(kd))m_z \end{pmatrix}. \tag{1.42}$$

Eq. 1.28 in matrix form takes form

$$\begin{pmatrix} \partial_t m_x \\ \partial_t M_{\text{S}} \\ \partial_t m_z \end{pmatrix} = -\gamma_G \begin{pmatrix} M_{\text{S}}H_{\text{eff,z}} - m_z H_{\text{eff,y}} \\ m_z H_{\text{eff,x}} - m_x H_{\text{eff,z}} \\ m_x H_{\text{eff,y}} - M_{\text{S}}H_{\text{eff,x}} \end{pmatrix}, \tag{1.43}$$

where ∂_t denotes partial derivative over time. As the static component of magnetisation does not vary with time $\partial_t M_{\text{S}} = 0$ and in the linear approximation both m_x and m_z components are much

smaller than M_S thus, the middle row in Eq. 1.43 can be omitted

$$\begin{pmatrix} \partial_t m_x \\ \partial_t m_z \end{pmatrix} = -\gamma_G \begin{pmatrix} M_\mathrm{S} H_{\mathrm{eff},z} - m_z H_{\mathrm{eff},y} \\ m_x H_{\mathrm{eff},y} - M_\mathrm{S} H_{\mathrm{eff},x} \end{pmatrix}. \tag{1.44}$$

Next, when the matrix equation is rewritten as a set of equations and the components of the magnetic field are taken from Eq. 1.42 the problem transforms to solving two linear differential equations

$$\begin{cases} \partial_t m_x = -\gamma_G \left(M_\mathrm{S} \lambda_\mathrm{ex}^2 \partial^2 m_z - M_\mathrm{S} \left(1 - \xi(kd)\right) m_z - H_\mathrm{ext} m_z \right) \\ \partial_t m_z = -\gamma_G \left(H_\mathrm{ext} m_x - M_\mathrm{S} \lambda_\mathrm{ex}^2 \partial^2 m_x + M_\mathrm{S} \sin^2(\theta) \xi(kd) m_x \right) \end{cases} \tag{1.45}$$

Taking into account the assumption of harmonic oscillations, Eq. 1.41, partial derivatives works as operators $\partial_t m = -i\omega m$, $\partial^2 m = -(k_x^2 m_x, k_y^2 m_y, k_z^2 m_z)$. Then the equations change to

$$\begin{cases} -i\omega m_x = -\gamma_G \left(-M_\mathrm{S} \lambda_\mathrm{ex}^2 k_z^2 - M_\mathrm{S} \left(1 - \xi(kd)\right) - H_\mathrm{ext} \right) m_z \\ -i\omega m_z = -\gamma_G \left(H_\mathrm{ext} + M_\mathrm{S} \lambda_\mathrm{ex}^2 k_x^2 + M_\mathrm{S} \sin^2(\theta) \xi(kd) \right) m_x \end{cases} \tag{1.46}$$

After solving this set of equations for ω the dispersion relation is expressed as

$$\omega = \omega_w \sqrt{\left(\lambda_\mathrm{ex}^2 k^2 + (1 - \xi(kd)) + H_\mathrm{ext}/M_\mathrm{S}\right) \left(\lambda_\mathrm{ex}^2 k^2 + \sin^2(\theta) \xi(kd) + H_\mathrm{ext}/M_\mathrm{S}\right)}, \tag{1.47}$$

where $\omega_w = \gamma_G M_\mathrm{S}$. Fig. 1.12 presents dispersion relation for in the case of $d = 10$ nm Py layer ($M_\mathrm{S} = 800$ kA/m, $A_\mathrm{ex} = 13$ pJ/m) with SWs propagating perpendicularly to the external magnetic field, $\theta = 90°$, of $\mu_0 \mathbf{H}_\mathrm{ext} = 50$ mT. The dispersion relation obtained by simplified analytical approach is presented with a solid green line. The colourmap in the background was derived by performing micromagnetic simulations with Finite Difference Method (FDM, more details in Chapter 3.) where full LL equation, Eq. 1.39, is solved. The dots display the results of simulations with Finite Element Method (FEM, more details in Chapter 3.) where linearised LL equation, Eq. 1.28, was solved. All methods of deriving the dispersion relation in this case are in good agreement in the small k range where the dipolar interaction is prevalent.

In the case of SWs propagating in a magnetic thin film three special configurations of the effective magnetic field and SW propagation directions can be distinguished:

- The effective magnetic field IP and SW propagating perpendicularly to the field, called Damon-Eshbach configuration [40], Fig. 1.13(a),

- The effective magnetic field IP and SW propagating parallel to the field, called backward volume configuration [41], Fig. 1.13(b),

- The effective magnetic field OOP and SW propagating IP, perpendicularly to the field, called forward volume configuration [42], Fig. 1.13(c).

The following subsections will be devoted to the descriptions of the dispersion relations in these configurations.
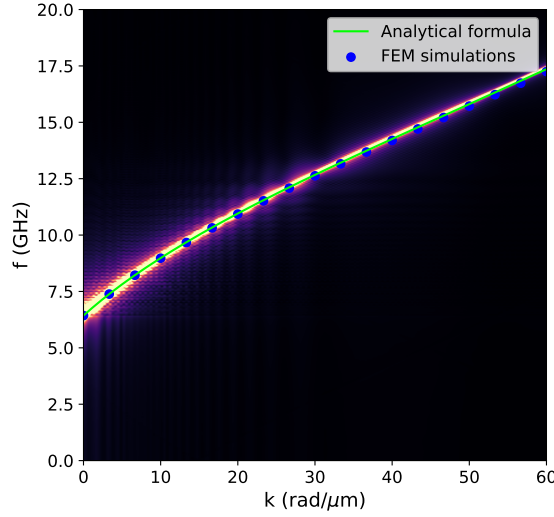
Figure 1.12 Comparison of three methods for obtaining the SW dispersion relation in a 10 nm-thick Py layer subjected to IP external magnetic field $\mu_0 \mathbf{H}_{\text{ext}} = 50$ mT. The solid line corresponds to the analytical expression given in Eq.1.47. Discrete data points represent results from micromagnetic simulations performed in the frequency domain using the linearised LL equation, which will be discussed in detail in Chapter 3. The colourmap shows the dispersion extracted from the time domain micromagnetic simulations based on the full LL equation, also described in Chapter 3. In this specific case, all three methods yield consistent results for the SW dispersion relation.

The knowledge of the dispersion relation allows for derivation of two velocities that charac-terise SWs. The first one is phase velocity given by the formula

$$\mathbf{v}_{\text{ph}} = \left(\frac{\omega}{k_{\text{x}}}, \frac{\omega}{k_{\text{y}}}, \frac{\omega}{k_{\text{z}}} \right).$$
(1.48)

This velocity describes how quickly a part of a wave of given phase moves through the space. The second velocity is the group velocity defined as

$$\mathbf{v}_{\text{ph}} = \left(\frac{\partial \omega}{\partial k_{\text{x}}}, \frac{\partial \omega}{\partial k_{\text{y}}}, \frac{\partial \omega}{\partial k_{\text{z}}} \right).$$
(1.49)

This velocity in turn specifies the velocity of energy which the SW carries.

If those two velocities are not equal to each other in given magnetic medium then this medium is regarded as dispersive. It means that in such a medium a wavepacket spreads out in space during propagation as its components have different group velocities.

1.5.2   Damon-Eshbach configuration

In Damon-Eshbach configuration (DE) SWs propagate perpendicularly to the direction of thin film IP magnetisation. SWs in DE characterise by an imaginary wavevector along the thickness of the film [1][p. 162]. It means that the SWs decay exponentially across film's thickness. Moreover, SWs in DE are non-reciprocal, depending on the direction of their propagation SWs
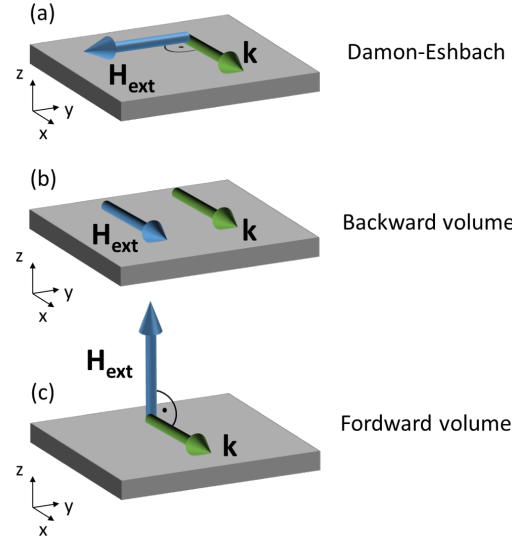
Figure 1.13 Special configurations of external magnetic field and SW propagation direction that can be distinguished in thin film geometry. (a) depicts Damon-Eshbach configuration where SW propagate perpendicular to IP applied external magnetic field, (b) shows configuration for backward-volume SWs where SW propagate parallel to applied IP external magnetic field, (c) presents configuration of forward-volume SWs which propagate perpendicular to external magnetic field applied OOP.

have the highest amplitude at different film's surfaces. Because of that direction-dependent amplitude concentration at thin film's surfaces these SWs are also called magnetostatic surface spin waves. The dispersion relation for SWs in this configuration was derived by Damon and Eshbach [40, 43], hence the name of configuration, and is described by the formula [1][p. 163]

$$\omega_{\text{DE}}(k) = \sqrt{\omega_{\text{H}}(k) \cdot (\omega_{\text{H}}(k) + \omega_{\text{M}}) + \frac{\omega_{\text{M}}^2}{4} \left(1 - e^{-2kd}\right)}, \tag{1.50}$$

where d is the thickness of thin film. The parameters ω_M and ω_H denote the frequencies of spin precession corresponding to the system's material properties and are defined as $\omega_M = \gamma\mu_0 M_S$ and $\omega_H(k) = \gamma\mu_0(H_{\text{ext}} - M_S\lambda_{\text{ex}}k^2)$. The part of $\omega_H(k)$ expression proportional to k^2 corresponds to the exchange interaction in the system. In the limit of $k \to 0$ Eq. 1.50 reduces to the expression for the FMR frequency of the IP magnetised thin film Eq. 1.36.

1.5.3 Backward volume configuration

Backward volume (BV) magnetostatic spin waves propagate parallel to the direction of IP magnetisation of thin film. The dispersion relation of this SW precession is given by the formula [1][p. 159]

$$\omega_{\text{BV}}(k) = \sqrt{\omega_{\text{H}}(k) \cdot \left(\omega_{\text{H}}(k) + \omega_{\text{M}} \cdot \frac{1 - e^{-kd}}{kd}\right)}. \tag{1.51}$$

The name of this configuration stems from the fact that SWs, of certain k wavevector range, propagating in this configuration exhibit negative group velocity, Eq. 1.49. With the phase velocity being positive, the energy seems to move backwards with respect to the direction of moving SW wavefronts. Another important information in the name of configuration is attached with the word "volume". In this configuration SWs do not concentrate at one of the film's surfaces but their amplitude is distributed uniformly in the volume of the film.

1.5.4   Forward volume configuration

In the last regarded configuration the film is magnetised OOP and the direction of SW propagation lies in the film, thus is perpendicular to the magnetisation vector. For this configuration the dispersion relation takes form [1][p. 155]

$$\omega_{\text{FV}}(k) = \sqrt{\omega_{\text{H}}(k) \cdot \left(\omega_{\text{H}}(k) + \omega_{\text{M}} \cdot \left(1 - \frac{1 - e^{-kd}}{kd} \right) \right)}. \tag{1.52}$$

In forward volume (FV) configuration both phase and group velocities are positive, thus the energy flows in the same direction as the SWs. Also in this case SW spread uniformly in the thin film as the word "volume" indicates. In this configuration any direction of SW propagation in the thin film magnetised OOP is perpendicular to the magnetisation, hence the dispersion relation is valid for all the direction of SWs propagating IP in this configuration.

1.5.5   General expression

In year 1986 Kalinikos and Slavin [44] derived more general expression for the SW dispersion relation. They used the perturbation theory to investigate SWs propagation in a thin ferromagnetic film where dipolar and exchange interactions were taken into account. The generality of their formulation lies in a possibility to chose arbitrarily the direction of external magnetic field. Additionally, in this derivation so called mixed-boundary conditions were used what means that the spins were not pinned to the edges of the considered system what was the difference with previous works on SW dispersion relations [45, 46].

The formula proposed by Kalinikos and Slavin can be written as

$$\omega_{\text{K}} = \sqrt{(\omega_{\text{H}}(k) + \omega_{\text{M}}\lambda_{\text{ex}}k^2)(\omega_{\text{H}}(k) + \omega_{\text{M}}\lambda_{\text{ex}}k^2 + \omega_{\text{M}}F)}, \tag{1.53}$$

where

$$F = P + \sin^2\theta \left(1 - P(1 + \cos^2\varphi) + \omega_{\text{M}} \frac{P(1 - P)\sin^2\varphi}{\omega_{\text{H}}(k) + \omega_{\text{M}}\lambda_{\text{ex}}k^2} \right), \tag{1.54}$$

$$P = 1 - \frac{1 - e^{-kd}}{kd}, \tag{1.55}$$

where θ is the angle between SW propagation direction and system's z axis and φ describes the angle between SW propagation direction and the external magnetic field $\mathbf{H}_{ext}$ direction. Thickness of the ferromagnetic layer under consideration is d.
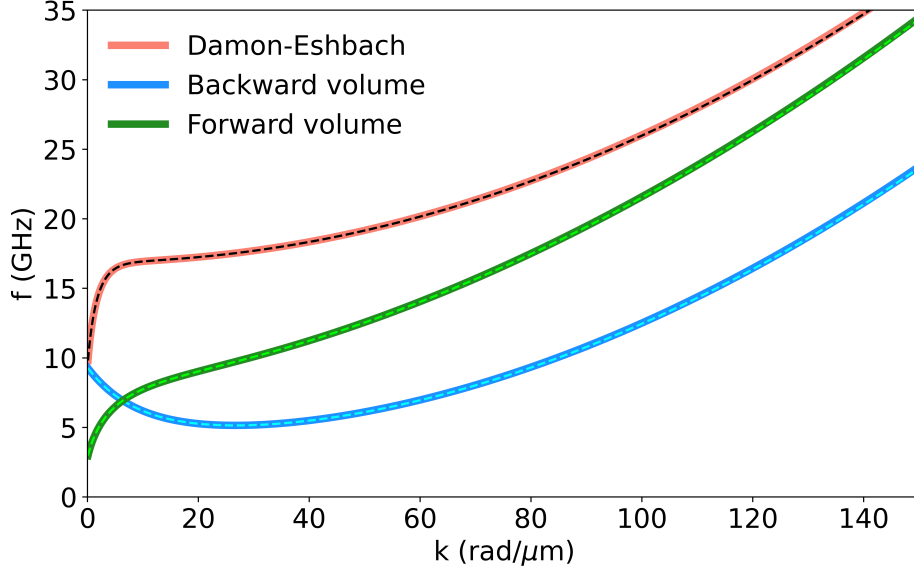
Figure 1.14 SW dispersion relations comparison for the special magnetic configurations, namely Damon-Eshbach configuration in red, backward volume configuration in blue, forward volume configuration in green. The solid lines were plotted using Eqs. 1.50, 1.51, 1.52 and the dashed lines were obtained from formula Eq. 1.53. All presented dispersion relations were derived for following material parameters, $\mu_0 \mathbf{H}_{ext} = 100$ mT, $M_S = 800$ kA/m, $A_{ex} = 13$ pJ/m, $d = 250$ nm (these parameters have been chosen to highlight the nature of the dispersion relations for main magnetic configurations, e.g. the global minimum in dispersion relation of backward volume configuration).

The Fig. 1.14 shows examples of dispersion relation of 250 nm thick Py layer in three magnetic configurations. The dispersion relations have been prepared based on Eqs 1.50, 1.51, 1.52 (solid lines) and Eq. 1.53 (dashed lines) where the angles θ and φ were chosen to correspond to main magnetic configurations. It is evident that the general expression for SW dispersion relation in thin magnetic layer proposed by Kalinikos and Slavin coincides with the expressions derived for the individual magnetic configurations with a high degree of accuracy. The relative difference between the formulas in each case is smaller than 1% in presented wavevector ranges.

1.6   Non-linear processes in magnonics

For the purpose of deriving SW dynamics from LL equation, Eq. 1.28 the magnetic interactions were expressed in terms of effective magnetic field components that they induce. However, this expression is not suitable for analysis of non-linear processes in magnonics. Because of that the

magnetic interactions may be presented in form of a Hamiltonian with S as a spin operator

$$
\begin{aligned}
\mathcal{H} = &-\mu_0\mu_B g \sum_i \mathbf{H}_{\text{ext,i}} \cdot \mathbf{S}_i - \mathcal{J} \sum_{i \neq j} \mathbf{S}_i \cdot \mathbf{S}_j + \\
&-\frac{\mu_0(\mu_B g)^2}{4\pi} \sum_{i<j} \frac{3(\mathbf{S}_i \cdot \mathbf{e}_{ij})(\mathbf{S}_j \cdot \mathbf{e}_{ij}) - \mathbf{S}_i \cdot \mathbf{S}_j}{|\mathbf{r}_{ij}|^3} + \mathcal{H}_a,
\end{aligned}
\tag{1.56}
$$

where the first component of the equation's right side corresponds to Zeeman energy, the second term comes from the energy of exchange interaction, the third from dipolar interaction and the last one comes from the energy of anisotropy.

According to Holstein–Primakoff transformation [47] Hamiltonian of magnetic interaction can be transformed into a series

$$
\mathcal{H} = \mathcal{H}^{(0)} + \mathcal{H}^{(2)} + \mathcal{H}^{(3)} + \mathcal{H}^{(4)} + \dots,
\tag{1.57}
$$

where $\mathcal{H}^{(0)}$ is the energy of system in the ground state and $\mathcal{H}^{(n)}$ are Hamiltonians of n-th order processes in the system. There are two three-magnon processes investigated in the main part of this thesis which are presented schematically in Fig. 1.15. The first one is called stimulated splitting process (SSP) during which a magnon described with frequency ω and wavevector $\mathbf{k}$ is split in two new magnons: the first of frequency ν and wavevector κ, and the second of parameters $(\omega - \nu, \mathbf{k} - \kappa)$, as shown in Fig. 1.15(a). The second process is called the confluence process (CP) where a magnon $(\omega, \mathbf{k})$ scattered on (ν, κ) magnon result in creation of a new magnon with $(\omega + \nu, \mathbf{k} + \kappa)$, Fig. 1.15(b).
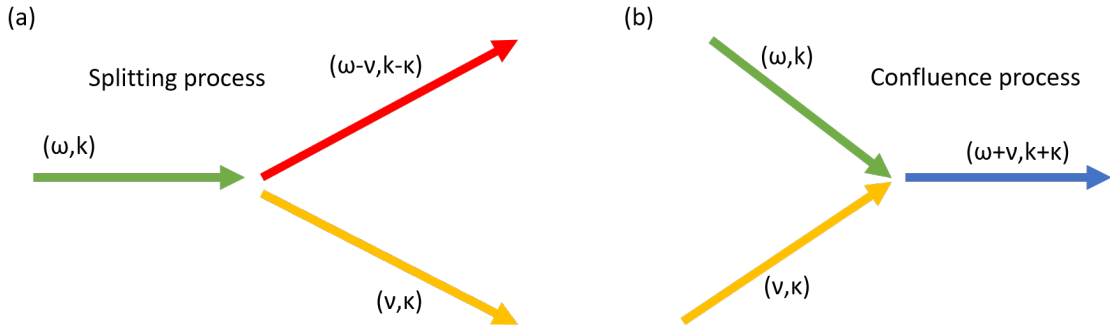
Figure 1.15 Scheme of three magnon processes which are investigated in the main part of the thesis. (a) depicts stimulated splitting process, during which an incoming wave (ω, k) splits into two new waves characterised by (ν, κ) and $(\omega - \nu, k - \kappa)$. (b) shows confluence process where two waves (ω, k) and (ν, κ) combined create a new wave of $(\omega + \nu, k + \kappa)$.

The description of three-magnon process Hamiltonian involves expressing spin operators in terms of annihilation and creation operators, $\hat{a}$ and $a^{\dagger}$ respectively. It can be written as [48]

$$\mathbf{S}_{\mathrm{i,x}} = \frac{\sqrt{2S}}{2}\left(\hat{a}_i + a_i^{\dagger} - \frac{a_i^{\dagger}\hat{a}_i\hat{a}_i + a_i^{\dagger}a_i^{\dagger}\hat{a}_i}{4S}\right),\tag{1.58}$$

$$\mathbf{S}_{\mathrm{i,y}} = \frac{\sqrt{2S}}{2i}\left(\hat{a}_i - a_i^{\dagger} - \frac{a_i^{\dagger}\hat{a}_i\hat{a}_i - a_i^{\dagger}a_i^{\dagger}\hat{a}_i}{4S}\right).\tag{1.59}$$

These operators should be used in Eq. 1.56 to express the Hamiltonian in terms of annihilation and creation operators. Subsequently, the components of Hamiltonian in the new representation can be grouped depending on the order of annihilation/creation operators, this order in turn corresponds to n-th order magnonic process. For three-magnon process the Hamiltonian takes from of

$$\mathcal{H}^{(3)} = \sum_{k,\kappa}\left(V'(k,\kappa)\hat{a}_k a_{\kappa}^{\dagger}a_{k-\kappa}^{\dagger} + V'^{\dagger}(k,\kappa)\hat{a}_k\hat{a}_{\kappa}a_{k+\kappa}^{\dagger}\right).\tag{1.60}$$

The first term of Eq. 1.60 refers to SP and the second term to CP, $V'(k,\kappa)$ is the coupling strength. The representation of annihilation/creation operators were changed to the reciprocal space by using a discreet Fourier transform $\hat{a}_k = 1/\sqrt{N}\sum_i \hat{a}_i e^{-i\mathbf{k}\cdot\mathbf{r}_i}$.

Chapter 2

Optics effects

In this chapter several concepts and effects from the field of optics will be described. The results of main investigations presented in this thesis show many parallels between optics and magnonics. Thus it is beneficial to create a theoretical base of chosen optical concepts before moving on to presentation of the main results.

2.1 Isofrequency contours

The dispersion relations discussed in Sec. 1.5 were presented as functions of wavevector magnitude k. However, SW wavevectors, like any other vector, can be broken down into components, thus an expression of dispersion relation as a multidimensional function of wavevector's components is also possible. In the case of two-dimensional waves the dispersion relation can be presented as a colourmap which coordinates denote wavevector components (k_x, k_y) and the colour at a given point expresses the frequency of SW.
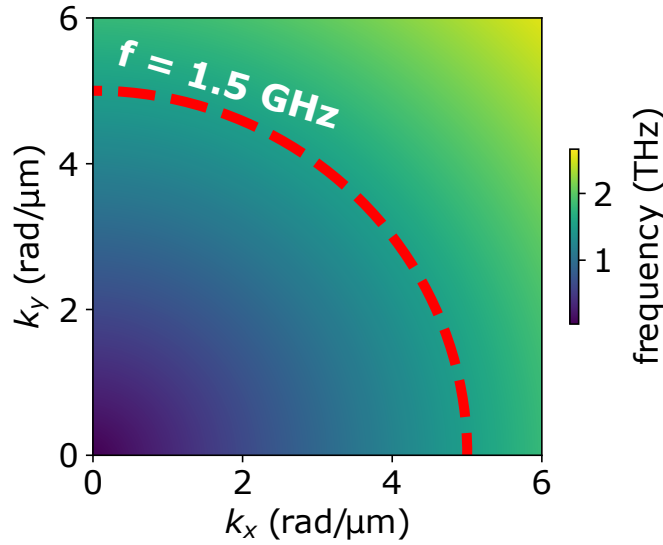
Figure 2.1 Dispersion of light presented as a two dimensional colourmap. The coordinates along x and y axes correspond to the components of light wavevector and the colour shows the frequency for given combination of wave components. The dashed, red curve indicates points of the same frequency $f = 1.5$ THz, called the isofrequency contour.

An easy to follow example of two-dimensional dispersion relation representation can be made for light. The dispersion relation of light in vacuum is

$$\omega(\mathbf{k}) = c_{\text{light}}\mathbf{k}, \tag{2.1}$$

where c_{light} is the speed of light. To include the components of light wavevector in two-dimensional space Eq. 2.1 has to be rewritten in a from of

$$\omega(k_x, k_y) = c_{\text{light}}\sqrt{k_x^2 + k_y^2}. \tag{2.2}$$

In Fig. 2.1 the formula Eq. 2.2 is presented. Additionally, the red dashed line corresponds to the points of the same frequency on dispersion relation, thus such a line is called an isofrequency contour [39].

The analysis of isofrequency contours provides important information on the waves at a given frequency in the investigated system. Especially important is the analysis of waves transmitted to a new medium, Fig. 2.2(a). In two different media the isofrequency contours corresponding to the same frequency will be different as shown schematically in Fig. 2.2(b). Because of the energy conservation principle, while entering the new medium, a wave cannot change its frequency as it would change its energy as well. Moreover, to satisfy the continuity rule the component of wavevector tangential to the interface between media has to be constant. With these two constraints the only parameter that is allowed to change is the wavevector's component normal to the interface. Fig. 2.2(b) presents the geometrical solution of this problem. The wavevectors presented there share the same tangential component but end on different isofrequency contours. With such an analysis it is possible to derive both the angles of waves propagation in different media and their wavelengths.
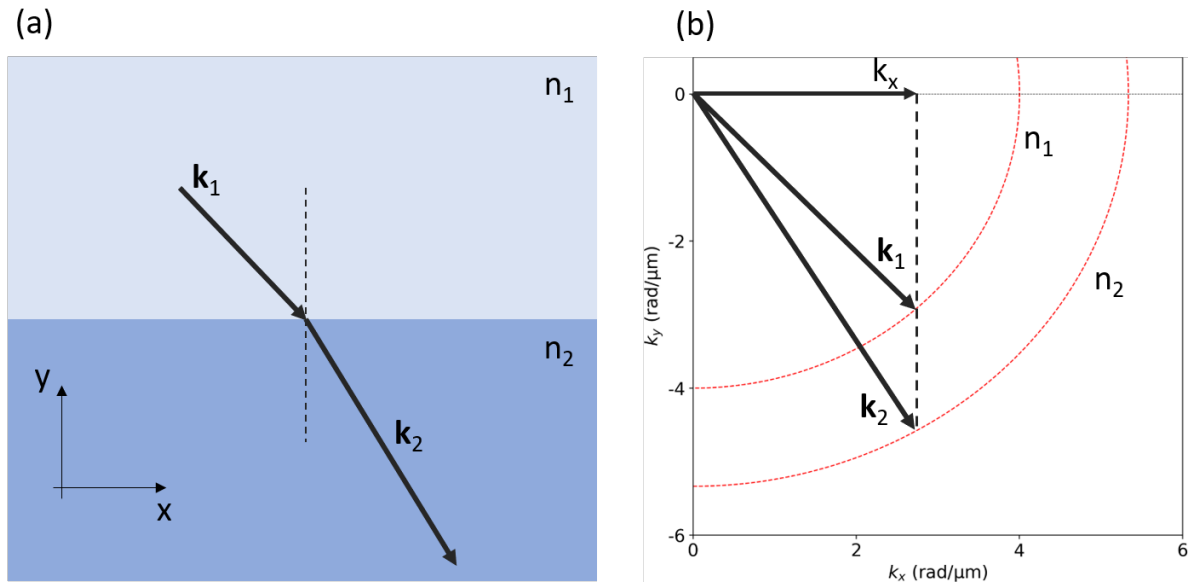
Figure 2.2 (a) Refraction of light entering a medium with different refraction index n_i. (b) Derivation of wavevectors during refraction presented on isofrequency contours.

In the case of light waves propagating in isotropic media the method of deriving wavevectors using isofrequency contours is equivalent to Snell's law of refraction. However, the isofrequency method provides much greater generality than Snell's law [49]. For example, the use of isofrequency method enables derivation of refracted wavevectors in anisotropic media as well since it allows to obtain information of both $\mathbf{k}$ and $\mathbf{v}_g$ of reflected and refracted waves. Such a possibility is extremely important in the investigations on SWs because of their anisotropic nature, as it has been shown in Sec. 1.5, their dispersion relation heavily depends on the direction of SW propagation with respect to the direction of external magnetic field.

The justification for using the isofrequency method for derivation of SW wavevectors is shown in Fig 2.3. Two isofrequency contours corresponding to $f = 22$ GHz are shown for CoFeB and YIG. The isofrequency contour of CoFeB, blue curve, is not circular at chosen frequency. This means that SWs in CoFeB are subject to the anisotropic propagation and their refraction cannot be described with any simple analogue to Snell's law. Then the geometrical solution based on isofrequency contours method provides the wavevector of the SWs transmitted from CoFeB to YIG as presented in Fig 2.3. Additionally, the isofrequency contours provide information on waves group velocities. As it is presented in Fig 2.3(b) with orange arrows, the group velocities vectors are perpendicular to isofrequency contour at allowed $f(k_x, k_y)$. For anisotropic waves, eg. SW propagating in YIG as presented in Fig 2.3(b), it is possible that the wavevector and group velocity vector do not align what causes that the wavefronts are not perpendicular to the direction of wave's propagation.
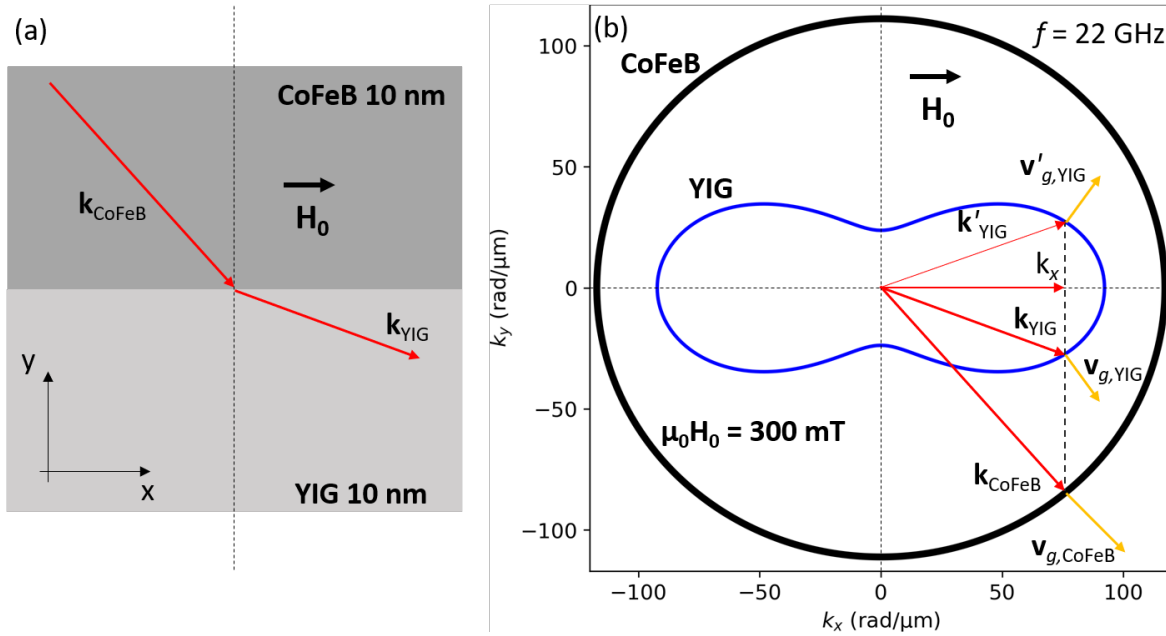
Figure 2.3 (a) A scheme of SW transmission from a thin (10 nm) CoFeB layer to another thin layer (10 nm) of YIG. The system is placed in the external magnetic field of $\mu_0 H_0 = 300$ mT directed along system's X axis. (b) Isofrequency contours for YIG (black contour) and CoFeB (blue contour) at frequency $f = 22$ GHz. The figure presents an example of SW transmission from CoFeB to YIG media in wavevector space. The derivation of wavevectors is analogous to the case of light refraction. However, as $f(k_x, k_y)$ depends on the wave propagation direction, is anisotropic, there is no straightforward analogue to the Snell's law for SWs. The red arrows indicate the wavevectors of waves sketched in (a), the orange arrows represent group velocities of the waves. The group velocity vector directions are derived as vectors normal to the isofrequency curvature for given wavevector.

Another advantage of using isofrequency contours is they applicability to derive wavevectors of inelastically scattered SWs [50]. In the non-linear processes described in Sec. 1.6 scattered SWs change their frequency and tangential wavevector components. The non-linear processes can be shown on the isofrequency contours as in Fig. 2.4, where the contours correspond to different frequencies instead of different media, as it was the case of refraction analysis. Additionally,

during the non-linear processes the tangential components of wavevector change what has to be taken into account in the isofrequency analysis. Then the derivation of the inelastically scattered wavevector is the same as in previously described case of wave refraction. Namely, the wavevector component orthogonal to the altered tangential component has to be chosen in such a way so the resulting wavevector will end on the isofrequency contour corresponding to changed SW frequency. Fig. 2.4 displays geometrical construction for wavevectors in both SSP and CP. Such an analysis was used in Section 5.6 to interpret the results of inelastic scattering of SW beam on a localised SW mode.

2.2 Interferometers

The interferometers are a wide-spread optical device which operation is based on interference of waves. The basic principle of interferometer operation is splitting an incoming wave in two and redirecting them into different paths. Depending of the type of interferometer these paths have uneven distances or different directions of propagation. Then the split waves are directed to a particular spot in space where they merge and are measured by a detector. Depending on the paths' lengths that waves travelled they acquire different phases. The relative difference of phases causes either constructive interference, destructive interference or certain intermediate state at the detector [51]. The interferometers have found applications in the waves analysis, measurements of distances [52], examination of various textures surfaces [53–55], and investigation of materials optical properties [56, 57].

In physics the interferometers were used in some of the most famous physical experiments. Michelson employed interferometers to disprove the concept of ether [58]. The interferometer system proposed by Mach and Zender contributed significantly to development of quantum physics [59, 60]. Relatively recently the interferometers were also used to measure gravitational waves propagating in the universe [61].

As the realisation of interferometer requires a carrier of wave-like nature, the magnonic interferometers for SWs were also introduced. A significant part of the investigations presented in this thesis is devoted to the influence of the interferometers' geometry and parameters on the propagation of SWs. The focus is on two geometries of interferometers, namely Gires-Tournois and Fabry-Perot geometries.

The geometry of Gires-Tournois interferometer (GTI) is presented in Fig. 2.5(a). It consist of two reflective surfaces. One of them has reflectivity close to unity and the other is semitransparent. The waves cast on GTI are reflected almost without any loses but they undergo phase shift which depends on the spacing between reflective surfaces and the wavelength of cast waves. The SW reflected from the left interface is described as $\sin(k_1 x + \phi_1)$ and the wave reflected from the right interface of GTI with width w is described as $\sin(-k_2 x - \phi_2)$. cf. Fig. 2.5(c). The criterion of constructive or destructive interference of the incoming and reflected waves depends on the
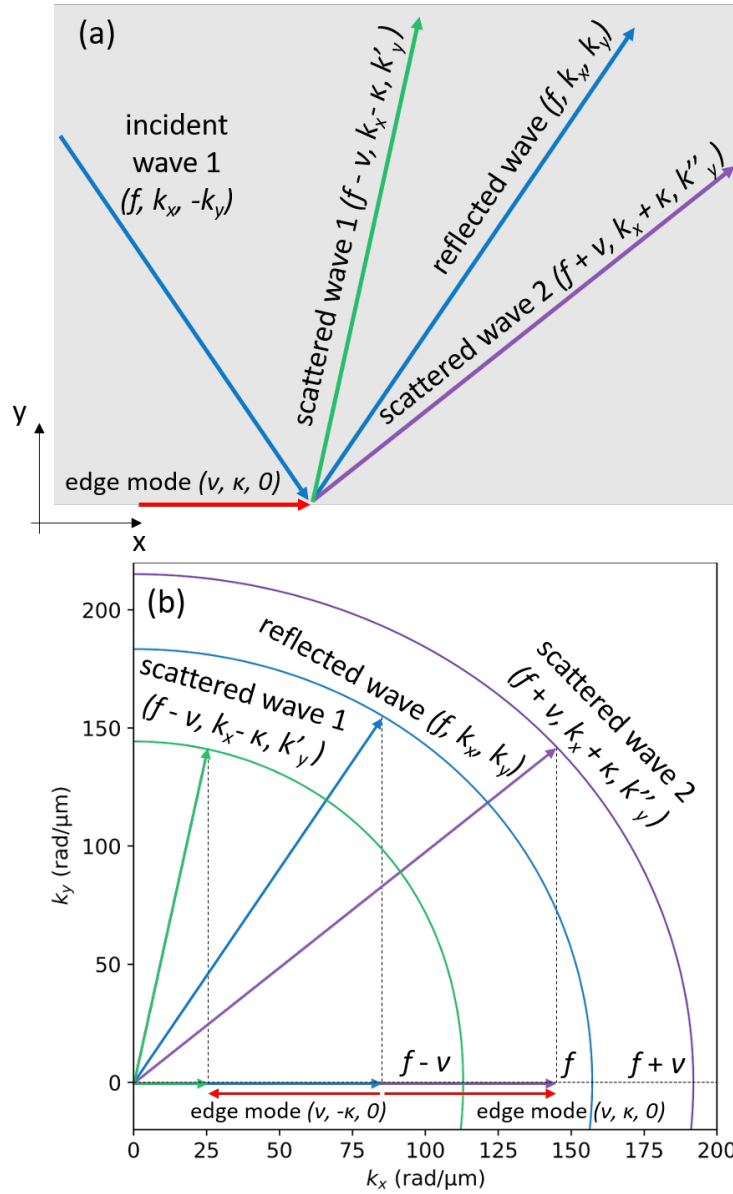
Figure 2.4 (a) Example of isofrequency construction for inelastic scattering of SWs. The reflected beam is presented with blue colour and is described by frequency f and wavevector (k_x, k_y). The wave is scattered on an edge mode of frequency v and wavevector $(\kappa, 0)$, marked with red colour. The inelastically scattered SWs are presented with green (SSP, $f - v$) and violet (CP, $f + v$) colours, cf. Sec. 1.6. (b) Representation of the inelastic scattering in the reciprocal space with isofrequency contours. The blue contour corresponds to the reflected wave, according to the conservation laws its frequency and tangential wavevector component are preserved. Two additional isofrequency contours correspond to two non-linear processes SSP and CP, green and violet contours respectively, with frequencies $f \pm v$. In the derivation of inelastically scattered waves the tangential wavevector component is not preserved and also the waves' frequencies change. The derivation of scattered wavevectors is done by finding k'_y and k''_y components on proper isofrequency contours for $k_x \pm \kappa$ values if it is possible.
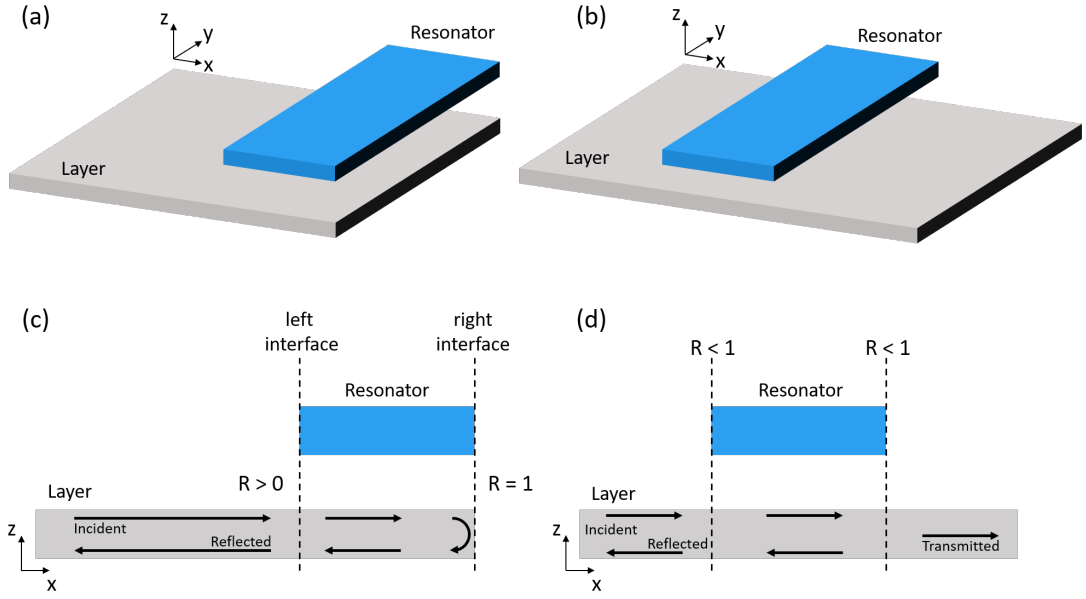
Figure 2.5 Two types of interferometers investigated in the main part of the thesis. (a,c) An interferometer in Gires-Tournois geometry, where the resonator's edge is aligned with the edge of layer. Such a geometry guarantees total reflection of waves from one side of the interferometer. (a) shows the interferometer from a broad perspective and (c) in the *xz* cutplane. The interferometer modulates the waves by introducing a phase shift which depends on resonator's width *w* and separation between interferometer's elements *s*. (b,d) display a scheme of Fabry-Perot interferometer. This type on interferometer introduces two interfaces in a system and thus modulates both the reflected and transmitted waves.

difference of the arguments of the functions describing the waves and can be expressed as

$$(k_1 + k_2)w + \phi_1 + \phi_2 = 2n\pi, \tag{2.3}$$

The constructive interference happens when *n* is an even integer and the destructive interference occurs when *n* is an odd integer. GTI can be realised in magnonics by placing a magnetic resonator above the edge of layer in which SW propagate as it is presented in Sections 5.2, 5.3, 5.5. GTI was proposed by French physicists F. Gires and P. Tournois hence the name of geometry [62]. When the positions of reflective surfaces are fixed, parameter *w* becomes constant and interferometer transforms into an etalon [63][p. 438].

The second geometry of interferometer investigated in this thesis is Fabry-Perot (FPI) geometry. An example of FPI is shown in Fig. 2.5(b). FPI differs from GTI by the fact that both of its reflective surfaces are semitransparent, Fig. 2.5(d). It means that FPI modulates not only reflected but also the transmitted waves. The intensity of transmitted waves I_T can be calculated from the formula [63]

$$I_T = I_i \frac{T^2}{1 + R^2 - 2R\cos\delta}, \tag{2.4}$$

where I_i is the amplitude of incoming waves, T is transmittance, R is reflectance and δ is the phase change caused by passing through FPI. Transmittance and reflectance are related to each

other by simple formula $T + R + A = 1$, where A stands for absorbance of the interferometer. The realisation of magnonic FPI may be done by placing a magnetic resonator in the middle of medium where SWs propagate, what is shown in Section 5.4.

In the case of both GTI and FPI the desired widths of the resonators should be a multiple of wavelength λ of the wave cast on interferometer. It can be expressed by a formula [63][p. 622]

$$2w = m\lambda, \tag{2.5}$$

where m is an integer. However in magnonics, because of high magnetic damping in most of the magnetic materials, short propagation distances are preferred what may constrain the use of interferometers. In Sections 5.2, 5.3, 5.4 it is shown that magnonic interferometers are able to create the resonances even with resonators narrower than the incoming SW wavelength, due to the possibility of excitation of much shorter wavelength SWs in the resonator. These findings allow for greater miniaturisation of magnonics elements. Additionally, the coupling between magnetic resonator and the layer is done by stray field which quickly dissipates in space, cf. Section 1.2.2. Thus the spacing between the elements of magnonic interferometers should be relatively small to harness the interaction between them effectively.

2.3 Goos-Hänchen effect

The Goos-Hänchen effect (GHE) manifest itself as a lateral shift of reflected waves from an interface. Fig. 2.6 presents a scheme of GHE with the lateral shift of reflected wave beam denoted as ΔX. The effect was first observed by German physicists F. Goos and H. Hänchen for the total internal reflection of a light beam [64]. A thorough analysis of total internal reflection, as illustrated in Fig. 2.6, explains the GHE. Since multiple layers of atoms at the edge are influenced by the propagating wave, they all contribute to the reflection. It appears as if the incident wave penetrates the interface to a certain depth δ, and the actual reflection occurs at a new interface behind the real one. If the trajectories of incident and reflected beams are drawn as shown in Fig. 2.6, the reflected waves appear shifted at the interface by a distance denoted as ΔX and the incident and reflected waves are connected by an evanescent wave propagating along the interface [63][p. 137]. The scope of GHE can be expressed with a formula [65, 66]

$$\Delta X = -\frac{\partial \phi}{\partial k_x}, \tag{2.6}$$

where ϕ is the phase shift of reflected wave at the interface and k_x is the tangential to the interface component of the wavevector.

The presence of GHE has been confirmed in many areas of physics involving waves. As mentioned, the original work on GHE had been done on beams of electromagnetic waves in the linear regime. However, the spatial shift of inelastically scattered electromagnetic waves was also reported [67, 68]. GHE was measured for the acoustic waves [69], neutron waves [70]
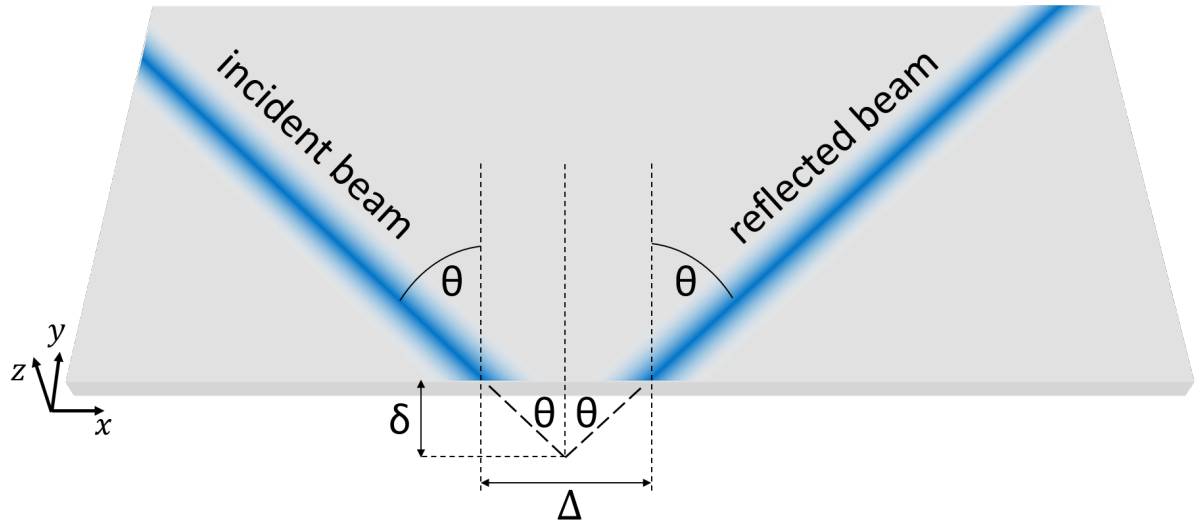
Figure 2.6 Illustration of Goos-Hänchen effect. When the trajectories of the incident and reflected beams are drawn, it appears that the reflection happens behind the real interface, at a distance δ, and because of that the reflected beam is shifted with respect to the incidence spot by a distance of ΔX at the interface.

and SWs. The first analytical prediction of GHE for SWs were shown in [66] with numerical simulation of this effect presented [71]. Later, the experimental confirmation of GHE for SWs was published by Stigholer [72]. GHE of SW beams is one of the topics presented in Section 5.5 and an analogue of GHE for inelastically scattered SW beams is shown in Section 5.6.

2.4   Wood's anomaly

In 1902, R. W. Wood observed a phenomenon which science at his time was unable to explain. Specifically, he showed that the amplitude of light reflected from a grating rapidly decreases at certain angles of incidence [73–75]. Unable to properly interpret the effect he observed, Wood referred to it as an anomaly. Lord Rayleigh [76] and Fano [77], among others, attempted to explain Wood's anomaly (WA), but their interpretations did not fully account for the effect. Only with the advent of the new field of physics, plasmonics was WA finally clarified.

Plasmonics is a field of physics which studies the excitation of electron density waves at metallic or dielectric interfaces at optical frequencies [78]. It explains WA as the excitation of surface plasmons on a grating. A metallic grating, such as the one used by Wood, possesses eigenstates that include surface modes. When light, with its magnetic field component polarised parallel to the grating, strikes the grating at a critical angle θ_c, phase matching occurs between the incident wave and the grating eigenstate. Under this condition, a portion of the incident light's energy is transferred to the grating's surface plasmons when the tangential wavevector component of the light, $k_{||}$, matches that of the plasmons, and both share the same frequency.

The excitation of surface plasmons is illustrated schematically in Fig.2.7. In Fig.2.7(a), the phase matching condition is not met, as the angle of incidence is inappropriate, and no plasmon

excitation occurs. In contrast, when the phase matching condition is fulfilled, as shown in Fig. 2.7(b), surface plasmon excitation takes place.

Although the origin of WA has been explained, the name of the phenomenon has remained unchanged for historical reasons. WA continue to be investigated in modern physics and have been observed in acoustic waves [79], photonic metamaterials [80], and time gratings [81]. However, WA has not been extensively studied in magnonics. In Section 5.5, we present one of the first studies of WA in magnonics.
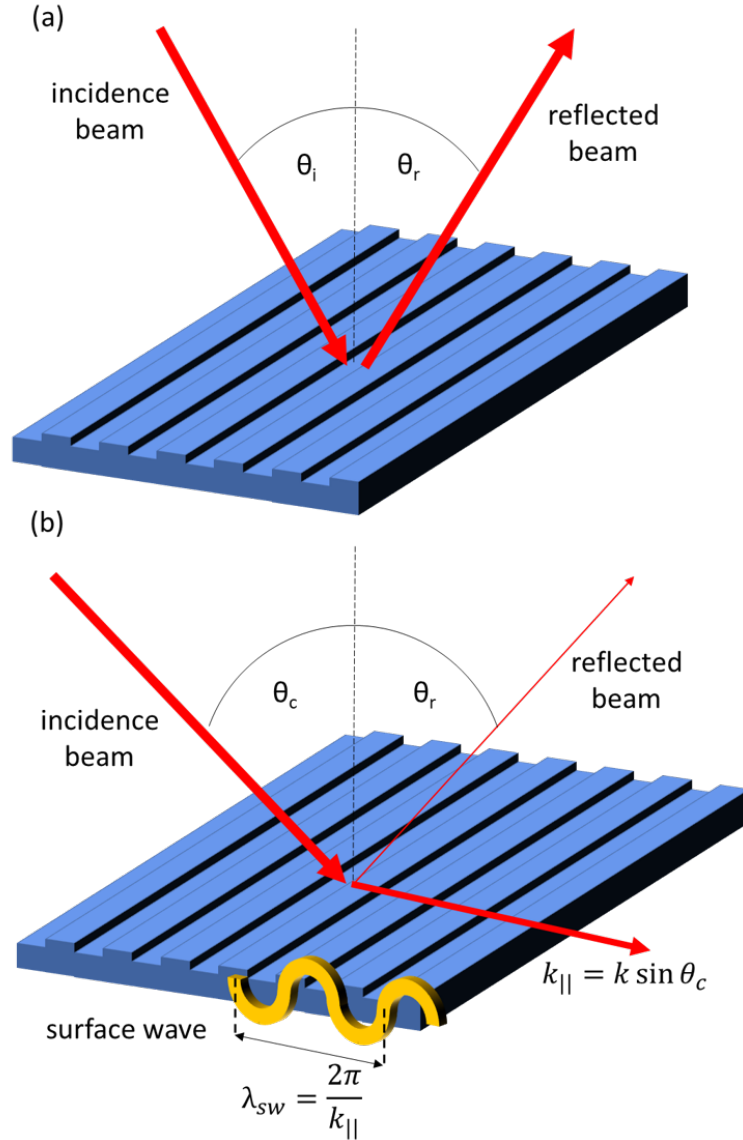
Figure 2.7 Sketch of Wood's anomaly. When a beam reflects from a grating at an arbitrary angle θ_i the amplitude of the reflected waves is the same as of the incident waves and the angles of propagation are the same (a). Wood's anomaly occurs when the incident waves cast at the critical angle θ_c excite grating's eigenmode which takes part of the incident wave energy. It results in the reflected waves having smaller amplitude (marked with thinner line) in comparison with the incident waves (b).

Chapter 3

Numerical simulations

In physics the changes in a given system are described by partial differential equations (PDE). Usually, these are second order PDEs and, depending of the physical problem, they are solved in time, space or frequency domains. Solving these equations in the vast majority of cases is cumbersome because as, the real physical systems consist of innumerable degrees of freedom. In the case of magnonics one can imagine that each spin in the system may be regarded as a separate degree of freedom. Thus, solving LLG equation for all the spins in the system at once would prove to be an unfeasible feat. To overcome this obstacle, not only in magnonics but in any other field of physics, special numerical methods were developed to make solving PDEs possible in a finite amount of time and with a finite amount of computational power. However, the cost of using the numerical approach to solving PDEs is reduced accuracy of the obtained results.

In the case of theoretical investigations on magnetism so called continuum theory was introduced to increase the feasibility of numerical simulations. According to the micromagnetic approximation, also known as the continuum theory, magnetisation is regarded as a continuous function in space and not as a set of separate magnetic moments [82, 83]. The value of $\mathbf{M}(\mathbf{r})$ in a particular point in space is an average of magnetic moments in a small volume around this point where magnetisation is approximately uniform. In the micromagnetism the magnitude of $\mathbf{M}(\mathbf{r})$ is preserved during computation and numerical simulations based on this approach are called micromagnetic simulations.

The research presented in this thesis is based on two numerical methods. The first was finite element method, where the calculations were performed in the real space and frequency domain in COMSOL Multiphysics software. The second method was finite difference method which simulations were carried out in the real space and time domain in an open-source MuMax3 environment. In this Chapter the detailed description of these two methods and software corresponding to them will be presented.

3.1   Finite element method

In FEM a physical problem is defined by its geometry, proper PDEs corresponding to the investigated physics and the boundary conditions that limit the number of possible solutions. The geometry of the system is divided into cells called finite elements, hence the name of the method itself [84]. The division of the geometry into finite elements transforms the problem of solving PDEs in a continuous space to a discrete set of equations that is much easier to compute. All of the finite elements with their vertices and edges create a web called mesh that represents system's geometry in FEM. An example of mesh used in FEM calculations is presented in Fig. 3.1(a). For the purpose of micromagnetic simulations the size of mesh should be smaller than the exchange length, λ_{ex}, of the investigated magnetic material, Eq. 1.18. as this is the length of the shortest-ranged interaction in the system. Because of using discrete meshes to map a system, the final results of FEM are approximations of the real solutions. However, this is a

compromise that has to be accepted in order to obtain the solution to a physical problem while being limited by the time and given computational possibilities.
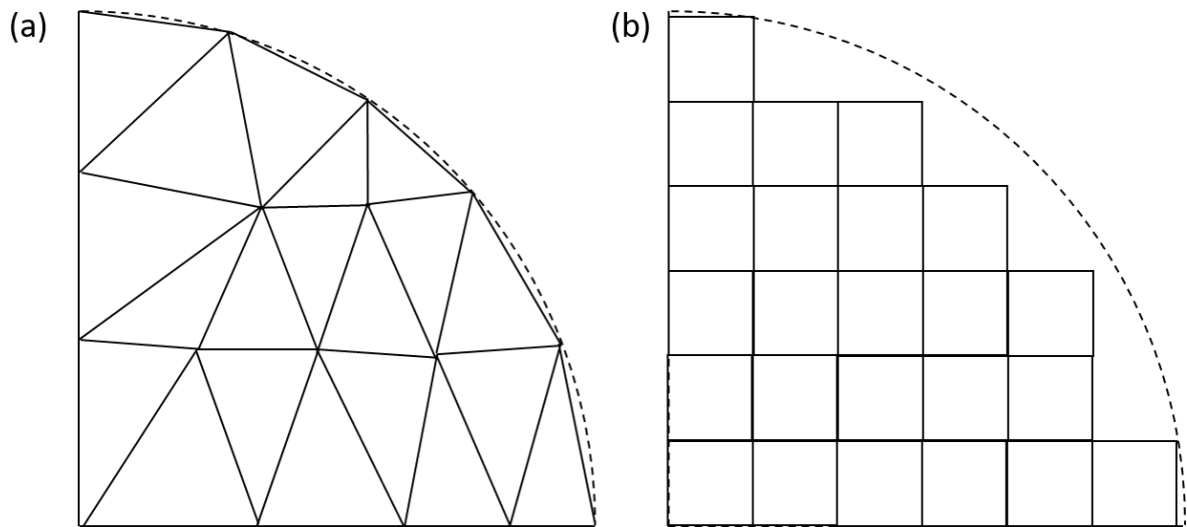
Figure 3.1 The difference between discretisation meshes used in FEM and FDM for the same type of simulated geometry. In FEM the discretisation mesh may consist of elements of different dimensions what in an example in (a) is presented with triangles (in 2D) of different shapes. However, FDM requires mesh with regular-sized elements, e.g. squares (in 2D), as shown in (b). The Figure shows also an important limitation of the regular meshes, namely the difficulty of discretising curved geometries.

After creating the mesh, the next step of FEM is to define so called shape functions inside the finite elements, which are mostly polynomials of low order such as linear functions. The purpose of these functions is to interpolate the results of PDEs among the nodes [85]. In FEM the shape functions are combined, each with particular coefficient, to create the base functions that stretch over whole system's geometry. The linear combination of base functions is used to approximate the result of PDEs. Thus, solving the system changes into solving a set of linear equations. The coefficients in this set of equations create so called the stiffness matrix, which elements correspond to the nodes in the system's mesh and their numerical values are obtained by integrating PDE's in the nodes. The proper definition of base functions causes that most of the elements of the stiffness matrix are zeros, because of that the matrix is also called the sparse matrix[86]. The fact that most of the sparse matrix elements are zero makes computation of the system's solution faster.

In the end the results of FEM have to be scrutinised for errors that might arise as a result of wrong definitions of systems properties, mistakes in defining PDEs and boundary conditions, and numerical errors related to used integration methods and definition of the base functions. If the numerical error is considered as an acceptable, the FEM results should be further processed. This usually involves retrieving a part of FEM solution that is of interest in particular investigation. Later this part of solution is postprocessed either by a self-developed code or with the tools provided by commercial programs dedicated to solve FEM.

3.2 Simulations in COMSOL Multiphysics

The results of numerical simulations in FEM presented in this thesis were done in COMSOL Multiphysics environment [87]. COMSOL Multiphysics is a commercial software dedicated to solving predefined PDEs corresponding to a wide range of different physical, chemical and engineering problems. One of the biggest advantages of COMSOL Multiphysics is the possibility to solve different PDEs describing various phenomena in the investigated system simultaneously. On top of that COMSOL Multiphysics allows users to define their own PDEs. This feature was crucial for the investigation presented in this thesis as it facilitated user-made implementation of LL equation what is not, at the time of writing this thesis, officially included in COMSOL Multiphysics software[1].

The definition of custom PDE in COMSOL Multiphysics is done by proper definition of coefficients of Sturm-Liouville equation which has a form of[2]

$$e_a \frac{\partial^2 \mathbf{u}}{\partial t^2} - d_a \frac{\partial \mathbf{u}}{\partial t} + \nabla \cdot (-c\nabla \mathbf{u} - \varepsilon \mathbf{u} + \rho) + \beta \cdot \nabla \mathbf{u} + a\mathbf{u} = f, \quad (3.1)$$

where $\mathbf{u}$ is a dependent variable vector, e_a is a mass coefficient, d_a is the damping coefficient, c is the diffusion coefficient, ε is the conservative flux convection coefficient, ρ is the conservative flux source, β is the convection source, a is the absorption coefficient and f is the source term. In the investigations the linearised version LL equation, Eq. 1.28, in two dimensional case was used, where $\mathbf{u} = (m_x, m_y)$. To implement such a version of LL equation the coefficients in Eq. 3.1 were defined as

$$d_a = \begin{pmatrix} 1 & 0 \\ 0 & 1 \end{pmatrix}, \quad (3.2)$$

$$c = \begin{pmatrix} \frac{2\gamma A_{ex}}{M_S} & 0 \\ 0 & \frac{2\gamma A_{ex}}{M_S} \end{pmatrix}, \quad (3.3)$$

$$a = \begin{pmatrix} -\gamma\mu_0 H_{ext} & i\omega \\ -i\omega & -\gamma\mu_0 H_{ext} \end{pmatrix}, \quad (3.4)$$

$$f = \begin{pmatrix} \gamma\mu_0 M_S \\ -\gamma\mu_0 M_S \end{pmatrix}. \quad (3.5)$$

The coefficients e_a, ε, ρ, β are set to zero.

In this implementation the dipolar interactions were not defined explicitly in the LL equation. The influence of the dipolar interaction was added in terms of the magnetostatic potential created by the magnetic dipoles in the system [88]. The behaviour of the magnetostatic potential is

---

[1]An example of unofficial implementation of LLG equation in COMSOL can be found in https://www.comsol.com/blogs/micromagnetic-simulation-with-comsol-multiphysics (access 13.01.2025).

[2]Sturm-Liouville equation presented in this thesis has two different symbols when compared to its implementation in COMSOL documentation. These two symbols were changed to not to duplicate notation used previously in this thesis.

described by Poisson equation which is defined in COMSOL Multiphysics as

$$\nabla \cdot (-c\nabla\phi + \rho) = f, \tag{3.6}$$

where ϕ is magnetostatic potential and coefficients c, ρ and f have the same meaning as in Eq. 3.1. The expression for magnetostatic potential, Eq. 3.6, is defined separately for magnetic and non-magnetic domains of the system. In the case of magnetic domains the coefficients of Eq. 3.6 are defined as $c = 1$, $f = 0$ and $\rho = (m_x, m_y)$ and in the non-magnetic domains as $c = 1$, $f = 0$ and $\rho = 0$.

Another important feature of COMSOL Multiphysics software is its ability to create a non-uniform mesh in the investigated system. The definition of mesh is not direct in COMSOL. The user can define general parameters of desired mesh in the simulation domains such as finite element shape and the range of shapes' dimensions. COMSOL offers two types of finite elements shapes, in two-dimensional simulations these are triangles and squares and in three-dimensional simulations these are tetrahedrons and cuboids. The dimensions of mesh elements can vary across the investigated system. This feature allows for significant reduction of computational resources demand in the simulations. The usual procedure is to define a dense mesh in the areas of interest. In micromagnetic simulations these are magnetic domains and in the case of the simulation of interacting magnetic bodies the space between them. To the rest of the simulation space a sparse discretisation may be assign as away from the magnetic domains only vanishing fields are expected. The use of a low-density discretisation grid at the periphery of the investigated system provides needed reduction in computational costs in the FEM simulations. Fig. 3.2 illustrates such a procedure with an example of mesh used in the investigations presented in Sections 5.2 and 5.3.
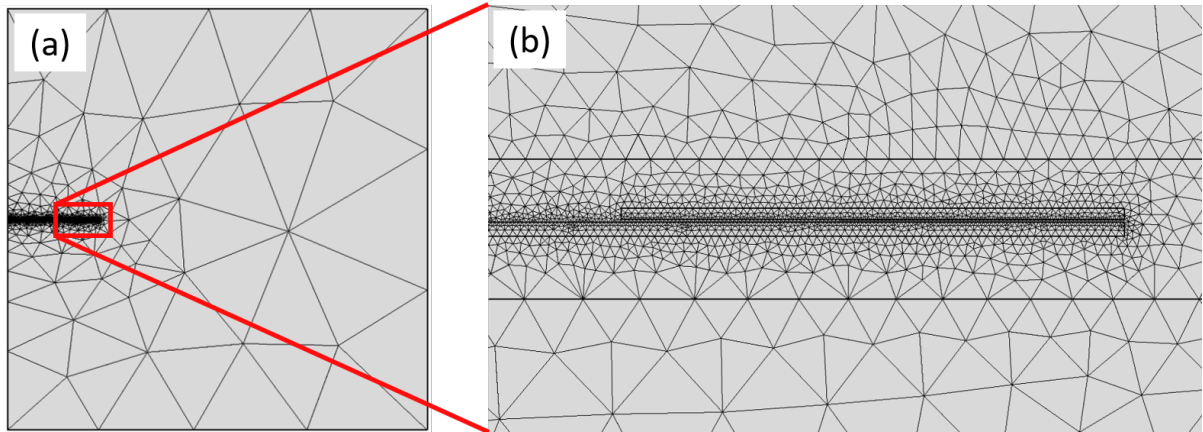
Figure 3.2 (a) Picture of the discretisation mesh employed in the investigations on magnonic interferometers conducted in COMOSOL Multiphysics. The denser mesh is applied in the middle of simulated space as the magnonic elements are placed there (marked with red rectangle). The area away from the magnonic elements is filled with sparser mesh as no magnetisation precession is predicted there, only potentials fading with the distance. (b) A zoom in on the area marked with the red rectangle. A very fine mesh structure is presented which is assigned to the investigated magnonic elements in the simulation.

The simulations performed in COMSOL Multiphysics were done in the eigenfrequency domain. It means that the results were the real space distributions of magnetisation and magneto-static potential that correspond to a particular eigenfrequency of the system. Such calculations are much faster comparing to the calculations in time domain which require system to reach its steady-state. Additionally, the simulations in eigenfrequency domain were used to calculate the investigated systems' dispersion relations after applying Bloch boundary condition depending on wavevector k in the system, for example in the case of magnetisation $m_i|_{x=0} = m_i|_{x=L}e^{ikL}$, where L is the width of the system along its x axis. The results of simulations carried out in FEM in COMSOL Multiphysics are presented in Sections 5.2, 5.3.

3.3   Finite difference method

Finite difference method (FDM) is another numerical technique used to solve PDEs. The main idea behind FDM is to convert continuous PDEs into a discrete problem by using an approximation formula for differential operator derived from Taylor's theorem

$$\frac{\partial f(\zeta)}{\partial \zeta} \approx \frac{f(\zeta + \Delta\zeta) - f(\zeta)}{\Delta\zeta}, \tag{3.7}$$

where $f(\zeta)$ is the solution to the problem and ζ is the domain in which calculations are done [89]. In FDM calculations are usually performed in space and time domains. The expression $\Delta\zeta$ denotes the difference between neighbouring points in the chosen domain. For the purpose of FDM this difference is always finite, thus the name of the method. Only in the limit of $\Delta\zeta \to 0$ Eq. 3.7 the expression is strictly differential, hence FDM yields approximated results depending primarily on the scope of chosen finite difference $\Delta\zeta$. The use of Eq. 3.7 to represent differentials allows to treat given physical problem as a linear algebra problem which is much easier to compute [90].

Similarly as for FEM, in FDM the system is divided into a discrete set of nodes; however, the difference is that the nodes have to be distributed on a regular grid, Fig. 3.1(b). In the two-dimensions simulations the grid is made of squares or rectangles and in three-dimensions is made of cubes or cuboids. The division into the uniform grid renders a few inconveniences in the numerical calculations. The first is a greater restriction on the possible shapes in the simulations. The grid made of rectangular units is not well suited to represent continuous curves thus simulations of spheres, cylinders and alike shapes are less accurate. The use of regular discretisation grid also does not allow to assign sparser discretisation in less important simulation's areas. For this reason saving the computational resources by defining coarse mesh in non-magnetic domains as is the case in FEM simulations is not accessible in FDM. The size of the discretisation units has observe the principle of being smaller than the distance of the shortest-ranged interaction in the investigated system. As described previously in Subsection 3.1, in the case of micromagnetic simulations this is the exchange length λ_{ex}, described by Eq. 1.18.

After establishing the discretisation in the investigated system, the next step in FDM is the choice of numerical method to compute the equations describing physics in the system. The approximation presented in Eq. 3.7 is the base of recursive Euler method, schematically presented in Fig. 3.3, which can be written as

$$f_{n+1} = f_n + f'_n \Delta \zeta. \tag{3.8}$$

This method allows to calculate the values of function f in all grid points when the initial value f_0 is known. However, this method is a subject to large numerical error which scales linearly with the $\Delta \zeta$ and additionally is prone to numerical instabilities. Thus, to achieve a satisfactory accuracy with Euler method, an extremely fine discretisation mesh is needed that causes huge demand for computational resources[91]. What is contrary to the aim of introducing numerical methods to solve PDEs.
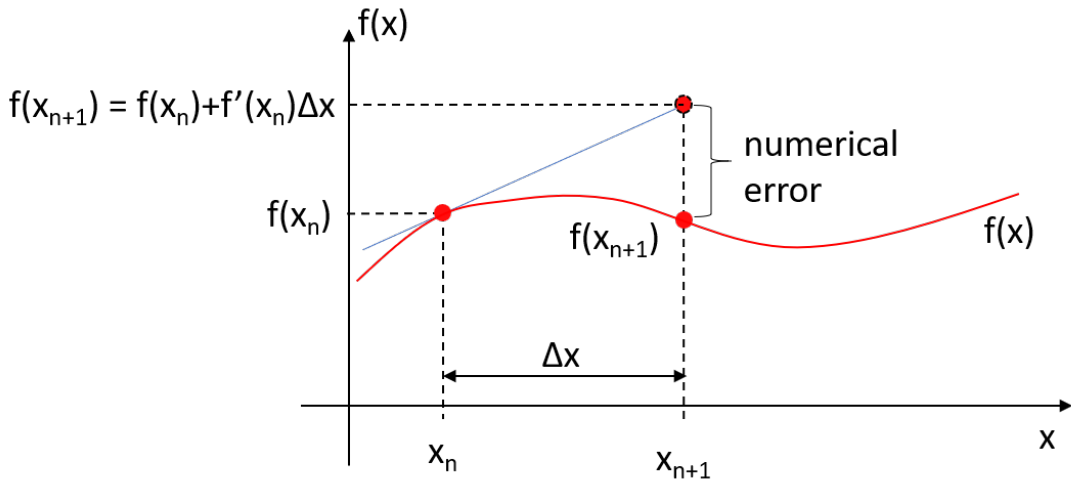
Figure 3.3 Illustration of Euler method for numerically solving of a differential equation $f'(x)$. Knowing the previous state $f(x_n)$ and the step between states Δx it is possible to derive the next steps following the formula $f(x_{n+1}) = f(x_n) + \Delta x f'(x)$. Because of relatively high numerical errors and tendency for numerical instabilities this method is rarely used in numerics but still serves as a good, starting example in explanations of numerical solving of differential equations.

As the Euler method proves unreliable in many simulation cases, another, more sophisticated numerical methods were developed to provide higher calculation accuracy with lower computational costs. These methods include Heun, backward differentiation formula, Bogaki-Shampine, Dormand-Prince, Fehlberg [92, 93]. However the prevailing numerical method used in this thesis in FDM simulations was Runge-Kutta method (RKM) [94, 95]. The main idea behind RKM is to add intermediary points in the finite difference $\Delta \zeta$ at which the derivatives are evaluated. Such a treatment provides more symmetry to the calculations when compared to the Euler method leading to reduced numerical errors. In the case of 4th-order RKM four intermediary points are chosen. In two dimensional space (x, t) 4th-order RKM calculated with a discreet time steps Δx

and Δt can be described by a relation [91][p. 108]

$$\frac{dx}{dt} = f(x,t), \tag{3.9}$$

$$x_{n+1} = x_n + \frac{k_1}{6} + \frac{k_2}{3} + \frac{k_3}{3} + \frac{k_4}{6}, \tag{3.10}$$

where

$$k_1 = \Delta t f(x_n, t_n), \tag{3.11}$$

$$k_2 = \Delta t f(x_n + k_1/2, t_n + \Delta t/2), \tag{3.12}$$

$$k_3 = \Delta t f(x_n + k_2/2, t_n + \Delta t/2), \tag{3.13}$$

$$k_4 = \Delta t f(x_n + k_3, t_n + \Delta t). \tag{3.14}$$

The numerical error related to the use of 4th-order RKM scales as $\Delta \zeta^5$, thus this method provides satisfactory accuracy. RKM of higher order are also possible to implement but as they involve more intermediary points in calculations they also require more computational power. Because of this reason 4th-order RKM is widely used as it is a good compromise between the accuracy of calculations and computational requirements.

3.4   Simulations in MuMax3

MuMax3 is an open-source, GPU-accelerated environment written in C++ and Go languages specialised to solve LLG equation [37]. It employs FDM to perform micromagnetic simulations in time and space domains. In comparison with other environments for FEM micromagnetic simulation such as TetraX [96], TetraMAG [97], FastMag [98], Nmag [99] and magpar [100], MuMax3 offers better performance at a cost of lower flexibility with possible shapes in the simulations.

The simulation script for MuMax3 is prepared using Go language syntax. There the user defines the discretisation grid on which the system's geometry is built. In contrast to COMSOL Multiphysics the user does not have to define LLG equation by themselves as the full version of LLG equation is already implemented in MuMax3. The magnetic interactions are introduced in the simulations by defining proper material parameters of the magnetic domains such as the exchange stiffness constant A_{ex} or anisotropy constant K_{u1}, cf. Eqs. 1.18, 1.21 respectively. Not defining one of the coefficients related to a particular magnetic interaction will be interpreted by MuMax3 as an absence of this interaction in the system. Additionally, MuMax3 allows to manually disable the dipolar interaction in the system to accelerate the calculations if there is a need for such a treatment. MuMax3 requires also to define the vector of the external magnetic field B_0 and the initial magnetic configuration. To solve LLG equation MuMax3 uses several possible solvers based on different numerical methods. In the investigations presented in this thesis the 4th-order RKM was mostly used.

MuMax3 offers a possibility to define different material parameters to different domains in the simulated system. The only exception is γ_G parameter which definition is universal in the system. The ability to define different material parameters in different parts of the system allows for very high damping parameter α values to be assigned in the vicinity of the edges of the system. With that feature a gradient of α defined close to the system's edge may be used to prevent reflections of SWs from these edge, what otherwise would cause an interference of the reflected waves in the simulation that would decrease the quality of results.

After defining the geometry, material parameters and the external magnetic field, the initial magnetic configuration in simulations have to be chosen. The initial magnetic configuration can be defined as a uniform distribution of magnetisation or as a complex magnetisation state, such as vortex. MuMax3 provides several predefined complex magnetisation distributions. In the case of multi-element systems there is possibility to assign different magnetisations saturation M_S to different elements. Additionally, for sophisticated simulations the initial magnetisation configuration can be uploaded from an external file.

When all of the system's parameters are set, the simulations in MuMax3 start with derivation of the magnetic configuration with lowest energy. This part of the simulations is called relaxation and MuMax3 has two predefined function that can be used to obtain relaxed magnetisation state. The first function is called *relax*() and disables the precessional movement of the spins in LL equation. Then the spins align with the direction of effective magnetic field that points to the minimum energy state. The second function is *minimize*() that employs the steepest gradient energy minimisation method. In this method the steepest change of the system's energy is sought iteratively, with the assumption that at the end of steepest energy change trajectory lies the global energy minimum of the system. Even with this two provided functions finding the relaxed state of the system is a non-trivial task. The system's energy depends on several parameters thus, the system's energy landscape is described by a multidimensional function. Not only calculation of the steepest gradient in this case would be difficult but additionally, the steepest gradient may points towards local minima or metastable states instead of a global maximum. Also the analysis of the direction of the effective magnetic field may be misleading. The addition of anisotropy to the system will create two directions along the easy-axes that point to the minimum energy states. One of the possible solutions to these problems is an additional relaxation of the system after applying a small dynamic magnetic field. Then the system will be removed from the initially found local minimal energy state. If after the subsequent relaxations of the system will reach the same relaxed state it will indicate that the system is indeed in the minimum energy state.

Finding of the system's minimal energy state concludes the static part of the micromagnetic simulations. The magnetic configuration of the relaxed system may be saved by MuMax3 as an external file for further postprocessing. In general, the results of MuMax3 simulations are snapshots of reduced magnetisation vector $\mathbf{M}/M_S$ distribution in the investigated system. However, if spins dynamics is the subject of investigations then a driving magnetic field has to be added to the simulations. In MuMax3 it can be done by several different approaches. It might include defining domains in the system where dynamic magnetic field is assigned

or adding a space-constrained dynamical component to the external magnetic field, so called mask. An another approach my be uploading a profile of magnetic field from an external file, for example when the profile of magnetic field induced by a particular model of antenna is calculated analytically or numerically using a different simulation. The next step is to choose time-dependent expression for the magnetic field. The most popular for this task is *sin* function which provides harmonic oscillations of the SWs. Time-dependent harmonic function can be additionally modulated by an another function of gradual amplitude increase, e.g. in form of $(1 - e^{-t})$. Such an addition is important to avoid transient states associated with a sudden field activation in the simulations. In the simulations with the numerical derivation of dispersion relation, dynamic magnetic field is described by *sinc* function. In the subsection 3.4.2 in-depth description of such an excitation is provided.

After defining the dynamics in the system, MuMax3 allows the user to adjust the solver's parameters. These correspond to maximal and minimal time step used in numerical calculations, respectively *MaxDt* and *MinDt*. Usually, they are defined with respect to dynamic field oscillation period. There is also a possibility to set desired toleration for numerical error with parameter *MaxErr*. In the end, user has to define the simulation time. The time needed for system to reach steady-state is chosen in most of the cases. After the simulation time MuMax3 saves the results of simulation as snapshots of reduced magnetisation, $\mathbf{M}/M_S$. The number of these snapshots and time spacing between them depends on the research needs and are defined by the user.

In contrast to COMSOL Multiphysics, MuMax3 does not provide built in tools to postprocess simulation results. In the case of micromagnetic simulations the postprocessing usually involves calculating FMR spectra, dispersion relations (in one and two dimensions) and visualisation of magnetic modes. Such a postprocessing of MuMax3 simulation results is usually done with a self-made code. The results presented in this thesis were prepared in self-made codes written in Python language.

In the following subsections several examples of codes used in MuMax3 simulations are will be presented with explanations.

3.4.1   Implementation of gradient of damping parameter

The code snippet shown below was used to define the gradient of damping parameter at the edges of simulated system. This code was prepared for the two-dimension simulations, the damping parameter gradient was defined along *x* and *y* directions.

```
1   grad_up := yrange(1,0)
2   grad_down   := yrange(1,0)
3   grad_left   := xrange(1,0)
4   grad_right  := xrange(1,0)
5   grad0 := xrange(1,0)
6
7   grad := 60
8   gr_step := 2
9   for i:=2; i<(grad+2); i++{
10      grad_up = yrange( ( (Ny*cy/2)-gr_step*(grad)*cy+i*gr_step*cy),
11                      ( (Ny*cy/2)-gr_step*(grad)*cy+gr_step*(i+1)*cy) )
12
13      grad_down   = yrange( (-(Ny*cy/2)+gr_step*(grad)*cy-gr_step*(i+1)*cy),
14                      (-(Ny*cy/2)+gr_step*(grad)*cy-gr_step*i*cy) )
15
16      grad_left = xrange( (-(Nx*cx/2)+gr_step*(grad)*cx-gr_step*(i+1)*cx),
17                      (-(Nx*cx/2)+gr_step*(grad)*cx-gr_step*i*cx) )
18
19      grad_right = xrange( ((Nx*cx/2)-gr_step*(grad)*cx+gr_step*i*cx),
20                      ((Nx*cx/2)-gr_step*(grad)*cx+gr_step*(i+1)*cx) )
21
22      grad0 = grad_up.add(grad_down.add(grad_left.add(grad_right)))
23
24      DefRegion(i, grad0 )
25  }
```

The discretisation of system is described by four parameters, N_x and N_y indicate the number of discretisation cells along the x and y axes respectively and c_x and c_y are spacing between neighbouring cells expressed in metres. The gradients of damping parameters are defined as ranges with *xrange* and *yrange* functions. In the lines $1 - 5$ the initiation of the ranges is presented. Then two additional parameters are defined. The parameter *grad* describes how many discretisation cells the gradient will consist of and the parameter gr_{step} specifies the width of a damping parameter cell in units of discretisation defined in a particular simulation. Because of limitation of MuMax3 *grad* parameter has to be smaller than 256, MuMax3 cannot simulate more regions in the system than that number. The total width of damping gradient along i direction is given by a simple formula

$$L_{\text{damp,i}} = grad \cdot gr_{\text{step}} \cdot c_i, \tag{3.15}$$

where c_i is the discretization along the desired direction. The *for* loop is used to define all steps of the gradient starting from the edges of simulate system. All of the gradient components in each loop's iteration are added to create a new region in the system, which in MuMax3 also require assigning an ordinal number. This definition is done with DefRegion() function. The picture of the defined regions that create damping gradient is shown in Fig. 3.4.

In the last step of this definition the numerical values of the damping parameter α has to be chosen. It can be done using the following code
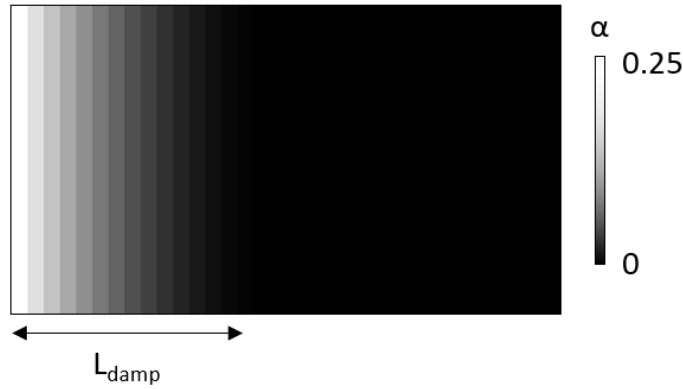
Figure 3.4 Illustration of damping coefficient α gradient created in MuMax3.

```
1  alpha0 := 0.001
2  alpha_edge := 0.5
3  for i:=2; i<(grad+2); i++{
4      dmp := alpha0 + (alpha_edge-alpha0)*((i-2)/grad)*((i-2)/grad)
5      alpha.setRegion(i, dmp )
6  }
```

where *alpha0* is the damping parameter value of the investigated ferromagnetic layer and *alpha_edge* is the maximal damping value assigned at the edges. The variable *dmp* describes the value of damping parameter at each gradient step. In the research presented in this thesis the value of damping parameter changes parabolically with space. This particular function shape was chosen as the value of damping parameter grows slow enough to minimise the reflections of SWs from the gradient [101]. The value of damping parameter is assigned to the proper gradient step with function *alpha.setRegion()* just as any other material parameter assigned in MuMax3.

3.4.2   Excitation of SWs for dispersion relation calculations

As described in Section 1.5 derivation of system's dispersion relation is crucial in the magnonic research. In the same Section a derivation of dispersion relation in special cases was presented with several formulas derived for main magnetic configurations. However, solving the full LLG equation to obtain dispersion relations in more complex magnetic structures would prove to be either cumbersome or impossible. Because of that it is much more sensible to employ micromagnetic simulations which provide numerical solutions of the investigated systems.

In the case of micromagnetic simulations carried out in COMSOL Multiphysics obtaining the dispersion relation of a given system is relatively simple. COMSOL Multiphysics is able to perform calculations in the frequency domain, thus it can derive the desired number of eigenfrequencies of the system for given value of SW wavevector. The examples of dispersion relation calculated in the frequency domain by COMSOL Multiphysics are presented in Sections 5.2, 5.3. The micromagnetic simulations in MuMax3 are performed in the time domain but obtaining the eigenmodes of the system is not as straightforward as in calculation with COMSOL Multiphysics. To derive the dispersion relation of a system in MuMax3 one has to define a proper SW excita-

tion in the system that would simultaneously excite SWs with wide ranges of frequencies and wavevectors and only then the response of the system can be calculated and further processed to extract the dispersion relation.

The excitation scheme which is able to induce a wide range of SWs simultaneously is described by *sinc* function that is defined as

$$sinc(\zeta) = \frac{sin(\zeta)}{\zeta}, \tag{3.16}$$

where ζ is function's domain. An example of this function in the time domain is presented in Fig. 3.5(a). The mathematical method to change the representation of a function to its reciprocal domain is called Fourier transform (FT) and is given by the formula

$$f(\eta) = \mathcal{F}\{f(\zeta)\} = \frac{1}{\sqrt{2\pi}} \int_{-\infty}^{\infty} f(\zeta)e^{-i\eta\zeta}d\zeta, \tag{3.17}$$

where η is function's modulation parameter in reciprocal space. The inverse Fourier transform (IFT) has a formula

$$f(\zeta) = \mathcal{F}^{-1}\{f(\eta)\} = \frac{1}{\sqrt{2\pi}} \int_{-\infty}^{\infty} f(\eta)e^{i\eta\zeta}d\eta. \tag{3.18}$$

Following the example of Fig. 3.5(a) its representation in the reciprocal space, here the frequency space, is shown in Fig. 3.5(b). It is evident that the signal described with *sinc* function in the reciprocal space is given by a rectangular function[3] what means that *sinc*-like signal consists of waves with equal amplitudes for frequencies up to certain value f_{cut} that will be called the cutoff frequency in this thesis. To derive the dispersion relation of a system the SW excitation scheme has to vary in time and space as *sinc* functions simultaneously. Such a formula for a microwave magnetic field perpendicular to the system's magnetisation can be expressed as

$$b_{rf} = \hat{\mathbf{b}}sinc(2\pi f_{cut}(t - t_0))sinc(\mathbf{k}_{cut} \cdot (\mathbf{r} - \mathbf{r}_0)), \tag{3.19}$$

where $\hat{\mathbf{b}}$ is the magnetic field vector which magnitude is the field's amplitude and is directed $\hat{\mathbf{b}} \perp \mathbf{M}$, f_{cut} and k_{cut} are respectively the frequency and wavenumber cutoffs, and t_0 and is the time shift of excitation scheme and $\mathbf{r}_0$ is the position of the excitation scheme centre. The parameter t_0 plays an important role in the dispersion relation calculations. The time shift has to be long enough so the *sinc* function will not start with its maximum at the beginning of simulation. Instead the excitation formula should start with a slow increase of the amplitude to avoid the transient states of magnetic configuration created by an abrupt change of the magnetic field.

---

[3]The disturbances visible around the frequencies $f = -f_{cut}$ and $f = f_{cut}$ in 3.5(b) are the evidence of so-called Gibbs phenomenon [102][p. 93], which occurs when a discontinuous point is approximated by a series of trigonometric functions as it is done in Fourier transform.
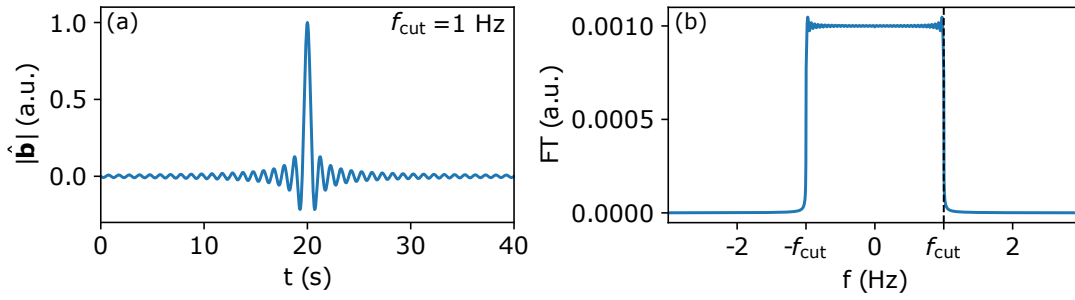
Figure 3.5 (a) An example of time dependent signal described with *sinc* function with cutoff frequency $f_{cut} = 1$ Hz, with its representation in the frequency domain (b). The signal is shifted in time by 20 s so the signal's maximum does not occur at the time of its excitation what prevents transients states from occurring. The representation in frequency domain, calculated with Fourier transform, is given as a rectangle function with the edge at $f = f_{cut}$, meaning that the time signal consists of signals with frequencies $f \leq f_{cut}$ with equal amplitudes. Such an excitation function is thus perfectly suited for dispersion relation calculations which demand parallel excitation of waves with different frequencies.

In MuMax3 simulations the resolution of dispersion relation, i.e. df - frequency resolution and dk - wavevector resolution, depends on the discretisation defined in the simulations. In time domain the number of taken samples N_t and time spacing between them dt define the resolution in frequency domain according to the formulas

$$df = \frac{1}{N_t dt}, \tag{3.20}$$

$$f_{max} = \frac{1}{2dt}, \tag{3.21}$$

where f_{max} is the maximum frequency derived in Fourier transform. Analogously, in the space domain, parameters describing space discretisation, the number of cells N_r and spacing between them c_r, are responsible for dispersion relation resolution in the wavevector space. It can be expressed as

$$dk = \frac{2\pi}{N_r c_r}, \tag{3.22}$$

$$k_{max} = \frac{\pi}{c_r}, \tag{3.23}$$

here k_{max} is the biggest wavevector in reciprocal space domain.

The dispersion relations derived with micromagnetic simulations are presented in the Sections 5.2, 5.5, 5.6. In each of these cases however the dispersion relations were calculated with use of slightly amended procedures than described earlier in this Section. The reason for applying these amendments was to reflect better different characteristics of the studied systems and thus the different SWs propagating in them. In the following paragraphs the changes applied to the dispersion relation derivations are described.
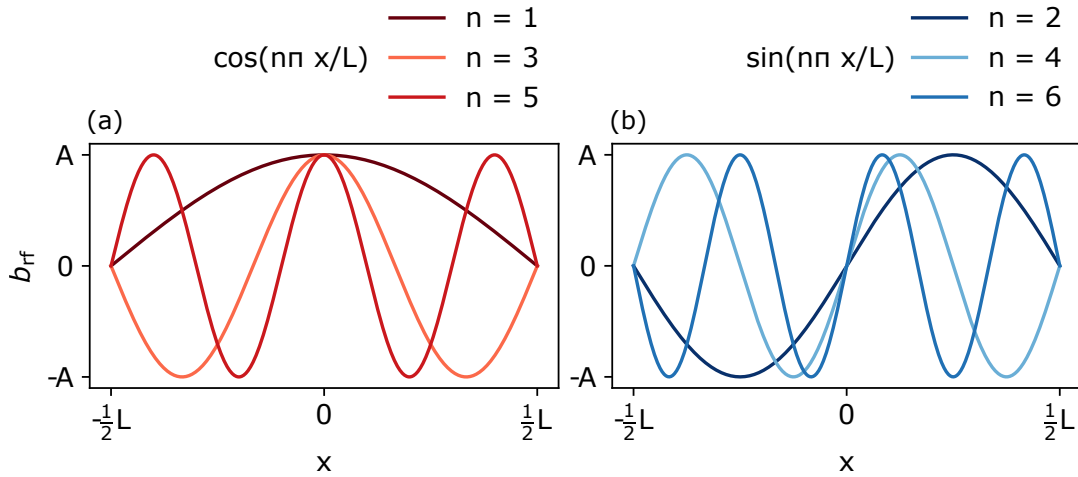
Figure 3.6 Illustration of the space profiles of width quantised modes. In both cases the modes are quantised in a space of width L, that can be understood as the width of magnonic interferometer. The even and odd modes are shown in subfigures (a) and (b), respectively. The even modes are symmetric with respect to the $x = 0$ point, i.e. there is an antinode in the middle of the space, thus they can be described with $\cos(n\pi\frac{x}{L})$ functions. In contrast the odd modes are antisymmetric and have nodes at $x = 0$, they are described as $\sin(n\pi\frac{x}{L})$ functions. In both cases the parameter n informs on the number of mode's antinodes in space. By using the presented space profiles of quantised waves in the micromagnetic simulations it is possible to enhance the higher bands of the SW dispersion relation. For the simplicity of illustration all presented modes have nodes at the space edges, however for real SWs it is not always the case.

3.4.2.1   Excitation of quantised modes

In the case of magnonic interferometers investigations, Section 5.5, SWs can be additionally quantised in the width of interferometer's resonator. Examples of these modes are presented in Fig 3.6, where in (a) the even (symmetric) modes are shown in red and (b) the odd (antisymmetric) modes are displayed in blue colours and they differ whether they have a node in the middle of the quantised space (odd modes) or an antinode (even modes). In different systems it is also possible to quantise the modes along the thickness of magnetic domain. In Fig. 3.6 all the presented modes have nodes at the edges of the quantised space which is not always the case. A more common picture involves SW that have non-zero amplitude at the edges. In such cases it is said that the pinning of SWs is not ideal what may influence the dispersion relation [45, 103].

These quantised modes constitute new SW bands in the dispersion relation. However, the higher bands are poorly excited by the driving magnetic field as described by Eq. 3.19. To overcome this problem the additional components in the dynamic field formula have to be added that correspond to the higher bands. Namely, previously described Eq. 3.19 has to be multiplied by *sin* and *cos* functions with modulations corresponding to the higher SW modes. The simulation code used in MuMax3 to excite the higher, width-quantised modes can be written as

```
1   x00 := (Nx*cx/2) - rez_width/2
2   mask := newVectorMask(Nx,Ny,Nz)
3   for i := 0; i<Nx; i++{
4       for j := 0; j<Ny; j++{
5
6           r := index2coord(i,j,2)
7           x := r.x()
8           y := r.y()
9           z := r.z()
10
11          Bxyz = 0.5*sinc(kcut*y)
12          x00 := (Nx*cx-rez_width)/2
13
14          // even modes
15          for n := 1; n < 6; n+2{
16              Bxyz = Bxyz + sinc(kcut*y)*cos(  n*pi*(x-x00)/rez_width    )
17          }
18
19          // odd modes
20          for n := 2; n < 7; n+2{
21              Bxyz = Bxyz + sinc(kcut*y)*sin(  n*pi*(x-x00)/rez_width    )
22          }
23
24          mask.setVector(i,j,2,vector(0, 0, Bxyz))
25
26      }
27  }
```

where *n* is the order number of excited higher SW mode and *rez_width* is the width of resonator. The even and odd modes are defined by the *sin* and *cos* spatial profiles, respectively, along the investigated resonator's width (the *x* axis in this case). The excitation along the longitudinal direction of resonator, *y* axis, is described as an ordinary *sinc* function with predefined wavenumber cutoff, *kcut*.

3.4.2.2 Excitation of omnidirectional spin waves

So far the dispersion relations for only particular magnetic configurations were discussed. However, in the investigations of so called extended waves [104], the waves that are not confined in any part of the system, it is also beneficiary to develop a method for deriving the dispersion relation of waves propagating in all directions at the same time. From the analytical point of view it is equivalent to calculating the Kalinikos formula, Eq. 1.53 for all possible angles of SW propagation and summing up the results. In the micromagnetic simulations, the analogous derivation of dispersion relation may be realised by placing an omnidirectional antenna in the system. Such an antenna, described in space by e.g. a two-dimensional Gaussian envelope, excites the dynamic magnetic field in all directions at the same time. The system's response to such an excitation yields the dispersion relation of the extended SWs, showing the continuum of SWs in the system. This procedure was employed in the investigations of inelastic scattering of SW beams presented in Section 5.6 where presented dispersion relation consists of the SW continuum corresponding to waves propagating freely in a ferromagnetic layer and a distinctive band of SWs localised in the system.

3.4.3   Spin-wave modes visualisation

After performing micromagnetic simulations, the dispersion relation of investigated system can be obtained by calculating fast Fourier transforms [102][p. 243] in the time and space domains. As it was described in Section 1.5 the dispersion relation is expressed as a function $f(\mathbf{k})$. In the one-dimensional case this relationship can be calculated with Fourier transform over time and space for one of the dynamic magnetisation components. The result of such calculation is presented in Fig 1.12, where the colourmap was obtained by performing a micromagnetic simulation in MuMax3. The knowledge of dispersion relation enables the visualisation of SW modes. In Fig. 3.7(a) a numerically-derived dispersion relation for thin YIG layer in DE configuration is presented. The dispersion relation is shown as $f(k_x)$ as the excited SWs propagate only along the X axis. The green circle indicates the SW mode of frequency 3.5 GHz and with positive wavevector. In Fig. 3.7(b) a cutline at $f = 3.5$ GHz is presented which shows two distinctive peaks of $\mathrm{FT}(m_x)(f = 3.5\mathrm{GHz}, k_y)$ function. The visualisation of the desired SW mode is done by calculating IFT at wavevector $k_x = 14$ rad/μm which corresponds to the investigated peak. Fig. 3.7(c) shows SW mode visualisation in the space domain which in the presented case is a plane wave[4]. The analysis of SW modes and their visualisations as presented in this paragraph were used throughout the papers included in this thesis with emphasis on investigations presented in Sections 5.5, 5.6.
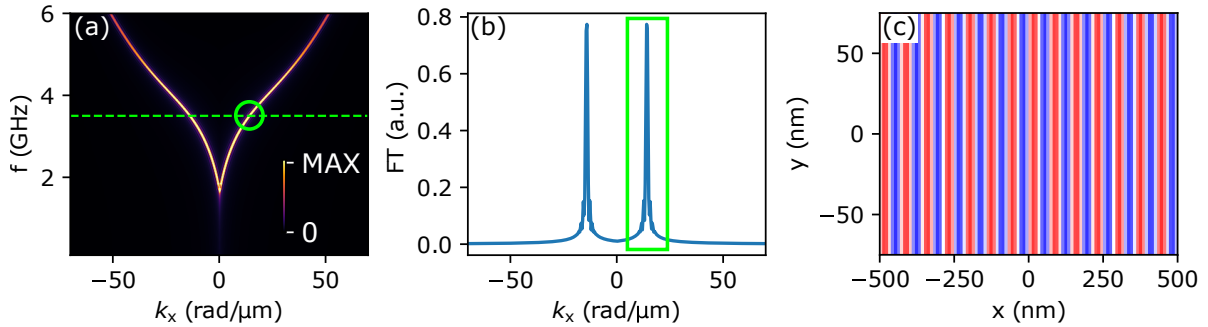
Figure 3.7 (a) Dispersion relation of SWs propagating in a thin YIG layer in DE configuration, (b) cutline through the dispersion relation at frequency $f = 3.5$ GHz indicated in (a) with the green dashed line, (c) visualisation of SW mode in the two-dimensional space domain. This picture was obtained by extending the result of IFT, calculated for the peak marked in (b) with the green rectangle, along the Y axis (SWs without any wavevector component along Y axis were assumed).

In the investigation of SWs propagating obliquely it is beneficial to represent the dispersion relation as a function of wavevector components $f(k_x, k_y)$. Then contributions of SWs propagating under different angles are evident. In an example of the incident and reflected beams as presented in Fig. 3.8(a) the representation of SW amplitude in the wavevector space takes form as presented in Fig. 3.8(b). In consist of two distinctive peaks in the wavevector domain with the same value of k_x and k_y wavevector component of different signs. To visualise one of these

---

[4]The SWs are presented in two-dimensional space in this picture as their wavefronts are extended along the Y axis, even though the Fourier analysis was performed in one-dimensional case. Such a treatment is justified as in this example SWs with wavevector components along the X axis only were assumed.

peaks an analogous method to the one described in the previous paragraph has to be used with an important alteration. The dispersion relation should be multiplied by a two-dimensional mask which cancels out all of the unwanted contributions in the dispersion relation. In the example presented in Fig. 3.8(b) the peak with coordinates k_{x0}, k_{y0} corresponding to the reflected beam (both components of k vector are positive) is marked with a green circle. The mask that would preserve the input from this peak only may be defined as

$$\Xi(k_x, k_y) = e^{-\frac{(k_x - k_{x0})^2}{2\Delta k_x^2}} e^{-\frac{(k_y - k_{y0})^2}{2\Delta k_y^2}}, \tag{3.24}$$

where Δk_x and Δk_y denote the spread of mask around the point k_{x0}, k_{y0}. The choice to use Gaussian functions as the mask is not arbitrary because this function does not change its shape under FT thus it will not generate any additional numerical errors in the further calculations. Then the SW amplitude distribution in wavevector space from Fig. 3.8(b) has to be multiplied by the mask described as Eq. 3.24 centred at the investigated peak and only then the end IFT is calculated. The result of this calculation is presented in Fig. 3.8(c) where only the reflected beam is evident. This procedure was used in Section 5.6 to determine the wavevectors of scattered SW beams and to visualise those beams.
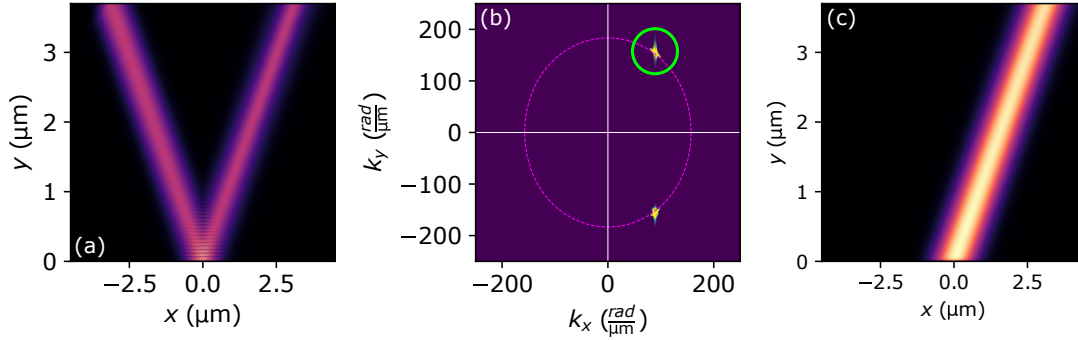
Figure 3.8 (a) Space distribution of the SW amplitude of incident and reflected beams, (b) representation of the SW amplitude in the wavevector space where two distinctive peaks are evident. These two peaks share the same k_x wavevector component and have k_y wavevector components of opposite signs. The amplitude distribution for only the reflected beam can be obtained from (a) by calculating IFT of the peak in (b) that corresponds to this beam, the peak is highlighted in green in (b). The results of the selective IFT is shown in (c) where only the reflected beam is present.

3.4.4 Unidirectional excitation of SWs

The plane SWs are not well suited to be used in investigations on GHE or WA described in Sections 2.3 and 2.4, respectively. Even though, the plane waves are relatively easy to excite, their use come with certain problems that hinder the analysis of investigated effects. For example, plane waves occupy a significant amount of space, thus the analysis of their reflection from an interface is difficult as it involves working with a broad SW interference pattern. Under such conditions the determination of SWs trajectories, necessary for GHE analysis, is arduous. Also

the analysis of interface mode's excitation with the plane wave is tedious as with the broad wavefront adds interference at the interface that can drown out processes taking place there.

To avoid such problems associated with the use of plane waves, SW beams were chosen in the investigations on GHE and WA in this thesis. The derivation of SW beam trajectory is relatively easy, especially when the beam is well-collimated and the medium in which it propagates is weakly dispersive. Then calculations of spatial shifts of reflected SWs at the interface are significantly less demanding. In addition, the beams reflect from the interface in a narrow space, making the analysis of the interfacial effects easier.

In MuMax3 micromagnetic simulations the excitation formula used to create the SW beam was inspired by the work of Whitehead [105]. The essence of this formula is to excite simultaneously two magnetic fields which vary in time and space. These fields induce SWs that interfere constructively only in one direction of propagation while interfering destructively in the other direction. The sum of such fields can be written as

$$B_{\mathrm{dyn}}(x,y,t) = b_0[\sin(k_0 x)\sin(2\pi f_0 t) + \cos(k_0 x)\cos(2\pi f_0 t)]\mathrm{Rect}(x/W)\mathrm{G}(y/L), \qquad (3.25)$$

where b_0 is excited field amplitude, k_0 and f_0 are the parameters of the excited SW beam, $\mathrm{Rect}(x/W)$ is the rectangular function which parameter W defined antenna's width along the x axis, and $\mathrm{G}(y/L)$ is Gaussian function which described antenna's length L along the y axis.

The implementation an antenna operating on the principle summarised by Eq. 3.25 in MuMax3 can be done as follows

```
1  field_1 := newVectorMask(Nx, Ny, Nz)
2  field_2 := newVectorMask(Nx, Ny, Nz)
3
4  for i := 0; i<Nx; i++{
5      for j := 0; j<Ny; j++{
6          for k := 0; k<Nz; k++{
7
8          r := index2coord(i,j,k)
9          x := r.x()
10         y := r.y()
11         z := r.z()
12         x_i :=  (x+x0)*cos(theta) + (y+y0)*sin(theta)
13         y_i := -(x+x0)*sin(theta) + (y+y0)*cos(theta)
14
15         gauss_y := exp( -0.5*pow((y_i/sigma_y),2) )
16         xi00 := -antWidth
17
18         field_1.setVector(i,j,k,
19         vector(
20         stimAmp*sin(k0*x_i)*gauss_y*heaviside(-(x_i)-xi00/2)*heaviside((x_i)-xi00/2),
21         0, 0)   )
22
23         field_2.setVector(i,j,k,
24         vector(
25         stimAmp*cos(k0*x_i)*gauss_y*heaviside(-(x_i)-xi00/2)*heaviside((x_i)-xi00/2),
26         0, 0)   )
27
28         }
29      }
30 }
31 B_ext.add(field_1, sin(omega*t)*(1-exp( -0.1*t*omega )  ) )
32 B_ext.add(field_2, cos(omega*t)*(1-exp( -0.1*t*omega )  ) )
```

The variables $field\_1$ and $field\_2$ contain the spatial distribution of magnetic fields, the fields are separated in terms of their modulation by either *sin* or *cos* function. In the *for* loops the spatial distributions of magnetic fields are defined. In the lines 11 and 12 modulation of the system's coordinates is presented. The new coordinates are not only shifted in space by values $x0$ and $y0$ but also rotated by an angle θ. Such a modulation of coordinates allows for an easy placing of the antenna in simulation system and pointing of the excited SW beam.

In the next step the shape of antenna is defined. The Gaussian envelope of the excited SW beam is described by the variable *gauss_y* which specifies the beam's shape along y_i direction. The length of the antenna along y_i direction in this example is governed by a_2 variable. Along its x_i axis the antenna is constrained by two Heaviside step-functions, thus has a rectangular shape in this direction with the width described by *antWidth* parameter. The antenna's width along x_i axis as to be in range of at least a few wavelengths to assure proper interference of the excited SWs so the antenna would excite an unidirectional beam.

At the last step both spatial modulations are multiplied by the *sin* or *cos* functions in the time domain and are added to the external magnetic field. Additionally, they are also modulated by the exponential increase function. This modulation causes the amplitude of the excited SWs to rise slowly and thus limits the excitation of the undesired frequencies during the initiation of excitation.

The Fig. 3.9(a) presents the unidirectional SW beam excited in a micromagnetic simulation. The figure was taken after the system has reached the steady-state. Additionally, with slightly amended simulation code it is also possible to excite SW wavepacket. The only difference is in defining time dependence of the dynamic field to disappear in time, e.g. time-dependent Gaussian function can be used such as

$$G_{\text{wavepacket}}(t) = e^{-\frac{1}{2}(\frac{t-t_0}{\sigma_t})^2}, \tag{3.26}$$

where σ_t is the time modulation of the excited wavepacket and t_0 is the excitation time shift. The FWHM of excited wavepacket in the time domain is given by an approximated formula $2\sqrt{2\ln(2)}\sigma_t$. An example of SW wavepacket excitation is shown in Fig. 3.9(b). The unidirectional excitation of SWs was used in investigations presented in Sections 5.5 and 5.6.
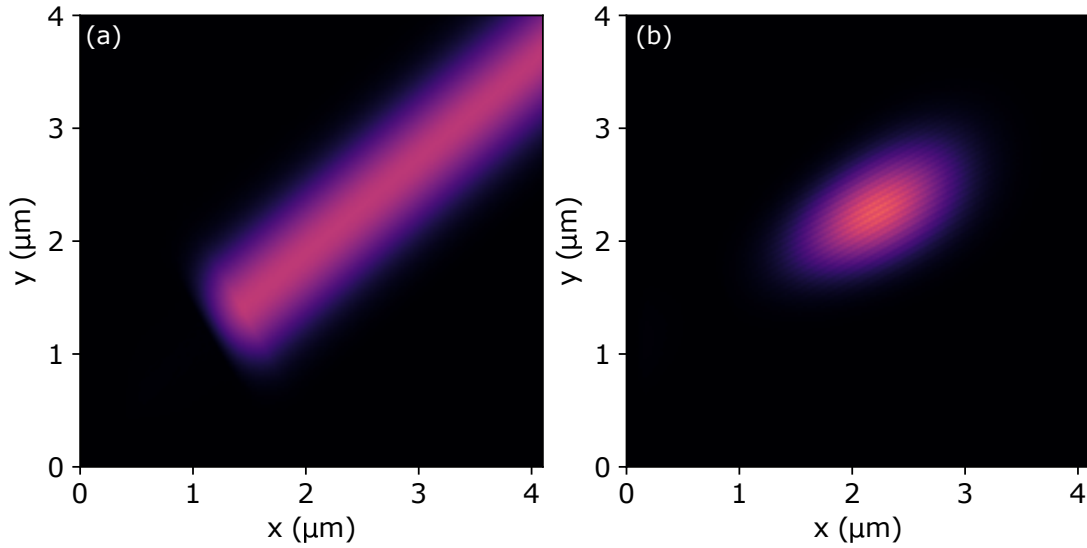

Figure 3.9 (a) An example of SW beam excited by an antenna defied with Eq. 3.25. (b) A SW wavepacket excited by the antenna described by Eq. 3.25 modified by Eq. 3.26.

Chapter 4

Synopsis of scientific work

4.1 Motivation

SWs described at length in Chapter 1 are believed to be a promising carrier of information in future data processing technologies [106]. The search for new approaches to data processing is needed as currently used technologies based on CMOS (Complementary Metal-Oxide-Semiconductor) are approaching their physical limits [107]. These limitations include problems such as circuitry miniaturisation caused by the Heisenberg uncertainty principle and overheating of CMOS based circuitry as a result of Joules heating related to the movement of electrons.

Science explores several alternative information carriers to replace the electrons used in CMOS technology. Among them are plasmons (studied in plasmonics) [108, 109], photons (photonics) [110], and SWs in magnonics. Plasmonics and photonics are developed alongside magnonics, as they offer higher operational frequencies compared to electronics. However, the key advantage of magnonics is that SWs operate at microwave frequencies similar to those used in the wireless communication, but with significantly shorter wavelengths. Theoretically, this enables an easier integration of magnonic devices with electronics while also allowing for a greater miniaturisation compared to electronic counterparts.

Miniaturisation is not the only advantage provided by of using SWs. Another key benefit is that information transmission via SWs does not involve Joule heating, unlike in electronics or plasmonics [111]. Joule heating is not an issue in magnonics, eliminating the problem of device overheating during operation. Additionally, SWs carry less energy than moving electrons, further reducing the energy consumption of magnonic-based technology. Moreover, magnonics, similar to photonics, enables a novel approach to computing based on wave interference. The combination of interference-based computing and the inherent non-linear nature of SWs makes them highly promising candidates for advanced data processing applications, such as the implementation of artificial neural networks [112].

Despite all of the advantages provided by using SWs the technology based on magnonics has not been implemented in everyday life devices, at the time of writing this thesis. There are several issues associated with using SWs that hinder development of magnonic technologies. Among them are sensitivity of low-energetic SWs to thermal fluctuations in the magnetic media, high SW damping in most of known magnetic materials, not enough of methods to reliably excite, control, and detect SW propagation in space. The aim of research presented in this thesis is to provide a theoretical base for the new methods of SW propagation control using magnonic interferometers. This task involves investigating both linear and non-linear resonance effects which accompany SW reflection from and transmission through magnonic interferometers. This research is a part of wider attempts to develop methods for SW propagation control by using magnonic interferometers. The theoretical works on magnonic resonators can be found also in [113, 114], while examples of experimental papers are represented by [115, 116].

4.2   Overview of scientific publications included in thesis

The following two chapters of this thesis present seven scientific papers published during the Author's PhD studies. Five of these papers form a cohesive series of investigations on resonance effects in both linear and non-linear SW dynamics and are included in Chapter 5. The remaining two papers, whose first pages are displayed in Chapter 6, explore additional SW-related topics beyond the Author's initial research plan. These studies were also published during the course of the PhD studies.

The first publication, presented in Section 5.2, opens the investigations on SW propagation control by describing the influence of GTI on reflected SWs. This paper contains both the results of numerical simulations and the results of a semi-analytical model based on LL equation to describe the change of SW parameters by magnonic interferometers. The second paper, Section 5.3, expands the results presented in the first paper by exploring different geometries of GTI. The third paper, Section 5.4, presents a detailed description of the semi-analytical model which results are shown in the first paper. In all of these three papers the numerical simulations were done in DE magnetic configuration, cf. Subsection 1.5.2, and in two-dimensional space as it was allowed by magnonic interferometers symmetry (infinitely wide interferometers were assumed). Both COMSOL Multiphysics and Mumax3 environments were used for these simulations, were COMSOL was more favoured for the first two papers as these simulations were done in the eigenfrequency domain.

The next paper, Section 5.5, was also devoted to investigation of GTI but in three-dimensional simulations carried out in the time domain, thus done in Mumax3 environment only. For purpose of the paper in Section 5.5 the magnetisation of GTI was uniform and the reflection of oblique SW beam was investigated.

In the last paper included in this thesis, Section 5.6, the non-linear resonance effects of scattered SWs were investigated. These simulations did not include magnonic interferometers, the localisation of SW modes required for inelastic scattering was realised by introducing a magnetisation field non-uniformity in the system. Additionally, again Mumax3 environment was chosen to perform simulations as full LLG equation implementation employed by Mumax3 allows for investigation of non-linear effects in magnonics.

The evolution of magnonics research presented in Chapter 5 may be understood as scientific path starting from simplified micromagnetic simulations of linear resonance effects governed by simplified LLG equation towards micromagnetic simulation with full LLG equation that focus on the non-linear effects of SW scattering.

The two papers presented in Chapter 6 are the result of Author's collaborations in different scientific projects. The paper in Section 6.1 presents the results of investigation on eigenstates of a complex, three-dimensional magnetic structure called a hopfion. The publication in Section 6.2 is devoted to the SW confinement in an external magnetic field non-uniformity created by a presence of a superconductor in the vicinity of a magnetic layer.

Chapter 5

Papers representing the main research

5.1 Co-authors declarations

Dr Piotr Graczyk

Institute of Molecular Physics,, Polish
Academy of Sciences, 60-179 Poznań, Poland

Declaration

Hereby I declare my contribution to the following papers:

1. K. Sobucki, W. Śmigaj, P. Graczyk, M. Krawczyk, P. Gruszecki, *"Magnon-Optic Effects with Spin-Wave Leaky Modes: Tunable Goos-Hänchen Shift and Wood's Anomaly"*, Nano Letters, 2023, 23, 15, 6979–6984;

I have performed additional simulations of the system described in the paper in COMSOL Multiphysics environment in the frequency domain. My results were used in the discussions leading to preparation of the manuscript but they were not included in the final version of the paper. I was involved in preparing the answers to the reviews of the paper.

23.04.2025
………………
Date

……………
Signature

Dr hab. Paweł Gruszecki, prof. UAM

Institute of Spintronics and Quantum
Information, Faculty of Physics, Adam Mickiewicz University,
61-614 Poznań, Poland

Declaration

Hereby I declare my contribution to the following papers:

1. K. Sobucki, W. Śmigaj, J. Rychły, M. Krawczyk, P. Gruszecki, *"Resonant subwavelength control of the phase of spin waves reflected from a Gires–Tournois interferometer."* Scientific Reports 11.1 (2021): 1-12.

I contributed to defining the investigation problem for this paper. My involvement also included discussions on the research methodology and result interpretation, as well as manuscript drafting and responding to reviewer comments. For Fig. 2(a,b,c), I prepared results derived from micromagnetic simulations I performed using Mumax3.

2. K. Sobucki, P. Gruszecki, J. Rychły, M. Krawczyk, *"Control of the phase of reflected spin-waves from magnonic Gires-Tournois interferometer of subwavelength width"* IEEE Transactions on Magnetics 58 (2), 1-5, (2021)

My contributions to this paper include defining the investigation problem and participating in discussions on the simulation result. I was also involved in drafting the manuscript and responding to reviews.

3. W. Śmigaj, K. Sobucki, P. Gruszecki, M. Krawczyk, *"Modal approach to modeling spin wave scattering"*, Physical Review B 108 (1), 014418

I was involved in discussions regarding the results, manuscript drafting, and addressing reviewers comments for this paper.

4. K. Sobucki, W. Śmigaj, P. Graczyk, M. Krawczyk, P. Gruszecki, *"Magnon-Optic Effects with Spin-Wave Leaky Modes: Tunable Goos-Hänchen Shift and Wood's Anomaly"*, Nano Letters, 2023, 23, 15, 6979–6984

I contributed to defining the investigation problem for this paper. My involvement also included discussions on the research methodology and interpretation of results, as well as manuscript drafting and responding reviewers' comments.

5. K. Sobucki, I. Lyubchanskii, M. Krawczyk, P. Gruszecki, *"Goos-Hänchen shift of inelastically scattered spin-wave beams and cascade nonlinear magnon processes"* Scientific Reports 15, 5538 (2025)

I contributed to defining the investigation problem for this paper. My involvement also included discussions on the research methodology and result interpretation, as well as manuscript drafting and responding to reviewer comments.

28.05.2025
....
Date

Paweł Gruszecki
....
Signature

Prof. Maciej Krawczyk

Institute of Spintronics and Quantum
Information, Faculty of Physics and Astronomy, Adam Mickiewicz University,
61-614 Poznań, Poland

Declaration

Hereby I declare my contribution to the following papers:

1. K. Sobucki, W. Śmigaj, J. Rychły, M. Krawczyk, P. Gruszecki, "*Resonant subwavelength control of the phase of spin waves reflected from a Gires–Tournois interferometer.*" Scientific Reports 11.1 (2021): 1-12.;

I contributed to defining the investigative problem and was involved in discussions about the simulation results, contributed to the writing of the manuscript and the preparation of responses to reviews.

2. K. Sobucki, P. Gruszecki, J. Rychły, M. Krawczyk, "*Control of the phase of reflected spin-waves from magnonic Gires-Tournois interferometer of subwavelength width*" IEEE Transactions on Magnetics 58 (2), 1-5, (2021);

I have contributed to defining the investigation problem, involved in the discussions on the results of simulations, checking the manuscript, and contributing to the preparation of responses to the reviews.

3. W. Śmigaj, K. Sobucki, P. Gruszecki, M. Krawczyk, "*Modal approach to modeling spin wave scattering*", Physical Review B 108 (1), 014418;

I have contributed to defining the investigation problem, involved in the discussions on the results of simulations, manuscript checking.

4. K. Sobucki, W. Śmigaj, P. Graczyk, M. Krawczyk, P. Gruszecki, *"Magnon-Optic Effects with Spin-Wave Leaky Modes: Tunable Goos-Hänchen Shift and Wood's Anomaly"*, Nano Letters, 2023, 23, 15, 6979–6984;

I have been involved in the discussions regarding the results presented in the paper, manuscript correction and contributing to the preparation of the responses to reviews.

5. K. Sobucki, I. Lyubchanskii, M. Krawczyk, P. Gruszecki, *"Goos-Hänchen shift of inelastically scattered spin-wave beams and cascade nonlinear magnon processes"* Scientific Reports 15, 5538 (2025)

I was involved in discussions regarding the results presented in the paper manuscript correction and contributing to the preparation of the responses to reviews.

29.05.2025　　　　　　　　　　　　　　……………
Date　　　　　　　　　　　　　　　　　Signature

prof. Igor Lyubchanskii

in collaboration with
Adam Mickiewicz University, Poznań

Declaration

Hereby I declare my contribution to the following papers:

1. K. Sobucki, I. Lyubchanskii, M. Krawczyk, P. Gruszecki, *"Goos-Hänchen shift of inelastically scattered spin-wave beams and cascade nonlinear magnon processes"*, Scientific Reports 15, 5538, 2025
I was the main initiator of the research that led to this publication and I was involved in the discussions concerning obtained results and the manuscript preparation.

23.04.2025
....
Date

....
Signature

/I. Lyubchanskii/

Dr Justyna Rychły-Gruszecka

Institute of Molecular Physics,
Polish Academy of Sciences, 60-179 Poznań, Poland

Declaration

Hereby I declare my contribution to the following papers:

1. K. Sobucki, W. Śmigaj, J. Rychły, M. Krawczyk, P. Gruszecki, *"Resonant subwavelength control of the phase of spin waves reflected from a Gires–Tournois interferometer."* Scientific Reports 11.1 (2021): 1-12.;

I have performed micromagnetic simulations in COMSOL Multiphysics environment to calculate the dispersion relations of the investigated systems. The results are presented in Fig. 2(a,b). I was involved in the discussions regarding the results presented in the paper. I also contributed to writing the manuscript and the responses to the reviews.

2. K. Sobucki, P. Gruszecki, J. Rychły, M. Krawczyk, *"Control of the phase of reflected spin-waves from magnonic Gires-Tournois interferometer of subwavelength width"* IEEE Transactions on Magnetics 58 (2), 1-5, (2021);

I have performed micromagnetic simulations in COMSOL Multiphysics environment to calculate the dispersion relations of the investigated systems. The results are presented in Fig. 2. I have written the description of the dispersion relation calculation in the manuscript. I was involved in the discussions regarding all simulation results included in the paper.

04 V 2025
....
Date

Rychły-Gruszecka
....
Signature

Dr Wojciech Śmigaj
Optopol Technology, Żabia 42, 42-400
Zawiercie, Poland

Declaration

Hereby I declare my contribution to the following papers:

1. K. Sobucki, W. Śmigaj, J. Rychły, M. Krawczyk, P. Gruszecki, *"Resonant subwavelength control of the phase of spin waves reflected from a Gires–Tournois interferometer."* Scientific Reports 11.1 (2021): 1-12.;
I have developed the two-mode model and I have employed this model to perform calculations of the system investigated in the paper to extend the analysis of the results presented in the paper. I was involved in the discussions concerning obtained results and the manuscript preparation.

2. W. Śmigaj, K. Sobucki, P. Gruszecki, M. Krawczyk, *"Modal approach to modeling spin wave scattering"*, Physical Review B 108 (1), 014418;
I have developed the semi-analytical model based on finite element method for spin-wave scattering calculations which was used to investigate spin-wave scattering on magnonic Fabry-Perot interferometer. I have written the first draft of the publication manuscript and I have prepared most of the figures included in the manuscript. I have prepared the answers to the reviewers during publication process.

3. K. Sobucki, W. Śmigaj, P. Graczyk, M. Krawczyk, P. Gruszecki, *"Magnon-Optic Effects with Spin-Wave Leaky Modes: Tunable Goos-Hänchen Shift and Wood's Anomaly"*, Nano Letters, 2023, 23, 15, 6979–6984;
I was involved in the discussion of the results obtained by the micromagnetic simulations. I have helped in writing of the manuscript and its evaluation.

7.5.2025
....
Date

Wojciech Śmigaj
....
Signature

5.2   Resonant subwavelength control of the phase of spin waves reflected from a Gires–Tournois interferometer

Ferromagnetic nanoresonators are believed to be a promising building block of magnonics devices as they can be used to shift phase of propagating SWs. Resonators placed in the vicinity of a magnetic layer where SWs propagate are realisation of magnonic interferometers which influence SWs. When the resonator is placed at the edge of magnetic layer an interferometer in so-called Gires-Tournois geometry is created. In this paper the main research goal was to investigate the influence of subwavelength-width magnonic interferometers on reflected SWs, which was a part of broader investigations on possibility to design magnonic metasurfaces. The investigation was conducted by means of numerical simulations. A strongly non-linear dependency between phase shift of reflected waves and the width of interferometer was described. It was shown that magnonic Gires-Tournois interferometers of width smaller than the incident SW wavelength were able to induce Fabry-Perot resonances, in contrast to the theory known in optics which states that the interferometer should have at least the width of incident wavelength. The induction of the Fabry-Perot resonance in subwavelength magnonic interferometer was possible as magnonic interferometers harbour multiple SW modes including short-wavelength SW modes that may be excited by the incoming SWs. During the resonances described magnonic interferometers significantly influence the reflected SWs, e.g. shift their phase by 360°. In the paper also an explanation of this behaviour is provided by a semi-analytical model. The model elucidates an influence of two types of interferometer's eigenmodes on phase shift and occurrence of the resonances in the system.

In this publication Author has carried out all numerical simulations both in COMSOL Multiphysics and MuMax3 environments, apart from dispersion relation calculations, and processed the data with self-developed code. The Author has written bulk of the manuscript as well as prepared all of the figures included in the manuscript apart from Fig. 2. The Author was responsible for communication with the journal together with Paweł Gruszecki.

---

scientific reports

Check for updates

OPEN

Resonant subwavelength control of the phase of spin waves reflected from a Gires–Tournois interferometer

Krzysztof Sobucki[1⊠], Wojciech Śmigaj[2], Justyna Rychły[3], Maciej Krawczyk[1] & Paweł Gruszecki[1⊠]

Subwavelength resonant elements are essential building blocks of metamaterials and metasurfaces, which have revolutionized photonics. Despite similarities between different wave phenomena, other types of interactions can make subwavelength coupling significantly distinct; its investigation in their context is therefore of interest both from the physics and applications perspective. In this work, we demonstrate a fully magnonic Gires–Tournois interferometer based on a subwavelength resonator made of a narrow ferromagnetic stripe lying above the edge of a ferromagnetic film. The bilayer formed by the stripe and the film underneath supports two propagative spin-wave modes, one strongly coupled with spin waves propagating in the rest of the film and another almost completely reflected at the ends of the bilayer. When the Fabry–Perot resonance conditions for this mode are satisfied, the weak coupling between both modes is sufficient to achieve high sensitivity of the phase of waves reflected from the resonator to the stripe width and, more interestingly, also to the stripe-film separation. Such spin-wave phase manipulation capabilities are a prerequisite for the design of spin-wave metasurfaces and may stimulate development of magnonic logic devices and sensors detecting magnetic nanoparticles.

The recent years have been marked by a rapidly growing demand for interconnected mobile devices. This emerging ecosystem of connected devices, preferably communicating wirelessly, is referred to as the Internet of Things. There are estimations that within the next few years, the number of WiFi-enabled devices will be at least four times larger than the total population of the world[1]. One of the essential components of the Internet of Things are small and energetically efficient devices processing signals converted from and then back to microwaves, within the edge computing paradigm. In this field, the application of spin waves (SWs), which are collective disturbances of magnetization oscillating at the same frequency range as microwaves and thus able to couple to them, opens up a new opportunity to increase the efficiency and functionality of microwave devices. Compared to exsisting microwave devices, SW components offer prospects for increased miniaturization (SWs can have wavelengths 3–5 orders of magnitude shorter than microwaves of the same frequency), easy external control of SW signals, reprogrammability, and significant decrease of energy demands due to lack of Joule heating related to SWs propagation[2–4]. In order to use this kind of waves as an information carrier, efficient methods of their excitation and control over their amplitude and phase must be developed.

In modern photonics, a breakthrough in the control of reflected and transmitted waves at subwavelength distances has recently been achieved through the use of arrays of nanostructured antennas absorbing and ree-mitting modified electromagnetic waves[5,6]. These arrays, so-called metasurfaces, are used to obtain anomalous refraction of incident waves or to design flat, ultra-narrow lenses able also to form holograms. Moreover, such nanostructured antennas can serve as color filters with subwavelenght pixels for printing purposes, as a replacement of chemical dyes[7,8].

There are several reports on the SW coupling of an uniform ferromagnetic film with small magnetic elements. Kruglyak et al. have shown that a narrow ferromagnetic element placed on top of a magnetic waveguide can be used to emit SWs, to control the phase of SWs passing below the resonator, and under some conditions even to absorb the energy of propagating SWs[9–11]. Yu at al. have demonstrated chiral excitation of SWs in a thin

[1]Faculty of Physics, Adam Mickiewicz University, Uniwersytetu Poznanskiego 2, 61-614 Poznan, Poland. [2]Met Office, FitzRoy Rd, Exeter EX1 3PB, UK. [3]Institute of Molecular Physics, Polish Academy of Sciences, Mariana Smoluchowskiego 17, 60-179 Poznan, Poland. ⊠email: krzsob@amu.edu.pl; gruszecki@amu.edu.pl
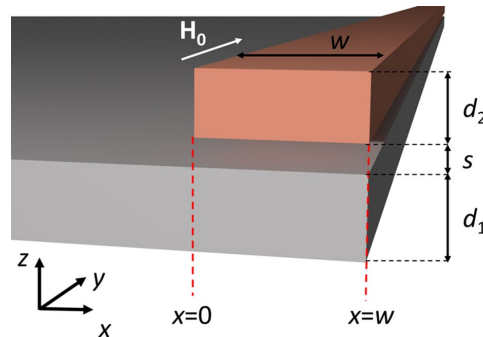
Figure 1. Geometry of the system used in simulations. A ferromagnetic stripe of width w and thickness d_2 is separated from a semi-infinite permalloy film of thickness d_1 by a distance s. The right edges of both layers are aligned at $x = w$. The whole system is placed in an external magnetic field $\mu_0 H_0 = 0.1\,\mathrm{T}$ parallel to the y axis. The geometry of the system is independent from y.

film through its dipolar coupling with a single nanowire or a grating of nanowires placed in a spatially uniform microwave-frequency magnetic field[12,13]. Subsequently, the existence of Fano resonances and their influence on the amplitude and phase of transmitted waves in a single-mode waveguide has been studied further by Al et al.[14], and Zhang et al. have demonstrated the application of a single dynamically tunable resonator in zero bias field placed on top of a waveguide to tune the phase of the transmitted SWs[15]. A grating coupler made up of an array of resonators has been used to excite short-wavelength SWs[16,17], and Graczyk et al.[18] have demonstrated that dynamical coupling of a homogeneous ferromagnetic film with a periodic array of ferromagnetic stripes placed underneath can lead to the formation of a magnonic band structure in the film. However, the effect of a resonator on the phase of the reflected wave has not been studied in magnonics; moreover, the conditions for the existence of Fabry–Perot resonances and their effect on both reflected and transmitted SWs, especially at subwavelength distances, remain almost unexplored[19], while both may be key ingredients in creating a magnonic metasurface.

In this paper, we investigate theoretically the interaction of a narrow, subwavelength-width stripe placed above the edge of a homogeneously magnetized film with propagating SWs, study its influence on the phase shift of reflected SWs, and finally demonstrate a magnonic Gires–Tournois interferometer[20]. Using frequency-domain finite-element (FD-FEM) calculations and micromagnetic simulations we find that this shift depends on the width of the stripe in a non-trivial way: an overall slow and steady increase of the phase shift with stripe width is repeatedly interrupted by sharp phase jumps by 360°. Treating the stripe and the underlying film as a non-reciprocal waveguide supporting two pairs of counter-propagating modes, we formulate a semi-analytical model that explains this behavior as a consequence of Fabry–Perot resonances produced by one of these mode pairs. We also show that by varying the film-stripe separation it is possible to switch between resonances of different order. Our results point to the importance of Fabry–Perot resonances appearing in locally bilayered ferromagnetic elements, with potential applications for the control of SW propagation in magnonic devices at subwavelength distances.

Results and discussion

Structure under consideration. We consider a system composed of non-magnetic and ferromagnetic materials. Its geometry is independent of the y coordinate and piecewise constant along x, as shown schematically in Fig. 1. The system consists of a semi-infinite permalloy (Py) film of thickness 50 nm and a ferromagnetic stripe of thickness 40 nm and finite width w. Both elements are separated by a distance s and their right edges are aligned to $x = w$. Throughout the paper, we will vary the width w of the stripe and its separation s from the film. We are interested in manipulating the phase of the reflected SWs using subwavelength elements; therefore the width of the stripe will be smaller than or comparable to the wavelength of SWs in the Py film at the frequency of operation. The system is magnetized by a uniform in-plane magnetic field of magnitude $\mu_0 H_0 = 0.1\,\mathrm{T}$ directed along the y axis. In all calculations we have taken the saturation magnetization of the film to be $M_S = 760\,\mathrm{kA/m}$ and its exchange constant, $A_{ex} = 13\,\mathrm{pJ/m}$. The stripe is made of a material (called FM2 from here on) with $M_S = 525\,\mathrm{kA/m}$ and $A_{ex} = 30\,\mathrm{pJ/m}$; lowering its saturation magnetization and increasing the exchange constant with respect to Py will allow us to exploit interactions of local resonances of the stripe with propagating waves in Py at frequencies characteristic for the dipolar and dipole-exchange SWs. Such a choice of the stripe's material shifts the SW spectrum down and flattens the first band for lower wavevectors with respect to the Py, as will be discussed in the next section. The gyromagnetic ratio of both ferromagnets is $\gamma = -176\,\mathrm{rad}$ GHz/T.
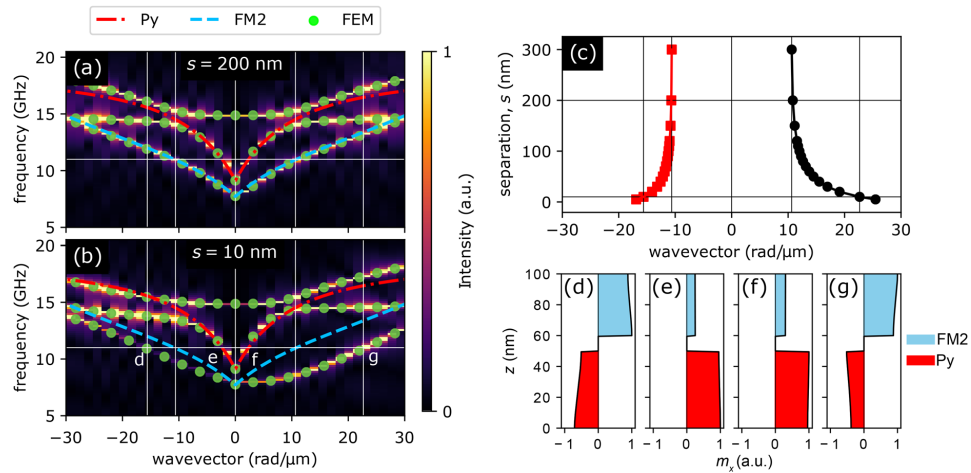
Figure 2. (**a,b**) Dispersion relations calculated for two infinite films made of Py and FM2 separated by a non-magnetic spacer of width (**a**) 200 nm and (**b**) 10 nm. Colormaps in the background present results obtained by means of micromagnetic simulations, whereas green points correspond to the results of FD-FEM calculations. The dashed blue and the dash-dotted red lines are the analytical dispersion relations of SWs supported by isolated FM2 and Py films, respectively. The horizontal line marks the frequency $f = 11$ GHz used in further calculations. (**c**) Dependence of the wavenumber of the slow modes, marked with d and g in (**b**), located predominantly in FM2, on the separation between films at frequency 11 GHz. (**d–g**) Profiles of the dynamic m_x component of the magnetization (normalized to a maximum of 1) of the (**d**), (**g**) slow and (**e,f**) fast modes of the Py/FM2 bilayer with spacer width 10 nm at frequency 11 GHz. The positions of these modes on the dispersion diagram are marked with letters d–g in panel (**b**).

Dispersion relation of bilayers. Before we study the coupling of a film with a finite-width stripe and SW reflection, let us first analyze the interaction between modes in infinitely extended films, i.e., in bilayers composed of an infinite Py film separated by a non-magnetic spacer from another infinite film made of FM2. Two example dispersion relations calculated using micromagnetic simulations and FD-FEM (see the "Methods" section for details) for bilayers with separations $s = 200$ nm and $s = 10$ nm are presented in Fig. 2a,b, respectively. It is clear that for a 200 nm-wide separation, the SW modes in Py and FM2 almost do not interact with each other: the calculated dispersion curve coincides with the analytical dispersion curves of isolated Py and FM2 films calculated using [21, Appendix C.7]:

$$\omega^2 = \omega_0(\omega_0 + \omega_M) + \frac{\omega_M^2}{4}\left[1 + e^{-2kd}\right], \qquad (1)$$

where d is the film thickness, $\omega = 2\pi f$ is the angular frequency of SWs (f denotes the frequency), k is the wavenumber, $\omega_0 = |\gamma|\mu_0(H_0 + M_S l^2 k^2)$ [22, Chapter 7.1], $l = \sqrt{2A_{ex}/(\mu_0 M_S^2)}$ is the exchange length, and $\omega_M = |\gamma|\mu_0 M_S$.

The only visible difference occurs at frequencies above 14 GHz where we can see a hybridization between the fundamental SW mode and the first mode quantized across the thickness, a so-called perpendicular standing SW[21]. This hybridization and perpendicular standing SWs, however, are not considered in the analytical model and in investigations presented in the following part of the paper.

At frequencies below 14 GHz the modes in the bilayered structure can be classified according to their origin and group velocity. The *fast* modes are related to SW dynamics in Py (see Fig. 2e,f) and are characterized by steeper dispersion (therefore higher group velocity) and longer wavelengths. In contrast, the *slow* modes originating in FM2 (see Fig. 2d,g) have lower group velocity and shorter wavelengths. It is worth noting that the wavelengths of SWs in separated layers do not depend on the direction of propagation, while the dynamic dipolar coupling between SW modes in both layers combined with the nonreciprocal nature of surface SW modes introduces asymmetry[23–25]. For $s = 200$ nm the coupling is still very weak and at the frequency of 11 GHz, which is used in further analysis and marked with the white horizontal line in Fig. 2a, the fast and slow modes have wavelengths of 2660 nm and 590 nm, respectively, for both propagation directions.

Reduction of the non-magnetic spacer width to $s = 10$ nm causes strong interaction between the modes. The wavelength of the slow modes decreases significantly and their dispersion relation becomes strongly non-reciprocal; at 11 GHz, the slow mode propagating leftwards has wavelength 390 nm and the one propagating rightwards, 270 nm. Fig. 2c shows that the asymmetry of the dispersion relation for slow modes grows as the films are brought closer to each other.
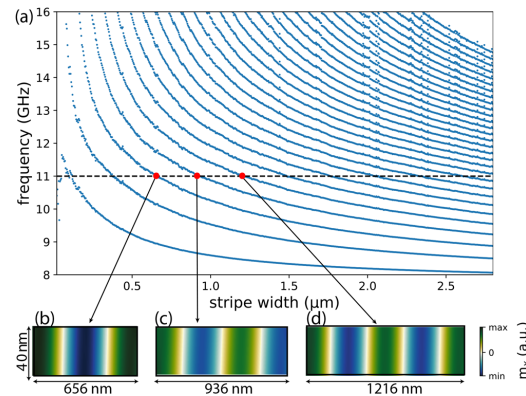
Figure 3. (**a**) Dependence of the frequency of stripe modes on the stripe width. The dashed line marks the frequency $f = 11$ GHz. (**b**–**d**) Profiles of modes supported by stripes of width 656 nm, 936 nm, and 1216 nm at frequency 11 GHz.

Eigenmodes of finite-width stripes. The dependence of the eigenmode spectrum of an isolated finite-width FM2 stripe on its width is displayed in Fig. 3a. These calculations were made with FD-FEM for the first thirty modes of stripes with widths up to 2800 nm; note that SW wavelength in uniform Py films at 11 GHz is 2660 nm. As intuitively expected, mode frequency decreases with increasing stripe width. The horizontal dashed line in Fig. 3 marks $f = 11$ GHz. It is visible that stripes of multiple widths support modes at this frequency. Profiles of three successive modes (for stripes of width 656 nm, 936 nm, and 1200 nm) are shown in Fig. 3b–d. Successive resonances appear for stripes of widths differing by approximately half of the wavelength of the eigenmode of a homogeneous FM2 film, i.e., $\Delta w \approx 280$ nm $\approx 0.5\lambda_{FM2}$.

Lateral mode confinement in a reciprocal medium leads to formation of standing waves and quantization of the wavenumber. The standing waves have the form $\exp(ik_n x) + \exp(-ik_n x)$, where n is the mode index, $k_n = r_n \pi/w$ and $r_n = n + \delta$ ($0 \leq \delta \leq 1$). For the Dirichlet (magnetic wall) boundary conditions, with the dynamic magnetization vanishing at the edges, we get $r_n = n + 1$, whereas for "free spins" at the edges, $r_n = n$. However, due to dipolar interactions, in magnetic stripes neither of these boundary conditions is correct and the magnetization is partially pinned at the stripe edges, $0 < \delta < 1$[26,27]. This can also be interpreted as the effective width of the waveguide being slightly larger than the real one, or in terms of a non-zero phase shift φ being experienced at the stripe edges by the SWs forming the standing wave. Thus, resonances occur when the following condition is met:

$$kw + \varphi = \pi n, \quad n = 1, 2, \ldots \tag{2}$$

According to this equation, successive resonances at frequency 11 GHz should appear for stripes of widths differing by ca. $\lambda/2 \approx 280$ nm; this is confirmed by the FD-FEM calculations.

Phase shift of the reflected SWs. Before studying the influence of the stripe's presence on the SW reflection, let us first discuss SW reflection from the edge of an isolated truncated film. According to Stigloher et al.[28], dynamic dipolar interactions induce a phase shift between the incident and reflected SWs. This phase shift is a natural consequence of the previously discussed dipolar pinning occurring at the boundaries of thin ferromagnetic film[26]. Interestingly, Verba et al.[29] have recently shown that a phase shift may also be introduced by a polarization mismatch between incident and reflected SW modes. Regardless of the physical mechanism responsible for the phase shift, we can extract its magnitude from the steady-state solutions formed far away from the edge. The phase shift manifests itself in the resulting interference pattern as a displacement of nodes with respect to the interface from which the waves are reflected. If the interface is located at $x = x_0$ and the reflection coefficient is $e^{i\varphi}$, where φ is the phase shift, the standing wave pattern sufficiently far from the interface (at $x \ll x_0$) will be

$$m(t; x) = \text{Re}\left\{A e^{-i2\pi ft}[e^{ik(x-x_0)} + e^{i\varphi} e^{-ik(x-x_0)}]\right\} = a(t) \cos[k(x - x_0) - \varphi/2], \tag{3}$$

where A and $a(t)$ are scaling coefficients independent of x. The change in the standing wave pattern due to varying phase shift is illustrated in Fig. 4a,b.

In practice, we calculate φ by fitting the expression on the right-hand side of Eq. (3) to a snapshot of m_x on the symmetry axis of the Py film obtained from micromagnetic or FD-FEM simulations. To avoid distortions caused by evanescent waves excited at the interface, only points lying at least one stripe width from the left of the interface are taken into account. The phase shift occurring at the edge of a 50-nm-thick Py film at frequency 11 GHz is found numerically to be 230°. The resulting standing wave pattern is shown in Fig. 4b.
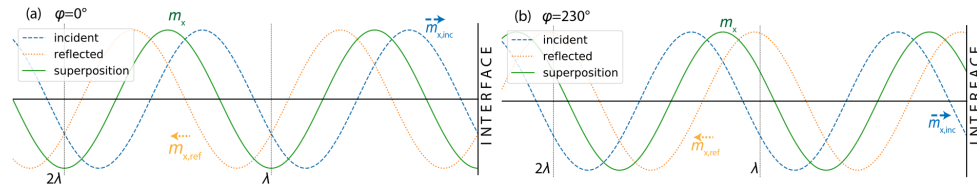
Figure 4. (**a**) Incident and reflected plane waves at an arbitrary time, and resulting interference pattern, in the zero phase shift case, i.e., $\varphi = 0°$. The dotted orange line and the dashed blue line correspond to the incident and reflected plane waves, respectively. The solid green line corresponds to the interference pattern. (**b**) The same for a phase shift of $\varphi = 230°$, i.e., the value obtained for SW reflection from the edge of a semi-infinite 50-nm-thick Py film.
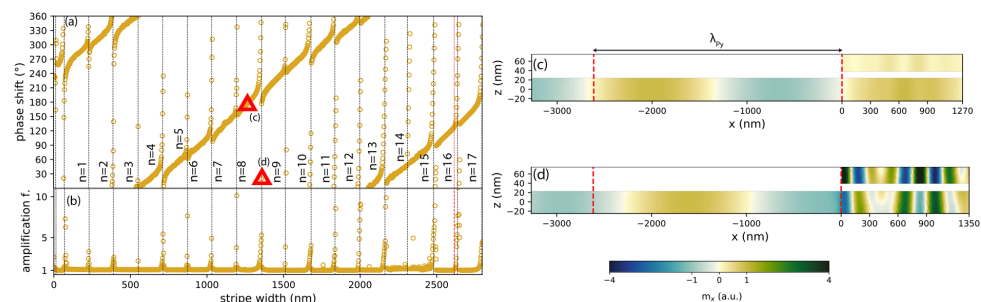

Figure 5. (**a**) Phase shift of SWs at frequency 11 GHz as a function of the stripe width, calculated by the FD-FEM. The stripe-film separation is $s = 10$ nm. Resonances (rapid changes of the phase shift, marked with vertical dotted lines) appear periodically with a period of ca. 160 nm. (**b**) SW amplification factor in Py below the stripe, obtained by dividing the maximum of $|m_x|$ in the part of the film lying below the stripe by the maximum of $|m_x|$ in the far field. (**c**) Snapshot of the dynamic magnetization m_x in a plateau region (stripe width: 1270 nm). (**d**) Snapshot of the system in resonance at 11 GHz (stripe width: 1350 nm). The distance between the red dashed lines in (**c**,**d**) corresponds to the SW wavelength in a uniform Py film at the same frequency.

Phase shift dependence on stripe width. The introduction of a stripe over the Py film edge locally modifies the environment in which SWs propagate due to dynamic dipolar interactions between the film and the stripe. In consequence, it influences also the phase shift of reflected waves. The variation of this phase shift with a stripe width at frequency 11 GHz, calculated using FD-FEM, is plotted in Fig. 5a. In general, this phase shift, defined according to Eq. (3) with the interface located at the left edge of the stripe, at $x = 0$, grows steadily with stripe width, however with periodic jumps by 360°. These jumps occur approximately every 160 nm and are accompanied by an increase of the amplitude of SWs in the Py film underneath the stripe, as shown in Fig. 5b. In fact, at these stripe widths SWs are amplified in the whole bilayer, indicating that a resonant mode of the bilayer is excited. This can be seen by comparing snapshots of m_x for stripes of width 1270 nm (slowly changing phase shift) and 1350 nm (rapidly changing phase shift) presented in Fig. 5c,d, respectively.

In addition to the enhancement of SW amplitude in the bilayer, Fig. 5c shows that the SWs in the stripe and in the underlying Py layer have approximately opposite phases. In view of the profiles of the *fast* and *slow* modes shown in Fig. 2d–g, we conclude that the slow modes dominate at observed resonances. However, the magnetization pattern in both layers is more complex than that of a typical standing wave composed of two counter-propagating waves with the same wavelength. Indeed, as discussed in "Dispersion relation of bilayers", the bilayer modes have an asymmetric dispersion relation[30]. For such a scenario, we can generalize the resonance condition Eq. (2) to

$$(k_l + k_r)w + \varphi_l + \varphi_r = 2\pi n, \quad n = 1, 2, \ldots, \tag{4}$$

where k_u and k_d are the wavenumbers of right- and left-propagating modes, and φ_l and φ_r are the phase shifts occurring at the left and right interfaces of the stripe. For $k_u = k_d = k$ and $\varphi_r = \varphi_l$ this equation reduces to Eq. (2). Substituting here the wavelengths of the slow modes of a bilayer with $s = 10$ nm given in "Dispersion relation of bilayers", we conclude that successive resonances should occur every 160 nm, which matches very well with the results of FD-FEM calculations shown in Fig. 5.

We have cross-checked these results against micromagnetic simulations made with a finite damping coefficient $\alpha = 0.0001$, see Fig. 6a for phase-width relation and Fig. 6b for amplitude-width relation. Due to computational demands, these have been performed for a narrower range of stripe widths, 0–490 nm, 1000–1650 nm, and
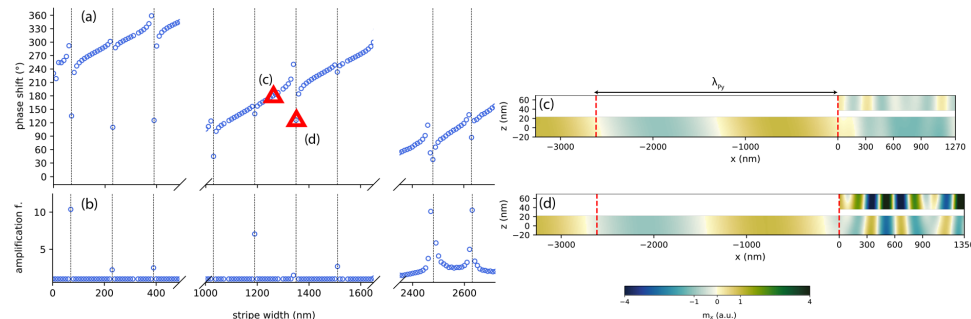
Figure 6. (**a**) Phase shift of SWs at frequency 11 GHz as a function of the stripe width obtained with micromagnetic simulations. (**b**) SW amplification factor in Py below the stripe, defined as in Fig. 5b. (**c**) Snapshot of the dynamic magnetization m_x in a system without a resonance at 11 GHz (stripe width: 1270 nm). (**d**) The same in a system possessing a resonance at 11 GHz (stripe width: 1350 nm). The distance between the red dashed lines in (**c,d**) corresponds to the SW wavelength in a uniform Py film at the same frequency.

2350–2720 nm, encompassing several resonances. The obtained results are consistent with those of FD-FEM calculations: the positions of resonances are the same as obtained by FD-FEM and the slope of the curve in intermediate regions is virtually identical. The almost perfect alignment of those results obtained by two different numerical methods confirms their correctness.

Snapshots of m_x in systems with stripes of width 1270 nm and 1350 nm are displayed in Fig. 6c,d, respectively. The former does not have a resonance at the chosen frequency, whereas the latter does. The obtained magnetization patterns are qualitatively similar to those calculated by FD-FEM [Fig. 5c,d].

Two-mode model analysis. The results presented above indicate that the bilayered part at the edge of the semi-infinite ferromagnetic film allows an efficient control of the phase of the reflected SWs. The phase changes rapidly when the width of the bilayered part fulfils the Fabry–Perot resonant condition, and thus the whole element can be treated as a magnonic Gires–Tournois interferometer[20]. In this section we develop a detailed semi-analytical model providing a clear justification and explanation of this process.

Wave scattering on the interface $x = 0$ separating the film and the bilayered part (see Fig. 1) can be described by a scattering matrix S linking the complex amplitudes of the incoming and outgoing modes on both sides of the interface. If both parts are sufficiently long for the amplitudes of all incoming evanescent modes to be negligible, the amplitudes of the outgoing propagative modes are given by

$$\begin{bmatrix} d_1 \\ u_2 \\ u_3 \end{bmatrix} = S \begin{bmatrix} u_1 \\ d_2 \\ d_3 \end{bmatrix} \equiv \begin{bmatrix} S_{11} & S_{12} & S_{13} \\ S_{21} & S_{22} & S_{23} \\ S_{31} & S_{32} & S_{33} \end{bmatrix} \begin{bmatrix} u_1 \\ d_2 \\ d_3 \end{bmatrix}. \tag{5}$$

Here, u_1 and d_1 are the amplitudes of the right- and left-propagating modes of the Py film, u_2 and d_2 are the amplitudes of the right- and left-propagating slow modes of the bilayer, and u_3 and d_3 are the amplitudes of the right- and left-propagating fast modes of the bilayer (see the dispersion relation shown in Fig. 2). All these amplitudes are measured at the interface between the film and the bilayer. The elements of the scattering matrix S can be calculated using the finite-element modal method (see "Numerical methods"). At 11 GHz, their numerical values are

$$S = \begin{bmatrix} 0.100 - 0.011i & 0.135 + 0.016i & 0.986 + 0.008i \\ -0.104 - 0.168i & -0.290 + 0.929i & 0.035 - 0.113i \\ 0.975 - 0.023i & 0.119 + 0.143i & -0.118 - 0.0273i \end{bmatrix} \tag{6}$$

(these values are obtained for modes normalized to carry unit power, with the phase at the interface chosen so that m_x is real and positive on the symmetry axis of the Py layer). It can be seen that the film mode is coupled primarily with the fast mode of the bilayer. The slow bilayer mode is strongly reflected. There is only weak, though non-negligible, coupling between the fast and slow bilayer modes.

Likewise, the interface $x = w$ between the bilayer and the vacuum can be described by a scattering matrix S':

$$\begin{bmatrix} d'_2 \\ d'_3 \end{bmatrix} = S' \begin{bmatrix} u'_2 \\ u'_3 \end{bmatrix} \equiv \begin{bmatrix} S'_{22} & S'_{23} \\ S'_{32} & S'_{33} \end{bmatrix} \begin{bmatrix} u'_2 \\ u'_3 \end{bmatrix}. \tag{7}$$

Here, u'_2 and d'_2 are the amplitudes of the right- and left-propagating slow modes of the bilayer, and u'_3 and d'_3 are the amplitudes of the right- and left-propagating fast modes of the bilayer, all measured at the bilayer-vacuum interface (hence the prime, used to distinguish them from the amplitudes measured at the film-bilayer interface). The numerical values of these scattering coefficients calculated at 11 GHz are

$$S' = \begin{bmatrix} -0.043 + 0.975i & -0.103 + 0.190i \\ 0.189 + 0.105i & -0.561 - 0.799i \end{bmatrix}. \tag{8}$$

Both modes are strongly reflected and there is only weak cross-coupling.

Mode amplitudes at the two interfaces are linked by

$$u'_i = \exp(ik_{iu}w)\, u_i \equiv \Phi_{iu} u_i, \tag{9a}$$

$$d_i = \exp(-ik_{id}w)\, d'_i \equiv \Phi_{id} d'_i, \quad i = 2, 3, \tag{9b}$$

where k_{iu} and k_{id} are the wave numbers of the right- and left-propagating modes, numerically determined to be $k_{2u} = 16.2$, $k_{3u} = 2.22$, $k_{2d} = -23.1$ and $k_{3d} = -1.90\ \text{rad/}\mu\text{m}$.

Together, Eq. (5), Eq. (7) and Eq. (9) form a system of nine equations for as many unknown mode amplitudes (the amplitude u_1 of the mode incident from the input film is treated as known). To obtain an intelligible expression for the reflection coefficient $r \equiv d_1/u_1$, it is advantageous to start by eliminating the amplitudes u_3, d_3, u'_3 and d'_3 of the fast bilayer mode, which is only weakly reflected at the interface with the Py film and hence will not give rise to strong Fabry–Perot-like resonances. This mimics the approach taken by Lecamp et al.[31] in their model of pillar microcavities. This procedure reduces the second row of Eq. (5) and the first row of Eq. (7) to

$$u_2 = \tilde{S}_{21} u_1 + \tilde{S}_{22} d_2, \tag{10a}$$

$$d'_2 = \tilde{S}'_{22} u'_2 + \tilde{S}'_{23} \Phi_{3u} S_{31} u_1, \tag{10b}$$

where

$$\left[\tilde{S}_{21}\ \tilde{S}_{22}\right] \equiv \frac{1}{1 - \kappa S_{23}\Phi_{3d}S'_{32}\Phi_{2u}} \left[S_{21} + \kappa S_{23}\Phi_{3d}S'_{33}\Phi_{3u}S_{31}\ \ S_{22} + \kappa S_{23}\Phi_{3d}S'_{33}\Phi_{3u}S_{32} \right], \tag{11a}$$

$$\left[\tilde{S}'_{22}\ \tilde{S}'_{23}\right] \equiv \frac{1}{1 - \kappa S'_{23}\Phi_{3u}S_{32}\Phi_{2d}} \left[S'_{22} + \kappa S'_{23}\Phi_{3u}S_{33}\Phi_{3d}S'_{32}\ \ \alpha S'_{23} \right] \tag{11b}$$

and

$$\kappa \equiv (1 - S_{33}\Phi_{3d}S'_{33}\Phi_{3u})^{-1}. \tag{12}$$

The fast bilayer mode is only weakly reflected at the interface with the film: $|S_{33}| \approx 0.12 \ll 1$. Therefore multiple reflections of the fast mode at bilayer interfaces do not give rise to strong Fabry–Perot resonances and the coefficient κ remains close to 1 for all bilayer lengths. Together with the fact that the cross-coupling coefficients S_{23}, S_{32}, S'_{23} and S'_{32} are small, this means we can expect the scattering coefficients with a tilde defined in Eq. (11) to be well approximated by

$$\begin{bmatrix} \tilde{S}_{21} & \tilde{S}_{22} \\ \tilde{S}'_{22} & \tilde{S}'_{23} \end{bmatrix} \approx \begin{bmatrix} S_{21} + S_{23}\Phi_{3d}S'_{33}\Phi_{3u}S_{31} & S_{22} \\ S'_{22} & S'_{23} \end{bmatrix}. \tag{13}$$

Solving the equations remaining after elimination of the amplitudes of the fast mode for the amplitudes of the slow mode and substituting the resulting expressions to the formula for d_1 in the first row in Eq. (5), we arrive at the following formula for the reflection coefficient:

$$r \equiv d_1/u_1 = (a + \beta b), \tag{14}$$

where

$$a \equiv \underline{S_{11}} + S_{13}\Phi_{3d}\kappa S'_{33}\Phi_{3u}S_{31}, \tag{15a}$$

$$\begin{aligned} b \equiv\ & \underline{S_{12}}\Phi_{2d}(\tilde{S}'_{22}\Phi_{2u}\underline{\tilde{S}_{21}} + \underline{\tilde{S}'_{23}}\Phi_{3u}S_{31}) \\ & + S_{13}\Phi_{3d}\kappa \left[S'_{33}\Phi_{3u}\underline{S_{32}}\Phi_{2d}(\tilde{S}'_{22}\Phi_{2u}\underline{\tilde{S}_{21}} + \underline{\tilde{S}'_{23}}\Phi_{3u}S_{31}) + \underline{S'_{32}}\Phi_{2u}(\underline{\tilde{S}_{21}} + \tilde{S}_{22}\Phi_{2d}\underline{\tilde{S}'_{23}}\Phi_{3u}S_{31}) \right] \end{aligned} \tag{15b}$$

and β represents the effect of multiple reflections of the slow mode:

$$\beta \equiv (1 - S_{22}\Phi_{2d}S'_{22}\Phi_{2u})^{-1}. \tag{16}$$

To facilitate the interpretation of Eqs. (14)–(16), the scattering coefficients with magnitude much smaller than 1 have been underlined.

It can be seen that the reflection coefficient r is made up of two terms. The first, a, is dominated by the phase shift acquired by the fast mode of the bilayer during a single round-trip across it. This term produces the slow but steady increase of the phase shift visible in Fig. 5a (also in Fig. 7). The second term, βb, is proportional to b, which is a superposition of six small terms, each containing a product of two scattering coefficients of small magnitude. Therefore βb has an appreciable effect on the reflection coefficient b only when the factor β, representing the combined effect of multiple reflections of the slow mode on both ends of the bilayer, is much greater than 1. This happens at stripe widths w corresponding to Fabry–Perot resonances of the slow mode, where
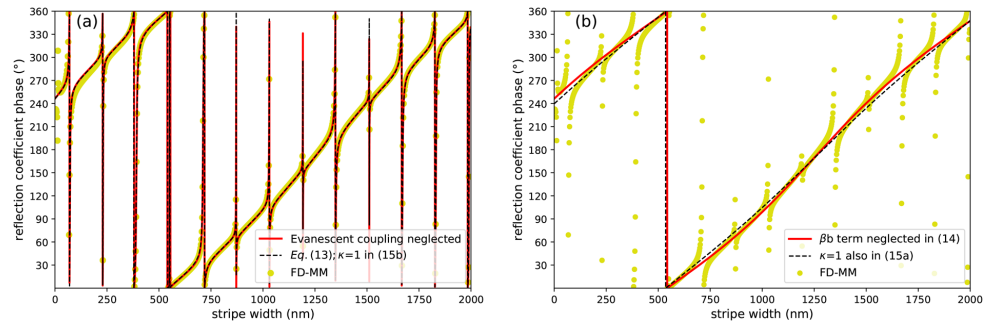
Figure 7. Comparison of the reflection coefficient phase calculated numerically using the finite-element modal method FD-MM (points) with the semi-analytical model from Eq. (14) at varying degrees of approximation (lines). Details in the plot legends and in the text.
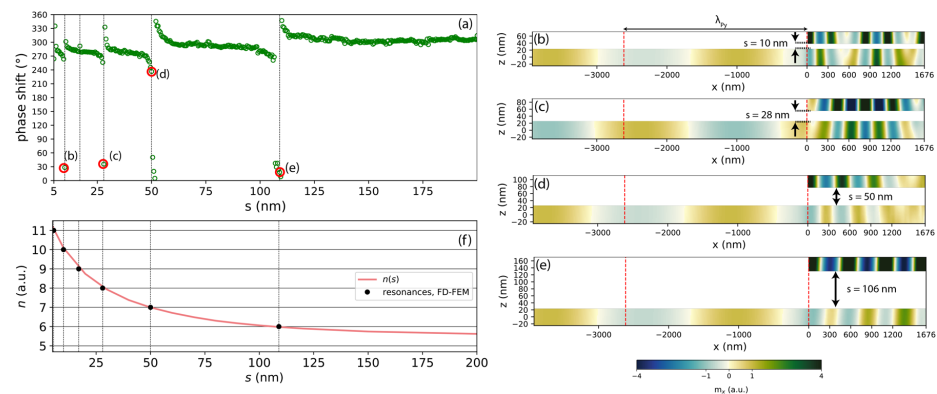

Figure 8. (**a**) Phase shift dependence on the separation between the FM2 stripe and Py film, calculated by the FD-FEM. (**b**–**e**) Snapshots of the dynamic magnetization m_x at separations 10, 28, 50 and 106 nm, corresponding to the resonances marked in plot (**a**). The dashed red lines mark the SW wavelength in the Py film. (**f**) Red line: dependence of the resonance index n calculated from Eq. (4) on the separation s, with $\varphi_l + \varphi_r$ set to the fitted value 0.12. Resonances are predicted to occur at integer values of n. Black circles: positions of resonances found in FD-FEM calculations.

[$\arg S_{22} + \arg S'_{22} + (k_{2u} + k_{2d})w$] is a multiple of 2π, justifying the postulated resonance condition Eq. (4). Since b is a combination of multiple terms of similar magnitude, its dependence on the stripe width is rather complicated. This explains the variability of the shapes of individual resonances in Fig. 5a (also in Fig. 7a).

To confirm this interpretation of the role of the various terms in Eq. (14), let us visualize and compare the effects of applying successively stronger approximations to it. In Fig. 7a,b, the golden symbols show the variation of the phase of the reflection coefficient obtained directly from numerical calculations made with the finite-element modal method (in close agreement with the FD-FEM results from Fig. 5a). The red solid curve in Fig. 7a shows the phase of the reflection coefficient calculated from Eq. (14). The only approximation made in its derivation was to neglect evanescent coupling between the left and right end of the bilayer; clearly, this approximation is very well satisfied everywhere except for stripes narrower than 250 nm. The black dashed curve in Fig. 7a shows the effect of applying the approximation Eq. (13) and setting κ to 1 in the formula Eq. (15b) for b (but not in the formula Eq. (15a) for a). This corresponds to neglecting terms proportional to products of more than two small scattering coefficients; the resulting curve is almost indistinguishable from the previous one. Neglecting the second term βb in Eq. (14) produces the red solid curve in Fig. 7b. The resonances are gone, but the long-term increase in phase shift with stripe width is still reproduced faithfully. Finally, the black dashed curve in Fig. 7b shows the result of approximating κ by 1 also in the formula Eq. (15a) for a. Its small deviation from the red curve confirms the minor role played by multiple reflections of the fast mode.

Phase shift dependence on the layer separation. In "Dispersion relation of bilayers" we observed that the separation influences the strength of the dynamical dipolar coupling between the infinitely wide stripe and Py film. It affects the SW dispersion relation, especially the wavelengths of the slow modes propagating leftwards and rightwards. Therefore, according to Eq. (4), by varying the separation s, and hence k_u and k_d, while keeping the stripe width w constant, it should be possible to sweep over resonances of different orders n. Indeed, we have found multiple resonances in dependence of the phase shift on the separation s, for a stripe of width $w = 1676$ nm, as shown in Fig. 8a.

Resonances do not appear periodically; the spacing between subsequent Fabry–Perot resonances increases with the altitude of the stripe, and for the chosen stripe width the last resonance occurs at the separation $s = 106$ nm. This is because with increasing s the coupling between the Py film and the stripe weakens and the wavenumbers k_u and k_d approach their asymptotic limits. Snapshots of the magnetization at the resonances found at separations 10, 28, 50 and 106 nm are shown in Fig. 8b–e. These figures demonstrate a clear enhancement of the SW amplitude below the stripe and a decrease in the number of nodal point with increasing separation, in line with the shift of the dispersion relation of the slow mode towards smaller wavenumbers shown in Fig. 2c.

Combining the Fabry–Perot resonance condition, Eq. (4), with the numerically calculated dispersion relations and setting $\varphi_l + \varphi_r$ to the fitted value of 0.12, we calculate the dependence of n on the separation between the stripe and the Py film, plotted with the red line in Fig. 8f. In the range from 106 down to 5 nm, we find six integer values of n, corresponding to successive resonances. These values agree well with the results of FD-FEM calculations, where six resonances, marked with black points in Fig. 8f, are detected in that range of separation.

Conclusions

We have studied theoretically the influence of a narrow ferromagnetic stripe of subwavelength width placed at the edge of a ferromagnetic film on the phase of reflected SWs. At the considered frequency (11 GHz) the bilayer formed by the film and the stripe supports two pairs of slow (short wavelength) and fast (long wavelength) guided SW modes propagating in opposite directions; these modes couple with the SW mode of the Py film. This allowed us to interpret the numerical results by modelling the system as a series of waveguides linked by junctions at which waveguide modes are scattered into each other.

We have found a strong nonlinear dependence of the phase shift on the stripe width. In particular, we have shown that the reflection coefficient, from which the phase shift can be derived, consists of two terms, each having a different origin. One produces a slow but steady increase of the phase shift with increasing bilayer width and is dominated by the phase accumulated by the fast mode during a single round-trip across the bilayer. The other term has an appreciable effect on the reflection coefficient only when multiple reflections of the slow mode on both edges of the bilayer interfere constructively, which corresponds to Fabry–Perot resonances of this mode. Interestingly, the incoming wave from the Py film couples strongly only to the fast mode, but at Fabry–Perot resonances, the phase of the reflected SW is controlled by the slow mode only weakly coupled to the propagating wave and to the fast mode of the bilayer. Essentially, this system is a realization of a Gires–Tournois interferometer[20] operating on SWs. However, in our design, its width is smaller than the wavelength of the incident wave and the interferometer utilizes two nonreciprocal SW modes present in the bilayer, thus offering further prospects for the design of subwavelength resonant elements with nonreciprocal properties for SW phase control and development of magnon logic.

We have also found that the phase shift of the reflected SW passes through a series of resonances as the separation between the stripe and the Py film is increased. This unexpected effect originates from the dependence of the wavelength of the slow SW in the bilayer on the strength of the dipolar coupling between the two layers. As a result, the bilayer width at which the Fabry–Perot condition is satisfied changes with the coupling strength as well, giving rise to the separation-dependent resonances. Increasing the stripe-film separation by 1 nm produces a 360-degree shift of the phase of the reflected wave; this high sensitivity is favorable for sensing applications.

Overall, this research shows that SW Gires–Tournois interferometer can be used to modify the phase of reflected SWs in a wide range by tiny changes of the bilayer part width or stripe-film distance. This is significant for the further development of magnonic devices where SW phase control is of key importance, in particular in integrated systems with components smaller than the SW wavelength. This may include the use of arrays of resonators in tunable SW optical elements, such as lenses, magnonic metasurfaces and phase shifters, as well as the sensing applications of magnonics, for example the development of magnonic counterparts of sensors utilizing surface plasmon resonances.

Methods

Governing equations. The magnetization dynamics is described by the Landau-Lifshitz equation:

$$\partial_t \mathbf{M} = -\frac{|\gamma|\mu_0}{1+\alpha^2}\left[\mathbf{M} \times \mathbf{H}_{\text{eff}} + \frac{\alpha}{M_S}\mathbf{M} \times (\mathbf{M} \times \mathbf{H}_{\text{eff}})\right], \tag{17}$$

where $\mathbf{M}$ is the magnetization vector, μ_0 is the permeability of vacuum, α is a dimensionless damping parameter, and $\mathbf{H}_{\text{eff}} = \mathbf{H}_0 + \mathbf{H}_M + \mathbf{H}_{\text{ex}}$ is the effective magnetic field. The latter is the sum of the external magnetic field $\mathbf{H}_0$, the magnetostatic field $\mathbf{H}_M$, and the isotropic Heisenberg exchange field $\mathbf{H}_{\text{ex}} = \nabla \cdot (l^2 \nabla \mathbf{M})$.

The magnetostatic field fulfils the magnetostatic Maxwell's equations

$$\nabla \cdot (\mathbf{M} + \mathbf{H}_M) = 0, \tag{18a}$$

$$\nabla \times \mathbf{H}_M = 0; \tag{18b}$$

the latter makes it possible to write it as $\mathbf{H}_M = -\nabla\varphi$, where φ is the magnetic scalar potential.

Assuming a harmonic time dependence [$\exp(-i\omega t)$], zero damping ($\alpha = 0$) and alignment of the external magnetic field H_0 with the y axis, splitting the magnetization $\mathbf{M}$ and magnetostatic field $\mathbf{H}_M$ into static ($M_S\hat{y}, H_0\hat{y}$) and dynamic (radio-frequency) components ($\mathbf{m} = [m_x, 0, m_z]$, $\mathbf{h}_M = [-\partial_x\varphi, 0, -\partial_z\varphi]$), linearizing the Landau-Lifshitz equation (17) (applicable only in the ferromagnetic layers) and coupling it with the Gauss law for magnetism, Eq. (18a) (applicable everywhere), we arrive at the following system of equations for the magnetic potential φ and the dynamic magnetization component $\mathbf{m}$:

$$\partial_x(m_x - \partial_x\varphi) + \partial_z(m_z - \partial_z\varphi) = 0, \tag{19a}$$

$$\partial_x\varphi - \nabla \cdot (l^2\nabla m_x) + \frac{H_0}{M_S}m_x - \frac{i\omega}{|\gamma|\mu_0 M_S}m_z = 0, \tag{19b}$$

$$\partial_z\varphi - \nabla \cdot (l^2\nabla m_z) + \frac{H_0}{M_S}m_z + \frac{i\omega}{|\gamma|\mu_0 M_S}m_x = 0. \tag{19c}$$

Numerical methods.   We have used three complementary numerical methods to study SW dynamics. First, we use micromagnetic simulations performed in the open-source mumax3 environment[32], which solves the full Landau-Lifshitz equation [Eq. (17)] with the finite-difference time-domain (FDTD) method. We use this method to calculate the dispersion relations of SWs and steady states obtainable after long continuous excitation of SWs by a specified source. Micromagnetic simulations were performed for magnetic parameters and geometry described in "Structure under consideration" and damping $\alpha = 0.0001$. The simulated structure was discretized with a mesh consisting of regular $5 \times 100 \times 5$ nm^3 (along the x, y, z axis) unit cells. In order to model a film infinitely extended along the y axis, we imposed periodic boundary conditions along the y axis with assumed 1024 repetitions of the system along this axis. After stabilizing the system with a magnetic field of value 0.1 T applied along the y axis, SWs were excited in the film by a local source of microwave-frequency magnetic field of frequency 11 GHz and amplitude 0.1 mT placed at 3.6 μm from the right edge. To prevent wave reflections from the left edge of the film, an absorbing zone with gradually increasing damping was defined on the left side of the system. A continuous harmonic SW excitation was maintained for 162.6 ns in order to reach a fully evolved (steady-state) interference pattern of the incident and reflected waves. The main disadvantage of this method is its high computational cost. Resonant systems can take a long time to reach steady state, and the cost of a single time step is pushed up by the need to discretize the whole system on a uniform grid whose resolution is dictated by the size of the smallest geometric features.

In order to avoid these limitations, we rely primarily on calculations using the frequency-domain finite element method (FD-FEM). Its major advantage is the possibility of refining the mesh locally, e.g. only around small geometric features, rather than globally. In addition, it allows direct and fast calculation of the eigenfrequencies and eigenmodes (mode profiles) of the system, which can be identified with its steady states. To perform the calculations, we have used the COMSOL Multiphysics software[33] to solve the linearized Landau-Lifshitz equation coupled with the Gauss law, Eqs. (19), as described in Refs.[34,35]. At the edges of the computational domain (far from the ferromagnetic materials) the Dirichlet boundary conditions, forcing the magnetic potential to vanish, are imposed.

In "Two-mode model analysis" we have formulated a semi-analytical model dependent on the numerical values of scattering matrices associated with interfaces separating parts of the system with different cross-sections. Calculation of these matrices with the methods mentioned above is cumbersome and produces results of relatively low accuracy. The scattering matrices must be obtained by fitting superpositions of complex exponentials to calculated field distributions; the results are affected by the presence of evanescent fields near material discontinuities and by spurious reflections from boundaries of the computational domain. Therefore we calculate the scattering matrices using a finite-element modal method; this technique, inspired by similar approaches used in photonics[36] will be described in detail in a forthcoming paper[37]. In essence, we proceed in two steps. First, Eq. (19) describing each x-invariant part of the system (a SW waveguide with a fixed cross-section) is transformed into an eigenproblem whose solutions are the wavenumbers and profiles of propagative and evanescent modes of that waveguide. This problem is then discretized by expanding the magnetic potential and dynamic magnetization profile in a finite-element basis and solved numerically. Second, fields in each x-invariant section are represented as a superposition of the eigenmodes calculated in the previous step. Imposition of the standard continuity conditions on the interface separating a pair of adjacent sections leads to a linear system whose solution yields the scattering matrix linking the complex amplitudes of modes impinging onto the interface with the amplitudes of outgoing modes. The scattering matrices of individual interfaces and finite-length sections can then be concatenated together using standard algorithms[38] to produce the scattering matrix of the complete system. In contrast to the previous two methods, the modal method produces results unaffected by spurious reflections from boundaries truncating the computational domain along x, since the radiation conditions at $x \to \pm\infty$ are fulfilled analytically. In addition, no fitting is required to obtain the scattering coefficients.

References

1. Ng, I. C. & Wakenshaw, S. Y. The internet-of-things: Review and research directions. *Int. J. Res. Mark.* **34**, 3–21 (2017).

2. Krawczyk, M. & Grundler, D. Review and prospects of magnonic crystals and devices with reprogrammable band structure. *J. Phys. Condens. Matter* **26**, 123202 (2014).
3. Chumak, A., Vasyuchka, V., Serga, A. & Hillebrands, B. Magnon spintronics. *Nat. Phys.* **11**, 453–461 (2015).
4. Chumak, A. V. Fundamentals of magnon-based computing. arXiv preprint arXiv:1901.08934 (2019).
5. Yu, N. & Capasso, F. Flat optics with designer metasurfaces. *Nat. Mater.* **13**, 139–150 (2014).
6. Yu, N. *et al.* Light propagation with phase discontinuities: Generalized laws of reflection and refraction. *Science* **334**, 333–337 (2011).
7. Kumar, K. *et al.* Printing colour at the optical diffraction limit. *Nat. Nanotechnol.* **7**, 557 (2012).
8. Vashistha, V., Vaidya, G., Gruszecki, P., Serebryannikov, A. E. & Krawczyk, M. Polarization tunable all-dielectric color filters based on cross-shaped Si nanoantennas. *Sci. Rep.* **7**, 8092 (2017).
9. Kruglyak, V. *et al.* Graded magnonic index and spin wave Fano resonances in magnetic structures: Excite, direct, capture. in *Spin Wave Confinement - Propagating Waves*, 2nd edn (eds Demokritov, S. O.) (Jenny Stanford Publishing, Boca Raton, 2017).
10. Au, Y., Dvornik, M., Dmytriiev, O. & Kruglyak, V. Nanoscale spin wave valve and phase shifter. *Appl. Phys. Lett.* **100**, 172408 (2012).
11. Au, Y. *et al.* Resonant microwave-to-spin-wave transducer. *Appl. Phys. Lett.* **100**, 182404 (2012).
12. Yu, T., Blanter, Y. M. & Bauer, G. E. Chiral pumping of spin waves. *Phys. Rev. Lett.* **123**, 247202 (2019).
13. Yu, T., Liu, C., Yu, H., Blanter, Y. M. & Bauer, G. E. Chiral excitation of spin waves in ferromagnetic films by magnetic nanowire gratings. *Phys. Rev. B* **99**, 134424 (2019).
14. Al-Wahsh, H. *et al.* Evidence of Fano-like resonances in mono-mode magnetic circuits. *Phys. Rev. B* **78**, 075401 (2008).
15. Zhang, Z. *et al.* Bias-free reconfigurable magnonic phase shifter based on a spin-current controlled ferromagnetic resonator. *J. Phys. D* **53**, 105002 (2020).
16. Yu, H. *et al.* Omnidirectional spin-wave nanograting coupler. *Nat. Commun.* **4**, 2702 (2013).
17. Yu, H. *et al.* Approaching soft x-ray wavelengths in nanomagnet-based microwave technology. *Nat. Commun.* **7**, 11255 (2016).
18. Graczyk, P. *et al.* Magnonic band gap and mode hybridization in continuous permalloy films induced by vertical dynamic coupling with an array of permalloy ellipses. *Phys. Rev. B* **98**, 174420 (2018).
19. Mieszczak, S. *et al.* Anomalous refraction of spin waves as a way to guide signals in curved magnonic multimode waveguides. *Phys. Rev. Appl.* **13**, 054038 (2020).
20. Gires, F. & Tournois, P. Interferometre utilisable pour la compression d'impulsions lumineuses modulées en frequence. *C. R. Acad. Sci. Paris.* **258**, 6112–6115 (1964).
21. Stancil, D. D. & Prabhakar, A. *Spin waves: Theory and applications* (Springer, Berlin, 2009).
22. Gurevich, A. G. & Melkov, G. A. *Magnetization Oscillations and Waves* (CRC Press, Boca Raton, 1996).
23. Mruczkiewicz, M. & Krawczyk, M. Nonreciprocal dispersion of spin waves in ferromagnetic thin films covered with a finite-conductivity metal. *J. Appl. Phys.* **115**, 113909 (2014).
24. Gallardo, R. *et al.* Reconfigurable spin-wave nonreciprocity induced by dipolar interaction in a coupled ferromagnetic bilayer. *Phys. Rev. Appl.* **12**, 034012 (2019).
25. An, K., Bhat, V., Mruczkiewicz, M., Dubs, C. & Grundler, D. Optimization of spin-wave propagation with enhanced group velocities by exchange-coupled ferrimagnet-ferromagnet bilayers. *Phys. Rev. Appl.* **11**, 034065 (2019).
26. Guslienko, K. Y., Demokritov, S. O., Hillebrands, B. & Slavin, A. N. Effective dipolar boundary conditions for dynamic magnetization in thin magnetic stripes. *Phys. Rev. B* **66**, 132402 (2002).
27. Centała, G. *et al.* Influence of nonmagnetic dielectric spacers on the spin-wave response of one-dimensional planar magnonic crystals. *Phys. Rev. B* **100**, 224428 (2019).
28. Stigloher, J. *et al.* Observation of a Goos-Hänchen-like phase shift for magnetostatic spin waves. *Phys. Rev. Lett.* **121**, 137201 (2018).
29. Verba, R., Tiberkevich, V. & Slavin, A. Spin-wave transmission through an internal boundary: Beyond the scalar approximation. *Phys. Rev. B* **101**, 144430 (2020).
30. Zingsem, B. W., Farle, M., Stamps, R. L. & Camley, R. E. Unusual nature of confined modes in a chiral system: Directional transport in standing waves. *Phys. Rev. B* **99**, 214429 (2019).
31. Lecamp, G., Lalanne, P., Hugonin, J. P. & Gerard, J.-M. Energy transfer through laterally confined Bragg mirrors and its impact on pillar microcavities. *IEEE J. Quant. Electron.* **41**, 1323–1329 (2005).
32. Vansteenkiste, A. *et al.* The design and verification of mumax3. *AIP Adv.* **4**, 107133 (2014).
33. COMSOL Multiphysics 5.1a, www.comsol.com, COMSOL AB, Stockholm, Sweden.
34. Rychły, J. & Kłos, J. W. Spin wave surface states in 1D planar magnonic crystals. *J. Phys. D: Appl. Phys.* **50**, 164004 (2017).
35. Graczyk, P., Zelent, M. & Krawczyk, M. Co-and contra-directional vertical coupling between ferromagnetic layers with grating for short-wavelength spin wave generation. *New J. Phys.* **20**, 053021 (2018).
36. Liu, Q.-H. & Chew, W. C. Numerical mode-matching method for the multiregion vertically stratified media. *IEEE Trans. Antennas Propag.* **38**, 498–506 (1990).
37. Śmigaj, W., Sobucki, K., Gruszecki, P. & Krawczyk, M. In preparation.
38. Li, L. Formulation and comparison of two recursive matrix algorithms for modeling layered diffraction gratings. *J. Opt. Soc. Am. A* **13**, 1024–1035 (1996).

Author contributions
K.S. performed frequency-domain finite-element and finite-difference time-domain simulations of the reflection of spin waves and processed the data. W.Ś. formulated the two-mode model and performed calculations with the finite-element modal method. J.R. and P.G. computed dispersion relations. K.S. and P.G. prepared figures. P.G. and M.K. supervised the study. All authors analysed the results and contributed to writing the manuscript.

Competing interests
The authors declare no competing interests.

Additional information
Correspondence and requests for materials should be addressed to K.S. or P.G.

Reprints and permissions information is available at www.nature.com/reprints.

5.3   Control of the Phase of Reflected Spin Waves From Magnonic Gires–Tournois Interferometer of Subwavelength Width

This paper is the direct continuation of previously presented research in "Resonant subwavelength control of the phase of spin waves reflected from a Gires–Tournois interferometer". Here the influence of different geometries of the Gires-Tournois interferometer on reflected SWs phase shift are investigated. Namely, the thicknesses of the bottom layer and the resonator were varied, as well as the separation between these two elements. This paper shows that the non-linear dependency between interferometer's width and reflected SW phase shift can be modified by changing interferometer geometry.

In this publication Author has performed all numerical simulations in COMSOL Multiphysics environment regarding phase shift of SWs reflected from investigated interferometers, apart from the dispersion relation calculations, and processed the these simulation results with the self-developed code. The Author has written the majority of manuscript, excluding the description of dispersion relation calculations, as well as prepared all of the figures included in the publication. The Author was responsible for communication with the journal.

Control of the Phase of Reflected Spin Waves From Magnonic Gires–Tournois Interferometer of Subwavelength Width

Krzysztof Sobucki[1], Paweł Gruszecki[1], Justyna Rychły[2], and Maciej Krawczyk[1]

[1]Institute of Spintronics and Quantum Information, Faculty of Physics, Adam Mickiewicz University, 61-614 Poznań, Poland
[2]Institute of Molecular Physics, Polish Academy of Sciences, 60-179 Poznań, Poland

The phase is one of the fundamental properties of a wave that allows to control interference effects and can be used to efficiently encode information. We examine numerically a magnonic resonator of the Gires–Tournois interferometer type, which enables the control of the phase of spin waves (SWs) reflected from the edge of the ferromagnetic film. The considered interferometer consists of a Py thin film and a thin, narrow Py stripe placed above its edge, both coupled magnetostatically. We show that the resonances and the phase of the reflected SWs are sensitive for a variation of the geometrical parameters of this bi-layered part of the system. The high sensitivity to film, stripe, and non-magnetic spacer thicknesses offers a prospect for developing magnonic metasurfaces and sensors.

***Index Terms*— Fabry–Perot interferometer, Gires–Tournois interferometer (GTI), magnonics, metasurfaces, spin waves (SWs), spin-wave phase.**

I. INTRODUCTION

CONTROLLING the phase of waves, regardless of their type, is very important from the application's point of view. Among other things, phase control enables to encode information, e.g., in phase shift keying digital modulation scheme, widely used in modern wireless communication [1], while a wavefront modulation makes it possible to control the direction of propagation and a wave focusing. Furthermore, by controlling the phase of the reflected waves, chromatic dispersion can be generated, which found application in laser pulse compression [2]. A commonly used optical system for this purpose is the Gires–Tournois interferometer (GTI) [3]. GTIs are Fabry–Perot interferometers operating in a reflection mode rather than a transmission mode. In practice, a GTI can be made of two mirrors, the first partially reflecting and the second completely reflecting the incident radiation. For wavelengths close to those satisfying the Fabry–Perot resonance condition, a strong phase dependence of the reflected waves on the wavelength of the incident radiation appears.

The subject of controlling the phase and amplitude of electromagnetic waves by 2-D surfaces composed of resonators of sub-wavelength dimensions has become central to the development of the concept of metasurfaces for electromagnetic waves [4]–[7]. This has contributed to the rapid development of photonics in recent years.

The concept of metasurfaces has also recently received attention in magnonics [8]–[10], which is a subfield of magnetism focused on spin waves (SWs), particularly in the context of their applications to information transfer and signal processing. The pioneering theoretical demonstration of metasurfaces acting on SWs enabled their focusing by applying

modulation of the exchange interaction alongside the interface between two interconnected ferromagnetic layers [11]. In the later studies, it was shown that continuously varying the value of the magnetocrystalline anisotropy or saturation magnetization in a narrow region between a ferromagnetic waveguide and a thin film, an anomalous refraction can be obtained for SWs, allowing SWs to be efficiently bent in the waveguides [12]. This closely connects the magnonic metasurface studies with the graded-index approach in the design of magnonic devices [13], [14].

Several reports are showing that the placement of ferromagnetic stripes over a ferromagnetic film or waveguide can be used to emit SWs or affect the amplitude and phase of SWs passing below that stripe [15]–[21]. Recently, we have demonstrated with micromagnetic simulations that the phase of reflected SWs can be controlled by using a resonator with a sub-wavelength width placed over the edge of a thin film [22]. In that study, a resonator made of a material with a lower saturation magnetization value than the thin film was considered, which allowed obtaining an additional pair of short-wavelength modes in the bi-layered region, being crucial for effective phase modulation. This was the demonstration of a GTI operating on SWs [22]. In this work, we continue the idea of the magnonic GTI and analyze the system suitable for the experimental realization. We study the interferometer composed of Permalloy (Py) and analyze how the thickness of the film and resonator, the width of the resonator, and the separation between them affect the phase of the reflected SWs.

This paper is organized as follows. Section II contains the definition of equations used in the calculations and an explanation of the post-processing of the raw data obtained in numerical simulations. In Section III, the geometry of the system under consideration is presented and there is an extensive description of the results obtained from our calculations. Section IV includes the final conclusions of our results.

II. METHODS

SW dynamics in ferromagnetic layers can be studied in a frame of the linearized Landau–Lifshitz equation with damping neglected, coupled with the Gauss law for magnetism. In the case of SW propagating along the x-axis, being perpendicular to the direction of the static magnetization (aligned along the y-axis) in the in-plane, uniformly magnetized layers, these equations read as

$$\partial_x \psi - \nabla \cdot (l^2 \nabla m_x) + \frac{H_0}{M_S} m_x - \frac{i\omega}{|\gamma| \mu_0 \, M_S} m_z = 0 \quad (1a)$$

$$\partial_z \psi - \nabla \cdot (l^2 \nabla m_z) + \frac{H_0}{M_S} m_z + \frac{i\omega}{|\gamma| \mu_0 M_S} m_x = 0 \quad (1b)$$

$$\partial_x (m_x - \partial_x \psi) + \partial_z (m_z - \partial_z \psi) = 0. \quad (1c)$$

Solving these equations allows us to find the values of the dynamical components of magnetization m_x and m_z and the magnetostatic potential ψ of the eigenmodes, as well as corresponding to them angular frequency $\omega = 2\pi f$. Coefficients in (1) are as follows: H_0 is the static, uniform external magnetic field directed along the y-axis, M_S is the saturation magnetization of the ferromagnetic material, γ is the gyromagnetic ratio, μ_0 is the vacuum permeability, and $l = (2A_{ex}/(\mu_0 M_S^2))^{1/2}$ is the exchange length, where A_{ex} is the exchange constant. The terms, including magnetostatic potential, represent the influence of the dipolar interactions, the terms with the exchange length—the exchange interactions. Further method details and the approximations used can be found in [23] and [24].

To solve (1), we use the frequency-domain finite-element method (FD-FEM) defined in COMSOL Multiphysics software [25], as described in [23]. At the edges of the computational domain (far from the ferromagnetic materials), the Dirichlet's boundary conditions, forcing the magnetostatic potential to vanish, are imposed.

The phase of SWs reflected from the interface located at $x = x_0$ can be extracted from the SW mode profiles (eigenmodes) calculated by FD-FEM. These mode profiles correspond to the steady state that forms the standing SWs. We can extract the phase from these steady-state solutions formed far away from the edge. In the interference pattern, the phase shift φ is related to a displacement of nodes with respect to the interface from which the waves are reflected. If the interface is located at $x = x_0$ and the refection coefficient is $e^{i\varphi}$, the standing wave pattern sufficiently far from the interface (at $x \ll 0$) will be

$$m_x(t; x) = a(t) \cos[k_x(x - x_0) - \varphi/2] \quad (2)$$

where $a(t)$ is independent of x and represents time dependence of m_x, i.e., $a(t) \propto \cos(2\pi f t)$. The phase of the reflected wave is later obtained by fitting (2) to the real part of m_x results from simulations. Results closer than 1 μm to the interface were discarded to avoid interference with an evanescent wave, which can be present near the interface [30]. Further details of post-processing can be found in [22].

Noteworthy, to numerically calculate the dispersion relations and, therefore, to obtain explicitly eigenfrequency dependence on k_x (the wave vector of SWs propagating along the x-axis),
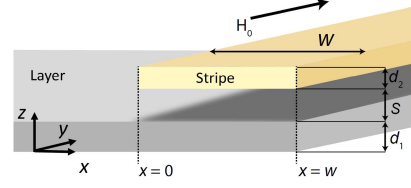

Fig. 1. Geometry of the system used in simulations. A Py stripe of thickness d_2 and width w is separated by a distance s from a semi-infinite Py layer of thickness d_1. Both elements have their right edges set at $x = w$. The system is placed in a uniform external magnetic field H_0, which is parallel to the y-axis.

we have implemented the Bloch boundary conditions at the lateral edges of an elementary cell of width $w = 30$ nm: $m_x(x, z) = \tilde{m}_x(x, z)e^{ik_x x}$, $m_z(x, z) = \tilde{m}_z(x, z)e^{ik_x x}$, and $\psi(x, z) = \tilde{\psi}(x, z)e^{ik_x x}$, where the functions with tilde on the right-hand side of equations are periodic functions of x, with the period w.

The dispersion relation of SWs propagating perpendicularly to the direction of the effective magnetic field in a single in-plane, uniformly magnetized infinite thin film can also be described analytically [26]

$$\omega^2 = \omega_0(\omega_0 + \omega_M) + \frac{\omega_M^2}{4}[1 + e^{-2k_x d}] \quad (3)$$

where d is the film thickness, $\omega_0 = |\gamma| \mu_0(H_0 + M_S l^2 k_x^2)$, and $\omega_M = |\gamma| \mu_0 M_S$ (see [27, Ch. 7.1]).

III. RESULTS

A. Description of the System

Let us consider a system presented in Fig. 1 that consists of two magnetic elements, a semi-infinite Py layer of thickness d_1, and a Py stripe of thickness d_2. The separation between the layer and the stripe is described by s. Both ferromagnetic elements are infinitely long along the y-axis direction and are submerged in a uniform external magnetic field of value $\mu_0 H_0 = 0.1$ T, which is parallel to the y-axis. Material parameters of Py were chosen as follows: $M_S = 760$ kA/m, $A_{ex} = 13$ pJ/m, and $\gamma = -176$ radGHz/T. To avoid the influence of the left edge of the system on the reflection of SWs from the right edge with the resonator, in the calculations, we considered a Py layer with the width 50 μm, being significantly longer than the wavelength of investigated SWs.

B. Dispersion Relations

Before analyzing how the presence of a stripe influences the reflection of SWs, let us examine how the dispersion relation of an infinitely extended bi-layered system changes with respect to the dispersion of a single Py film. The analytically derived dispersion using (3) for a 10 nm-thick Py film is presented in Fig. 2 by the black solid line. The FD-FEM computed dispersions for three bi-layered systems with three combinations of Py-layer thicknesses and separation between them is presented by color dots in Fig. 2, with the
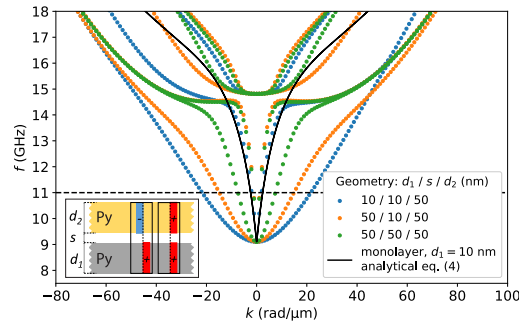
Fig. 2. Black solid line represents the dispersion calculated for a layer of thickness $d_1 = 10$ nm using 3. The blue and orange dots represent the dispersion relations calculated numerically for layer $d_1 = 10$ nm (stripe $d_2 = 50$ nm and separation $s = 10$ nm) and for a layer $d_1 = 50$ nm (stripe $d_2 = 50$ nm and separation $s = 10$ nm), respectively. The green dots show the dispersion calculated for separation $s = 50$ nm (in this case, $d_1 = d_2 = 50$ nm). In all the cases, the dispersion was calculated for infinitely long and wide layers and stripes. The dashed, horizontal line indicates 11 GHz frequency used in the subsequent calculations. Inset: sketch of the system used in the dispersions calculations with simplified visualization of antisymmetrical short-wavelength (on the left) and symmetrical long-wavelength (on the right) modes.

inset explaining the geometry and the symmetry of the modes. For frequencies below 14 GHz, we have two bands instead of one in the case of a single Py film. The band of smaller wavenumber at a selected frequency is related to the symmetric mode of the bi-layer (see the schematic representation in the inset), and it resembles a typical Damon–Eshbach dispersion. Therefore, this band is very similar to the band of a single Py film. The second band is related to the antisymmetric mode for which magnetization oscillates in antiphase in the layers (see the schematic in the inset), the dispersion of which is parabolic, and has much shorter wavelengths in comparison to the previous band.

Comparing the dispersion for different bi-layers shown in Fig. 2, we find that in the case of a bi-layer with a smaller value of $d_1 = 10$ nm, the SWs associated with the short-wavelength band are shorter than in the case of $d_1 = 50$ nm. One may conclude that while the separation increases, the wavelengths of the short-wavelength band also increase since the interaction between both layers decreases (see results obtained for $d_1 = d_2 = 50$ nm, $s = 10$ nm, and $s = 50$ nm in Fig. 2 represented by orange and green dots, respectively). As expected, in the case of symmetric geometry ($d_1 = 50$ nm, $s = 10$ nm, and $d_2 = 50$ nm) dispersion relation is fully reciprocal, i.e., a mirror symmetry of dispersion with respect to $k = 0$ is present. Interestingly, for the geometry $d_1 = 10$ nm, $s = 10$ nm, and $d_2 = 50$ nm, a small nonreciprocity is visible (see frequencies above $f = 14$ GHz), although the system is composed only of Py. Overall, it means that even in the case of bi-layers composed of the same material, one may easily modify the wavelength of SWs corresponding to short-wavelength bands by changing a separation or the thickness of one of the layers.

The analysis of dispersion relations in single- and bi-layered Py films shows that if we consider a system presented in Fig. 1,

we have one long-wavelength mode of SWs in a single Py film and two, short- and long-wavelength modes in the bi-layered part. In Section III-C, we will analyze the effect of the resonance related to the short-wavelength mode on the phase of the reflected SWs for the finite width of the bi-layered part. For these investigations, we selected the frequency 11 GHz, which is well below the perpendicular standing SWs frequency. Notably, the wavelength of SW in Py film of thickness 10, 50, and 90 nm is 584, 2651, and 4724 nm, respectively. These wavelengths are almost the same as the wavelengths of long-wavelength SW mode in the bi-layer, i.e., 590 nm for $d_1 = 10$ nm, 2650 nm for $d_1 = 50$ nm, and 4600 nm for $d_1 = 90$ nm.

C. Influence of the Py-Layer's Thickness and Bi-Layer Geometry on the Phase of Reflected SWs

Let us examine how the ferromagnetic layer, stripe, and non-magnetic spacer thicknesses influence the phase shift dependence on the resonator's width, w. For this purpose, we have performed several FD-FEM computations for geometry presented in Fig. 1. In each simulation, a sweep over the stripe's width w is performed in the range from 2 to 500 nm with the 2 nm step. Thicknesses of the layer and the stripe, as well as separation, were changed separately for each simulation.

First, we analyze how the thickness of the layer d_1 influences the phase at constant separation $s = 10$ nm and the thickness of stripe $d_2 = 50$ nm (see Fig. 3). In Fig. 3(a), the phase shift as a function of the stripe's width is shown for five different layer thicknesses equal to 10, 50, 70, and 90 nm.

Overall, the phase width dependence has the same features regardless of the layer thickness. Every dependence is characterized by areas of rapid, resonance-like, phase changes, which appear periodically. Those areas are divided by regions of smaller phase change. In Fig. 3(d), the visualization of the mode in the resonance area is presented. Here, an amplitude of SW below the resonator is noticeably bigger compared with the rest of the system and an alternating pattern of SW is visible. We found also an anti-symmetrical character of the mode in the bi-layer (SWs in Py film and stripe oscillate in antiphase). Moreover, the wavelength of SWs in the bilayer is shorter than in the Py film, indicating that the resonance effect is related to the short-wavelength antisymmetric mode. Fig. 3(c) presents the mode in the region out of resonance, and in this case, an increase of the amplitude is absent.

Analyzing how the layer's thickness influences $\varphi(w)$, one may conclude that with increasing thickness of the layer, the subsequent resonances appear for greater values of w. This result can be explained by referring to the dispersion relations (see Fig. 2), which show that with decreasing the layer thickness, the wavelength associated with short SW mode decreases. Therefore, the subsequent resonances appear for shorter w. In addition, for the thinner layer, the areas where phase changes abruptly are wider. In Fig. 3(b), the position of the first resonance as a function of the layer's thickness is presented. Position of the first resonance at 11 GHz shifts to wider stripes with increasing the layer thickness, starting
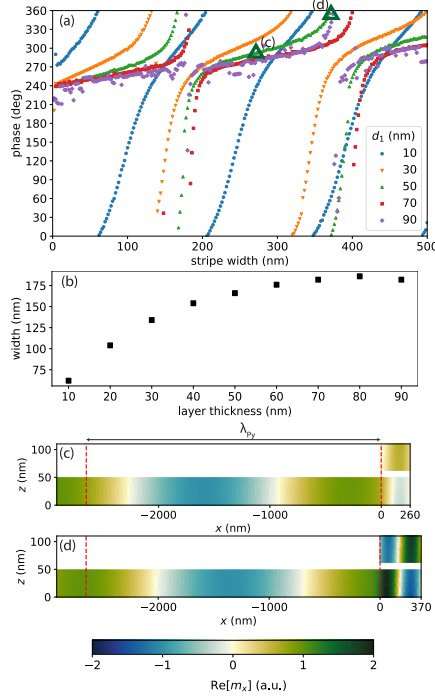
92 Papers representing the main research

Fig. 3.   (a) Phase shift as a function of stripe width for layers of different thicknesses at fixed both the separation $s = 10$ nm and the stripe thickness $d_2 = 50$ nm for frequency $f = 11$ GHz. (b) Width of the stripe for which the first resonance occurs as a function of layer thickness. (c) and (d) Visualization of the real part of m_x of the SW modes in the system ($d_1 = 50$ nm, $s = 10$ nm, and $d_2 = 50$ nm). (c) Stripe $w = 260$ nm—the system is out of resonance. (d) Stripe $w = 370$ nm—the system is in the resonance.

Fig. 4.   (a) Phase shift as a function of stripe width for the stripes of different thicknesses, with fixed both the separation $s = 10$ nm and the layer thickness $d_1 = 50$ nm and frequency of $f = 11$ GHz. (b) Width of the stripe at which the first resonance occurs as a function of stripe thickness.

Fig. 5.   (a) Phase shift as a function of the stripe width for different separations s between the layer and the stripe at $d_1 = d_2 = 50$ nm and frequency of $f = 11$ GHz. (b) Width of the stripe for which the first resonance occurs as a function of separation.

from $w < 70$ nm up to $w \approx 175$ nm with the increase of d_1 from 10 to 90 nm, respectively. The stripe's widths with the first resonances are significantly smaller than wavelengths in a single Py layers of checked thicknesses what emphasizes the subwavelength character of the interferometer (see dispersion presented in Fig. 2). For bigger thicknesses, the dependence becomes too complex to clearly identify the first resonance, due to the quantization of the SWs across the layer thickness.

In Fig. 4, the results of simulations with different stripe thicknesses d_2 are shown for fixed $d_1 = 50$ nm and $s = 10$ nm. Fig. 4(a) shows the phase of the SW as a function of the stripe width. Here, increasing the thickness of the stripe shifts the position of the first resonance similar to the case presented in Fig. 3(a). This results from the fact that the thinner one of the layers (d_1 or d_2) in the bi-layer is, the shorter the wavelength of the short-wavelength SW mode is (see also Fig. 2). The main difference between the results in Figs. 3(a) and 4(a) is the fact that the shape of the function $\varphi(w)$, in particular the width of resonances, does not change significantly with changing the thickness of the magnetic element. Resonance areas are separated by plateau

areas with the same slope, regardless of the stripe thickness. The position of the first resonance [Fig. 4(b)] shifts toward the wider stripes (from 100 nm) and reaches a plateau ($\approx$170 nm) for the stripe of thickness 60 nm and then remains constant for stripes up to 100 nm. For thicker stripes, a complex phase width dependence is observed again.

Fig. 5 shows the results of the simulations with different separations between the layer and the stripe at fixed $d_1 = d_2 = 50$ nm. An increase of separation shifts the position of the first resonance to larger widths of the stripe and the shape of dependence evolves as well, as shown in Fig. 5(a). In this case, the shape changes in the opposite manner compared to the results in Fig. 3(a), namely with the increase of separation, the plateau region becomes steeper, while in Fig. 3(a), it becomes flatter. In addition, as shown in Fig. 5(b), the position of the first resonance shifts con-

tinuously with the increase of separation, and for maximal considered values of s, a maximum shift was not found.

IV. Conclusion

We investigated the reflection of SWs from the bilayer part of a Py film with a narrow Py stripe. We show with FD-FEM numerical simulations that the phase of the reflected SWs can change by 2π with dependence on the stripe width. This demonstrates a resonance character which we attribute to the Fabry–Perot resonance of the short-wavelength mode in the bi-layered part of the system. Thus, the proposed system operates as a GTI offering control of the SW phase at sub-wavelength distances, the property important for magnonic applications [28], [29].

We showed that using a single-material-based system, the widths, and the positions of resonances in the magnonic GTI can be controlled over a wide range. In particular, the resonance character depends on the ferromagnetic layer thickness, showing 2π-phase change in a narrow and wide range of the stripe widths, for thick and thin films, respectively. The system with the phase steadily varying with the width of the resonator may find application in the design of a metasurface lens for SWs by proper modulation of the stripe width along its length. In addition, the GTI with a sharp phase change in dependence on the stripe width and its sensitivity for separation between the layers may find application in the design of sensors.

References

[1] R. E. Blahut, *Principles and Practice of Information Theory*. Reading, MA, USA: Addison-Wesley, 1987.

[2] J. Kuhl and J. Heppner, "Compression of femtosecond optical pulses with dielectric multilayer interferometers," *IEEE J. Quantum Electron.*, vol. QE-22, no. 1, pp. 182–185, Jan. 1986.

[3] F. Gires and P. Tournois, "Interferometre utilisable pour la compression dimpulsions lumineuses modulees en frequence," *Comptes Rendus Hebdomadaires Des Seances De L Academie Des Sci.*, vol. 258, no. 25, pp. 6112–6115, 1964.

[4] N. Yu and F. Capasso, "Flat optics with designer metasurfaces," *Nature Mater.*, vol. 13, no. 2, pp. 139–150, Feb. 2014.

[5] N. Yu *et al.*, "Light propagation with phase discontinuities: Generalized laws of reflection and refraction," *Science*, vol. 334, no. 6054, pp. 333–337, Oct. 2011.

[6] K. Kumar, H. Duan, R. Hegde, S. C. W. Koh, J. N. Wei, and J. K. W. Yang, "Printing colour at the optical diffraction limit," *Nature Nanotechnol.*, vol. 7, no. 9, pp. 557–561, 2012.

[7] V. Vashistha, G. Vaidya, P. Gruszecki, A. E. Serebryannikov, and M. Krawczyk, "Polarization tunable all-dielectric color filters based on cross-shaped Si nanoantennas," *Sci. Rep.*, vol. 7, no. 1, p. 8092, Dec. 2017.

[8] M. Krawczyk and D. Grundler, "Review and prospects of magnonic crystals and devices with reprogrammable band structure," *J. Phys., Condens. Matter*, vol. 26, no. 12, Mar. 2014, Art. no. 123202.

[9] A. V. Chumak, V. I. Vasyuchka, A. A. Serga, and B. Hillebrands, "Magnon spintronics," *Nature Phys.*, vol. 11, no. 6, pp. 453–461, Jun. 2015.

[10] A. V. Chumak, "Fundamentals of Magnon-based computing," 2019, *arXiv:1901.08934*. [Online]. Available: http://arxiv.org/abs/1901.08934

[11] M. Zelent *et al.*, "Spin wave collimation using a flat metasurface," *Nanoscale*, vol. 11, no. 19, pp. 9743–9748, 2019.

[12] S. Mieszczak, O. Busel, P. Gruszecki, A. N. Kuchko, J. W. Kłos, and M. Krawczyk, "Anomalous refraction of spin waves as a way to guide signals in curved magnonic multimode waveguides," *Phys. Rev. A, Gen. Phys.*, vol. 13, no. 5, May 2020, Art. no. 054038.

[13] N. J. Whitehead, S. A. R. Horsley, T. G. Philbin, and V. V. Kruglyak, "A Luneburg lens for spin waves," *Appl. Phys. Lett.*, vol. 113, no. 21, Nov. 2018, Art. no. 212404.

[14] N. J. Whitehead, S. A. R. Horsley, T. G. Philbin, and V. V. Kruglyak, "Graded index lenses for spin wave steering," *Phys. Rev. B, Condens. Matter*, vol. 100, no. 9, Sep. 2019, Art. no. 094404.

[15] V. Kruglyak *et al.*, "Graded magnonic index and spin wave Fano resonances in magnetic structures: Excite, direct, capture," in *Spin-Wave Confinment*, S. O. Demokritov, Ed. Jenny Stanford Publishing, Aug. 2017, pp. 11–46.

[16] Y. Au, M. Dvornik, O. Dmytriiev, and V. V. Kruglyak, "Nanoscale spin wave valve and phase shifter," *Appl. Phys. Lett.*, vol. 100, no. 17, Apr. 2012, Art. no. 172408.

[17] Y. Au, E. Ahmad, O. Dmytriiev, M. Dvornik, T. Davison, and V. V. Kruglyak, "Resonant microwave-to-spin-wave transducer," *Appl. Phys. Lett.*, vol. 100, no. 18, Apr. 2012, Art. no. 182404.

[18] H. Al-Wahsh, E. H. E. Boudouti, B. Djafari-Rouhani, A. Akjouj, T. Mrabti, and L. Dobrzynski, "Evidence of Fano-like resonances in mono-mode magnetic circuits," *Phys. Rev. B, Condens. Matter*, vol. 78, no. 7, Aug. 2008, Art. no. 075401.

[19] Z. Zhang *et al.*, "Bias-free reconfigurable magnonic phase shifter based on a spin-current controlled ferromagnetic resonator," *J. Phys. D, Appl. Phys.*, vol. 53, no. 10, Mar. 2020, Art. no. 105002.

[20] T. Yu, Y. M. Blanter, and G. E. W. Bauer, "Chiral pumping of spin waves," *Phys. Rev. Lett.*, vol. 123, no. 24, Dec. 2019, Art. no. 247202.

[21] P. Che, K. Baumgaertl, A. Kúkoľová, C. Dubs, and D. Grundler, "Efficient wavelength conversion of exchange Magnons below 100 nm by magnetic coplanar waveguides," *Nature Commun.*, vol. 11, no. 1, p. 1445, Dec. 2020.

[22] K. Sobucki, W. Śmigaj, J. Rychły, M. Krawczyk, and P. Gruszecki, "Resonant subwavelength control of the phase of spin waves reflected from a Gires–Tournois interferometer," *Sci. Rep.*, vol. 11, no. 1, pp. 1–12, Dec. 2021.

[23] J. Rychły and J. W. Kłos, "Spin wave surface states in 1D planar magnonic crystals," *J. Phys. D, Appl. Phys.*, vol. 50, no. 16, Apr. 2017, Art. no. 164004.

[24] J. Rychły, J. W. Kłos, and M. Krawczyk, "Spin wave damping in periodic and quasiperiodic magnonic structures," *J. Phys. D, Appl. Phys.*, vol. 49, no. 17, May 2016, Art. no. 175001.

[25] *COMSOL Multiphysics 5.1a*. COMSOL AB, Stockholm, Sweden. [Online]. Available: www.comsol.com

[26] D. D. Stancil and A. Prabhakar, *Spin Waves: Theory and Applications, Appendix C.7*. New York, NY, USA: Springer, 2009.

[27] A. G. Gurevich and G. A. Melkov, *Magnetization Oscillations and Waves*. Boca Raton, FL, USA: CRC Press, 1996.

[28] K. Baumgaertl, S. Watanabe, and D. Grundler, "Phase control of spin waves based on a magnetic defect in a one-dimensional magnonic crystal," *Appl. Phys. Lett.*, vol. 112, no. 14, Apr. 2018, Art. no. 142405.

[29] O. V. Dobrovolskiy *et al.*, "Spin-wave phase inverter upon a single nanodefect," *ACS Appl. Mater. Interfaces*, vol. 11, no. 19, pp. 17654–17662, 2019.

[30] R. Verba, V. Tiberkevich, and A. Slavin, "Spin-wave transmission through an internal boundary: Beyond the scalar approximation," *Phys. Rev. B, Condens. Matter*, vol. 101, no. 14, Apr. 2020, Art. no. 144430.

5.4   Modal approach to modeling spin wave scattering

In this paper a semi-analytical model for derivation of SWs reflected from and transmitted through a magnonic interferometer is presented. This model divides a magnonic system with an interferometer into several segments. Then in each segment its eigenmodes are calculated numerically. With the knowledge of the system's eigenmodes different scattering parameters are derived such as reflectance, transmittance and phases of reflected and transmitted waves. The paper provides an example of SW scattering on a magnonic interferometer in Fabry-Perot geometry. The results of the semi-analytical model are compared with the results obtained with micromagnetic simulations performed in MuMax3 environment.

The Author contributed to this paper by performing the micromagnetic simulations in MuMax3 which results were used to validate the semi-analytical model results, presented in Fig. 5. The Author also provided the description of the simulations in the paper and prepared the figures regarding the results of micromagnetic simulations.

Modal approach to modeling spin wave scattering

Wojciech Śmigaj[*]
Met Office, FitzRoy Road, Exeter EX1 3PB, United Kingdom

Krzysztof Sobucki ◉,[†] Paweł Gruszecki ◉,[‡] and Maciej Krawczyk ◉[§]
Institute of Spintronics and Quantum Information, Faculty of Physics, Adam Mickiewicz University,
Uniwersytetu Poznańskiego 2, 61-614 Poznań, Poland

Efficient numerical methods are required for the design of optimized devices. In magnonics, the primary computational tool is micromagnetic simulations, which solve the Landau-Lifshitz equation discretized in time and space. However, their computational cost is high, and the complexity of their output hinders insight into the physics of the simulated system, especially in the case of multimode propagating-wave-based devices. We propose a finite-element modal method allowing an efficient solution of the scattering problem for dipole-exchange spin waves propagating perpendicularly to the magnetization direction. The method gives direct access to the scattering matrix of the whole system and its components. We extend the formula for the power carried by a magnetostatic mode in the Damon-Eshbach configuration to the case with exchange, allowing the scattering coefficients to be normalized to represent the fraction of the input power transferred to each output channel. We apply the method to the analysis of spin wave scattering on a basic functional block of magnonic circuits, consisting of a resonator dynamically coupled to a thin film. The results and the method are validated by comparison with micromagnetic simulations.

I. INTRODUCTION

In recent years, we have observed rapid progress in the development of components for magnonic circuitry. Conduits for single-mode and multimode spin wave transfer [1–5], phase control [6–9], spin wave valves [10], couplers [11,12], resonators [13–15], transducers, diodes [16], and logic gates [17,18] are only selected examples based on various physical principles. To understand the physics of the spin wave phenomena behind the observed functionalities, increase the effectiveness of their operation, and find their new realizations, researchers need suitable models and numerical methods.

The primary approach used in magnonics is micromagnetism, where the nonlinear Landau-Lifshitz (LL) torque equation is used to describe magnetization dynamics. It is usually solved in time and space with micromagnetic simulations based on the continuum model [19,20]. These methods offer a faithful description of the experimental realizations, including nonlinear and temperature effects. There are two principal implementations of micromagnetic solvers, one based on the finite-difference method [21,22] and the second based on the finite-element method [23]. However, micromagnetic

simulations are time-consuming and require extensive computational power. Their outputs are raw time- and space-dependent data, and extensive postprocessing is necessary to elucidate the physical mechanisms underlying complex magnetic systems. In addition, simulations of wave dynamics over time require selecting a source of these waves; the obtained spectrum is source dependent, and mode identification may be ambiguous.

Other approaches are based on solving the LL equation in the frequency domain and either wave-vector or real space; they are commonly referred to as spectral methods. Spectral methods enable calculation of the response of a magnetic system to a time-harmonic excitation with high precision and at a lower computational cost, though at the price of approximations, one of which is linearization. An example of a spectral method is the plane wave method, applicable to systems with discrete translational symmetry. It was introduced and used to calculate the band structure of bulk [24] and thin-film magnonic crystals [25–27] as well as magnonic quasicrystals [28,29]. In the latter case, full magnetic saturation and homogeneity across the film thickness were assumed. Here, the LL equation is transformed into an infinite set of algebraic equations in the frequency and wave-vector domain. The equations are indexed by the reciprocal lattice vectors. The eigenproblem formed by the truncated system is solved numerically with standard numerical routines.

The dynamical matrix method [30,31] overcomes some limitations of the plane wave method. It uses the finite-difference method to solve the LL equation formulated in real space and linearized about the magnetization ground state

---

[*]Present address: Optopol Technology, Żabia 42, 42-400 Zawiercie, Poland; w.smigaj@optopol.com.pl

[†]krzsob@amu.edu.pl
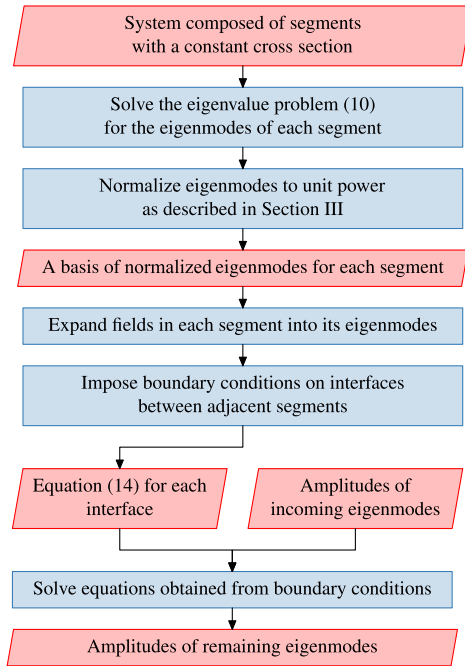[‡]gruszecki@amu.edu.pl
[§]krawczyk@amu.edu.pl

FIG. 1. Steps required for the solution of a scattering problem with the proposed modal method. Inputs and outputs are denoted with parallelograms, and processes are denoted with rectangles.

derived from micromagnetic simulations. This is a powerful method used to calculate normal modes in isolated nanoelements [30] and thin-film magnonic crystals with nanoscale periodicity [31]. However, the large matrices involved here make the solution of the eigenproblem and analysis of the normal modes time-consuming. Furthermore, the method does not make it possible to study spin wave scattering and transmission. An extension of the normal mode calculation method proposed in Ref. [32] allows damping and, to some extent, nonlinear effects to be taken into account. The resulting eigenproblem can be discretized either with finite differences or finite elements [33]. However, these methods do not encompass calculation of the transmission, reflection, or scattering matrices for spin waves in nanoscale objects.

In this paper, we develop an efficient finite-element modal method to solve the scattering problem for dipole-exchange spin waves propagating in a system composed of one or more ferromagnetic layers or stripes magnetized perpendicularly to the wave propagation direction. The proposed computational procedure is outlined in Fig. 1. We decompose the system into segments with a constant cross section and find the normal modes of each segment by solving the linearized LL equation discretized with finite elements. We expand the dynamical components of the magnetization and magnetostatic potential in each segment in the basis of its normal modes. These expansions are tied together by imposing appropriate

boundary conditions on each interface. The resulting system of linear equations is solved for the amplitudes of outgoing (transmitted and reflected) modes produced by incoming modes with known amplitudes. Optionally, the subset of these equations associated with a particular interface can also be solved for the scattering matrix of that interface. Interfacial scattering matrices supply valuable information about the contribution of individual scattering pathways to the output signal and the role of particular normal modes excited within each segment. This yields deeper insight into the physics of the system under consideration and can help its designer optimize its geometry for a specific application.

Another contribution of this paper is the generalization of the Lorentz reciprocity theorem, the mode orthogonality relations, and the formula for the power carried by propagating spin wave modes of a tangentially magnetized multilayer to the case of dipole-exchange waves. These results enable propagative normal modes used in field expansions to be normalized to unit power, letting squared scattering coefficients be identified with the power passed to the corresponding scattering channels.

We use the proposed method to study the transmission and reflection of spin waves on a ferromagnetic stripe coupled with a ferromagnetic film. This system can be considered as a basic building block of magnonic circuits possessing various functionalities [10,13,14,16,34–38]. We elucidate the important role played by pairs of modes with contrasting group velocities supported by the bilayer formed by the film and the stripe. The validity of the modal method is confirmed by an excellent agreement of its predictions with results of micromagnetic simulations.

The paper is organized as follows. In the next section, we describe the finite-element modal method, discussing first the determination of eigenmodes (Sec. II B) and then the mode-matching equations (Sec. II C). In Sec. III and Appendix B we derive the Lorentz reciprocity theorem, the mode orthogonality relations, and a formula for the power carried by dipole-exchange spin waves in the Damon-Eshbach configuration. In Sec. IV we use the proposed method to analyze the scattering of spin waves propagating along a thin ferromagnetic film on a resonant element placed in its vicinity. After validating its predictions against results of micromagnetic simulations, we feed the calculated mode propagation constants and scattering coefficients into a semianalytical model of the system under consideration, which allows us to explain the physical origin of notable features visible in its reflection and transmission spectra.

II. FINITE-ELEMENT MODAL METHOD

A. Introduction

We consider a system composed of ferromagnetic and nonferromagnetic materials. Its geometry is independent of the y coordinate and piecewise constant along x. The system is placed in an external static magnetic field oriented along the y axis; this field is assumed to be sufficiently strong to saturate all magnetic materials and orient their static magnetization along y. An example of such a system is shown schematically in Fig. 2.
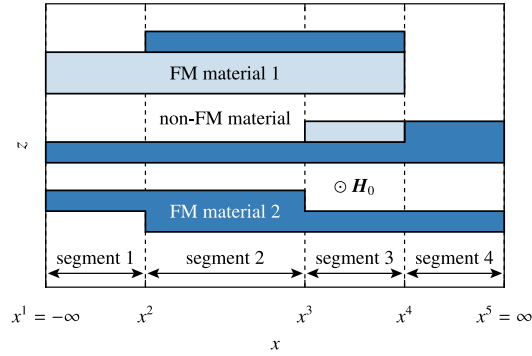
FIG. 2. An example system whose geometry satisfies the assumptions made in Sec. II A. The system contains four segments with uniform cross sections in the xy plane. FM, ferromagnetic.

In a modal method, each x-invariant region is treated as a finite or semi-infinite segment of a waveguide with a uniform cross section. The fields inside each segment are expressed as a superposition of eigenmodes of the corresponding waveguide. These eigenmode expansions are coupled through boundary conditions imposed on the interfaces $x = x^i$ ($i = 2, 3, \ldots, n$, where n is the number of segments) separating adjacent segments; imposition of these conditions produces a linear system of equations for the mode amplitudes (excitation coefficients). Typically, the excitation coefficients of modes incoming from the left and right are known, and the quantities of interest, obtained by solving the system of equations, are the coefficients of the outgoing modes in the first and last segment.

B. Determination of waveguide eigenmodes

As stated above, the fields in each x-invariant segment of the system are expanded in the eigenmodes, both propagative and evanescent, of an x- and y-invariant waveguide whose profile along z matches that of the segment. These eigenmodes are determined numerically using the finite-element method. The waveguide is governed by the Gauss law for magnetism (applicable everywhere),

$$\nabla \cdot \boldsymbol{B} = 0, \tag{1}$$

and the LL equation with a Gilbert damping term (Ref. [39], Sec. 3.8 therein; applicable only in the ferromagnetic layers),

$$\partial_t \boldsymbol{M} = \gamma \mu_0 \boldsymbol{M} \times \boldsymbol{H}_{\text{eff}} + \frac{\alpha}{M_S} \boldsymbol{M} \times \partial_t \boldsymbol{M}, \tag{2}$$

where $\boldsymbol{M}$ is the magnetization, $\boldsymbol{H}_{\text{eff}}$ is the effective magnetic field, γ is the gyromagnetic ratio, μ_0 is the vacuum permeability, M_S is the saturation magnetization, and α is the damping coefficient. The effective magnetic field is taken to be a superposition of the static external magnetic field $\boldsymbol{H}_0$, the magnetostatic magnetic field $\boldsymbol{H}_{\text{m}}$, and the exchange magnetic field $\boldsymbol{H}_{\text{ex}}$:

$$\boldsymbol{H}_{\text{eff}} = \boldsymbol{H}_0 + \boldsymbol{H}_{\text{m}} + \boldsymbol{H}_{\text{ex}}. \tag{3}$$

Assuming a harmonic time dependence [$\exp(-i\omega t)$], splitting the magnetization $\boldsymbol{M}$ and magnetostatic magnetic field $\boldsymbol{H}_{\text{m}}$ into static and dynamic (radio frequency) components, expressing the latter as a gradient of the magnetostatic potential ($\boldsymbol{h} = -\nabla \phi$), writing the exchange magnetic field as $\boldsymbol{H}_{\text{ex}} = \nabla \cdot (l^2 \nabla \boldsymbol{m})$ (with l denoting the exchange length) [40], and linearizing the LL equation, we arrive at the following system of equations:

$$\partial_x (m_x - \partial_x \phi) + \partial_z (m_z - \partial_z \phi) = 0, \tag{4a}$$

$$\partial_x \phi - \nabla \cdot (l^2 \nabla m_x) + \frac{H_0}{M_S} m_x + \frac{i\omega}{\gamma \mu_0 M_S} (m_z + \alpha m_x) = 0, \tag{4b}$$

$$\partial_z \phi - \nabla \cdot (l^2 \nabla m_z) + \frac{H_0}{M_S} m_z - \frac{i\omega}{\gamma \mu_0 M_S} (m_x - \alpha m_z) = 0, \tag{4c}$$

where all material coefficients are functions of z only. The ϕ, m_x, and m_z fields of a waveguide eigenmode have a harmonic dependence on x:

$$\left\{ \begin{array}{c} \phi(x, z) \\ m_x(x, z) \\ m_z(x, z) \end{array} \right\} = \left\{ \begin{array}{c} \phi(z) \\ m_x(z) \\ m_z(z) \end{array} \right\} \exp(ik_x x), \tag{5}$$

where k_x is the mode wave number. Taking advantage of this fact and introducing the symbols $\tilde{m}_x := im_x$, $\omega_M := -\gamma \mu_0 M_S$, and $\omega_0 := -\gamma \mu_0 H_0$, we can rewrite the equations in the form

$$k_x (\tilde{m}_x + k_x \phi) + \partial_z (m_z - \partial_z \phi) = 0, \tag{6a}$$

$$k_x \phi + \partial_z (l^2 \partial_z \tilde{m}_x) - k_x^2 l^2 \tilde{m}_x - \frac{\omega_0 - i\alpha\omega}{\omega_M} \tilde{m}_x - \frac{\omega}{\omega_M} m_z = 0, \tag{6b}$$

$$\partial_z \phi - \partial_z (l^2 \partial_z m_z) + k_x^2 l^2 m_z + \frac{\omega_0 - i\alpha\omega}{\omega_M} m_z + \frac{\omega}{\omega_M} \tilde{m}_x = 0. \tag{6c}$$

This is a quadratic eigenvalue problem in k_x; its approximate solution can be found by discretizing the above equations with the finite-element method. This requires transforming them into a *weak form*, which forces the integrals of their residuals weighted with an appropriate set of *test functions* to vanish [41,42]. To this end, we multiply the equations by test functions ψ, $\tilde{n}_x$, and n_z, respectively, and integrate by parts over z to reduce the order of differentiation and thus lower the smoothness requirements on the *trial functions* into

which ϕ, $\tilde{m}_x$, and m_z will be expanded. Application of the boundary and continuity conditions—(i) $\lim_{z \to \pm\infty} \phi(z) = 0$, (ii) $b_z \equiv m_z - \partial_z \phi$ is continuous along z, and (iii) $l^2 \partial_z \tilde{m}_x$ and $l^2 \partial_z m_z$ are continuous along z (which implies, in particular, that $\partial_z m_x = \partial_z m_z = 0$ on interfaces between layers with and without exchange magnetic field)—annihilates the boundary terms produced by integration by parts and leads to the following weak form: Find k_x, ϕ, $\tilde{m}_x$, and m_z such that for all ψ, $\tilde{n}_x$, and n_z

$$\langle \partial_z \psi, \partial_z \phi \rangle + k_x^2 \langle \psi, \phi \rangle + k_x \langle \psi, \tilde{m}_x \rangle - \langle \partial_z \psi, m_z \rangle = 0, \tag{7a}$$

$$k_x \langle \tilde{n}_x, \phi \rangle - \langle \partial_z \tilde{n}_x, l^2 \partial_z \tilde{m}_x \rangle - k_x^2 \langle \tilde{n}_x, l^2 \tilde{m}_x \rangle - \left\langle \tilde{n}_x, \frac{\omega_0 - i\alpha\omega}{\omega_M} \tilde{m}_x \right\rangle - \left\langle \tilde{n}_x, \frac{\omega}{\omega_M} m_z \right\rangle = 0, \tag{7b}$$

$$-\langle n_z, \partial_z \phi \rangle - \left\langle n_z, \frac{\omega}{\omega_M} \tilde{m}_x \right\rangle - \langle \partial_z n_z, l^2 \partial_z m_z \rangle - k_x^2 \langle n_z, l^2 m_z \rangle - \left\langle n_z, \frac{\omega_0 - i\alpha\omega}{\omega_M} m_z \right\rangle = 0, \tag{7c}$$

where

$$\langle f, g \rangle := \int f(z)\, g(z)\, dz. \tag{8}$$

The solutions $(\phi, \tilde{m}_x, m_z)$ and the test functions $(\psi, \tilde{n}_x, n_z)$ are required to satisfy the *essential* boundary and continuity conditions, i.e., those not involving derivatives.

This weak form can be discretized using the Galerkin method. The fields ϕ, $\tilde{m}_x$, and m_z are expressed as finite linear combinations of appropriate basis functions [defined on a sufficiently long but finite interval $z_{\min} \leqslant z \leqslant z_{\max}$ in the case of ϕ and on the union of the intervals where $l^2(z) > 0$ in the cases of $\tilde{m}_x$ and m_z], and the weak form is evaluated with the test functions ψ, $\tilde{n}_x$, and n_z set to each of these basis functions in turn. This leads to a quadratic algebraic eigenvalue problem

$$\mathbf{A}\boldsymbol{x} + k_x \mathbf{B}\boldsymbol{x} + k_x^2 \mathbf{C}\boldsymbol{x} = 0, \tag{9}$$

where $\boldsymbol{x}$ is the vector of expansion coefficients of ϕ, $\tilde{m}_x$, and m_z, and $\mathbf{A}$, $\mathbf{B}$, and $\mathbf{C}$ are matrices independent from k_x. This quadratic eigenvalue problem can be rewritten as a generalized linear eigenvalue problem:

$$\begin{bmatrix} \mathbf{A} & \mathbf{B} \\ & \mathbf{I} \end{bmatrix} \begin{bmatrix} \boldsymbol{x} \\ \boldsymbol{y} \end{bmatrix} = k_x \begin{bmatrix} & -\mathbf{C} \\ \mathbf{I} & \end{bmatrix} \begin{bmatrix} \boldsymbol{x} \\ \boldsymbol{y} \end{bmatrix}, \tag{10}$$

which can be solved using the standard QZ algorithm [43]. When damping is neglected, all matrices in the eigenproblem written in terms of ϕ, $\tilde{m}_x$, and m_z are real; so the phases of eigenvectors corresponding to propagative modes (modes with real k_x) can be chosen so that the profiles $\phi(z)$ and $m_z(z)$ are real whereas $m_x(z)$ is imaginary.

C. Mode matching

The fields in the ith x-invariant waveguide segment, sandwiched between the planes $x = x^i$ and $x = x^{i+1}$, are expanded in the basis of eigenmodes determined as described in the

previous section:

$$\phi(x, z) = \sum_j U_j^i(x)\, \phi_j^{iu}(z) + \sum_j D_j^i(x)\, \phi_j^{id}(z)$$
$$\text{for } x^i \leqslant x \leqslant x^{i+1}, \quad \tag{11}$$

and similarly for m_x and m_z. The first sum runs over modes propagating or decaying rightwards (towards $x = \infty$); the second sum runs over modes propagating or decaying leftwards (towards $x = -\infty$). The symbol $U_j^i(x)$ denotes the position-dependent excitation coefficient of the jth rightward mode of the ith segment with magnetostatic potential profile $\phi_j^{iu}(z)$. Analogous symbols containing the letter d are used for leftward modes. Within each segment, $U_j^i(x)$ and $D_j^i(x)$ vary harmonically and can be written as

$$U_j^i(x) = U_j^i(x^{iu}) \exp\left[ik_{xj}^{iu}(x - x^{iu})\right], \tag{12a}$$

$$D_j^i(x) = D_j^i(x^{id}) \exp\left[ik_{xj}^{id}(x - x^{id})\right], \tag{12b}$$

where k_{xj}^{iu} and k_{xj}^{id} are mode wave numbers. It is convenient to choose the reference positions x^{iu} and x^{id} as

$$x^{iu} = x^{\max(i,2)}, \quad x^{id} = x^{\min(i+1,n)}. \tag{13}$$

This ensures that imposition of boundary conditions on segment interfaces leads to equations [Eq. (14) below] containing exponentials whose magnitude does not exceed 1, which could compromise numerical stability.

The fields in adjacent waveguide segments are linked by the following boundary conditions that must hold on the interfaces between these segments: (i) ϕ is continuous along x on the whole interface, (ii) b_x is continuous along x on the whole interface, (iii) m_x and m_z are continuous along x on interfaces separating pairs of layers such that $l^2 > 0$ in both layers, and (iv) $l^2 \partial_x m_x$ and $l^2 \partial_x m_z$ are continuous along x on interfaces separating pairs of layers such that $l^2 > 0$ in at least one layer.

These boundary conditions are imposed by multiplying them with the basis functions used to expand the fields in all layers (for the first two boundary conditions) or in the layers fulfilling the specified criteria (for the last two boundary

conditions) and integrating over z. For each interface, this leads to a set of linear equations that can be written symbolically as

$$[\mathsf{V}^{iu} \quad \mathsf{V}^{id}]\begin{bmatrix} \mathsf{E}^{iu}(x^{i+1}-x^{iu}) & \\ & \mathsf{I} \end{bmatrix}\begin{bmatrix} \boldsymbol{u}^i \\ \boldsymbol{d}^i \end{bmatrix}$$

$$= [\mathsf{W}^{i+1,u} \quad \mathsf{W}^{i+1,d}]\begin{bmatrix} \mathsf{I} & \\ & \mathsf{E}^{i+1,d}(x^{i+1}-x^{i+1,d}) \end{bmatrix}\begin{bmatrix} \boldsymbol{u}^{i+1} \\ \boldsymbol{d}^{i+1} \end{bmatrix},$$

$$(14)$$

where $i+1$ is the index of the interface. In this formula, $\mathsf{E}^{\cdots}(\Delta x)$ are diagonal matrices of exponentials dependent on the length of segments adjacent to x^{i+1}, whereas the matrices $\mathsf{V}^{\cdots}$ and $\mathsf{W}^{\cdots}$ are independent from that length. Explicit expressions for these matrices are provided in Appendix A. The symbols $\boldsymbol{u}^i$ and $\boldsymbol{d}^i$ denote vectors of the excitation coefficients $u^i_j := U^i_j(x^{iu})$ and $d^i_j := D^i_j(x^{id})$ $(j = 1, 2, \dots)$ at the reference positions x^{iu} and x^{id}.

D. Solution of the scattering problem

The excitation coefficients of the outgoing modes of the semi-infinite waveguide segments—as well as the excitation coefficients of modes of any finite segments—can be calculated by solving the system of equations obtained by combining equations of the form (14) for $i = 2, 3, \dots, n$, with the coefficients of the incoming modes, $\boldsymbol{u}^1$ and $\boldsymbol{d}^n$, treated as known. Alternatively, the scattering matrices of individual interfaces can be calculated independently and then concatenated using the algorithm from Ref. [44] to reduce the computational expense.

III. MODE NORMALIZATION AND POWER FLUX

Frequently, the main quantities of interest in the solution of a scattering problem are the reflectance and transmittance of the structure in question. As we show below, in the absence of damping, these can be identified with the squared magnitudes of the elements of $\boldsymbol{d}^1$ and $\boldsymbol{u}^n$ corresponding to propagating modes, provided that the mode profiles are normalized to unit power.

Stancil and Prabhakar (Ref. [39], Sec. 6.1 therein) identify the time-averaged Poynting vector of exchange-free magnetostatic waves with

$$\langle \boldsymbol{S}_{\text{ex.-free}} \rangle = \tfrac{1}{2}\mathrm{Re}(-i\omega\phi^* \boldsymbol{b}). \quad (15)$$

It follows that, in the exchange-free approximation, the power carried by time-harmonic spin waves propagating along the x axis of an x- and y-invariant waveguide is given by

$$P_{\text{ex.-free}} = \int_{-\infty}^{\infty} \langle S_{\text{ex.-free},x} \rangle \, dz$$

$$= \frac{1}{2}\int_{-\infty}^{\infty} \mathrm{Re}(-i\omega\phi^* b_x) \, dz$$

$$= \frac{1}{2}\int_{-\infty}^{\infty} \mathrm{Im}(\omega\phi^* b_x) \, dz. \quad (16)$$

We will now generalize this expression to dipole-exchange spin waves (in the Damon-Eshbach configuration). In Appendix B we derive an orthogonality relation between a pair of dipole-exchange eigenmodes of an x- and y-invariant waveguide with negligible damping:

$$\int_{-\infty}^{\infty} \left[\mu_0^{-1}(-\phi_a b_{bx}^* + \phi_b^* b_{ax}) + il^2(k_{xa}+k_{xb}^*)\boldsymbol{m}_a \cdot \boldsymbol{m}_b^* \right] dz = 0$$

$$\text{if } k_{xa} \neq k_{xb}^*. \quad (17)$$

Here, $\phi_a(z)$, $\boldsymbol{m}_a(z)$, and k_{xa} are the field profiles and the wave number of eigenmode a; $\phi_b(z)$, $\boldsymbol{m}_b(z)$, and k_{xb} are those of eigenmode b; and $b_{ix}(z) = \mu_0(m_{ix} - \partial_x\phi_i)$ for $i = a, b$. Using the identities $ik_{xa}\boldsymbol{m}_a = \partial_x\boldsymbol{m}_a$ and $ik_{xb}\boldsymbol{m}_b = \partial_x\boldsymbol{m}_b$, we can rewrite this relation in a wave-number-free form:

$$\int_{-\infty}^{\infty} \Big[\mu_0^{-1}(-\phi_a b_{bx}^* + \phi_b^* b_{ax})$$

$$+ l^2(-\boldsymbol{m}_a \cdot \partial_x\boldsymbol{m}_b^* + \boldsymbol{m}_b^* \cdot \partial_x\boldsymbol{m}_a) \Big] dz = 0 \text{ if } k_{xa} \neq k_{xb}^*. \quad (18)$$

When a and b refer to the same mode, the integral from the above equation (omitting the now redundant mode index) reduces to

$$P' := \int_{-\infty}^{\infty} \Big[\mu_0^{-1}(-\phi b_x^* + \phi^* b_x)$$

$$+ l^2(-\boldsymbol{m} \cdot \partial_x\boldsymbol{m}^* + \boldsymbol{m}^* \cdot \partial_x\boldsymbol{m}) \Big] dz$$

$$= 2i \int_{-\infty}^{\infty} \mathrm{Im}(\mu_0^{-1}\phi^* b_x + l^2\boldsymbol{m}^* \cdot \partial_x\boldsymbol{m}) \, dz. \quad (19)$$

Comparison with Eq. (16) shows that

$$P := -\frac{1}{4}i\mu_0\omega P' = \frac{1}{2}\int_{-\infty}^{\infty} \mathrm{Im}(\omega\phi^* b_x + \omega\mu_0 l^2\boldsymbol{m}^* \cdot \partial_x\boldsymbol{m}) \, dz$$

$$(20)$$

reduces to the expression from Eq. (16) when the exchange interaction is neglected, i.e., when $l = 0$. This motivates identifying P with the power carried by a dipole-exchange spin wave in the Damon-Eshbach configuration.

In general, the spin wave will be a superposition of multiple waveguide modes:

$$\begin{Bmatrix} \phi(x,z) \\ \boldsymbol{m}(x,z) \end{Bmatrix} = \sum_i a_i \exp(ik_{xi}x) \begin{Bmatrix} \phi_i(z) \\ \boldsymbol{m}_i(z) \end{Bmatrix}, \quad (21)$$

where $[\phi_i(z), \boldsymbol{m}_i(z)]$ are the field profiles of the ith mode, k_{xi} is its wave number, and a_i is its excitation coefficient. From Eq. (20), the total power carried by these modes will be

$$P = \frac{i\mu_0\omega}{4}\int_{-\infty}^{\infty} \Big[\mu_0^{-1}(\phi b_x^* - \phi^* b_x)$$

$$+ l^2(\boldsymbol{m} \cdot \partial_x\boldsymbol{m}^* - \boldsymbol{m}^* \cdot \partial_x\boldsymbol{m}) \Big] dz$$

$$= \sum_{i,j} a_i a_j^* P_{ij}, \quad (22)$$

where

$$P_{ij} := \frac{i\mu_0\omega}{4}\int_{-\infty}^{\infty} \Big[\mu_0^{-1}(\phi_i b_{xj}^* - \phi_j^* b_{xi})$$

$$+ l^2(\boldsymbol{m}_i \cdot \partial_x\boldsymbol{m}_j^* - \boldsymbol{m}_j^* \cdot \partial_x\boldsymbol{m}_i) \Big] dz. \quad (23)$$

The orthogonality relation (18) implies that, in the absence of damping and of degenerate modes, the integral P_{ij} vanishes unless (a) $i = j$ and mode i is propagative (k_{xi} is real) or (b) mode i is an evanescent mode (k_{xi} is not real) and mode

j is its complex-conjugate counterpart ($k_{xj} = k_{xi}^*$). Therefore under these assumptions the total power carried by a superposition of waveguide modes is the sum of powers carried by individual propagative modes and pairs of evanescent modes with complex-conjugate wave numbers:

$$P = \sum_{\text{propagative modes } i} |a_i|^2 P_{ii}$$
$$+ \sum_{\text{evanescent modes } i} \text{Re}[a_i a_{\text{conj}(i)}^* P_{i,\text{conj}(i)}], \qquad (24)$$

where conj(i) denotes the index of the mode with wave number k_{xi}^*. In practice, it is convenient to normalize mode profiles so that $P_{ii} = 1$ for propagative modes and $P_{i,\text{conj}(i)} = 1$ for evanescent ones, since this makes it possible to obtain the power carried by individual modes or pairs of modes directly from their excitation coefficients.

Importantly, Eq. (23) enables unit-power mode normalization even when the profiles of the incoming and outgoing modes in a system are neither identical nor related by symmetry, e.g., when the input and output waveguides are multimodal or have different geometries.

If degenerate modes exist, Eq. (24) is still valid provided that such modes have been suitably orthogonalized. On the other hand, when damping is present, Eq. (18) loses its validity, and so the total power cannot in general be decomposed into a simple sum of powers carried by individual modes: The cross terms proportional to P_{ij} with $i \neq j$ do not disappear. However, if the damping is low enough, such a decomposition may still be accurate enough for practical purposes, as will be shown numerically in the next section.

IV. APPLICATIONS

A. Introduction

In this section we use the finite-element modal method described above to simulate the scattering of spin waves traveling along a thin ferromagnetic film on a stripe of another ferromagnetic material placed above the film. We validate the method by comparing its predictions against results of micromagnetic simulations. Finally, to understand the variation of the scattering coefficients with the stripe width, we develop a semianalytical model elucidating the roles played by the two pairs of modes supported by the bilayer made of the film and the stripe. The numerical inputs required by the model—mode wave numbers and scattering matrices—are obtained directly from simulations made with the modal method.

B. The system under consideration

Figure 3 shows the geometry of the system under consideration. It is composed of a film of thickness 30 nm made of a CoFeB alloy [45] with static magnetization $M_S = 1270$ kA/m and exchange constant $A \equiv \mu_0 M_S^2 l^2/2 = 15$ pJ/m and a stripe of the same thickness made of permalloy with $M_S = 760$ kA/m and exchange constant $A = 13$ pJ/m, separated from the film by a nonmagnetic gap of thickness 10 nm. The stripe width w will be varied in the calculation described below. The gyromagnetic coefficient of both materials is taken to be $\gamma = -176$ GHz/T, and the damping coefficient $\alpha = 0.0002$.
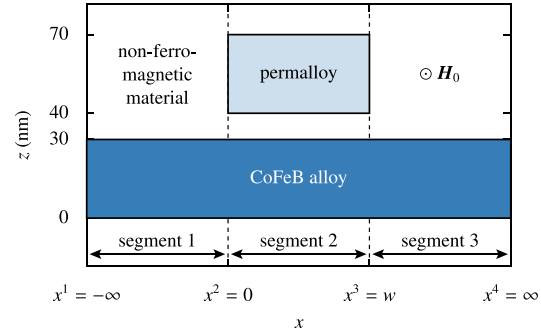

FIG. 3. xz-plane cross section of the y-invariant system analyzed in Sec. IV.

The whole system is placed in a uniform external magnetic field $\mu_0 H = 0.1$ T directed along the negative y axis and parallel to the stripe.

C. Eigenmodes

Evidently, this system is composed of three x-invariant segments, two of which (the first and the third) are identical. The eigenmodes of each segment are calculated in the manner described in Sec. II B: Eqs. (7a)–(7c) are discretized and turned into an algebraic generalized eigenvalue problem [Eq. (10)] by expanding the fields ϕ, $\tilde{m}_x$, and m_z into fifth-order Lagrange finite elements defined on a one-dimensional (1D) mesh covering an interval of length 12.19 μm with the film at the center. The same mesh is used in all three x-invariant segments. Mesh nodes are distributed so that the mesh is geometry-conforming in all segments; node spacing increases away from the ferromagnetic films. Dirichlet boundary conditions are imposed on ϕ at the top and bottom of the computational domain. In total, 224 degrees of freedom are used for ϕ, and 6 degrees of freedom per ferromagnetic layer are used for $\tilde{m}_x$ and m_z.

All calculations are done at the frequency 17 GHz. At this frequency, we find that the CoFeB film supports a pair of counterpropagating propagative eigenmodes with wavelength 1020 nm and (amplitude) attenuation length 123 μm. The CoFeB-permalloy bilayer supports two pairs of counterpropagating propagative eigenmodes; those propagating to the right have wavelengths 1299 and 108 nm and attenuation lengths 165 and 39 μm, whereas those propagating to the left have wavelengths 973 and 145 nm and attenuation lengths 99 and 27 μm. These values agree (to the number of digits shown) with ones obtained with the method of De Wames and Wolfram [46], which does not require any domain truncation or discretization.

The bilayer eigenmodes with wavelengths 1299 and 973 nm are concentrated primarily in the CoFeB layer and have larger group velocities than the modes with wavelengths 108 and 145 nm, concentrated in the permalloy layer. Therefore, in the following, we shall call the former pair of modes the *fast modes* and the latter the *slow modes*. The $\phi(z)$, $m_x(z)$, and $m_z(z)$ profiles of all propagative modes of the film and the bilayer are plotted in Fig. 4.
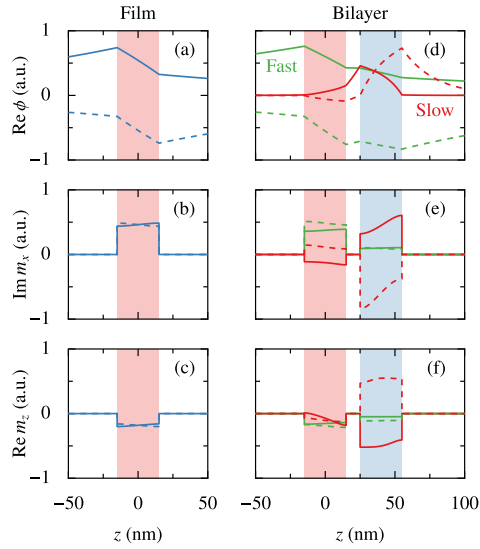
FIG. 4. Profiles of the magnetostatic potential $\phi(z)$ and the x and z components of the dynamic magnetization $\boldsymbol{m}(z)$ of the eigenmodes of (a)–(c) the CoFeB film and (d)–(f) the bilayer. Solid lines, right-propagating modes; dashed lines, left-propagating modes. The areas taken by the CoFeB film and the permalloy film are shaded in red and blue, respectively. All plots show only the dominant real or imaginary component; the L^2 norm of the other one is over 100 times smaller.

Here and throughout the rest of this paper, the phases of all mode profiles are chosen so that m_z is real and negative at the midplane of the CoFeB film.

D. Scattering: Numerical simulations

Suppose a right-propagating mode of the CoFeB film is excited by an antenna located to the left of segment 2. In that case, it will be scattered on the bilayer, giving rise to a reflected mode propagating to the left along segment 1 and a transmitted mode propagating to the right along segment 3. We are interested in the dependence of the power and phase of the reflected and transmitted modes on the width of the bilayer. We calculate the scattering coefficients in the manner described in Sec. II D, setting $\boldsymbol{u}^1$ to $[1, 0, 0, \dots]^\mathrm{T}$ (i.e., assuming the incident field in segment 1 consists solely of its right-propagating propagative eigenmode with unit power, arriving at the interface between segments 1 and 2 with phase $0°$) and $\boldsymbol{d}^3$ to $[0, 0, \dots]^\mathrm{T}$ (i.e., assuming there is no wave incident from the right in segment 3). The results of these calculations are plotted in Fig. 5 (solid curves). The four subplots show the reflectance and transmittance ($|d_1^1/u_1^1|^2$ and $|u_1^3/u_1^1|^2$, respectively) and the phase shifts of the reflected and transmitted waves, defined as $\arg(d_1^1/u_1^1)$ and $\arg\{u_1^3/[u_1^1 \exp(ik_{x1}^{1u}w)]\}$. (The phase shift of the transmitted wave is defined as the difference of the phase of the transmitted wave and the phase that would be acquired by the incident wave if the stripe was removed.) As mentioned at the end of Sec. III, in the presence of damping, waveguide eigenmodes are not strictly power orthogonal. However, in the system under
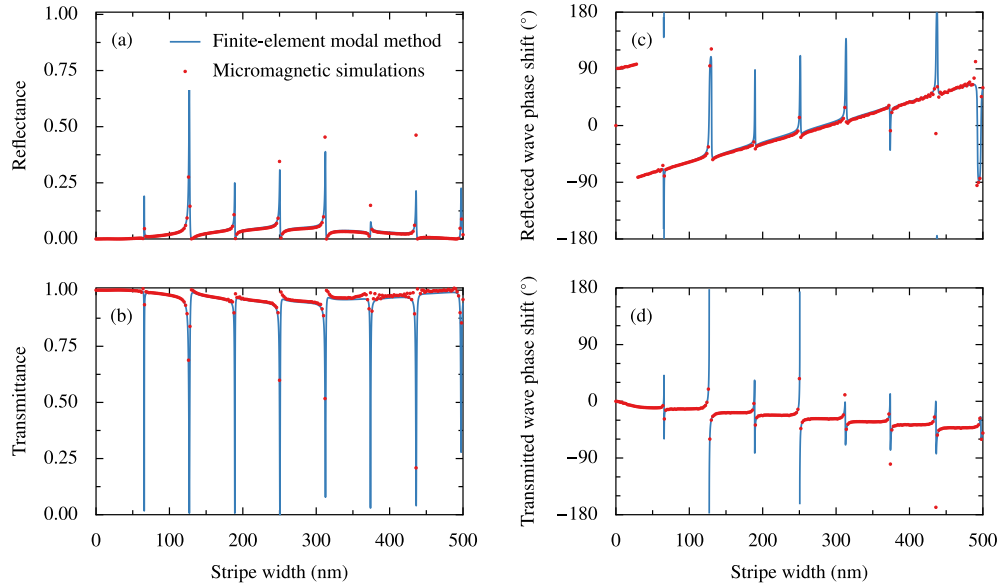

FIG. 5. (a)–(d) Dependence of the scattering coefficients of the bilayer, obtained from numerical simulations done with the finite-element modal method and micromagnetic simulations, on the stripe width. All calculations were performed at frequency 17 GHz.
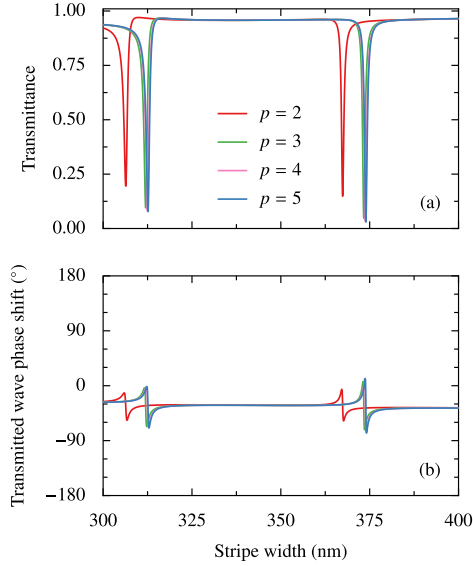
FIG. 6. Convergence of (a) the transmittance and (b) the phase shift of the transmitted wave with increasing polynomial degree p of the finite elements used in calculations.

consideration the damping is small, and the total cross power [the sum of the terms proportional to P_{ij}, $i \neq j$, in the expansion from Eq. (22)] on both sides of the stripe never rises above 1% of the incident power; so we neglect it in the following discussion.

On the reflectance curve from Fig. 5(a), we can see a regularly spaced series of narrow asymmetric peaks followed by zero crossings (the familiar Fano resonance shape), superimposed on a slow oscillation with a period of approximately 500 nm. As expected from the energy conservation principle, the transmittance curve in Fig. 5(b) is a mirror image of the reflectance curve. The narrow peaks and dips in the reflectance and transmittance curves are accompanied by rapid changes in the phase shifts of the reflected and transmitted waves. Away from these narrow features, the phase shift of the transmitted wave decreases steadily with increasing stripe width, indicating that the phase of the transmitted wave lags more and more behind that of the unscattered incident wave.

The red circles in Fig. 5 are data points obtained from micromagnetic simulations performed with MUMAX3 [21], described in detail in Appendix C. The results of these simulations agree well with those obtained with the finite-element modal method. The latter can produce a highly precise solution to the linearized Landau-Lifshitz equations (4a)–(4c). Figure 6 shows the effect of increasing the polynomial degree of elements on the positions and shapes of two narrow features in the curves from Figs. 5(b) and 5(d). The curves obtained with elements of order 4 and 5 are visually almost indistinguishable. We have also verified that increasing the size of the computational domain in the z direction by a factor of 4 makes no perceptible difference to the shape of

the curves. Computation of the scattering coefficients of the system under consideration (using the mesh and element order described in Sec. IV C) with the finite-element modal method on a laptop PC takes 1.5 s. Over 97% of this time is spent on the calculation of waveguide eigenmodes and interface scattering matrices, which needs to be done only once even if the scattering coefficients are to be computed for multiple stripe widths; the method is therefore particularly well suited for the modeling of structures containing waveguide segments whose lengths are allowed to vary. In contrast, micromagnetic simulations of the same system take approximately 1 h for each value of w.

E. Scattering: Semianalytical model

To understand the origin of the features visible in the plots from Fig. 5, we formulate a semianalytical model similar to that presented in Ref. [14] for a system with segment 3 containing no magnetic materials. We start by noting that wave scattering on an interface $x = x^{i+1}$ separating segments i and $i + 1$ can be described by a scattering matrix S^{i+1} linking the complex amplitudes of the incoming and outgoing modes on both sides of the interface,

$$\begin{bmatrix} \boldsymbol{D}^i(x^{i+1}) \\ \boldsymbol{U}^{i+1}(x^{i+1}) \end{bmatrix} = \mathsf{S}^{i+1} \begin{bmatrix} \boldsymbol{U}^i(x^{i+1}) \\ \boldsymbol{D}^{i+1}(x^{i+1}) \end{bmatrix}. \quad (25)$$

This matrix can be easily calculated using the finite-element modal method; in the notation of Eq. (14),

$$\mathsf{S}^{i+1} = [-\mathsf{V}^{iu} \quad \mathsf{W}^{i+1,d}]^{-1} [\mathsf{V}^{id} \quad -\mathsf{W}^{i+1,u}]. \quad (26)$$

If segments i and $i + 1$ are long enough, all incoming evanescent modes decay away and become negligible before reaching the interface between these segments. To obtain the amplitudes of the outgoing propagative modes, it is therefore sufficient to consider only the rows and columns of S^{i+1} corresponding to propagative modes.

Consider first the interface $x = x^2$ at the left end of the bilayer. To simplify the notation, let us denote with u_i and d_i the complex amplitudes of the right- and left-propagating modes of the input film (segment 1) and with u_s and d_s (u_f and d_f) the amplitudes of the right- and left-propagating slow (fast) modes of the bilayer (segment 2), all measured at $x = x^2$. If the bilayer is wide enough for the evanescent coupling between its ends to be negligible, then

$$\begin{bmatrix} d_i \\ u_s \\ u_f \end{bmatrix} = \begin{bmatrix} S_{ii} & S_{is} & S_{if} \\ S_{si} & S_{ss} & S_{sf} \\ S_{fi} & S_{fs} & S_{ff} \end{bmatrix} \begin{bmatrix} u_i \\ d_s \\ d_f \end{bmatrix}, \quad (27)$$

where S_{ii}, etc., are appropriate elements of the scattering matrix S^2. At 17 GHz, their numerical values found with the finite-element modal method are

$$\begin{bmatrix} S_{ii} & S_{is} & S_{if} \\ S_{si} & S_{ss} & S_{sf} \\ S_{fi} & S_{fs} & S_{ff} \end{bmatrix}$$

$$= \begin{bmatrix} 0.117e^{-0.04i} & 0.089e^{-0.78i} & 0.989e^{0.03i} \\ 0.145e^{-1.35i} & 0.984e^{2.95i} & 0.095e^{0.80i} \\ 0.983e^{-0.05i} & 0.149e^{1.17i} & 0.111e^{-3.00i} \end{bmatrix} \quad (28)$$

(these values are obtained for modes normalized to carry unit power, with phases chosen so that m_z is real and negative on

the midplane of the CoFeB film). It can be seen that the film mode is coupled primarily with the fast mode of the bilayer. The slow bilayer mode is strongly reflected. The fast and slow bilayer modes are only weakly coupled.

Likewise, amplitudes of the incoming and outgoing modes at the right end of the bilayer ($x = x^3$) are tied by

$$
\begin{bmatrix} d'_s \\ d'_f \\ u'_o \end{bmatrix} = \begin{bmatrix} S'_{ss} & S'_{sf} \\ S'_{fs} & S'_{ff} \\ S'_{os} & S'_{of} \end{bmatrix} \begin{bmatrix} u'_s \\ u'_f \end{bmatrix}, \tag{29}
$$

where u'_s and d'_s (u'_f and d'_f) are the amplitudes of the right- and left-propagating slow (fast) modes of the bilayer and u'_o is the amplitude of the right-propagating mode of the CoFeB film, all measured at $x = x^3$. Numerically [47],

$$
\begin{bmatrix} S'_{ss} & S'_{sf} \\ S'_{fs} & S'_{ff} \\ S'_{os} & S'_{of} \end{bmatrix} = \begin{bmatrix} 0.984e^{2.95i} & 0.149e^{1.17i} \\ 0.095e^{0.80i} & 0.111e^{-3.00i} \\ 0.145e^{-1.34i} & 0.983e^{-0.05i} \end{bmatrix}. \tag{30}
$$

Mode amplitudes at the two ends of the bilayer are linked by

$$
u'_i = \exp(ik_{iu}w)\, u_i =: \Phi_{iu} u_i, \tag{31a}
$$

$$
d_i = \exp(-ik_{id}w)\, d'_i =: \Phi_{id} d'_i \quad \text{for } i = s, f, \tag{31b}
$$

where k_{iu} and k_{id} are the wave numbers of the right- and left-propagating modes, numerically determined to be $k_{su} = 58.3 + 0.026i$, $k_{fu} = 4.84 + 0.006i$, $k_{sd} = -43.4 - 0.037i$, and $k_{fd} = -6.46 - 0.010i$ rad/µm.

Together, Eqs. (27), (29), (31a), and (31b) form a system of ten equations for as many unknown mode amplitudes (the amplitude u_i of the mode incident from the input film is treated as known). To obtain intelligible expressions for the scattering coefficients $r \equiv d_i/u_i$ and $t \equiv u_o/u_i$, it is advantageous to start by eliminating the amplitudes u_f, d_f, u'_f, and d'_f of the fast bilayer mode, which is only weakly reflected at the interface with the CoFeB film and hence will not give rise to strong Fabry-Pérot-like resonances. This mimics the approach taken by Lecamp *et al.* [48] in their model of pillar microcavities. This reduces the second row of Eq. (27) and the first row of Eq. (29) to

$$
u_s = \tilde{S}_{si} u_i + \tilde{S}_{ss} d_s, \tag{32a}
$$

$$
d'_s = \tilde{S}'_{ss} u'_s + \tilde{S}'_{sf} \Phi_{fu} S_{fi} u_i, \tag{32b}
$$

where

$$
\tilde{S}_{si} := \frac{S_{si} + \alpha_f S_{sf} \Phi_{fd} S'_{ff} \Phi_{fu} S_{fi}}{1 - \alpha_f S_{sf} \Phi_{fd} S'_{fs} \Phi_{su}}, \tag{33a}
$$

$$
\tilde{S}_{ss} := \frac{S_{ss} + \alpha_f S_{sf} \Phi_{fd} S'_{ff} \Phi_{fu} S_{fs}}{1 - \alpha_f S_{sf} \Phi_{fd} S'_{fs} \Phi_{su}}, \tag{33b}
$$

$$
\tilde{S}'_{ss} := \frac{S'_{ss} + \alpha_f S'_{sf} \Phi_{fu} S_{ff} \Phi_{fd} S'_{fs}}{1 - \alpha_f S'_{sf} \Phi_{fu} S_{fs} \Phi_{sd}}, \tag{33c}
$$

$$
\tilde{S}'_{sf} := \frac{\alpha_f S'_{sf}}{1 - \alpha_f S'_{sf} \Phi_{fu} S_{fs} \Phi_{sd}} \tag{33d}
$$

and

$$
\alpha_f := (1 - S_{ff} \Phi_{fd} S'_{ff} \Phi_{fu})^{-1}. \tag{34}
$$

The fast bilayer mode is only weakly reflected at the interface with the film: $|S_{ff}| = |S'_{ff}| \approx 0.111 \ll 1$. Therefore multiple

reflections of the fast mode at bilayer interfaces do not give rise to strong Fabry-Pérot resonances, and the coefficient α_f remains close to 1 for all bilayer widths. Given that, in addition, all reflection coefficients except S_{ss} and S'_{ss} are small, we can expect the scattering coefficients with a tilde defined in Eqs. (33a)–(33d) to be close to the corresponding coefficients without a tilde.

Having eliminated the amplitudes of the fast modes, we solve the remaining equations for the amplitudes of the slow modes and substitute the resulting expressions into the formulas for d_i in the first row of Eq. (27) and u'_o in the last row of Eq. (29). This yields the following formulas for the reflection and transmission coefficients:

$$
r \equiv d_i/u_i = r_f + \alpha_s r_s, \tag{35a}
$$

$$
t \equiv u_o/u_i = t_f + \alpha_s t_s, \tag{35b}
$$

where

$$
\alpha_s := (1 - \tilde{S}_{ss} \Phi_{sd} \tilde{S}'_{ss} \Phi_{su})^{-1} \tag{36}
$$

represents the effect of multiple reflections of the slow mode and

$$
r_f := \underline{S_{ii}} + \alpha_f S_{if} \Phi_{fd} \underline{S'_{ff}} \Phi_{fu} S_{fi}, \tag{37a}
$$

$$
\begin{aligned}
r_s := {}& \underline{S_{is}} \Phi_{sd} (\tilde{S}'_{ss} \Phi_{su} \underline{\tilde{S}_{si}} + \underline{\tilde{S}'_{sf}} \Phi_{fu} S_{fi}) \\
& + \alpha_f S_{if} \Phi_{fd} \big[\underline{S'_{fs}} \Phi_{su} (\underline{\tilde{S}_{si}} + \tilde{S}_{ss} \Phi_{sd} \underline{\tilde{S}'_{sf}} \Phi_{fu} S_{fi}) \\
& + S'_{ff} \Phi_{fu} \underline{S_{fs}} \Phi_{sd} (\tilde{S}'_{ss} \Phi_{su} \underline{\tilde{S}_{si}} + \underline{\tilde{S}'_{sf}} \Phi_{fu} S_{fi}) \big], \tag{37b}
\end{aligned}
$$

$$
t_f := \alpha_f S'_{of} \Phi_{fu} S_{fi}, \tag{37c}
$$

$$
\begin{aligned}
t_s := {}& S'_{os} \Phi_{su} (\underline{\tilde{S}_{si}} + \tilde{S}_{ss} \Phi_{sd} \underline{\tilde{S}'_{sf}} \Phi_{fu} S_{fi}) \\
& + \alpha_f S'_{of} \Phi_{fu} \big[\underline{S_{fs}} \Phi_{sd} (\underline{\tilde{S}'_{sf}} \Phi_{fu} S_{fi} + \tilde{S}'_{ss} \Phi_{su} \underline{\tilde{S}_{si}}) \\
& + \underline{S_{ff}} \Phi_{fd} \underline{S'_{fs}} \Phi_{su} (\underline{\tilde{S}_{si}} + \tilde{S}_{ss} \Phi_{sd} \underline{\tilde{S}'_{sf}} \Phi_{fu} S_{fi}) \big] \tag{37d}
\end{aligned}
$$

(to facilitate interpretation, scattering coefficients of magnitude much less than 1 have been underlined). It can be seen that both scattering coefficients are made up of two terms.

The first term, r_f or t_f, is free from the resonant factor α_s and the rapidly varying phase factors Φ_{sd} and Φ_{su}. Both terms in r_f contain one small reflection coefficient, whereas t_f contains none. Therefore the transmittance $|t|^2$ is usually larger than the reflectance $|r|^2$.

The other term, $\alpha_s r_s$ or $\alpha_s t_s$, is proportional to the factor α_s, which is normally close to unity but whose magnitude can grow to over 60 near Fabry-Pérot resonances of the slow mode of the bilayer. These occur approximately at stripe widths

$$
w_n = \frac{2\pi n - \arg(S_{ss} S'_{ss})}{\text{Re}(k_{su} + k_{sd})} \quad \text{where } n = 1, 2, \ldots \tag{38}
$$

(neglecting the small difference between $S_{ss}S'_{ss}$ and $\tilde{S}_{ss}\tilde{S}'_{ss}$). Away from these resonances, this term is small, since each of the terms making up r_s or t_s is proportional to a product of at least two scattering coefficients of small magnitude (less than 0.15). All these terms also contain the phase factors Φ_{su} and/or Φ_{sd}; so their phases vary rapidly.
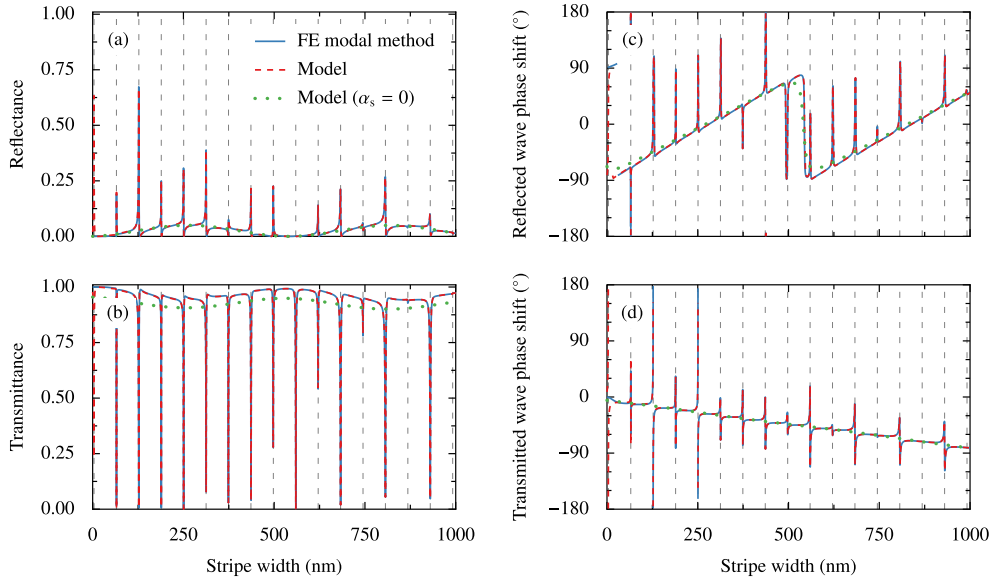
FIG. 7. (a)–(d) Comparison of the values of the bilayer's scattering coefficients predicted by the model from Sec. IV E with results of numerical simulations done with the finite-element (FE) modal method. The dashed vertical lines are the positions of resonances predicted with Eq. (38).

In Fig. 7 we compare the power and phase shift of the reflected and transmitted modes calculated from Eqs. (35a) and (35b) (red dashed curves) with results of full numerical simulations made with the finite-element modal method (blue solid curves). The two data series agree very well except for very narrow stripes, for which evanescent coupling between the two ends of the bilayer, neglected in the model from which Eqs. (35a) and (35b) were derived, plays a large role. The dashed vertical lines indicate the positions of resonances predicted from Eq. (38); their agreement with the full numerical simulations justifies approximating $\tilde{S}_{ss}\tilde{S}'_{ss}$ with $S_{ss}S'_{ss}$ in the derivation of that equation.

The green dotted curves in Fig. 7 show the result of neglecting the terms proportional to α_s in Eqs. (35a) and (35b). As expected, the sharp resonances are gone; however, the curves continue to reproduce faithfully long-term trends. Thus the slow oscillations of the reflectance and transmittance as a function of stripe width are due to the weak Fabry-Pérot resonances of the fast mode encapsulated in the α_f factor. The propagation constant of the right-propagating fast mode is smaller than that of the eigenmodes of the CoFeB film; hence the phase shift of the transmitted wave decreases steadily with stripe width.

V. CONCLUSIONS

We have introduced a finite-element modal method for the simulation of spin waves in the dipole-exchange regime and the Damon-Eshbach configuration. We have complemented it with a derivation of the Lorentz reciprocity theorem and mode orthogonality relations applicable to this class of systems and extended the formula for the power carried by magnetostatic

modes to the case of dipole-exchange spin waves. We have used a system composed of a CoFeB thin film decorated with a dynamically coupled permalloy stripe to illustrate the usefulness of the proposed method for the calculation of spin wave transmittance, reflectance, and the phase shift of scattered waves. Its predictions were successfully validated against micromagnetic simulations. We found the calculation of scattering coefficients with our method to be over 1000 times faster than calculation with micromagnetic simulations, clearly demonstrating its potential in the design of elements of magnonic circuits. Table I highlights the main differences between the modal method and micromagnetic simulations.

We have formulated a detailed semianalytical model of spin wave propagation in the system mentioned above. The only numerical inputs required by the model, namely, propagation constants of individual waveguide modes and normalized mode scattering coefficients associated with interfaces separating waveguide segments with different geometry, were obtained directly with the modal method (with no post-processing required). The model highlights the contrasting roles played by the two pairs of normal modes supported by the bilayered part of the system and makes it possible to quantify the contributions of individual scattering pathways. In particular, we have found the slow modes to be responsible for the formation of sharp Fabry-Pérot-like resonances observed in the transmission spectra, as in the Gires-Tournois interferometer [14], and the fast modes to account for low-amplitude transmittance oscillations with a larger spatial period. This provides a deepened physical interpretation of the results of recent experiments [13] and a tool for future research and optimization of magnonic devices.

TABLE I. Comparison between the finite-element modal method and micromagnetic simulations.

Aspect	Modal method	Micromagnetic simulations
Physically relevant outputs (scattering coefficients and matrices)	Obtained directly without any postprocessing	Require postprocessing (see Appendix C)
Outgoing boundary conditions in input and output waveguides	Fulfilled automatically	Fulfillment requires introducing boundary layers with a suitable damping profile
Individual mode excitation	Straightforward (via the $\boldsymbol{u}^1$ and $\boldsymbol{d}^n$ amplitude vectors)	Nontrivial (requires designing an appropriate antenna) unless the mode to be excited is the only one with a specific symmetry
Number of unknowns	Low (a few hundred per segment)	High (864×10^6 for the three-segment system simulated in this paper)
Simulation time	Short (1 s per point for the system studied in this paper)	Long (1 h per point for the system studied in this paper)
Potential for reuse of precalculated results	Segment eigenmodes can be precalculated and reused in simulations of multiple systems containing segments with the same cross section; simulations at each frequency must be done separately	Each change in geometry requires running the simulation from scratch; a single simulation with a wideband source provides information about system behavior at multiple frequencies
Precision	High: only a modest computational cost is required to reduce numerical errors (caused by the finite mesh size and density and finite polynomial expansion order) far below those resulting from the adopted mathematical model (e.g., linearization of the LL equation, piecewise constant material properties, idealized geometry)	Typically low: numerical errors are difficult to eliminate especially when lowest-order finite differences are employed
Temporal behavior	Time-harmonic field variation assumed and exploited to simplify and accelerate computations	Not limited to time-harmonic field variation but unable to exploit it if present (requires time integration until steady state)
Nonlinearity of the LL equation	Neglected (small-perturbations regime assumed)	Fully taken into account
System geometry	Limited to systems that can be split into segments with constant cross sections[a]	Arbitrary
Static magnetization	Required to be spatially piecewise constant in terms of both magnitude and orientation[a]	Arbitrary

[a]Segments with variable cross sections or non-negligible spatial variability of static magnetization could, however, be discretized with standard nonmodal finite elements, as in photonics (Ref. [42], Sec. 11.1.3 therein).

APPENDIX A: MODE-MATCHING MATRICES

Let $\{f_q(z)\}_{q=1}^{N^f}$ be the set of (continuous) basis functions used to expand the magnetostatic potential profiles of the eigenmodes of all waveguide segments. Let $\{g_q^{\mathcal{L}}(z)\}_{q=1}^{N^g(\mathcal{L})}$ be the (possibly empty) set of basis functions obtained by restricting all basis functions $f_q(z)$ to a set of intervals $\mathcal{L} \subset [z_{\min}, z_{\max}]$ and keeping only those that are not identically zero. Let $\mathcal{L}^i \subset [z_{\min}, z_{\max}]$ be the set of intervals with nonva-

nishing $l^2(z)$ in the ith segment. The set $\{g_q^{\mathcal{L}^i}(z)\}_{q=1}^{N^g(\mathcal{L}^i)}$ is then the set of basis functions used to expand the magnetization profiles of the eigenmodes of the ith waveguide segment.

The solution of the eigenproblem (10) for each segment i yields a family of $2[N^f + 2N^g(\mathcal{L}^i)]$ eigenmodes; the field profiles of the jth mode propagating or decaying to the right with wave number k_{xj}^{iu} are

$$\phi_j^{iu}(z) = \sum_{q=1}^{N^f} f_q(z) F_{qj}^{iu}, \tag{A1a}$$

$$\tilde{m}_{xj}^{iu}(z) = \sum_{q=1}^{N^g(\mathcal{L}^i)} g_q^{\mathcal{L}^i}(z) \bar{M}_{xqj}^{iu}, \tag{A1b}$$

$$m_{zj}^{iu}(z) = \sum_{q=1}^{N^g(\mathcal{L}^i)} g_q^{\mathcal{L}^i}(z) M_{zqj}^{iu}, \tag{A1c}$$

where F_{qj}^{iu}, $\tilde{M}_{xqj}^{iu}$, and M_{zqj}^{iu} are elements of one of the eigenvectors (optionally scaled to normalize the mode to unit power). Replacement of the superscript u with d yields analogous expressions for the jth mode propagating or decaying to the left.

Imposition of the boundary conditions listed in Sec. II C at the interface $x = x^{i+1}$ between segments i and $i+1$ produces Eq. (14) with $\mathsf{E}^{iu}(\Delta x)$ defined as the diagonal matrix whose jth diagonal element is $\exp(ik_{xj}^{iu}\Delta x)$ and the V^{iu} and $\mathsf{W}^{i+1,u}$ matrices defined as

$$
\mathsf{V}^{iu} = \begin{bmatrix}
\mathsf{J}^{\phi\phi}\mathsf{F}^{iu} \\
\mathsf{J}^{\phi m_i}\tilde{\mathsf{M}}_x^{iu} - i\mathsf{J}^{\phi\phi}\mathsf{F}^{iu}\mathsf{K}_x^{iu} \\
\mathsf{J}^{m_{i\cap i+1}m_i}\tilde{\mathsf{M}}_x^{iu} \\
\mathsf{J}^{m_{i\cap i+1}m_i}\mathsf{M}_z^{iu} \\
\mathsf{J}_{l^2}^{m_{i\cup i+1}m_i}\tilde{\mathsf{M}}_x^{iu} \\
\mathsf{J}_{l^2}^{m_{i\cup i+1}m_i}\mathsf{M}_z^{iu}
\end{bmatrix}
\qquad (A2)
$$

and

$$
\mathsf{W}^{i+1,u} = \begin{bmatrix}
\mathsf{J}^{\phi\phi}\mathsf{F}^{i+1,u} \\
\mathsf{J}^{\phi m_{i+1}}\tilde{\mathsf{M}}_x^{i+1,u} - i\mathsf{J}^{\phi\phi}\mathsf{F}^{i+1,u}\mathsf{K}_x^{i+1,u} \\
\mathsf{J}^{m_{i\cap i+1}m_{i+1}}\tilde{\mathsf{M}}_x^{i+1,u} \\
\mathsf{J}^{m_{i\cap i+1}m_{i+1}}\mathsf{M}_z^{i+1,u} \\
\mathsf{J}_{l^2}^{m_{i\cup i+1}m_{i+1}}\tilde{\mathsf{M}}_x^{i+1,u} \\
\mathsf{J}_{l^2}^{m_{i\cup i+1}m_{i+1}}\mathsf{M}_z^{i+1,u}
\end{bmatrix}.
\qquad (A3)
$$

In the equations above, F^{iu}, $\tilde{\mathsf{M}}_x^{iu}$, and M_z^{iu} are matrices of the mode field expansion coefficients F_{qj}^{iu}, $\tilde{M}_{xqj}^{iu}$, and M_{zqj}^{iu} introduced in Eqs. (A1a)–(A1c), whereas the elements of matrices $\mathsf{J}^{\cdots}$ are defined as

$$
J_{pq}^{\phi\phi} = \int f_p(z) f_q(z)\, dz, \qquad (A4a)
$$

$$
J_{pq}^{\phi m_j} = \int f_p(z) g_q^{\mathcal{L}^j}(z)\, dz, \qquad (A4b)
$$

$$
J_{pq}^{m_{i\cap i+1}m_j} = \int g_p^{\mathcal{L}^i\cap\mathcal{L}^{i+1}}(z) g_q^{\mathcal{L}^j}(z)\, dz, \qquad (A4c)
$$

$$
J_{l^2,pq}^{m_{i\cup i+1}m_j} = \int l_j^2(z) g_p^{\mathcal{L}^i\cup\mathcal{L}^{i+1}}(z) g_q^{\mathcal{L}^j}(z)\, dz, \qquad (A4d)
$$

with $l_j^2(z)$ representing the profile of the squared exchange length in segment j. Finally, K_x^{iu} is the diagonal matrix of mode wave numbers k_{xj}^{iu}. The formulas for $\mathsf{E}^{id}(\Delta x)$, V^{id}, and $\mathsf{W}^{i+1,d}$ can be obtained by replacing the superscript u with d.

APPENDIX B: MODE ORTHOGONALITY RELATIONS

In this Appendix, we derive a version of the Lorentz reciprocity theorem applicable to dipole-exchange spin waves in the Damon-Eshbach configuration and a number of orthogonality relations binding pairs of eigenmodes of such structures. In this paper, these relations are utilized to deduce the formula for mode power [Eq. (23)]. However, they can also be useful in their own right, for instance, to extract the contribution of a particular mode to the total magnetization calculated with a nonmodal method [49].

1. Lorentz reciprocity theorem for dipole-exchange spin waves

Consider a magnetostatic potential ϕ_a and magnetization $\boldsymbol{m}_a$ satisfying the system of equations (4a)–(4c), comprising the Gauss law for magnetism and the linearized LL equation with a damping term, which can be rewritten in the following form:

$$
\nabla \cdot (\boldsymbol{m}_a - \nabla\phi_a) = 0, \qquad (B1a)
$$

$$
\nabla\phi_a - \sum_{i=x,z}\boldsymbol{e}_i[\nabla\cdot(l^2\nabla m_{ai})]
$$
$$
+ \frac{\omega_0 - i\omega\alpha}{\omega_M}\boldsymbol{m}_a - i\frac{\omega}{\omega_M}\boldsymbol{e}_y\times\boldsymbol{m}_a = 0, \quad (B1b)
$$

where $\boldsymbol{e}_i$ $(i = x, y, z)$ denotes the unit vector directed along axis i. Consider also another magnetostatic potential ϕ_b' and magnetization $\boldsymbol{m}_b'$ satisfying the corresponding equations in the complementary system, i.e., one obtained by reversing the direction of the static external magnetic field and the static magnetization and replacing damping with gain:

$$
\nabla \cdot (\boldsymbol{m}_b' - \nabla\phi_b') = 0, \qquad (B2a)
$$

$$
\nabla\phi_b' - \sum_{i=x,z}\boldsymbol{e}_i[\nabla\cdot(l^2\nabla m_{bi}')]
$$
$$
+ \frac{\omega_0 - i\omega\alpha}{\omega_M}\boldsymbol{m}_b' + i\frac{\omega}{\omega_M}\boldsymbol{e}_y\times\boldsymbol{m}_b' = 0. \quad (B2b)
$$

Multiplying Eq. (B1a) by ϕ_b' and Eq. (B2a) by ϕ_a and subtracting the results, we obtain

$$
\phi_b'\nabla\cdot\boldsymbol{m}_a - \phi_a\nabla\cdot\boldsymbol{m}_b' - \phi_b'\nabla^2\phi_a + \phi_a\nabla^2\phi_b' = 0. \quad (B3)
$$

Similarly, multiplying Eq. (B1b) by $\boldsymbol{m}_b'$ and Eq. (B2b) by $\boldsymbol{m}_a$ and subtracting the results, we obtain

$$
\boldsymbol{m}_b'\cdot\nabla\phi_a - \boldsymbol{m}_a\cdot\nabla\phi_b' - \sum_{i=x,z}m_{bi}'\nabla\cdot(l^2\nabla m_{ai})
$$
$$
+ \sum_{i=x,z}m_{ai}\nabla\cdot(l^2\nabla m_{bi}') = 0. \qquad (B4)
$$

Subtraction of Eq. (B3) from Eq. (B4) yields

$$
\boldsymbol{m}_b'\cdot\nabla\phi_a - \boldsymbol{m}_a\cdot\nabla\phi_b' - \phi_b'\nabla\cdot\boldsymbol{m}_a + \phi_a\nabla\cdot\boldsymbol{m}_b'
$$
$$
+ \phi_b'\nabla^2\phi_a - \phi_a\nabla^2\phi_b' - \sum_{i=x,z}m_{bi}'\nabla\cdot(l^2\nabla m_{ai})
$$
$$
+ \sum_{i=x,z}m_{ai}\nabla\cdot(l^2\nabla m_{bi}') = 0. \qquad (B5)
$$

Using the relationship $\boldsymbol{b} = \mu_0(\boldsymbol{m} + \boldsymbol{h}) = \mu_0(\boldsymbol{m} - \nabla\phi)$ and the identity $\nabla\cdot(f\boldsymbol{g}) = (\nabla f)\cdot\boldsymbol{g} + f\nabla\cdot\boldsymbol{g}$, this equation can be reduced to

$$
\nabla\cdot\left[\mu_0^{-1}(\phi_a\boldsymbol{b}_b' - \phi_b'\boldsymbol{b}_a) + \sum_{i=x,z}l^2(m_{ai}\nabla m_{bi}' - m_{bi}'\nabla m_{ai})\right] = 0.
$$
$$
(B6)
$$

This is an analog of the Lorentz reciprocity theorem, known from classical electromagnetism [50], for magnetostatic waves with exchange interaction. As in electromagnetism [51], it can be used to derive orthogonality relations for waveguide modes.

2. Orthogonality relation between modes of complementary waveguides

Let ϕ_a and $\boldsymbol{m}_a$ be the magnetostatic potential and magnetization of an eigenmode of an x-invariant waveguide, with k_{xa} being the mode wave number, and ϕ'_b and $\boldsymbol{m}'_b$ be the corresponding fields of the complementary waveguide, with wave number k'_{xb}. Applying the Lorentz reciprocity theorem (B6) to these fields and taking advantage of the fact that they can be written as a product of $\exp(ik_{xa}x)$ or $\exp(ik'_{xb}x)$ and a z-dependent factor, we get

$$i(k_{xa} + k'_{xb})\left[\mu_0^{-1}(\phi_a b'_{bx} - \phi'_b b_{ax}) - il^2(k_{xa} - k'_{xb})\boldsymbol{m}_a \cdot \boldsymbol{m}'_b\right]$$
$$+ \partial_z\left[\mu_0^{-1}(\phi_a b'_{bz} - \phi'_b b_{az}) + l^2(\boldsymbol{m}_a \partial_z \boldsymbol{m}'_b - \boldsymbol{m}'_b \partial_z \boldsymbol{m}_a)\right] = 0.$$

$$(B7)$$

Integrating over z and noting that ϕ, b_z, and $\boldsymbol{m} \cdot l^2\partial_z\boldsymbol{m}$ are continuous functions of z and (at least when any magnetic layers have finite thickness) ϕ and $\boldsymbol{m}$ decay to 0 as $z \to \pm\infty$, we see that the second term $\int_{-\infty}^{\infty} \partial_z(\cdots)\,dz$ vanishes, leaving us with

$$(k_{xa} + k'_{xb})\int_{-\infty}^{\infty}\left[\mu_0^{-1}(\phi_a b'_{bx} - \phi'_b b_{ax})\right.$$
$$\left. - il^2(k_{xa} - k'_{xb})\boldsymbol{m}_a \cdot \boldsymbol{m}'_b\right]dz = 0. \quad (B8)$$

This implies the following orthogonality relation:

$$\int_{-\infty}^{\infty}[\mu_0^{-1}(-\phi_a b'_{bx} + \phi'_b b_{ax}) + il^2(k_{xa} - k'_{xb})\boldsymbol{m}_a \cdot \boldsymbol{m}'_b]\,dz = 0$$
$$\text{if } k_{xa} \neq -k'_{xb}. \quad (B9)$$

3. Orthogonality relation between modes of a single waveguide (without conjugation)

Let $[\phi_a(z), m_{ax}(z), m_{az}(z)]$ and $[\phi_b(z), m_{bx}(z), m_{bz}(z)]$ be the field profiles of two eigenmodes, with wave numbers k_{xa} and k_{xb}, of the same waveguide. Direct inspection of Eqs. (6a)–(6c) shows that $[\phi_b'(z), m_{bx}'(z), m_{bz}'(z)] := [\phi_b(z), -m_{bx}(z), m_{bz}(z)]$ are the field profiles of an eigenmode with wave number $k_{xb}' = -k_{xb}$ of the complementary waveguide. Substitution of these field profiles into Eq. (B9) yields an orthogonality relation between two modes of the same waveguide:

$$\int_{-\infty}^{\infty}\left[\mu_0^{-1}(\phi_a b_{bx} + \phi_b b_{ax})\right.$$
$$\left. + il^2(k_{xa} + k_{xb})(-m_{ax}m_{bx} + m_{az}m_{bz})\right]dz = 0$$
$$\text{if } k_{xa} \neq k_{xb}. \quad (B10)$$

4. Orthogonality relation between modes of a single waveguide (with conjugation)

Comparison of Eqs. (B1a) and (B1b) with Eqs. (B2a) and (B2b) shows that, *in the absence of damping*, if $(\phi, \boldsymbol{m})$ satisfy Eqs. (B1a) and (B1b), then the complex-conjugate fields $(\phi^*, \boldsymbol{m}^*)$ satisfy Eqs. (B2a) and (B2b) governing the complementary system. Therefore if $[\phi_b(z), m_{bx}(z), m_{bz}(z)]$ are the field profiles of a waveguide mode with wave number k_{xb}, then $[\phi_b^*(z), m_{bx}^*(z), m_{bz}^*(z)]$ are the field profiles of a mode with wave number $-k_{xb}^*$ of the complementary waveguide. Substi-

tution of these profiles into Eq. (B9) yields another orthogonality relation between two modes of the same waveguide:

$$\int_{-\infty}^{\infty}\left[\mu_0^{-1}(-\phi_a b_{bx}^* + \phi_b^* b_{ax}) + il^2(k_{xa} + k_{xb}^*)\boldsymbol{m}_a \cdot \boldsymbol{m}_b^*\right]dz = 0$$
$$\text{if } k_{xa} \neq k_{xb}^*, \quad (B11)$$

which is Eq. (17). It should be stressed once again that this relation holds only when damping is neglected.

APPENDIX C: MICROMAGNETIC SIMULATIONS

To perform micromagnetic simulations, we use the open-source MUMAX3 environment [21], which solves the full LL equation

$$\partial_t\mathbf{M} = -\frac{|\gamma|\mu_0}{1 + \alpha^2}\left[\mathbf{M} \times \mathbf{H}_{\text{eff}} + \frac{\alpha}{M_S}\mathbf{M} \times (\mathbf{M} \times \mathbf{H}_{\text{eff}})\right], \quad (C1)$$

with the finite-difference time-domain (FDTD) method.

We carry out simulations for the geometry presented in Fig. 3 modeled with two rectangular ferromagnetic slabs with dimensions and parameters described in Sec. IV B. We discretize the system into unit cells of size $2 \times 100 \times 5$ nm^3 along the x, y, and z axes, respectively. Additionally, to make the system independent of the y coordinate, we impose periodic boundary conditions along the y axis with 1024 repetitions of the system image. We place the system in a spatially uniform in-plane magnetic field of value $\mu_0 H_0 = 0.1$ T aligned along the y axis. The damping coefficient α from Eq. (C1) is set to $\alpha_0 = 0.0002$ in both magnetic domains. The length of the computational domain along the x axis is 37.5 μm. To prevent reflections from the outer boundaries of the modeled system, we introduce absorbing boundary conditions. Within each 9-μm-wide absorbing boundary layer, the damping coefficient increases quadratically up to the value of $\alpha_{\text{edge}} = 0.5$ at the outer domain boundaries, $\alpha(\xi) = \alpha_0 + (\alpha_{\text{edge}} - \alpha_0)\xi^2/L^2$, where ξ is the distance from the domain boundary and L is the width of the absorbing boundary layer.

We perform the simulations with a sweep over the stripe's width in the range from 0 to 500 nm with a step of 2 nm. The initial stage of each simulation is the relaxation, which finds a stable magnetic configuration required in each simulation's dynamic part. We excite spin waves by a steady microwave field at frequency $f_0 = 17$ GHz, locally applied in an 8-nm-wide region. The antenna is placed 9.25 μm from the left boundary of the system. To achieve the steady state, we continuously excite the spin waves for 100 ns. After this time, MUMAX3 saves 40 snapshots of the dynamic out-of-plane component of magnetization of the system with the sampling interval 0.003 ns.

The results of micromagnetic simulations are saved in the form of a matrix that contains the x component of the magnetization as a function of time and space, $m(t; x, y, z)$. The elements of the matrix are real numbers. In the first step of the postprocessing, we perform the fast Fourier transform over time. This operation transforms the initial matrix from time dependent to frequency dependent, and $\tilde{m}(f, x, y, z)$ and its elements become complex numbers. In the following calculations we only consider the slice of $\tilde{m}$ at the pumping frequency $f = f_0$. Fourier transform calculations show that

only spin waves with frequency f_0 are excited, since the only peak in the Fourier spectrum appears at this frequency. This operation reduces the visibility of undesired numerical noise and transforms the data to a more easily interpretable form. It enables us to easily separate the amplitude and phase of propagating waves, $|\tilde{m}|$ and $\arg(\tilde{m})$.

We calculate the transmittance in the system by dividing maximal values of the squared absolute value of magnetization ($|\tilde{m}|^2$) obtained from simulations with the stripe and the reference simulation without the stripe. In each calculation step, values from the same interval $x \in (2.5; 7.5)$ μm placed in segment 3 (cf. Fig. 3) are compared. We obtain the phase shift of the transmitted wave Δ_t by comparing phases of spin waves from the reference simulation and the simulation with a stripe of a given width. The phases of these waves are calculated as a mean value of $\arg(\tilde{m})$ for reference simulation results and simulation with the stripe results in the interval $x \in (2.5; 7.5)$ μm. Finally, we define $\Delta\varphi_t$ as the difference between the phases of the transmitted and reference waves, $\Delta\varphi_t = \phi_t - \phi_{ref}$, normalized to the interval $(-180°, 180°]$.

Calculations of the reflected wave parameters are more complicated, since the interference of incident and reflected waves is present in segment 1. Before calculating the reflectance, the contribution of the incident wave needs to be canceled. We achieve this by subtracting the reference simulation results from each result of the simulation with the stripe. The reflectance is then obtained by comparing the maximal absolute value of the spin wave amplitude of the reflected wave in the interval $x \in (-7.5; -2.5)$ μm in segment 1 with an analogous value from the reference simulation but from another interval placed in segment 3. The new interval $x \in (2.5; 7.5)$ μm is positioned at a distance from the stripe that is similar to the distance from the stripe of the interval in segment 1, and the new interval has the same length as the interval in segment 1. This method ensures that the attenuation in the layer influences both reflected and reference waves in the same magnitude in the calculations.

To calculate the phase shift of the reflected spin wave $\Delta\varphi_r$, we use a similar approach to that used in Ref. [14]. In this paper, very high reflectance is assumed, which is not the case in the current calculations. Thus we assume different amplitudes of the incident and reflected waves. We obtain $\Delta\varphi_r$ by fitting a formula $(I - R) + 2R\cos(2kx + \Delta\varphi_r)$ to the absolute value of simulation results $\tilde{m}$ in an interval $x \in (-5; -2.5)$ μm in segment 1. Here, I denotes the amplitude of the incident wave, and R denotes the amplitude of the reflected wave. Like $\Delta\phi_t$, the phase shift $\Delta\phi_r$ is normalized to the interval $(-180°, 180°]$.

[1] A. V. Sadovnikov, E. N. Beginin, S. E. Sheshukova, D. V. Romanenko, Y. P. Sharaevskii, and S. A. Nikitov, Directional multimode coupler for planar magnonics: Side-coupled magnetic stripes, Appl. Phys. Lett. **107**, 202405 (2015).

[2] B. Rana and Y. Otani, Voltage-Controlled Reconfigurable Spin-Wave Nanochannels and Logic Devices, Phys. Rev. Appl. **9**, 014033 (2018).

[3] B. Heinz, Q. Wang, M. Schneider, E. Weiß, A. Lentfert, B. Lägel, T. Brächer, C. Dubs, O. V. Dobrovolskiy, P. Pirro, and A. V. Chumak, Long-range spin-wave propagation in transversely magnetized nano-scaled conduits, Appl. Phys. Lett. **118**, 132406 (2021).

[4] A. Haldar and A. O. Adeyeye, Functional magnetic waveguides for magnonics, Appl. Phys. Lett. **119**, 060501 (2021).

[5] S. Sahoo, S. N. Panda, S. Barman, Y. Otani, and A. Barman, Nanochannels for spin-wave manipulation in $Ni_{80}Fe_{20}$ nanodot arrays, J. Magn. Magn. Mater. **522**, 167550 (2021).

[6] S. Louis, I. Lisenkov, S. Nikitov, V. Tyberkevych, and A. Slavin, Bias-free spin-wave phase shifter for magnonic logic, AIP Adv. **6**, 065103 (2016).

[7] X.-G. Wang, L. Chotorlishvili, G.-H. Guo, and J. Berakdar, Electric field controlled spin waveguide phase shifter in YIG, J. Appl. Phys. **124**, 073903 (2018).

[8] O. V. Dobrovolskiy, R. Sachser, S. A. Bunyaev, D. Navas, V. M. Bevz, M. Zelent, W. Śmigaj, J. Rychły, M. Krawczyk, R. V. Vovk, M. Huth, and G. N. Kakazei, Spin-wave phase inverter upon a single nanodefect, ACS Appl. Mater. Interfaces **11**, 17654 (2019).

[9] K. Baumgaertl and D. Grundler, Bistable nanomagnet as programmable phase inverter for spin waves, Appl. Phys. Lett. **118**, 162402 (2021).

[10] Y. Au, M. Dvornik, O. Dmytriiev, and V. V. Kruglyak, Nanoscale spin wave valve and phase shifter, Appl. Phys. Lett. **100**, 172408 (2012).

[11] Q. Wang, P. Pirro, R. Verba, A. Slavin, B. Hillebrands, and A. V. Chumak, Reconfigurable nanoscale spin-wave directional coupler, Sci. Adv. **4**, e1701517 (2018).

[12] P. Graczyk, M. Zelent, and M. Krawczyk, Co- and contra-directional vertical coupling between ferromagnetic layers with grating for short-wavelength spin wave generation, New J. Phys. **20**, 053021 (2018).

[13] H. Qin, R. B. Holländer, L. Flajšman, F. Hermann, R. Dreyer, G. Woltersdorf, and S. van Dijken, Nanoscale magnonic Fabry-Pérot resonator for low-loss spin-wave manipulation, Nat. Commun. **12**, 2293 (2021).

[14] K. Sobucki, W. Śmigaj, J. Rychły, M. Krawczyk, and P. Gruszecki, Resonant subwavelength control of the phase of spin waves reflected from a Gires–Tournois interferometer, Sci. Rep. **11**, 4428 (2021).

[15] A. Grachev, E. Beginin, S. Sheshukova, and A. Sadovnikov, Tunable Fano resonances in irregular magnonic structure, IEEE Trans. Magn. **58**, 1 (2022).

[16] K. Szulc, P. Graczyk, M. Mruczkiewicz, G. Gubbiotti, and M. Krawczyk, Spin-Wave Diode and Circulator Based on Unidirectional Coupling, Phys. Rev. Appl. **14**, 034063 (2020).

[17] M. P. Kostylev, A. A. Serga, T. Schneider, B. Leven, and B. Hillebrands, Spin-wave logical gates, Appl. Phys. Lett. **87**, 153501 (2005).

[18] T. Fischer, M. Kewenig, D. A. Bozhko, A. A. Serga, I. I. Syvorotka, F. Ciubotaru, C. Adelmann, B. Hillebrands, and A. V. Chumak, Experimental prototype of a spin-wave majority gate, Appl. Phys. Lett. **110**, 152401 (2017).

[19] D. Kumar and A. O. Adeyeye, Techniques in micromagnetic simulation and analysis, J. Phys. D: Appl. Phys. **50**, 343001 (2017).

[20] C. Abert, Micromagnetics and spintronics: models and numerical methods, Eur. Phys. J. B **92**, 120 (2019).

[21] A. Vansteenkiste, J. Leliaert, M. Dvornik, M. Helsen, F. Garcia-Sanchez, and B. Van Waeyenberge, The design and verification of MuMax3, AIP Adv. **4**, 107133 (2014).

[22] S. Lepadatu, Boris computational spintronics—High performance multi-mesh magnetic and spin transport modeling software, J. Appl. Phys. **128**, 243902 (2020).

[23] T. Schrefl, G. Hrkac, S. Bance, D. Suess, O. Ertl, and J. Fidler, Numerical methods in micromagnetics (finite element method), in *Handbook of Magnetism and Advanced Magnetic Materials* (Wiley, New York, 2007), Vol. 2, pp. 765–794.

[24] M. Krawczyk and H. Puszkarski, Plane-wave theory of three-dimensional magnonic crystals, Phys. Rev. B **77**, 054437 (2008).

[25] M. L. Sokolovskyy and M. Krawczyk, The magnetostatic modes in planar one-dimensional magnonic crystals with nanoscale sizes, J. Nanopart. Res. **13**, 6085 (2011).

[26] R. A. Gallardo, T. Schneider, A. Roldán-Molina, M. Langer, J. Fassbender, K. Lenz, J. Lindner, and P. Landeros, Dipolar interaction induced band gaps and flat modes in surface-modulated magnonic crystals, Phys. Rev. B **97**, 144405 (2018).

[27] C. L. Chang, S. Mieszczak, M. Zelent, V. Besse, U. Martens, R. Tamming, J. Janusonis, P. Graczyk, M. Münzenberg, J. Kłos, and R. I. Tobey, Driving Magnetization Dynamics in an On-Demand Magnonic Crystal via the Magnetoelastic Interactions, Phys. Rev. Appl. **10**, 064051 (2018).

[28] J. Rychły, S. Mieszczak, and J. Kłos, Spin waves in planar quasicrystal of Penrose tiling, J. Magn. Magn. Mater. **450**, 18 (2018).

[29] S. Watanabe, V. S. Bhat, K. Baumgaertl, M. Hamdi, and D. Grundler, Direct observation of multiband transport in magnonic Penrose quasicrystals via broadband and phase-resolved spectroscopy, Sci. Adv. **7**, eabg3771 (2021).

[30] M. Grimsditch, L. Giovannini, F. Montoncello, F. Nizzoli, G. K. Leaf, and H. G. Kaper, Magnetic normal modes in ferromagnetic nanoparticles: A dynamical matrix approach, Phys. Rev. B **70**, 054409 (2004).

[31] S. Tacchi, F. Montoncello, M. Madami, G. Gubbiotti, G. Carlotti, L. Giovannini, R. Zivieri, F. Nizzoli, S. Jain, A. O. Adeyeye, and N. Singh, Band Diagram of Spin Waves in a Two-Dimensional Magnonic Crystal, Phys. Rev. Lett. **107**, 127204 (2011).

[32] M. d'Aquino, C. Serpico, G. Miano, and C. Forestiere, A novel formulation for the numerical computation of magnetization modes in complex micromagnetic systems, J. Comput. Phys. **228**, 6130 (2009).

[33] S. Perna, F. Bruckner, C. Serpico, D. Suess, and M. d'Aquino, Computational micromagnetics based on normal modes: bridging the gap between macrospin and full spatial discretization, J. Magn. Magn. Mater. **546**, 168683 (2022).

[34] T. Yu, Y. M. Blanter, and G. E. Bauer, Chiral Pumping of Spin Waves, Phys. Rev. Lett. **123**, 247202 (2019).

[35] T. Yu, C. Liu, H. Yu, Y. M. Blanter, and G. E. W. Bauer, Chiral excitation of spin waves in ferromagnetic films

by magnetic nanowire gratings, Phys. Rev. B **99**, 134424 (2019).

[36] H. Wang, J. Chen, T. Yu, C. Liu, C. Guo, S. Liu, K. Shen, H. Jia, T. Liu, J. Zhang, M. A. Cabero, Q. Song, S. Tu, M. Wu, X. Han, K. Xia, D. Yu, G. E. W. Bauer, and H. Yu, Nonreciprocal coherent coupling of nanomagnets by exchange spin waves, Nano Res. **14**, 2133 (2021).

[37] P. Roberjot, K. Szulc, J. W. Kłos, and M. Krawczyk, Multi-functional operation of the double-layer ferromagnetic structure coupled by a rectangular nanoresonator, Appl. Phys. Lett. **118**, 182406 (2021).

[38] K. G. Fripp, A. V. Shytov, and V. V. Kruglyak, Spin-wave control using dark modes in chiral magnonic resonators, Phys. Rev. B **104**, 054437 (2021).

[39] D. D. Stancil and A. Prabhakar, *Spin Waves: Theory and Applications* (Springer, New York, 2009).

[40] M. Krawczyk, M. L. Sokolovskyy, J. W. Kłos, and S. Mamica, On the formulation of the exchange field in the Landau-Lifshitz equation for spin-wave calculation in magnonic crystals, Adv. Condens. Matter Phys. **2012**, 764783 (2012).

[41] T. J. R. Hughes, *The Finite Element Method: Linear Static and Dynamic Finite Element Analysis* (Dover, Mineola, NY, 2000).

[42] J.-M. Jin, *The Finite Element Method in Electromagnetics* (Wiley, New York, 2015).

[43] In practice, for better numerical stability, it is advantageous to rewrite the weak form in terms of the scaled variables $\tilde{m}'_x := a\tilde{m}_x$, $m'_z := am_z$, and $k'_x := ak_x$, where a is a length comparable to the thickness of the ferromagnetic layers. This ensures that the elements of all matrix blocks have similar magnitude.

[44] L. Li, Formulation and comparison of two recursive matrix algorithms for modeling layered diffraction gratings, J. Opt. Soc. Am. A **13**, 1024 (1996).

[45] A. Conca, E. T. Papaioannou, S. Klingler, J. Greser, T. Sebastian, B. Leven, J. Lösch, and B. Hillebrands, Annealing influence on the Gilbert damping parameter and the exchange constant of CoFeB thin films, Appl. Phys. Lett. **104**, 182407 (2014).

[46] R. E. De Wames and T. Wolfram, Dipole-exchange spin waves in ferromagnetic films, J. Appl. Phys. **41**, 987 (1970).

[47] Owing to the geometrical symmetry of the system, $S'_{kl} \approx S_{lk}$ and $S'_{ok} \approx S_{ki}$ for $k, l =$ f, s. The equality would be exact if the modes were orthonormalized with respect to the unconjugated inner product defined in Eq. (B10) rather than normalized to unit power.

[48] G. Lecamp, P. Lalanne, J. P. Hugonin, and J. M. Gérard, Energy transfer through laterally confined Bragg mirrors and its impact on pillar microcavities, IEEE J. Quantum Electron. **41**, 1323 (2005).

[49] P. R. McIsaac, Mode orthogonality in reciprocal and nonreciprocal waveguides, IEEE Trans. Microwave Theory Tech. **39**, 1808 (1991).

[50] A. T. Villeneuve and R. F. Harrington, Reciprocity relationships for gyrotropic media, IRE Trans. Microwave Theory Tech. **6**, 308 (1958).

[51] A. T. Villeneuve, Orthogonality relationships for waveguides and cavities with inhomogeneous anisotropic media, IRE Trans. Microwave Theory Tech. **7**, 441 (1959).

5.5   Magnon-Optic Effects with Spin-Wave Leaky Modes: Tunable Goos-Hänchen Shift and Wood's Anomaly

This paper is devoted to the investigation of oblique SW beam incidence on Gires-Tournois magnonic interferometer. The investigations were performed by means of micromagnetic simulations in MuMax3 environment. In the presented system two magnonic effects were observed which are analogues to two effects known in optics. The first one being Goos-Hänchen effect which manifests as a lateral shift of waves reflected from an interface, here a magnonic interferometer. The second effect is so called Wood's anomaly which is a decrease of reflected wave's amplitude due excitation of an eigenmode at the interface. In the paper the condition for magnonic Wood's anomaly was established and additionally, it was shown that under the same conditions lateral shift of reflected SW beam also increases. The interferometer eigenmode excited by the incident SW beam proves to be weakly confined and emits the SWs back to the system, thus it was named 'leaky-mode'.

The Author's contribution to this paper was to perform all of micromagnetic simulations which results are presented in the paper. The simulations carried out by the Author were performed in MuMax3 environment exclusively. The Author processed the results of the micromagnetic simulations. The Author also has written the bulk of manuscript with supplementary materials as well as prepared all of the figures and movies included with the publication. The Author has maintained an e-mail contact with the journal during the publication process.

NANO LETTERS

Letter

Magnon-Optic Effects with Spin-Wave Leaky Modes: Tunable Goos-Hänchen Shift and Wood's Anomaly

Krzysztof Sobucki,* Wojciech Śmigaj, Piotr Graczyk, Maciej Krawczyk, and Paweł Gruszecki*

Read Online

| ACCESS | | ılıl Metrics & More | | Article Recommendations | | SI Supporting Information |

ABSTRACT: We demonstrate numerically how a spin wave (SW) beam obliquely incident on the edge of a thin film placed below a ferromagnetic stripe can excite leaky SWs guided along the stripe. During propagation, leaky waves emit energy back into the layer in the form of plane waves and several laterally shifted parallel SW beams. This resonance excitation, combined with interference effects of the reflected and re-emitted waves, results in the magnonic Wood's anomaly and a significant increase of the Goos-Hänchen shift magnitude. This yields a unique platform to control SW reflection and transdimensional magnonic router that can transfer SWs from a 2D platform into a 1D guided mode.

KEYWORDS: *spin waves, magnonics, magnon-optics, leaky modes, Goos-Hänchen effect, Wood's anomaly*
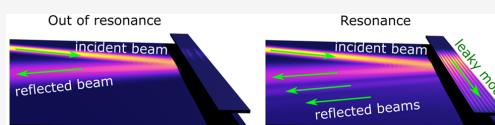
In wave physics, extended and bound modes can be recognized due to their amplitude spatial distribution. The most common are the extended states, which propagate freely in a system. Examples of the second type, which do not necessarily require a structural constraint, include bound states in the continuum (BICs) and leaky modes (LMs).[1] BIC is a state that exists in the continuous part of the spectrum but is perfectly localized. It was predicted by von Neumann and Wigner for electron waves[2] and later experimentally observed for photons[3−5] and phonons.[6,7] LMs are another type of mode, which are localized but can store energy only for a limited time due to their coupling with extended states. Therefore, LMs can be excited by propagating modes and leak energy into them. Hence, the LM wavenumber is complex, and its imaginary part expresses the rate of energy leakage.[8−10] The LMs facilitate the occurrence of Wood's anomaly, which manifests itself as a decrease in the amplitude of reflected waves and is caused by the excitation of an evanescent wave at the interface with some element. It was first reported for light reflected from a grating.[10−12]

An intriguing wave type is the spin wave (SW), that is, a collective precessional disturbance of magnetization in magnetic materials, which is believed to be a promising candidate for information carriers in beyond-CMOS devices.[13−16] SW optics is more complex than its electromagnetic counterpart and rich in optical phenomena.[17−25] Many effects from photonics have already been transferred to magnonics, for instance, negative refraction,[26] anomalous refraction,[25] graded refractive index effects,[27−29] and the Goos-Hänchen (GH) effect,[30] i.e., the lateral shift of the waves' reflection point at an interface.[31−35] While the GH effect has been predicted theoretically, it has not yet been experimentally observed for SW beams. Also, the BICs,[36] LMs, Wood's anomalies, and

resonance effects widely explored in photonics[37] remain poorly investigated in magnonics.

The use of nanoresonators in the form of ferromagnetic stripes placed over a thin film to modulate SWs has recently attracted attention.[38−50] In this letter, we numerically study the oblique reflection of a SW beam from the edge of a ferromagnetic film ending with a resonant stripe element[45,46] [see Figure 1(a)]. We find that a SW beam can excite an LM when resonance conditions are met. The LM emits SWs back into the film while propagating along the stripe. As a result, we observe a decrease in the amplitude of reflected waves, which we interpret as a magnonic counterpart of the Wood's anomaly. Moreover, we detect multiple reflected beams with tunable positions. Thus, the excitation of LMs allows tuning of the GH shift by several wavelengths. Our results open a route for the exploitation of the demonstrated effects in various magnonic applications, including designing resonant SW metasurfaces in planar structures suitable for integration with magnonic devices, converting extended SWs into waves guided along a stripe and exploiting the third dimension in integrated magnonic systems.

We consider a half-infinite CoFeB layer of thickness $d_1 = 5$ nm with a saturation magnetization of 1200 kA/m and exchange constant of 15 pJ/m. Above the film lies a ferromagnetic stripe of width $w = 155$ nm and thickness $d_2 = 5$ nm aligned with the layer's edge. We assume that the
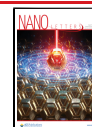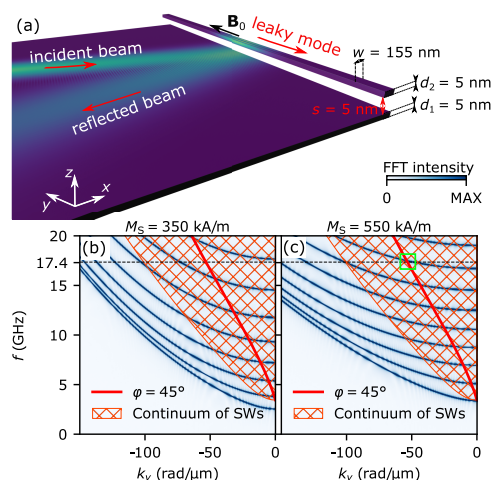
Figure 1. (a) Geometry of the system. Color represents the SW amplitude and indicates the incident and reflected SW beams in the film as well as the LM in the stripe. (b,c) Dispersion relation of SWs. The blue colormaps in the background represent dispersion relations of the resonant-stripe element of the SWs propagating along the stripe with (b) M_S = 350 kA/m and (c) M_S = 550 kA/m. The hatched region displays the continuum of SWs in the CoFeB layer. The thick red line represents the analytical dispersion relation of SWs propagating in the film at an angle of φ = 45° to $\mathbf{B}_0$. The horizontal black dashed line indicates the frequency f_0 = 17.4 GHz used in the steady-state simulations. The green square in (c) shows the crossing at f_0 = 17.4 GHz of the beam and stripe dispersion relations.

exchange constant in the stripe equals 3.7 pJ/m, and the value of its saturation magnetization M_S varies. Both elements are separated by a dielectric nonmagnetic layer of thickness s = 5 nm; see Figure 1(a). We will refer to the stripe and the layer directly below it as the bilayer. The system is uniformly magnetized by an external magnetic field $B_0 = \mu_0 H_0$ = 0.01 T directed along the stripe (the y-axis). We set the damping parameter α to 0.0004 and the gyromagnetic ratio γ to −176 rad GHz/T. At normal SW incidence, this geometry is a magnonic realization of the Gires−Tournois interferometer, offering multiple Fabry−Pérot resonances.[45] We analyze the oblique incidence of a 775-nm-wide SW beam at the frequency f_0 = 17.4 GHz (wavelength λ = 103 nm) and at an angle of 45° (angle of the phase velocity with respect to the x-axis). We employ MuMax3[51] to perform micromagnetic simulations of the dynamics of the magnetization $\mathbf{m}(\mathbf{r},t)$ in the system (for more details see Supporting Information).

The dispersion relations of SWs propagating along the stripe placed above the layer for two selected values of the stripe magnetization M_S, i.e., 350 kA/m and 550 kA/m, are shown by the blue colormaps in Figure 1(b) and (c), respectively. The hatched area is the continuum spectrum of propagating SWs in the CoFeB film, calculated analytically,[52] and the red line is the dispersion of the SW beam (see Supporting Information). For M_S = 550 kA/m, the analytical dispersion crosses the bilayer dispersion at the frequency of the SW beam f_0 = 17.4 GHz; see the green square in Figure 1(c). Here, the wavevector component k_y of the incident wave matches the wavenumber of a stripe mode; therefore, we expect the incident SW beam to

excite that mode. For M_S = 350 kA/m, there is no phase matching at f_0 = 17.4 GHz; thus, the coupling between the incident SW and stripe modes is suppressed.

To verify our predictions, we examine the reflection of the SW beam from the bilayer edge for the two considered values of M_S in the stripe. In the simulations, we use a continuous excitation of the SW beam and analyze the linear response for the steady-state SW distribution in the system (see Supporting Information). Figure 2 presents the steady-state $|m_x|$ amplitude distributions for the stripe magnetizations M_S = 350 and 550 kA/m, respectively.

In the case of M_S = 350 kA/m [Figure 2(a)], the SWs are excited, but oscillations are present only in the region directly above the incident spot. Their amplitude is an order of magnitude smaller than in the layer. In the far field, we see only
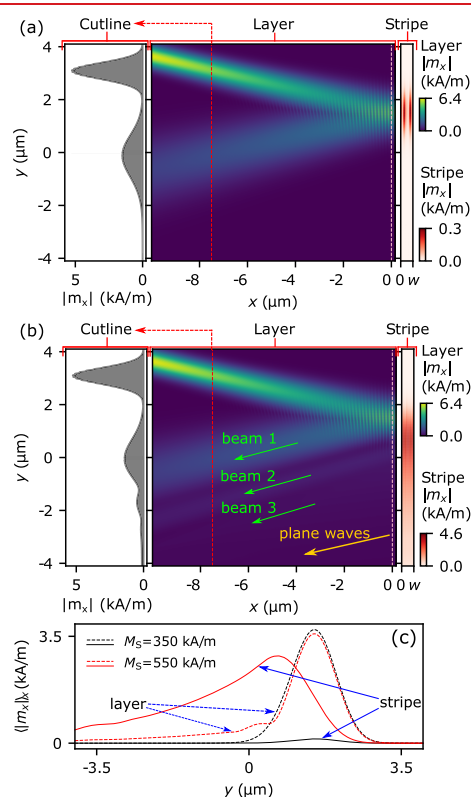

Figure 2. (a,b) Colormaps of the SW amplitude distribution of magnetization's in-plane dynamic component $|m_x|$. Middle panels show $|m_x|$ in the CoFeB layer. The colormaps in the bars on the right present $|m_x|$ in the stripe. The panels on the left show $|m_x|$ in the layer in a cutline through the layer at the position x = −7.5 μm indicated with a red-dashed line in the central panel. Results for the system with a stripe of (a) M_S = 350 kA/m and (b) M_S = 550 kA/m. (c) Averaged $\langle|m_x|\rangle_x \left(= \frac{1}{w} \int_0^w |m_x| dx \right)$ as a function of y in the stripe (solid lines) and in the layer directly under the stripe (dashed lines). The black and red lines represent results for the system with M_S = 350 kA/m and M_S = 550 kA/m, respectively.

a single reflected SW beam (cf. the left panel in Figure 2(a)). Both the incident and reflected beams have Gaussian envelopes with an apparent increase in width due to beam divergence.

We observe a different behavior in the case of M_S = 550 kA/m. First, the SW amplitude in the stripe is comparable with that of the SW beam in the layer. Moreover, we observe the propagation of SWs along the stripe in the direction opposite to the y-axis, which is consistent with the group velocity direction extracted from the dispersion relation for SWs in the stripe. The mode in the bilayer emits SWs back to the layer during its propagation, which is a clear indication of its LM nature. Furthermore, we observe the formation of new SW beams in the layer that are parallel to the primary beam (see Figure 2(b)). Two new beams are clearly visible in the left panel, which shows the SW intensity cross-section taken at x = −7.5 μm. Note that there are also plane waves propagating outward from the interface.

Let us examine the change in the SW amplitude as it propagates along the bilayer. In Figure 2(c) we see a significant difference between the SW modes in the two considered cases. As expected, for the stripe with M_S = 350 kA/m, the SW amplitude in the stripe is negligible. However, when the phase-matching condition is fulfilled at M_S = 550 kA/m, we see an efficient excitation of the LM that propagates in the −y-direction (see the solid red line in Figure 2(c)). Note that the distribution of the amplitude $\langle |m_x| \rangle_x$ in the layer below the resonator along the y-axis can be decomposed into several superimposed Gaussian functions (discussed in detail in the following paragraph), namely, a dominant one associated with the primary reflected SW beam and several additional ones with smaller amplitudes (see the dashed red line). This opens channels for energy leakage from the LM to the film.

To gain a deeper insight into how LM emission occurs over time, we perform simulations of a SW packet to complement the steady-state simulations discussed previously (see also Supporting Information). The full width at half-maximum (FWHM) of the packet is 0.5 ns and the angle of incidence is 45°. In Figure 3, we present two snapshots of the reflected

Figure 3. Reflection of the SW wavepacket on the bilayer resonant-stripe element (M_S = 550 kA/m) for (a) t = 10.9 ns and (b) t = 12.6 ns. Note that the amplitudes of SWs are amplified to better visualize SWs reemited by a leaky mode in the stripe; see the colorbars.

wavepacket from the simulation with the stripe magnetization M_S = 550 kA/m (the video in Supporting Information, Movie S5). These simulations confirm that the leaky mode excited by the incident SWs propagates along the bilayer and reemits SWs in the form of plane waves without a constant supply of SWs from the incident SW beam. In addition, Movie S5 shows that the amplitude of the excited mode in the stripe bounces

obliquely between the edges of the stripe (this is apparent especially at lower SW amplitudes). We stipulate that this bouncing in the stripe is the source of a spatial shift of the third and next reflected beams. The bouncing mode re-emits its energy at a higher rate when it reflects from the left edge of the resonator, giving rise to new reflected beams in the system.

To understand the formation of multiple reflected beams at resonance [Figure 2 (b)] we perform the analysis proposed by Tamir and Bertoni[10] to explain the formation of an additional reflected beam in the case of electromagnetic waves. The reflectance coefficient of the incident SW beam at an interface with the LM can be described as $\rho(k_y) = e^{i\Delta}(k_y - k_p^*)/(k_y - k_p)$, where Δ is the phase shift between the incident and reflected beams; k_y is the tangential component of the incident wavevector; and $k_p = \kappa + i\nu$ is the LM wavenumber. Because of the tangential component conservation rule, both k_y and k_p have the same direction of propagation with respect to the y-axis. As the Tamir−Bertoni model shows, when the stripe mode has a bound (non-leaky) character, i.e., $\nu = 0$, the LM is not excited by the incident beam; thus, it has no effect on the reflected beam. Excitation of the stripe mode occurs when it takes on a leaky character and becomes more effective as the imaginary component ν increases. Concurrently, an increase in ν accelerates the transfer of energy back into the layer; hence, at a specific value of ν, the secondary beam overshadows the main reflected beam. This is qualitatively reflected in our simulation results (Supporting Information). However, our simulations show the presence of several reflected beams instead of two, as in the Tamir−Bertoni model. This discrepancy may be due to some differences between the Tamir−Bertoni model and our system, such as neglecting the higher-order poles of the reflection coefficient in the Tamir−Bertoni model, the finite stripe width, and bouncing of the SW amplitude between the edges of the stripe described in the previous paragraph.

Let us examine how the reflection is affected by the change of the stripe's M_S while going through resonance. Figure 4(a) illustrates the dependence of the average SW amplitude within the stripe, $\langle |m_x| \rangle_{stripe}$, on M_S in the range 350−750 kA/m. It shows an increase of the amplitude for $M_S \in$ (450−650) kA/m with a maximum reached at 590 kA/m. Therefore, a band crossing occurs near 17.4 GHz for a wide range of M_S. The origin of this broadband resonance effect together with dispersion relations for various values of M_S can be found in the Supporting Information.

In Figure 4(b), we superimpose several cutlines through the layer's $|m_x|$ distributions in the far field for different values of M_S. We quantify the positions and amplitudes of reflected beams by fitting Gaussian curves to the cutlines in the far field; more details are given in Supporting Information. We mark the positions of the maxima of the primary reflected beam with black squares and those of the secondary beam with red triangles. The position $y = 0$ represents the position of the reflected beam for M_S = 350 kA/m at x = −7.5 μm. It is evident that the positions and amplitudes of the reflected beams change with M_S. As we approach the resonance and LM excitation is observed, the primary beam becomes weaker (see Figure 4(c)), its amplitude decreasing by almost 40% at $M_S \approx$ 615 kA/m. We interpret this decrease as a magnonic analogue to the Wood's anomaly[11] since the amplitude of the reflected beam decreases due to the excitation of the stripe's localized mode. As the primary beam amplitude decreases, the amplitude of the secondary beam increases, and for $M_S \approx$
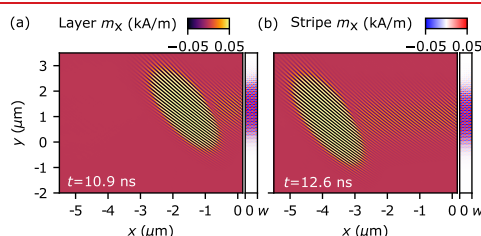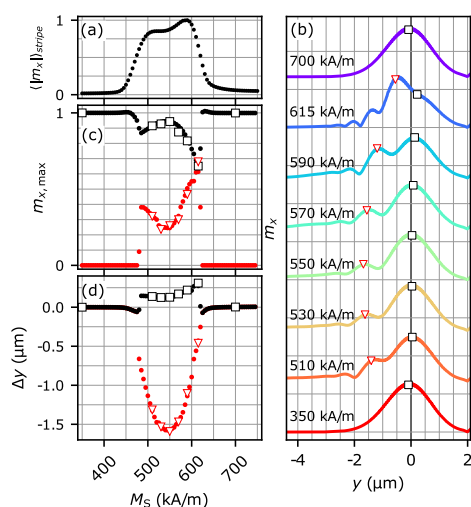
Figure 4. (a) Averaged $|m_x|$ over the volume of the stripe as a function of its M_S. (b) Comparison of several reflected beam cutlines at $x = -7.5$ μm for different values of M_S. The maximal amplitudes of the primary and secondary beams are marked with black squares and red triangles, respectively. (c) The maximal amplitudes of the primary and secondary beams in arbitrary units as a function of M_S. (d) The spatial GH shift of the beams' maxima with respect to the system with $M_S = 350$ kA/m as a function of M_S.

615 kA/m, it is even higher than the amplitude of the primary beam. These facts adequately reflect the Tamir–Bertoni analytical model and indicate an increase of the imaginary part of the LM wavenumber, meaning that more energy is leaked by the LM and that the energy of the incident beam is more efficiently directed to the secondary reflected beams.

As shown in Figure 4(d), the reflected beams are shifted with respect to the reference nonresonant scenario, i.e., $M_S = 350$ kA/m. This implies the possibility of manipulating the value of the GH shift, which for $M_S = 350$ kA/m takes the value of +12 nm, namely, around 10% of the incident SW wavelength. It is a typical value of GH shifts for SWs, which are usually smaller than the SW wavelength.[31,32,34] The positions of the primary and secondary reflected beams change when LMs are excited (cf. Figures 4(a) and (d)). The primary and secondary beams move toward positive and negative y-coordinates, respectively. The displacement of the primary beam ranges from −71 to 300 nm, reaching a maximum at $M_S = 615$ kA/m. Therefore, by adding a stripe above the edge, we can profit from the resonance effect to significantly enhance and manipulate the value of the GH shift, reaching the value of up to almost three wavelengths. This is already a measurable value, which is essential for the experimental verification of the GH shift for SW beams. Moreover, the shift of the secondary beam is even larger and reaches up to −1600 nm. Notably, for $M_S \approx 615$ kA/m (the case where the amplitude of the secondary beam is greater than the amplitude of the primary beam), the lateral beam displacement is −456 nm.

In conclusion, we have shown a new way to control SW propagation in a thin ferromagnetic film using a magnonic resonance element formed by depositing a ferromagnetic stripe on top of the film. We found a magnonic counterpart to

Wood's anomaly as well as a GH shift measurable with state-of-the-art experimental techniques. Our results have several important implications for magnonics and its application. First, our system is a platform for studying the controlled reflection and scattering of SWs. Under certain conditions, the incident SW beam can excite an LM in the resonance element, which emits a portion of its energy in the form of new SW beams. Note that the resonance criterion is fulfilled in the system not for a specific M_S but for quite a broad range of M_S, covering standard values of Py. This indicates the feasibility of an experimental realization of such an interferometer. Moreover, our system allows an easy change of the GH shift magnitude by several wavelengths, up to 450 nm for the primary beam and 1600 nm for the secondary beam. The resonant coupling described in this paper adopts properties from a spectrum between a mode strictly confined to the bilayer and an SW from the continuum of modes in the film. Thus, the same effects are expected for other angles of incidence and other confined modes at different frequencies. Although the analysis in the main part of the paper was done by varying the stripe magnetization M_S, in the Supporting Information we show that similar effects can be observed when the modulated parameter is the frequency or the stripe width, which can be changed more easily in experiments. Moreover, for the near-resonance scenario, the amplitude of the secondary beam can exceed the amplitude of the primary reflected beam to an even greater extent. Finally, the proposed geometry allows transferring the energy of a SW beam propagating in the film to the stripe; i.e., it allows a high-efficiency transfer of SWs from 2D platforms into 1D waveguides, forming a transdimensional magnonic router in a similar manner to the one that was proposed for plasmons.[53] This is crucial for designing magnonic circuits and exploiting the third dimension for signal processing.

■ ASSOCIATED CONTENT

ⓢ Supporting Information

The Supporting Information is available free of charge at https://pubs.acs.org/doi/10.1021/acs.nanolett.3c01592.

> Description of the numerical methods, the data postprocessing, and the results of additional simulations (PDF)
> Video of the calculated steady-state SW intensity distribution as a function of the stripe magnetization M_S (MP4)
> Video of the calculated steady-state SW intensity distribution as a function of the beam frequency (MP4)
> Video of the system's dispersion relation as a function of the stripe magnetization M_S (MP4)
> Video of the wavepacket reflection from an interferometer with stripe magnetization $M_S = 350$ kA/m (MP4)
> Video of the wavepacket reflection from an interferometer with stripe magnetization $M_S = 550$ kA/m (MP4)

■ AUTHOR INFORMATION

Corresponding Authors

Krzysztof Sobucki − Institute of Spintronics and Quantum Information, Faculty of Physics, Adam Mickiewicz University, 61-614 Poznań, Poland; ⓞ orcid.org/0000-0003-3273-2305; Email: krzsob@st.amu.edu.pl

Paweł Gruszecki − *Institute of Spintronics and Quantum Information, Faculty of Physics, Adam Mickiewicz University, 61-614 Poznań, Poland;* ⊙ orcid.org/0000-0003-3529-1744; Email: gruszecki@amu.edu.pl

Authors

Wojciech Śmigaj − *Met Office, Exeter EX1 3PB, U.K.;* Present Address: Optopol Technology, Żabia 42, 42-400 Zawiercie, Poland

Piotr Graczyk − *Institute of Molecular Physics,, Polish Academy of Sciences, 60-179 Poznań, Poland;* ⊙ orcid.org/0000-0003-1260-9860

Maciej Krawczyk − *Institute of Spintronics and Quantum Information, Faculty of Physics, Adam Mickiewicz University, 61-614 Poznań, Poland;* ⊙ orcid.org/0000-0002-0870-717X

Complete contact information is available at:
https://pubs.acs.org/10.1021/acs.nanolett.3c01592

Notes

The authors declare no competing financial interest.

■ REFERENCES

(1) Hsu, C. W.; Zhen, B.; Stone, A.; Joannopoulos, J.; Soljačić, M. Bound states in the continuum. *Nat. Rev. Mater.* **2016**, *1*, 16048.

(2) von Neumann, J.; Wigner, E. P. *The Collected Works of Eugene Paul Wigner*; Springer: Berlin, Heidelberg, 1993; pp 291−293.

(3) Capasso, F.; Sirtori, C.; Faist, J.; Sivco, D. L.; Chu, S.-N. G.; Cho, A. Y. Observation of an electronic bound state above a potential well. *Nature* **1992**, *358*, 565−567.

(4) Hsu, C. W.; Zhen, B.; Lee, J.; Chua, S.-L.; Johnson, S. G.; Joannopoulos, J. D.; Soljačić, M. Observation of trapped light within the radiation continuum. *Nature* **2013**, *499*, 188−191.

(5) Bykov, D. A.; Bezus, E. A.; Doskolovich, L. L. Bound states in the continuum and strong phase resonances in integrated Gires-Tournois interferometer. *Nanophotonics* **2020**, *9*, 83−92.

(6) Stegeman, G. Normal-mode surface waves in the pseudobranch on the (001) plane of gallium arsenide. *J. Appl. Phys.* **1976**, *47*, 1712−1713.

(7) Aleksandrov, V.; Velichkina, T.; Potapova, J. B.; Yakovlev, I. Mandelstamm-Brillouin studies of peculiarities of the phonon frequency distribution at cubic crystal (001) surfaces. *Phys. Lett. A* **1992**, *171*, 103−106.

(8) Moiseyev, N. *Non-Hermitian Quantum Mechanics*; Cambridge University Press: Cambridge, 2011; p 87.

(9) Kukulin, H. *Krasnopol'sky Theory of Resonances*; Springer: Dordrecht, 1989; p 90.

(10) Tamir, T.; Bertoni, H. Lateral displacement of optical beams at multilayered and periodic structures. *J. Opt. Soc. Am.* **1971**, *61*, 1397−1413.

(11) Wood, R. W. On a remarkable case of uneven distribution of light in a diffraction grating spectrum. *London, Edinburgh, and Dublin Philosophical Magazine and Journal of Science* **1902**, *4*, 396−402.

(12) Hessel, A.; Oliner, A. A new theory of Wood's anomalies on optical gratings. *Appl. Opt.* **1965**, *4*, 1275−1297.

(13) Nikonov, D.; Young, I. Overview of Beyond-CMOS Devices and a Uniform Methodology for Their Benchmarking. *Proceedings of the IEEE* **2013**, *101*, 2498−2533.

(14) Manipatruni, S.; Nikonov, D. E.; Young, I. A. Beyond CMOS computing with spin and polarization. *Nat. Phys.* **2018**, *14*, 338−343.

(15) Csaba, G.; Papp, A.; Porod, W. Perspectives of using spin waves for computing and signal processing. *Phys. Lett. A* **2017**, *381*, 1471−1476.

(16) Chumak, A. V.; et al. Advances in Magnetics Roadmap on Spin-Wave Computing. *IEEE Trans. Magn.* **2022**, *58* (39), 1.

(17) Hoefer, M.; Silva, T. J.; Stiles, M. D. Model for a collimated spin-wave beam generated by a single-layer spin torque nanocontact. *Phys. Rev. B* **2008**, *77*, 144401.

(18) Gruszecki, P.; Kasprzak, M.; Serebryannikov, A. E.; Krawczyk, M.; Śmigaj, W. Microwave excitation of spin wave beams in thin ferromagnetic films. *Sci. Rep.* **2016**, *6*, 1−8.

(19) Heussner, F.; Nabinger, M.; Fischer, T.; Brächer, T.; Serga, A. A.; Hillebrands, B.; Pirro, P. Frequency-Division Multiplexing in Magnonic Logic Networks Based on Caustic-Like Spin-Wave Beams. *physica status solidi (RRL)-Rapid Research Letters* **2018**, *12*, 1800409.

(20) Stigloher, J.; Decker, M.; Körner, H. S.; Tanabe, K.; Moriyama, T.; Taniguchi, T.; Hata, H.; Madami, M.; Gubbiotti, G.; Kobayashi, K.; et al. Snell's law for spin waves. *Phys. Rev. Lett.* **2016**, *117*, 037204.

(21) Hioki, T.; Tsuboi, R.; Johansen, T. H.; Hashimoto, Y.; Saitoh, E. Snell's law for spin waves at a 90° magnetic domain wall. *Appl. Phys. Lett.* **2020**, *116*, 112402.

(22) Yu, W.; Lan, J.; Wu, R.; Xiao, J.; et al. Magnetic Snell's law and spin-wave fiber with Dzyaloshinskii-Moriya interaction. *Phys. Rev. B* **2016**, *94*, 140410.

(23) Gołębiewski, M.; Gruszecki, P.; Krawczyk, M.; Serebryannikov, A. E. Spin-wave Talbot effect in a thin ferromagnetic film. *Phys. Rev. B* **2020**, *102*, 134402.

(24) Gołębiewski, M.; Gruszecki, P.; Krawczyk, M. Self-Imaging Based Programmable Spin-Wave Lookup Tables. *Adv. Electron. Mater.* **2022**, *8*, 2200373.

(25) Mieszczak, S.; Busel, O.; Gruszecki, P.; Kuchko, A. N.; Kłos, J. W.; Krawczyk, M. Anomalous refraction of spin waves as a way to guide signals in curved magnonic multimode waveguides. *Phys. Rev. Appl.* **2020**, *13*, 054038.

(26) Kim, S.-K.; Choi, S.; Lee, K.-S.; Han, D.-S.; Jung, D.-E.; Choi, Y.-S. Negative refraction of dipole-exchange spin waves through a magnetic twin interface in restricted geometry. *Appl. Phys. Lett.* **2008**, *92*, 212501.

(27) Gruszecki, P.; Krawczyk, M. Spin-wave beam propagation in ferromagnetic thin films with graded refractive index: Mirage effect and prospective applications. *Phys. Rev. B* **2018**, *97*, 094424.

(28) Whitehead, N. J.; Horsley, S. A. R.; Philbin, T. G.; Kruglyak, V. V. A Luneburg lens for spin waves. *Appl. Phys. Lett.* **2018**, *113*, 212404.

(29) Whitehead, N.; Horsley, S.; Philbin, T.; Kruglyak, V. Graded index lenses for spin wave steering. *Phys. Rev. B* **2019**, *100*, 094404.

(30) Goos, F.; Hänchen, H. Ein neuer und fundamentaler Versuch zur Totalreflexion. *Ann. Phys. (Berlin, Ger.)* **1947**, *436*, 333−346.

(31) Gruszecki, P.; Romero-Vivas, J.; Dadoenkova, Y. S.; Dadoenkova, N.; Lyubchanskii, I.; Krawczyk, M. Goos-Hänchen effect and bending of spin wave beams in thin magnetic films. *Appl. Phys. Lett.* **2014**, *105*, 242406.

(32) Gruszecki, P.; Dadoenkova, Y. S.; Dadoenkova, N.; Lyubchanskii, I.; Romero-Vivas, J.; Guslienko, K.; Krawczyk, M. Influence of magnetic surface anisotropy on spin wave reflection from the edge of ferromagnetic film. *Phys. Rev. B* **2015**, *92*, 054427.

(33) Stigloher, J.; Taniguchi, T.; Madami, M.; Decker, M.; Körner, H. S.; Moriyama, T.; Gubbiotti, G.; Ono, T.; Back, C. H. Spin-wave wavelength down-conversion at thickness steps. *Appl. Phys. Express* **2018**, *11*, 053002.

(34) Laliena, V.; Campo, J. Magnonic Goos−Hänchen Effect Induced by 1D Solitons. *Adv. Electron. Mater.* **2022**, *8*, 2100782.

(35) Zhen, W.; Deng, D. Giant Goos−Hänchen shift of a reflected spin wave from the ultrathin interface separating two antiferromagnetically coupled ferromagnets. *Opt. Commun.* **2020**, *474*, 126067.

(36) Yang, Y.; Wang, Y.-P.; Rao, J.; Gui, Y.; Yao, B.; Lu, W.; Hu, C.-M. Unconventional singularity in anti-parity-time symmetric cavity magnonics. *Phys. Rev. Lett.* **2020**, *125*, 147202.

(37) Yu, H.; Chen, J.; Cros, V.; Bortolotti, P.; Wang, H.; Guo, C.; Brandl, F.; Heimbach, F.; Han, X.; Anane, A.; et al. Active ferromagnetic metasurface with topologically protected spin texture for spectral filters. *Adv. Funct. Mater.* **2022**, *32*, 2203466.

(38) Kruglyak, V.; Davies, C.; Au, Y.; Mushenok, F.; Hrkac, G.; Whitehead, N.; Horsley, S.; Philbin, T.; Poimanov, V.; Dost, R. et al. *Spin Wave Confinement*, 2nd ed.; Jenny Stanford Publishing: New York, 2017; pp 11−46.

(39) Kruglyak, V. Chiral magnonic resonators: Rediscovering the basic magnetic chirality in magnonics. *Appl. Phys. Lett.* **2021**, *119*, 200502.

(40) Au, Y.; Dvornik, M.; Dmytriiev, O.; Kruglyak, V. Nanoscale spin wave valve and phase shifter. *Appl. Phys. Lett.* **2012**, *100*, 172408.

(41) Au, Y.; Ahmad, E.; Dmytriiev, O.; Dvornik, M.; Davison, T.; Kruglyak, V. Resonant microwave-to-spin-wave transducer. *Appl. Phys. Lett.* **2012**, *100*, 182404.

(42) Al-Wahsh, H.; El Boudouti, E.; Djafari-Rouhani, B.; Akjouj, A.; Mrabti, T.; Dobrzynski, L. Evidence of Fano-like resonances in mono-mode magnetic circuits. *Phys. Rev. B* **2008**, *78*, 075401.

(43) Zhang, Z.; Liu, S.; Wen, T.; Zhang, D.; Jin, L.; Liao, Y.; Tang, X.-L.; Zhong, Z. Bias-free reconfigurable magnonic phase shifter based on a spin-current controlled ferromagnetic resonator. *J. Phys. D: Appl. Phys.* **2020**, *53*, 105002.

(44) Fripp, K.; Shytov, A.; Kruglyak, V. Spin-wave control using dark modes in chiral magnonic resonators. *Phys. Rev. B* **2021**, *104*, 054437.

(45) Sobucki, K.; Śmigaj, W.; Rychly, J.; Krawczyk, M.; Gruszecki, P. Resonant subwavelength control of the phase of spin waves reflected from a Gires−Tournois interferometer. *Sci. Rep.* **2021**, *11*, 1−12.

(46) Sobucki, K.; Gruszecki, P.; Rychly, J.; Krawczyk, M. Control of the phase of reflected spin-waves from magnonic Gires-Tournois interferometer of subwavelength width. *IEEE Trans. Magn.* **2022**, *58*, 1−5.

(47) Śmigaj, W.; Sobucki, K.; Gruszecki, P.; Krawczyk, M. Modal approach to modeling spin wave scattering. *Phys. Rev. B* **2023**, *108*, 014418.

(48) Qin, H.; Holländer, R. B.; Flajšman, L.; Hermann, F.; Dreyer, R.; Woltersdorf, G.; van Dijken, S. Nanoscale magnonic Fabry-Pérot resonator for low-loss spin-wave manipulation. *Nat. Commun.* **2021**, *12*, 2293.

(49) Talapatra, A.; Qin, H.; Schulz, F.; Yao, L.; Flajšman, L.; Weigand, M.; Wintz, S.; van Dijken, S. Imaging of short-wavelength spin waves in a nanometer-thick YIG/Co bilayer. *Appl. Phys. Lett.* **2023**, *122*, 202404.

(50) Aquino, H. R. O.; Connelly, D.; Orlov, A.; Chisum, J.; Bernstein, G. H.; Porod, W. Short-Wavelength Spin-Wave Transducer Using the Transmission of Spin-Waves Across Two Magnetic Films. *IEEE Trans. Magn.* **2023**, *59*, 1−8.

(51) Vansteenkiste, A.; Leliaert, J.; Dvornik, M.; Helsen, M.; Garcia-Sanchez, F.; Van Waeyenberge, B. The design and verification of MuMax3. *AIP Adv.* **2014**, *4*, 107133.

(52) Kalinikos, B.; Slavin, A. Theory of dipole-exchange spin wave spectrum for ferromagnetic films with mixed exchange boundary conditions. *Journal of Physics C: Solid State Physics* **1986**, *19*, 7013.

(53) Dong, S.; Zhang, Q.; Cao, G.; Ni, J.; Shi, T.; Li, S.; Duan, J.; Wang, J.; Li, Y.; Sun, S.; et al. On-chip trans-dimensional plasmonic router. *Nanophotonics* **2020**, *9*, 3357−3365.

Magnon-optic effects with spin-wave leaky modes: tunable Goos-Hänchen shift and Wood's anomaly

Krzysztof Sobucki,[1, *] Wojciech Śmigaj,[2] Piotr Graczyk,[3] Maciej Krawczyk,[1] and Paweł Gruszecki[1, †]

[1]*Faculty of Physics, Adam Mickiewicz University,*
Uniwersytetu Poznańskiego 2, 61-614 Poznań, Poland
[2]*Met Office, FitzRoy Rd, Exeter, EX1 3PB, UK*
[3]*Institute of Molecular Physics, Polish Academy of Sciences,*
Mariana Smoluchowskiego 17, 60-179 Poznań, Poland

I. SUPPLEMENTARY MATERIALS

1. Numerical methods

To perform numerical simulations, we employ the open-source environment Mumax3 [1]. This environment solves Landau-Lifshitz-Gilbert equation using the finite-difference method in the time domain. The simulated system has dimensions 12.7 µm, 10.2 µm and 15 nm (along the x, y, z axis, respectively). We discretize the simulated domain with a regular mesh of unit cell $5 \times 5 \times 5$ nm^3 (along the x, y, z axes). In order to simulate an infinitely long system in y-axis and half-infinite system along the x-axis, we impose at all edges of the system except the one where the stripe is located, absorbing regions where the damping constant α increases quadratically to the value $\alpha_{\text{edge}} = 0.5$ at length of $L = 625$ nm.

We perform three types of simulations:

- calculations of the dispersion relation of the system for different values of stripe's M_{S},

- calculations of the steady-state for oblique incidence of continuously emitted spin-wave (SW) beam,

- reflection of a wave-packet with step-by-step observation of SWs reflection from the bilayer interface.

2. Dispersion relation computations

To accelerate dispersion relation computation for SWs propagating along the stripe, we perform simulations for a narrower system of width 1270 nm along the x-axis since, as we verified, it provides exactly the same results as simulations for the system of widths 12.7 µm. In this type of simulations, we place the SW source in the stripe parallel to the x-axis in the central part of the stripe. To excite SWs for all wavevectors up to the cut-off wavevector $k_{\text{cut}} = 150$ rad/µm and frequencies up to the cut-off frequency $f_{\text{cut}} = 20$ GHz, we use the following spatial and temporal distribution of the microwave field being linearly polarized along the z-axis

$$
h_z(t; x, y) = h_0 \text{sinc}(k_{\text{cut}} y) \text{sinc}(2\pi f_{\text{cut}}(t - 8/f_{\text{cut}})
$$
$$
\times \sum_{n=0}^{N} \left[\cos(2\pi n \ x/w) + \sin(2\pi n x/w) \right], \tag{S1}
$$

where the summation of n is used to increase the efficiency of the higher order modes excitation (we assume $N = 5$). We use the time sampling $t_{\text{sampl}} = (2.2 f_{\text{cut}})^{-1}$ and save first 1000 snapshots of the system's response to the microwave excitation. To obtain the dispersion relation $D(f, k_y)$ we employ following formula

$$
D(f, k_y) = \langle |F_{t,y}\{m_x(t, y, x)\}| \rangle_{x \in \langle 0, w \rangle}, \tag{S2}
$$

where $F_{t,y}$ is the two-dimensional (t, y) fast Fourier transform (FFT), $m_{\text{x}}(t, y, x)$ is the magnetic response taken only from the stripe. The absolute value of the outcome of FFT ($|F_{t,y}\{m_x(t, y, x)\}|$) is a space-averaged along resonator's width $x \in \langle 0, w \rangle$ and represents $D(f, k_y)$.

———

* krzsob@st.amu.edu.pl
† gruszecki@amu.edu.pl

The results of the dispersion relation calculations for different values of stripe M_S are compiled into a short video that can be found in supplementary materials, Movie S3. With an increase in the value of M_S, the positions and shape of the dispersion relation bands change. For easier analysis, the dashed lines indicate the parameters of the SW beam excited in the simulations. We show in the video that only in a specific range of M_S values, the bands cross the lines that represent the parameters of the incident SW beam. We interpret this range of M_S as a region of efficient SW excitation in the magnetic stripe.

3. Steady-state simulations

In order to excite SW beam, we use microwave magnetic field located at the left upper quarter of the layer. The spatial distribution of the dynamic magnetic field is in the rotated coordinate system (x', y') by 45° with respect to the y-axis. The spatio-temporal function of the dynamic magnetic field is given by a formula

$$
\begin{aligned}
B_{\text{ext},x}(t, x', y') &= A(1 - e^{-0.2\pi f_0 t})R(x')G(y') \\
&\times [\sin(k_0 x')\sin(2\pi f_0 t) + \cos(k_0 x')\cos(2\pi f_0 t)],
\end{aligned}
\tag{S3}
$$

where $A = 0.1B_0$ is the amplitude of the dynamic field (B_0 is the external magnetic field set along the system's y-axis of magnitude $B_0 = 0.01$ T), $R(x') = \Theta(-x' + \frac{w_a}{2})\Theta(x' + \frac{w_a}{2})$ is a rectangle function, which describes antenna's shape along its x' coordinate (Θ is Heaviside step function, antenna's width $w_a = 30$ nm), $G(y') = \exp(-\frac{y'^2}{4\sigma_y^2})$ is a Gaussian function defining antenna's shape along the y'-axis ($\sigma_y = 330$ nm), $k_0 = 60.96 \frac{\text{rad}}{\mu\text{m}}$ is the wavevector and $f_0 = 17.4$ GHz is the frequency of the excited SWs. Eq. (S3) enables unidirectional emission of SWs[2]. We use the antenna to constantly emit the SW beam for 41 ns, after this time the system reaches the steady-state. Subsequently, we store time and space dependence of magnetization distribution for one period of SWs excitation in form of 25 snapshots of magnetization distribution in the system with a sampling interval $1/(25f_0)$.

The stored magnetization dependence on time in the steady-state can be converted into complex SW amplitude distribution at frequency f_0. It simplifies the analysis of the SW amplitude and phase. To make such a conversion, we calculate pointwise FFT over time and select results only for f_0.

4. Simulations of the reflection of wave-packet

To simulate the wave-packet reflection, we use the same spatial distribution of the dynamic magnetic field as in Eq. (S3). However, the time dependence of the formula is multiplied by the Gaussian envelope described by the expression $\exp(-(\frac{t}{2\sigma_f})^2)$, with $\sigma_f = 0.05f_0$. It provides the packet with full width at half maximum (FWHM) in the time domain of 0.5 ns. As the result of the simulations, we save 250 snapshots of the propagating wave-packet with a time step of 0.057 ns. The results of simulations with stripe's $M_S = \{350, 550\}$ kA/m are compiled into short movies that can be found in supplementary materials, Movies S4 and S5. In the movie for the $M_S = 350$ kA/m stripe, the packet is reflected from the interface without any substantial excitation of the SWs in the stripe. However, in the movie with the $M_S = 550$ kA/m stripe, the excitation of the SWs in the stripe is evident. The mode formed in the stripe propagates along the stripe, and the re-emission of additional SWs to the layer is visible in the magnification.

5. Influence of the beam width on excitation of modes in the stripe

We check the influence of the beam width on excitation of the modes in stripe for $M_S = 460$ kA/m as for this value of M_S for a beam with FWHM = 775 nm, used in the main simulations, we observe the beginning of stripe's mode excitation. We perform series of simulations with beam of varying FWHM. In Fig. S1 we show the results of simulations for beams with FWHM = $\{517, 775.5, 1551\}$ nm. In Figs. S1(a,b) we present SW intensity distributions in the layer for two beams with FWHM = 517 nm (a) and FWHM = 1551 nm (b). In Fig. S1(a) with the narrow beam several reflected beams are evident. Their number is bigger than we presented in the main body of the paper. Conversely for a wide beam, as in Fig. S1(b), no reflected beam stratification is visible. For easier analysis in Fig. S1(c) we provide a plot with cutlines through SW intensity distributions for different SW beams, the cutlines are marked with red dashed lines in Figs. S1 (a,b). The result of the narrowest beam is presented with the orange line. In this case the amplitude of the primary beam is the smallest but a phalanx of additional reflected beams are well visible. The results for the widest beam is shown with red line, here the reflected beam has regular Gaussian envelope and no additional reflected beams are visible. The green line presents the results for the beam with FWHM = 775.5 nm,
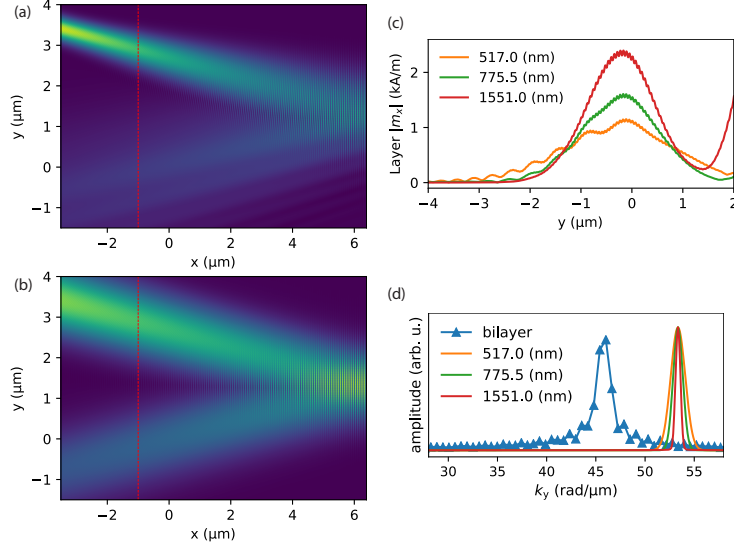
FIG. S1. Beam width sweep. (a) SW intensity distribution in the layer with SW beam with FWHM 517 nm at the antenna. (b) SW intensity distribution in the layer with SW beam with FWHM 1551 nm at the antenna. (c) Comparision between SW intensity cutlines (marked with red dashed lines in (a,b)) for SW beam with FWHM $517, 775.5$ and 1551 nm (orange, green and red lines respectively). The increase of the amplitude for the red line at $y > 1.5$ µm is caused by the widened incident beam. (d) Overlap of the beams width in the inverse space with the system's dispersion relation at $f = 17.4$ GHz (blue line).

used in the main simulations. This case is intermediary between previously presented narrow and wide beams. The secondary reflected beams are present although there are not as distinctive as in the case of the narrowest beam.

We propose following explanation to the fact that narrow SW beam is able to excite the resonator's mode more efficiently than a wide beam. We bind the efficiency of mode excitation with an overlap between the beam's dispersion relation and the bilayer's dispersion relation. In Fig. S1(d) we show the cutlines through bilayer's dispersion relation at frequency $f = 17.4$ GHz and dispersion relations of the beams. The dispersion relations of the beams are presented as Gaussian curves, which centres are calculated from the Kalinikos-Slavin formula [3], and their widths are obtained by calculating beam's widths in the reciprocal space. It is evident that the narrowest beam has the biggest width in the reciprocal space and because of that has the biggest overlap with bilayer's dispersion relation. Such a situation leads to more efficient coupling between the beam and the bilayer than in any other case presented in this analysis. Thus, the narrower beams have possibility to excite resonator's mode more efficiently in our system. The analysis presented here is more qualitative rather than quantitative as the beams widen during their propagation and during reflections have bigger FWHM than at the antenna. Thus the overlap of dispersion relation at the reflection is even smaller than presented in Fig. S1(d). However, the ratio between the overlap and the width of particular beam is the same as presented, so our explanation is justified.

6. Results of comparision with Tamir-Bertoni model

In this section we compare the results of our simulations with an analytical model proposed by Tamir and Bertoni[4] in more detail. Tamir and Bertoni showed that an incident beam of light is able to excite a leaky mode (LM) at the edge of the system. The excited edge mode propagates along the edge and emits waves back to the system. As our findings are a close analog to Tamir-Bertoni model but in the realm of magnonics, we try to apply Tamir-Bertoni mathematical description to our simulation's results. Tamir and Bertoni proposed the reflectance coefficient in the form of $\rho(k_y) = e^{i\Delta}(k_y - k_p^*)/(k_y - k_p)$, where $k_p = \kappa + i\nu$ is a complex wave vector of the LM. They solved the system analytically under assumptions of well collimated beam incident and an angle of perfect coupling between the beam and edge mode. Additionally they also assumed that only the first pole in reflectance coefficient $\rho(k_y)$ provides a substantial input to the calculations. Their formula of the reflected light amplitude has two components which
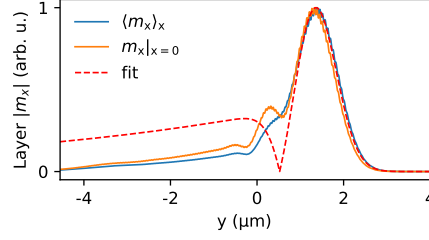
4

FIG. S2. Comparision between simulation results (blue line mean values of SW intensity in the layer under the stripe, orange line SW intensity cutline in the layer under the left edge of the stripe) and Tamir's model numerical fit (red dashed line) to the SW intensity mean value.

describe the primary E_0 and the secondary beam E_1

$$E_{\text{refl}} = E_0 + E_1,$$
$$E_0 = Ae^{-((y-y_0)/w_b)^2}, \tag{S4}$$
$$E_1 = -E_0(2 - \pi^{\frac{1}{2}}\nu w_b e^{(\gamma')^2}\text{erfc}(\gamma')),$$

where A is the amplitude of the primary beam, y_0 is the centre of primary beam, w_b is the width of beam at $\frac{1}{e}$ of its amplitude, ν is the imaginary part of the LM wave-vector, γ' is a new coordinate system defined for the secondary beam as $\gamma' = \frac{\nu w_b}{2} - \frac{y-y_0}{w_b}$ and erfc is the Gauss error function.

In Fig. (S2) we present a numerical fit of Eq. (S4) to the simulation data. The blue line in Fig. (S2) shows the mean value of SW intensity averaged in the volume of the layer directly under the stripe. The dashed red line is the numerical fit to this data. It is evident that the analytical model provided by Tamir and Bertoni agrees only qualitatively with the results of our simulation. Namely, Tamir-Bertoni model describes properly the primary beam in our simulations but fails to precisely fit to the secondary beam. In this case analytical model only indicates separation between the primary and secondary reflected beams. However, it does not recreate the shape of secondary beam, it only shows a long tail of nonzero amplitude left to the primary beam. We see a several reasons why Tamir-Bertoni model does not work properly with our simulation's results. Firstly, Tamir-Bertoni model was developed for the light beam, which physics is governed by Helmholtz equation, while in our case we deal with SWs that are described by Landau-Lifshitz equation. Secondly, in Tamir-Bertoni model the edge of the system is infinitely narrow but in our simulations we regard the bilayer with finite width as an edge. We show the difference between the approach of wide and narrow edges in Fig. (S2). Here, the blue line describes average SW intensity under the stripe and the orange line is a cutline through SW intensity in the layer under the left edge of the stripe. The results of the edge cutline have more distinctive peaks with bigger amplitudes nevetherless in our calculations we have to choose the average values of SW intensity to take into account contribution from whole bilayer width. At last Tamir-Bertoni model is based on several assumptions, such as choosing an optimal incident beam angle to couple with the edge mode, that are not met in our numerical simulations. We did not look for the ideal conditions for the SW beam incident in our simulations as their are impractical in designing experiments to confirm our numerical findings.

7. Influence of stripe's width on reflection

We explored new resonances cases by performing simulations with fixed material parameters but with varying resonator's width. We chose $M_S = 550$ kA/m value as in the paper's main body which corresponds to the case with the most pronounced spread among the secondary beams. Then we run several simulations with stripes of widths w in a range from 100 nm to 205 nm. In Fig. S3(a) we present the SW intensity density in the stripe as a function of stripe's width (the values in the plot are normalised to the highest value for $w = 155$ nm). In Fig. S3(a) we can see several peaks for certain values of $w = \{110, 135, 155, 175, 200\}$ nm. For each of these cases there is an excitation of LM in the stripe and creation of the secondary beams in the layer below the stripe, Fig. S3(b-d). Thus we prove that the resonance conditions in described system can be also achieved by changing other parameters of the system than its material parameters.
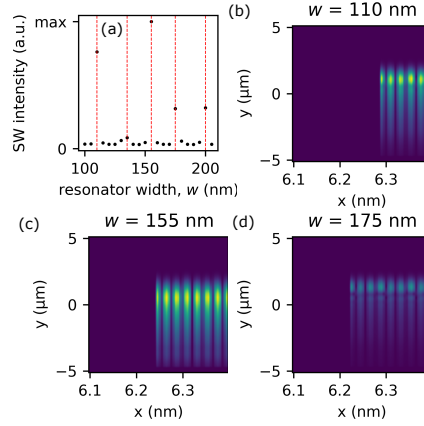
FIG. S3. (a) Intensity of SW in the stripe as a function of stripe's width. (b-d) Visualisations of the modes excited in the stripe for different values of stripe's width as SW intensity distribution, (b) width 110 nm, (c) width 155 nm, (d) width 175 nm. All (b-d) figures have the same colour scale normalized to the highest value in case 155 nm (c).

8. Influence of SW frequency on reflection

We obtain parameters of the reflected beams by fitting a sum of Gaussian functions to the cutline through SW intensity distribution in the far-field. The far-field is defined at $x = -7.5$ µm and is indicated with a red dashed line in Figs. S1(a,b). We present our method of calculating reflected beams parameters in Fig. S4, where the blue solid line shows the simulation results, the dashed lines indicate component Gaussian functions and the orange solid line is the sum of all Gaussian curves in a given case. In the ranges of stripe's M_S when LM starts and ends to be excited the beams in the far-field strongly overlap as we show in Figs. S4(a,c) where $M_S = 475$ kA/m and $M_S = 615$ kA/m. In these cases we need to use a sum of six Gaussian functions to precisely fit our function to the simulation results. For the stripe's M_S values between these regions three distinctive beams and a range with plane waves are visible in the far-field as shown in Fig. S4(b) for $M_S = 550$ kA/m. Hence, we use as a fitting function the sum of four Gaussian curves only in this range of M_S (three to describe the beams and one to describe the plane waves).

In Fig. S5 we plot amplitudes and positions of the primary and secondary beams in the far-field as functions of stripe's M_S. The blue colour represents parameters of the primary beams and the red colour depicts the secondary beam. Additionally in Fig. S5 we also confront the results for simulations with different frequencies, namely the dots show results for $f = 17.3$ GHz and the diamonds represent the results for $f = 17.4$ GHz. The change in frequency affects overlap between dispersion relations of the SW beam and the bilayer thus changing the excitation properties of LM in the stripe. We chose only a small change in frequency to avoid bigger change of SW wavelength which would affect the wavelength-discretization ratio in the numerical simulations. The change of frequency in the system affects the amplitudes of reflected beams as presented in Fig. S5(a). The increase of frequency to $f = 17.4$ GHz leads to increase of the primary beam's amplitude, compare blue dots and diamonds, and decrease of the secondary beam's amplitudes, compare red dots and diamonds. The same increase of frequency affect the spatial shift of the primary beam only slightly, as shown in Fig. S5(b) with blue dots and diamonds. However, the frequency increase causes substantial increase in spatial shift of the secondary beam, shown with red dots and diamonds. For $f = 17.4$ GHz the maximal shift of the secondary beam is equal to -1.6 µm and it is 0.35 µm bigger than spatial shift calculated for $f = 17.3$ GHz and the same value of stripe's M_S.

9. Movie S1–steady-state with a sweep over resonator's M_S value

The movie. S1 represents the colourmaps of the distribution of $|m_x|$ at frequency $f = 17.4$ GHz as the dependence of the stripe's value of M_S similarly as displayed in Fig. 2(a,b). You can see that the distribution of $|m_x|$ is strongly affected by M_S and 3-6 reflected parallel laterally shifted beams can be seen depending on the M_S value.
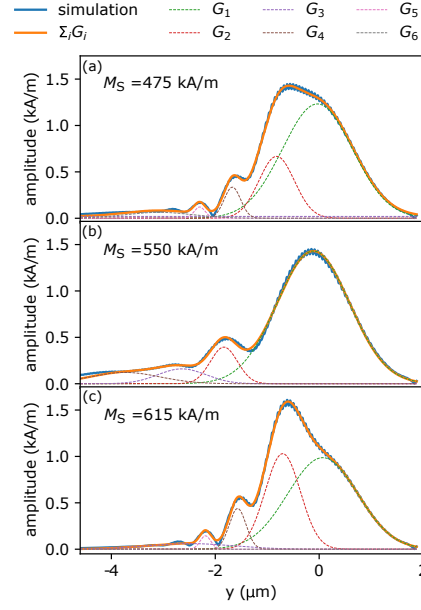
FIG. S4. Calculating parameters of the reflected beams by fitting Gaussian curves in the far-field marked in Fig. S1 with dashed-red line. (a) Fitting a sum of six Gaussian curves to the simulation results for resonator $M_S = 475$ kA/m. (b) Fitting a sum of four Gaussian curves to the simulation results for resonator $M_S = 550$ kA/m. (c) Fitting a sum of six Gaussian curves to the simulation results for resonator $M_S = 615$ kA/m.
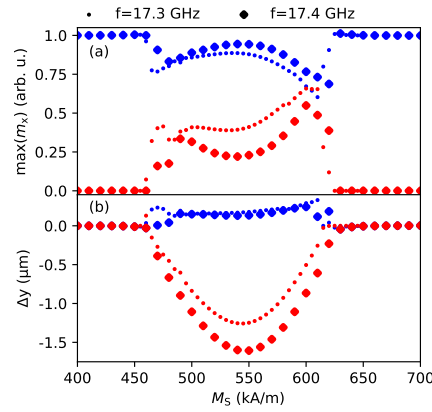
FIG. S5. Parameters of the reflected beams in simulations with different SW frequencies. (a) Amplitudes of the primary (blue) and the secondary (red) beams calculated by fitting Gaussian functions to simulation data, cf. S4, dots represent results for frequency $f = 17.3$ GHz, diamonds represent results for $f = 17.4$ GHz. (b) Positions of the primary (blue) and the secondary (red) beams calculated by fitting Gaussian functions to simulation data, symbols as represent frequencies as in (a).

10. Movie S2–steady-state with a sweep over frequency

The movie. S2 depicts the colourmaps of the distribution of $|m_x|$ as the dependence on the value of frequency for resonator with $M_S = 550$ kA/m. We assume frequencies in the range from 17.0 to 18.0 GHz. Although, it is a narrow range, we can see that m_x distribution changes significantly. While entering the resonance multiple reflected beams emerges and than again disappears. It is very similar result as for the sweep over resonator's M_S.

11. Movie S3–dispersion relation dependence on resonator's M_S

The movie. S3 depicts how the dispersion relation in the stripe depends on the value of stripe's M_S. For the values of M_S from 420 kA/m to 650 kA/m we can see the crossing at $f = 17.4$ GHz and $k_y = -53.5$ $\frac{\text{rad}}{\mu\text{m}}$ of the dispersion relation plotted for the stripe (colourmap in the background) and the dispersion plotted for SWs propagating in the layer with $\varphi = 45°$ (bold black line). For this particular band crossing in the dispersion for SWs in the layer, at the considered M_S range, the decrease in exchange energy is compensated by an increase of the magnetostatic energy. Namely, the exchange energy is proportional to M_S^{-1}, while the magnetostatic energy is proportional to M_S. It explains the origin of the broad range of M_S showed in Fig. 4 in the main part of the manuscript where the resonance condition are fulfilled.

12. Movies S4-S5–reflection of wavepackets for different M_S

The movie. S4 shows the reflection of wavepacket from the resonant-stripe element in case of stripe $M_S = 350$ kA/m. In Movie. S4 the antenna in simulation has width $w_a = 200$ nm. The movie. S5 shows SWs wavepacket reflection in case of stripe's $M_S = 550$ kA/m. Comparing the results of wavepacket simulations for cases $M_S = 350$ kA/m and $M_S = 550$ kA/m it is evident that for latter the excitation of the SWs in the stripe is much more efficient. Without the constant SWs pumping by the SWs beam we can see propagation of a mode in the stripe as an obliquely bouncing between stripe's edges and reemition of SWs back to the layer clearly. Interestingly, in $M_S = 350$ kA/m stripe case we still are able to see excitation of a mode in the stripe and the SWs reemition, however with much smaller magnitude comparing to the case with $M_S = 550$ kA/m stripe. We explain this particular result by pointing that a SW wavepacket contains a range of frequencies described by a gaussian curve in our case centred at $f_0 = 17.4$ GHz with FWHM ≈ 2 GHz. It means that the part of wavepacket spectrum still overlaps with the frequencies of resonant-stripe element's modes. This effect has small magnitude and is therefore virtually invisible in simulation results with continuous SW beam excitation.

---

[1] A. Vansteenkiste, J. Leliaert, M. Dvornik, M. Helsen, F. Garcia-Sanchez, and B. Van Waeyenberge, The design and verification of mumax3, AIP Adv. **4**, 107133 (2014).

[2] N. Whitehead, S. Horsley, T. Philbin, and V. Kruglyak, Graded index lenses for spin wave steering, Phy. Rev. B **100**, 094404 (2019).

[3] B. Kalinikos and A. Slavin, Theory of dipole-exchange spin wave spectrum for ferromagnetic films with mixed exchange boundary conditions, Journal of Physics C: Solid State Physics **19**, 7013 (1986).

[4] T. Tamir and H. Bertoni, Lateral displacement of optical beams at multilayered and periodic structures, J. Opt. Soc. A **61**, 1397 (1971).

5.6 Goos-Hänchen-like shift of inelastically scattered spin-wave beams

In this paper, the inelastic scattering process of SW beams on edge-localised SW mode is presented. The result of the inelastic scattering is creation of new SWs with frequencies that are linear combinations of the incident SW beam and edge-mode frequencies. The main focus was put on two processes, namely, stimulated splitting and confluence processes, which produce new SWs whose frequency is lowered and increased, respectively. It was shown that scattered SWs take a form of beams and undergo lateral shift at the interface analogous to the Goos-Hänchen effect. The paper presents several different cases of SW scattering with different angles of SW beam incidence and edge modes propagating in different directions. Additionally, it was shown that in certain cases a cascade of non-linear processes happens which results in creation of SW plane waves propagating away from the interface behind the SW beam incidence point. Moreover, the cascade process is accompanied by a noticeable increase of lateral shift of the scattered SW beam in the confluence process.

The Author contributed to this paper by carrying out all of the micromagnetic simulations using the MuMax3 environment and analysing the results of simulations. The Author drafted the manuscript, excluding the introduction, and prepared all the figures in the paper. The Author prepared the responses to the reviews which required performing additional simulations. The Author also managed the correspondence with journal throughout publication process.

---

scientific reports

Check for updates

OPEN

Goos–Hänchen shift of inelastically scattered spin-wave beams and cascade nonlinear magnon processes

Krzysztof Sobucki[1✉], Igor Lyubchanskii[2], Maciej Krawczyk[1] & Paweł Gruszecki[1]

We study, using micromagnetic simulations, the inelastic scattering of spin-wave beams on edge-localized spin-wave modes in a thin ferromagnetic film. In the splitting and confluence processes, the new spin-wave beams are generated with frequencies shifted by the edge-mode frequency. We report that inelastically scattered spin-wave beams in both processes not only change their direction of propagation but also undergo lateral shifts along the interface, analogous to the Goos–Hänchen effect known in optics. These shifts of inelastically scattered beams, for a few special cases described in the paper, can be in the range of several wavelengths, which is larger than the Goos–Hänchen shift of elastically reflected beam. Unexpectedly, at selected frequencies, we found a significant increase in the value of the lateral shifts of the scattered spin-wave beams formed in the confluence process. We show that this effect is associated with the cascading nonlinear processes taking place at the edge of the film and involving the primary edge spin wave. Our results make an important contribution to the understanding of the nonlinear nature of spin waves and provide a way to exploit it in signal processing with magnons.

Spin waves (SWs), propagating precessional magnetization disturbances, are a promising candidate for information carriers, especially in the context of their applications in beyond-CMOS[1] and artificial neural networks[2,3]. One of the SWs advantages is their intrinsic nonlinearity, a key element for their advanced applications such as neuromorphic computing[4,5]. Another advantage is the possibility of the SWs confinement in a small part of a magnetic material allowing for the large miniaturization of the magnonic devices. For instance, SWs may be confined in a nanoscale-wide potential well induced by the static demagnetization field near the layer's edge[6–9]. Such edge-localized SW modes are called edge SWs or edge modes, and usually, their frequencies are lower compared with the SWs propagating outside of the well. Recently, there has been considerable attention devoted to the research on inelastic scattering of SWs on localized modes, mostly to obtain frequency combs[10–13], but also for other applications, like sensing[14] or SW demultiplexing[15]. Several spatially localized modes on which propagating SWs are inelastically scattered have been considered. These include, nonlinear scattering on the skyrmion gyrotropic mode[11,16,17], azimuthal SWs in vortex[13,18–20], domain wall mode[12,21,22], and the SW edge mode[15]. In the last case, the inelastic scattering of an obliquely incident SW beam of frequency f at the edge of a Permalloy (Py) thin film on a propagating SW edge mode of frequency ν results in two primary three-magnon processes, i.e., stimulated splitting process[23–25] (SSP) and confluence process[23,24] (CP). CP causes two modes at frequencies f and ν to merge (confluence) into a new SW at frequency $f + \nu$. On the other hand, SSP causes the splitting of the mode at frequency f into two modes at frequencies $f - \nu$ and ν with the assistance of the edge mode at frequency ν, which stimulates this process and increases the intensity of the new waves. It has been shown that SSP could be used to realize the magnon-based transistor[26], while both SSP and CP could be used for demultiplexing[15]. In the second example, the scattered SW beams created in nonlinear processes propagate under different angles compared to the reflected SW beam and the angles of propagation depend on the edge mode frequency ν. The mechanism of this phenomenon was explained by employing the isofrequency contours analysis and conservation of the tangential component of beam wavevectors[27,28].

The reflection of the wave beam from the edge of the material is in some cases associated with non-specular behavior well-known as the Goose-Hänchen (GH) effect as first predicted, observed and described in optics[29–32] and manifests itself as a spatial shift of a totally internally reflected light beam along the interface.

[1]Institute of Spintronics and Quantum Information, Faculty of Physics, Adam Mickiewicz University, Uniwersytetu Poznańskiego 2, 61-614 Poznań, Poland. [2] in association with Adam Mickiewicz University, Poznan, Poland. ✉email: krzsob@amu.edu.pl

The origin of this effect is the phase acquisition of the waves during reflection. In optical experiments, the GH shift ranges from a few nanometers (fractions of light wavelengths) up to a few micrometers[33–36]. In magnetic materials the magneto-optical GH effect was theoretically studied in Refs.[37–41] and experimentally observed for BK7 prism/Fe/Au[42] and Ni-based magneto-plasmonic crystals[43]. Since the GH effect is due to the wave nature, the analogous effect has been observed for different types of waves. For instance, the GH effect has been confirmed for plasmons[44–46], electrons[47], neutrons[48], seismic waves[49] and SWs[50–55]. Theoretical predictions have recently shown that an analogous phenomenon to the GH shift can also be found for inelastically scattered electromagnetic waves during Brillouin scattering on phonons[56]. However, to date, there has been no report on the GH effect of the inelastically scattered SWs.

In this paper, we report the GH shift for the SW beam that is inelastically scattered on the propagating edge mode. We numerically demonstrate this effect in an in-plane magnetized thin Py film for the beams generated in the SSP and CP processes taking place at the very edge of the film. We show that the edge mode frequency and wavevector, as well as the angle of propagation of the incident SW beam, affect the GH shift. Unexpectedly, we found a significant enhancement of the GH shift of the SW beam generated in the CP process at a certain frequency of the edge mode. We show that this effect is related to the cascade of three nonlinear processes involving the edge mode and generated high-frequency SW leaky waves propagating into the film. These results demonstrate new effects in magnonics and provide a basis for unexplored methods of SW beam control in thin ferromagnetic films, which can be exploited for practical applications in magnonic technology for high-frequency and low-energy computing systems.

Results

We analyze the dynamics of SWs in a 10 nm thick Py layer using micromagnetic simulations performed in the Mumax3 environment[57]. We use typical material parameters of Py ($Ni_{80}Fe_{20}$), namely $M_S = 800$ kA/m, $A_{ex} = 13$ pJ/m, but with reduced damping parameter $\alpha = 0.0001$ for easier analysis of SW propagation in the far field. The layer is semi-infinite, i.e., it has only one sharp edge and is nominally infinite in all other in-plane directions, Fig. 1(a). The external uniform magnetic field $B_0 = \mu_0 H_0 = 300$ mT is applied perpendicular to the layer's edge, $H_0 = H_0\hat{y}$, which induces a demagnetizing field on the edge that locally lowers the effective static field, Fig. 1(b). This non-uniformity serves as a potential well in which the SW-localized mode can be confined[9,58,59]. Accordingly, the dispersion relation shown in Fig. 1(c) consists of a part representing a continuum of SWs freely propagating far from the interface and a distinct band representing the edge mode with frequencies downshifted with respect to the SW continuum. The gap between the modes is from 11 GHz to 15.5 GHz at wavenumber $k_x = 0$. This implies that in this frequency range, the propagating SWs are confined to the system's edge. This situation provides us with a straightforward way to excite only edge modes at low frequencies and to study the inelastic scattering of higher frequency SWs incident from the thin layer on the layer edge.

We study the inelastic scattering of a SW beam of frequency 45 GHz (corresponding to the wavelength of 35.7 nm), full width at half maximum 760 nm, incident obliquely at the edge where an edge mode of frequency ν is localized. Throughout the paper, the frequency of the SW edge mode is kept below the bottom of the SW continuum, 15.5 GHz, so the edge mode cannot leak the energy to the bulk of the Py layer. We place two antennas, which emit local oscillating magnetic fields to excite both types of SWs (see yellow stripes in Fig. 1a). The first antenna is placed at the very edge of the system and is responsible for exciting edge mode with frequency ν. The second antenna is placed about 3.84 μm from the edge and excites the SW beam with frequency $f = 45$ GHz. The second antenna excites unidirectionally propagating SW beam towards the edge[60,61] at a specific angle of incidence (angle between the wavevector of incident SW beam and the normal to the interface, i.e., the y-axis). More details are given in the "Methods" section.

In the numerical simulations, we change three parameters, the angle of SW beam incidence θ and edge mode frequency (which also changes the wavenumber of the edge mode κ), and the sign of κ. The angle of incidence is controlled by the orientation of the antenna relative to the edge of the layer. We use the following set of angles $\theta = \{30°, 32.5°, 35°, 37.5°, 40°, 45°\}$. We choose the sign of the edge mode wavevector by changing the position of the edge antenna with respect to the incident beam spot at the edge. If the edge antenna is placed to the left of the incident SW beam spot, the edge mode wavevector κ is positive. If the antenna is to the right, κ is negative. For each configuration with the chosen θ and sign of κ, we run a series of simulations with different edge mode frequencies. These frequencies are in the range of $\nu \in \langle 11, 15.5 \rangle$ GHz.

Figue 1d shows the SW spectrum of the system obtained in the steady state in the case of $f = 45$ GHz, $\nu = 12.5$ GHz, $\kappa > 0$, $\theta = 30°$. We display the maxima of the m_z magnetization component at a given frequency, calculated with Fourier transform. Two peaks highlighted in blue correspond to the frequency of SW beam f and its second harmonics. Several peaks highlighted in red represent the edge mode ν and its higher harmonics[9]. Two peaks of the main interest are marked with green and purple colors. These correspond to the frequencies of SSP $f - \nu$ and CP $f + \nu$ respectively, which confirms the existence of these phenomena in the studied system. We focus on these waves throughout the paper. Apart from the mentioned peaks, we also see several other peaks at frequencies corresponding to higher-order nonlinear processes (e.g. $f - 2\nu = 20$ GHz). These are beyond the scope of this paper and will be omitted in further analysis.

For edge modes propagating to the right (i.e., $\kappa > 0$), the angles of the group velocity of the inelastically scattered beams incident at $\theta = 30°$ change monotonically with the change of ν, see Fig. 2a (green circles and purple squares). Later in the text, we call the angle of the group velocity Θ_i as the angle of propagation. The angle of propagation of the beam generated in SSP (green circles) decreases monotonically with increasing ν, and changes by $17°$ in the examined range of ν. The changes for the CP beams (purple squares) are opposite to SSP. Here the angle increases with increasing ν, and in the investigated range of ν the angle changes by $10°$. The results for other angles of propagation of the incident SW beams are qualitatively the same. These changes in the angle of the propagation of inelastically scattered beams can be explained using isofrequency contour analysis[15].
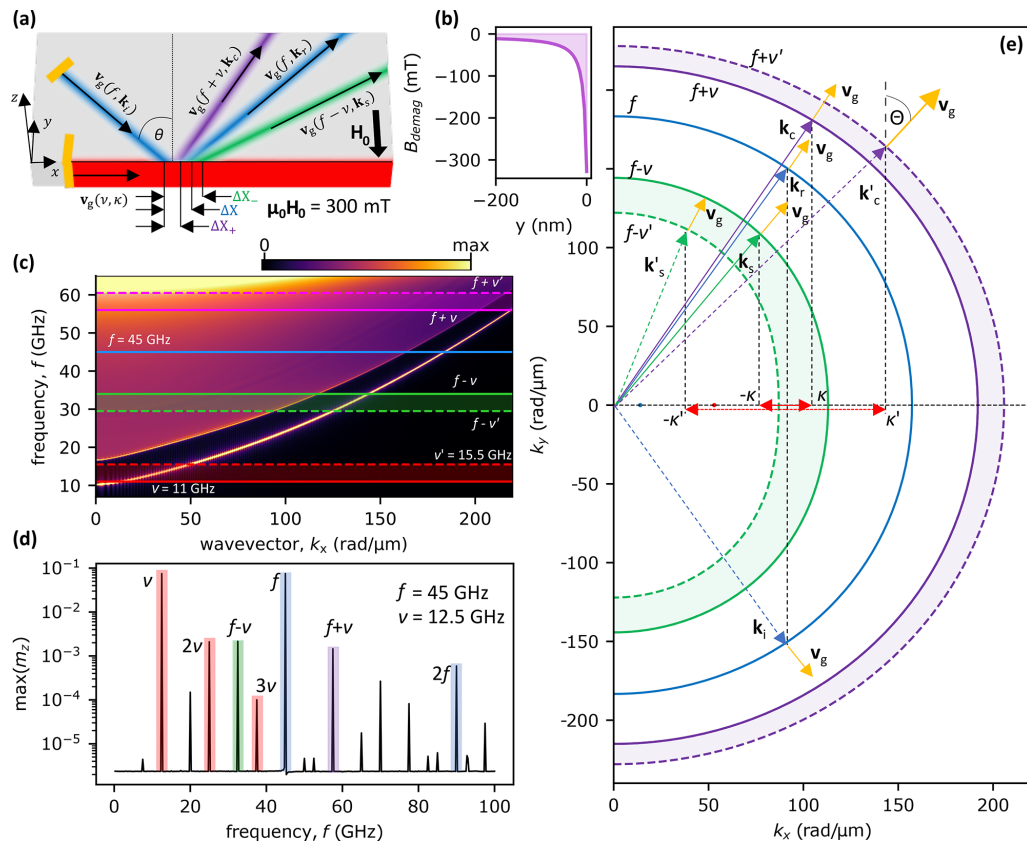
Figure 1. System's geometry and dispersion relation with isofrequency contours construction. (**a**) Geometry of the investigated system, i.e., Py layer with thickness 10 nm placed in a uniform external magnetic field $\mu_0 H_0 = 300$ mT along the y axis with a schematic representation of SWs propagating at different frequencies. The blue color represents incident and elastically reflected beams. The purple and green colors represent inelastically scattered beams as a result of CP and SSP, respectively. The red color depicts the edge mode. The black arrows denote the directions of the group velocities v_g associated with the respective SWs. The orange lines represent the antennas used to excite the incident SW beam and the edge modes. ΔX, ΔX_-, and ΔX_+ represent the lateral displacement between the incident beam spot and the beams from reflection, SSP, and CP, respectively. (**b**) Demagnetization field drops at the edge of the system, facilitating the localization of the SW edge mode in the system. (**c**) Numerically calculated dispersion relation in dependence on the tangential to the interface component of the wavevector. The color-shaded areas on the plot indicate investigated ranges of frequencies. (**d**) Spectrum of the SWs for the system response to the incident SW beam at a frequency $f = 45$ GHz on the edge mode at a frequency $\nu = 12.5$ GHz. The blue highlighted peaks correspond to the incident SW beam and its second harmonic. The red peaks represent the edge mode and its harmonics. SSP and CP are highlighted in green and purple, respectively. These frequencies are also marked with horizontal lines in (**c**). (**e**) Isofrequency construction illustrating the principle of selecting wavevectors of inelastically scattered SW beams on the edge mode propagating to the right, i.e., with $\kappa > 0$. The blue, green, and purple curves represent isofrequency contours for SWs at frequencies of the incident SW beam $f = 45$ GHz, reduced in frequency by the edge mode frequency ($f - \nu$ or $f - \nu'$) corresponding to SSP, and increased in frequency by the edge mode frequency ($f + \nu$ or $f + \nu'$) corresponding to CP. The green and purple isofrequency contours are plotted for two edge mode frequencies, i.e., solid lines for $\nu = 11$ and dashed lines for $\nu' = 15.5$ GHz. We keep the same color code as in the previous figures to represent the undergoing processes. The red, blue, green, and purple arrows represent successively the wavevectors of the edge SWs, the incident SW beam, and the inelastically scattered SW beams resulting from SSP and CP. In addition, we mark the group velocities of the SW beams with yellow vectors, which are normal to the curvatures of the contours. The angle between the group velocity and the normal to the interface of a given SW beam is denoted as Θ and it is the angle of beam propagation.
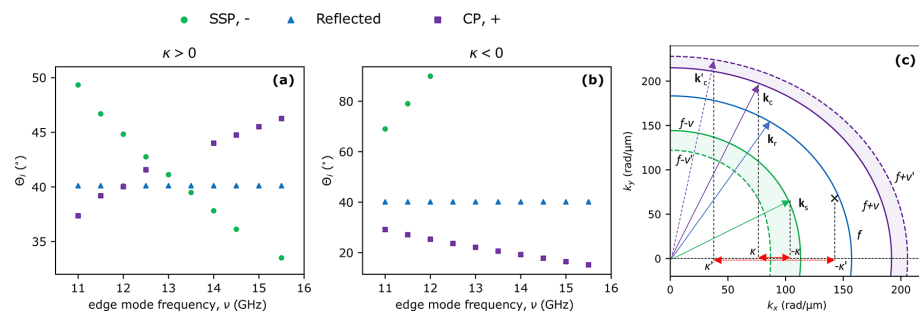
Figure 2. Dependencies showing the SW beams group velocity angles Θ_i. **(a,b)** Angles of the group velocity of SW beams (angles of propagation) as a function of edge mode frequency ν, blue triangles represent the reflected beam, green circles display SW beam created in SSP, and purple squares represent the SW beam created in CP. The results were obtained for the angle of incidence $\theta = 30°$ and for both, the edge modes with **(a)** $\kappa > 0$ and **(b)** $\kappa < 0$. **(c)** Isofrequency construction in the case of $\kappa < 0$. Here, for $-|\kappa'|$ there is no geometric solution in the SSP, which would correspond to SWs scattered on the higher frequency edge mode. Thus, for $\kappa < 0$ there is a critical value of κ (and ν) above which SSP is not allowed, as shown in **(b)**.

We present the considered inelastic scattering of SW beams on edge mode with $\kappa > 0$ on isofrequency plots in Fig. 1e. The blue curve represents all available solutions for the frequency f and $k_x > 0$. The blue dashed arrow represents the wavevector associated with the incident SW beam ($\mathbf{k}_i$). The solid blue arrow marks the opposite quadrant of (k_x, k_y) space and is plotted according to the rule of the conservation of wavevector tangential component (k_x), i.e., Snell's law. It represents the wavevector associated with the reflected SW beam ($\mathbf{k}_r$), which must be located on the isofrequency contour for frequency f. The beam propagation directions are related to the directions of the group velocities $v_g(f, \mathbf{k})$ (marked with orange arrows), which are perpendicular to the constant frequency contour for the corresponding wavevectors. Taking into account the conservation of energy ($f' = f + \nu$ for CP and $f' = f - \nu$ for SSP) and the conservation of the tangential component of the wavevector to the interface ($k_{c,x} = k_x + \kappa$ for CP and $k_{s,x} = k_x - \kappa$ for SSP), a similar construction can be made for inelastically scattered SWs. These contours, for SSP (green curves) and CP (purple curves), are marked for two examples of edge mode frequencies $\nu = 11$ GHz and $\nu' = 15.5$ GHz, solid and dashed lines, respectively. It can be seen that for the lower edge mode frequency, the propagation angle relative to the normal to the interface (y-axis) is smaller, which is consistent with the simulation results shown in Fig. 2a. A similar construction is done for SSP for the isofrequency contour $f - \nu$ and for the x-component of the wavevector equal to $k_{s,x} = k_x - \kappa$. Therefore, we observe that for the lower value of the edge SWs frequency, the angle of propagation of the inelastically scattered beam increases, which is also in agreement with Fig. 2a. Later in the text, we present dependencies of angles of propagation on the edge mode frequency for other simulation cases.

In the case of the left propagating edge mode, i.e. $\kappa < 0$, the SSP can only exist at frequencies ν below some critical value (see green dots in Fig. 2b where the waves formed in the SSP are only below 12 GHz), which depends on the angle of incidence. As shown in the isofrequency contour construction in Fig. 2c for $\theta = 30°$, for $k_{s,x} = k_x - (-|\kappa|)$ corresponding to $f - \nu$ frequencies, there are solutions only for small κ vectors. The angles of propagation of these rays are above 70°, i.e., their amplitude distribution overlaps with the interface, and therefore it is difficult to derive their trajectories. For the CP, the angle of propagation of the inelastically scattered beam decreases with increasing edge mode frequency (Fig. 2b) and varies by 14° in the considered range of ν. This is in agreement with the analysis of the changes in the group velocity directions shown in Fig. 2c. This situation is the opposite of the results obtained in the simulations with the positive value of the wavevector of the edge SW.

A detailed analysis of the rays of inelastically scattered SW beams shows that they are laterally shifted along the interface relative to the incident SW beam spot. This effect is analogous to the GH effect, which appears as a lateral shift of the elastically reflected SW wave beam with respect to the incident wave beam, e.g., electromagnetic waves[29–31] or SWs[50,51,53]. The results of simulations with edge mode of wavevector $\kappa > 0$ and for $\kappa < 0$ for different incident beam angles are displayed in Fig. 3a,b and in c–f, respectively.

The value of the spatial shift for the elastically reflected SW beam, i.e., standard GH shift, weakly depends on the frequency of the edge mode besides one case described later in the paper. We report the smallest $\Delta X = -3.8$ nm for the angle of incidence 35° and the biggest -14.5 nm at 45° with $\kappa > 0$ (see, Fig. S1. in the Supplementary), for $\kappa > 0$ the GH shift variation is similar, i.e., between 4 nm (for $\theta = 35°$) and 15 nm ($\theta = 45°$) as shown in Fig. 3c–f. These are rather small values of the GH shift but close to the expectations. In a paper with conditions similar to those presented in this work, the scope of GH shift for SWs was reported to be up to 40 nm in a system SW wavelength of 60 nm[52]. Some other papers have reported significant values of GH-shift but for special cases, e.g., in strong magnetic fields and with incident SWs propagating at grazing angles to the interface[50,62]. However, there is no report so far on the GH shift of beams generated in inelastic scattering.

The scope of spatial shifts of the beams created in SSP scattered on the edge mode with $\kappa > 0$ depends on the angle of the SW incidence beam and the edge mode frequency, see Fig. 3a (additional more detailed plots
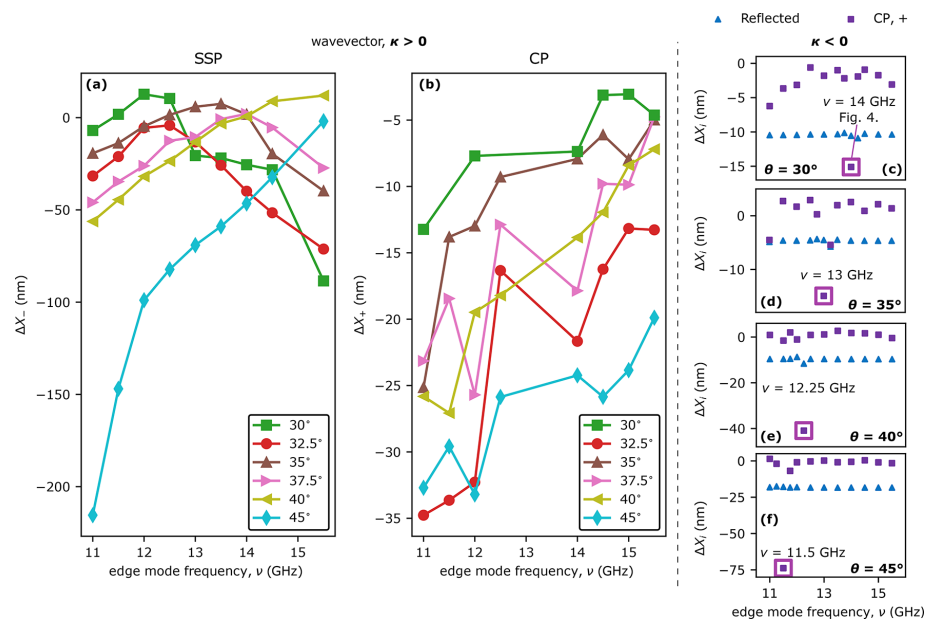
Figure 3. Dependencies of the lateral shifts ΔX_i along the interface of reflected and inelastically scattered beams for different angles of SW beam incidence (θ), and edge SWs frequencies (ν), and wavevector sign $\kappa > 0$ and $\kappa < 0$. On the left side of the black dashed line (subfigures (**a,b**)), lateral shifts of the scattered beams are presented in the case of edge mode with $\kappa > 0$. (**a**) Lateral shifts of the beams generated in SSP, and (**b**) in CP for all simulated angles of SW beam incidence. To the right of the black dashed line (subfigures (**c**)–(**f**)) the lateral shifts of the edge modes with $\kappa < 0$. The blue triangles show the lateral shifts of the elastically reflected beams and purple squares show the results corresponding to CP. The empty squares indicate the frequencies with the enhanced magnitude of $|\Delta X_+|$.

are also shown in Fig. S1. in the Supplementary). Interestingly, the function $\Delta X_-(\nu)$ is not monotonous. For instance, for $\theta \leq 37.5°$ the function $\Delta X_-(\nu)$ has in the analyzed ν range a maximum corresponding to a very small positive value of the GH shift with negative values (approx. -20 and -50 nm) at the sides of the considered range (11 and 15 GHz, respectively).

As the angle of incidence θ increases above $37.5°$, the position of the extreme shifts towards the greater edge mode frequencies. Therefore, for angles $40°$ and $45°$, the ΔX_- dependence becomes monotonic in the analyzed edge mode frequency range. With decreasing θ from $37.5°$, the maximum shifts to lower frequencies. Although the observed dependencies are regular, the reason for this behavior is unclear and difficult to explain without an appropriate analytical model.

Although the dependencies of $\Delta X_-(\nu)$ have maximum, the largest absolute magnitudes of the shifts ΔX_- are negative, and in the range of tens of nanometers. Thus, the spatial shifts are relatively small compared to the incident beam width. However, the wavelengths of the scattered beams generated in the SSP are in the range of 48 nm to 58 nm, varying slightly with different angles and edge mode frequencies. Thus, the reported spatial shifts are comparable to the scattered SW wavelengths. Exceptions to this rule are the results for $\theta = 45°$ and low edge mode frequencies which are in the range of hundreds of nanometers, e.g. for $\nu = 11$ GHz $\Delta X_- = -215$ nm, which are several wavelengths of the scattered SWs. In the results presented in Fig. 3(a) we omit the edge mode frequency $\nu = 15$ GHz as the frequency resulting in SSP is $f - \nu = 30$ GHz, which is the second harmonic of edge mode excitation that overlaps with the bulk SW spectra thus interfering with the derivation of SW beam trajectory.

The dependencies of the spatial shifts of the beams generated in CP at $\kappa > 0$ on ν are shown in Fig. 3b (additional more detailed plots are also shown in Fig. S1. in the Supplementary). For all angles of incidence θ, despite the variation in the lateral shift value $\Delta X_+(\nu)$, there is a general tendency for the magnitude of the negative $\Delta X_+(\nu)$ to decrease as the edge SW frequency increases. The scope of ΔX_+ is smaller in comparison to the spatial shifts calculated for beams created in SSP, and are in the range from -35 nm to 0. These values are comparable or smaller in comparison to scattered SWs wavelengths, which are in the range of 28 nm and 30 nm for CP. In Fig. 3b, the results for frequencies $\nu = 13$ GHz and $\nu = 13.5$ GHz are not displayed because for these frequencies the amplitudes of the scattered beams are very low, and derivation of their trajectories is unreliable.

The analysis of scattered SWs amplitude dependency on the edge mode frequency is beyond the scope of this paper and will be the subject of a further forthcoming study.

Figure 3c–f show the results of spatial shift of SW beams scattered on the edge mode with $\kappa < 0$. In most of the cases, the SSP does not occur, as was explained before, and in the few cases where this process does occur the scattered beams are almost grazing the edge thus, the derivation of their spatial shifts is inaccurate. For that reason in the case of $\kappa < 0$, we only present spatial shifts of beams created in CP. In all simulations with different angles of incidence, the derived spatial shifts of the scattered beams in CP are very small, in the range of a few nanometers, where the wavelengths of the scattered SWs are in the range of 26 nm to 29 nm. However, we can find a certain value of the edge mode frequency (14, 13, 12.25, and 11.5 GHz at $\theta = 30°$, $35°$, $40°$ and $45°$, respectively) for which a significant enhancement of the GH shift value appears, see purple squares in Fig. 3c–f. The origin of this phenomenon will be explained in the following paragraphs.

Let us first focus on the case shown in Fig. 3c, i.e., for the angle of incidence $30°$ and the frequency of the edge mode $\nu = 14$ GHz. The spatial distributions of the SW amplitude at frequencies $\nu = 14$ GHz, $f = 45$ GHz, and $f + \nu = 59$ GHz are shown in Fig. 4d, f, g, respectively. Surprisingly, in addition to the beams (incident and reflected at 45 GHz, and scattered at 59 GHz), we can also see a brightened region representing the plane waves with the same wavevector as the SWs from the beam. This effect can be explained as a result of a cascade nonlinear excitation of plane waves at the layer's edge. Figure 4a shows a scheme of the proposed nonlinear cascade process in the case of an incident SW beam propagating at the angle $\theta = 30°$ and scattered on a propagating edge mode of frequency $\nu = 14$ GHz. The first phase of this process is the SSP of the incident SW beam, marked by the blue oval, on the edge mode I, dashed red oval. As described before, there is no allowed solution to this process in the bulk of the Py layer. However, in this particular case, the result of the SSP is the generation of SWs with frequency $f - \nu = 31$ GHz and wavevector $k_x - |-\kappa| = 130$ rad/μm, which coincides with one of the allowed edge states in the system, as shown in Fig. 4b, later in this paper we will call this mode as the edge mode II. Figure 4e shows the spatial distribution of the SW amplitude of this mode, confirming its existence. According to the conservation of energy and momentum laws, this SSP must also generate SWs with frequency $\nu = 14$ GHz and wavevector $|\kappa| = -40$ rad/μm corresponding to the primary excited edge mode (edge mode I, marked in red with an asterisk). The analysis of this edge mode I amplitude presented in Fig. 4c shows a 2.5% boost just behind the spot where the incident beam reaches the edge. It indicates the creation of new edge SWs that propagate along and oscillate in phase with the antenna-excited edge mode I, and can be considered as an amplification of the propagating edge mode[15]. In Fig. 4e, where edge mode II is presented, there is a distinctive gap left to the point of SW beam incidence ($x = -3.7$ μm), which indicates that edge mode II is created at the SW beam incidence spot and propagates in opposite direction to edge mode I, Fig. 4d. It is evident by calculating the Fourier transform from the space to wavevector domain, as presented in Fig. 4h,i. Both of the edge modes have wavevectors of opposite signs and their numerical values agree with the analytically derived values shown in scheme Fig. 4a.

The excited edge mode II propagating along the edge interacts with the edge mode I excited directly by the antenna, Fig. 4a, it is Phase II. It causes CP to occur along the length of the edge beyond the point of SW beam incidence. The outcome of this process is the creation of a new SW at the edge with $f = 45$ GHz and wavevector $k_x = 90$ rad/μm, which corresponds to the incident SW beam. Taking into consideration the isofrequency contours, newly-created SWs at the edge also have to gain a wavevector component perpendicular to the edge, since there is no such solution for pure edge mode. For that reason, these SWs leak the energy from the edge and propagate into the bulk of the system with their wavefronts parallel to the reflected SW beam. It is shown in Fig. 4f, where an area of nonzero SW amplitude is right to the reflected beam. Additionally, the spatial Fourier transform of that distribution, shown in Fig. 4j, consists of only two distinctive peaks that overlap with isofrequency at $f = 45$ GHz and correspond to the incident and reflected SWs. Thus, no SWs with new wavevectors at this frequency are excited in the system. Since we are dealing with a nonlinear cascade process in which the interaction of two edge modes of different frequencies ultimately leads to energy leakage from the edge, this process is a nonlinear analog of a leaky mode excitation, which we have already reported[61]. Therefore, we refer to this phenomenon as nonlinear cascade leaky mode excitation.

Furthermore, this newly created SW at the edge interacts with the antenna-excited edge mode I, Phase III. This interaction is yet another CP occurring at the system's edge right to the incidence spot. In this CP new SW plane waves are excited, which propagate parallel to the scattered SW beam, Phase IV. We show this wave in Fig. 4g where the distribution of $|m_z|$ at frequency $f = 59$ GHz has nonzero amplitude only to the right of the scattered SW beam created in CP, i.e., in the direction of propagating edge mode II. Fig. 4k presents the space-domain Fourier transform of the $|m_z|$ distribution. There is only one peak that coincides with the isofrequency contour of $f = 59$ GHz confirming that the new SW plane wave has the same wavevector as the inelastically scattered SW beam.

In the scheme in Fig. 4a we wrote down the amplitudes (A) of all SWs types considered in the described cascade process. It points out that the amplitudes of created SWs in each phase are proportional to the product of the amplitudes in the previous phase. In Figs. 4d-g we mark positions where the $|m_z|$ amplitude values have been taken from the simulation results with circles, which colors correspond to the SWs modes shown in the Fig. 4a. The comparison between the incident beam and plane waves created in CP amplitudes of the plane waves created in CP shows a decrease in the range of 10^4 factor over the course of three process phases. Despite such a minuscule magnitude of new SWs they seem to have a noticeable impact on the lateral shift of scattered beams as shown in Fig. 3c-f. Indeed, a closer analysis of Fig. 4f,g shows that there is a narrow, yet distinctive drop in SW amplitude between the beams and plane waves. Such a drop in amplitude is a result of the destructive interference of these two kinds of SWs, thus the newly excited SWs at the edge have to be significantly shifted in phase.
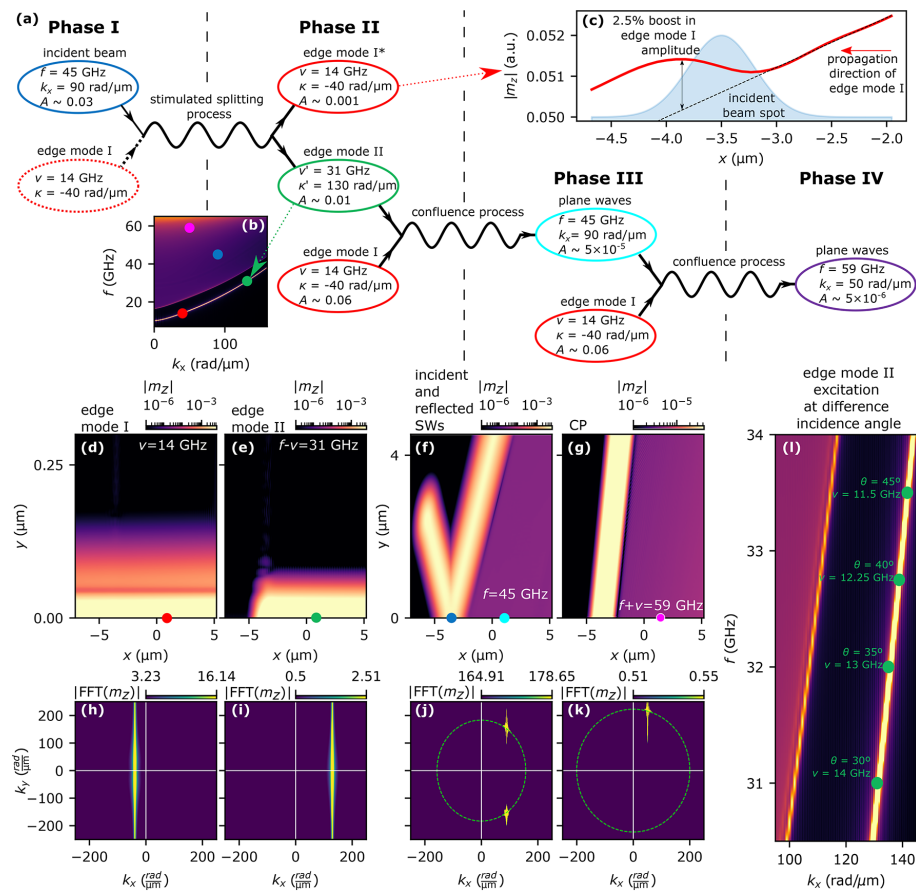
Figure 4. Cascade nonlinear excitation of SW leaky modes. (**a**) Scheme of nonlinear cascade process explaining the excitation of edge and plane SW in the system with an incident SW beam of frequency $f = 45$ GHz propagating under angle $\theta = 30°$. The SW modes are symbolized with ovals whose colors indicate the modes of the same characteristics. The proposed cascade process is divided into four phases connected by SSP and two CPs. (**b**) Dispersion relation of the system with the marked modes shown in (**a**) (the color of the dots corresponds to the colors of the ovals). (**c**) Amplitude $|m_z|$ of the edge mode I (red, solid line) at the layer edge in the vicinity of the incidence spot of the incident SW beam. The black, dashed line is the extrapolation of the antenna-excited edge mode I behind the incident beam spot, i.e., for $x > -3$ μm. (**d–g**) Space distributions of $|m_z|$ at frequencies $\nu = 14$ GHz, $f - \nu = 31$ GHz, $f = 45$ GHz, $f + \nu = 59$ GHz, respectively. The dots indicate spots where SW modes amplitudes, A indicated in (**a**), were taken. (**h–k**) Results of the two-dimensional Fourier transform from the space to wavevector domain of SW amplitude distribution are shown in (**d–g**). Figures (**j,k**) additionally contain isofrequency contours that correspond to frequencies of SWs presented in these pictures. (**l**) Investigated system's dispersion relation with marked frequencies for which excitation of SW plane waves occurs at different angles of incidence (this picture shares the colorbar with Fig.1b).

We also confirmed numerically that the nonzero amplitude background behind the scattered SW beams does not cause a false illusion of the beam shift. To confirm that adding a small-amplitude background to only one side of the Gaussian curve does not contribute the most to the calculated beam shift, we set up a numerical test. Namely, we added to a Gauss curve (with dimensions corresponding to the simulation results) a Heaviside step function with a height smaller by two orders of magnitude in comparison to the maximal amplitude of the Gauss curve. Then we run the same post-processing for this data as for simulated scattered beams. In the case of a numerically plotted Gauss curve, the addition of amplitude background alters the derived lateral shift by only a few nanometers. In the simulations, the scattered beams undergo lateral shifts up to tens of nanometers. These

calculations confirm that adding a small-amplitude background does not change substantially the obtained values of lateral shifts of simulated SW beams.

In Fig. 4l we show a part of the system's dispersion relation where the parameters of edge modes II are marked for all simulated angles of SW beam incidence. It is evident that in the investigated cases of SW beams scattered on the edge mode I with $\kappa < 0$ only a limited number of (ν, κ) and (f, k_x) combinations will yield excitation of new edge modes. The reason for this is the relatively small width of the edge mode band in dispersion relation which allows only a narrow range of SWs to be excited at the edge. For that reason the enhancement of the GH shifts in Fig.3c-f exists only at a narrow range of edge mode I frequencies.

Conclusions

In summary, we showed that the inelastically scattered SW beams on the edge wave confined to the edge of the ferromagnetic film undergo spatial shifts $\Delta X_{-,+}$ along the film edge, which we interpret as an analog of the GH effect. The obtained GH-like shifts are negative in the majority of cases, but dependencies of the $\Delta X_{-,+}(\nu)$ for the beams formed in SSP and CP processes are different. For beams generated in SSP and positive wavevector of the edge wave, the $\Delta X_-(\nu)$ dependence is parabolic like, with $\Delta X_- \approx 0$ at maximum and decreasing values for larger and smaller ν. We found that for high-incidence angles, e.g., $45°$, and edge modes of low-frequency with positive wavevectors, the spatial shifts of the beams created in SSP can even reach 200 nm, i.e., several wavelengths of the scattered SWs. For the beams generated in CP, the GH-like shift is small and there is a weak dependence of ΔX_+ on ν. However, we found a peculiar phenomenon at certain edge mode frequencies when the wavevector $\kappa < 0$. In these cases, we observed an enhancement of the GH shift from a few nm to even tens of nm. Interestingly, this effect is associated with the excitation of new higher-frequency edge modes in a cascading nonlinear process, consisting of two additional CPs. In these CPs, there are generated SWs with frequencies and wavevectors that overlap with the band of the propagating SWs in the film, i.e., they radiate from the film edge and propagate as plane waves. Thus, the proposed process can be considered as a nonlinear version of magnonic leaky-mode excitation[61]. Even though the lateral shifts of scattered beams have small magnitudes and are not a significant factor in the physical realization of magnonic devices, they still serve as indirect indicators of other phenomena happening in the system. As presented in this paper, a visible increase of lateral shift of SW beams created in CP hinted an occurrence of the cascade process that, up-to-date, has not been described.

The results presented in this work contribute with nonlinear effects to a new subfield of magnonics called SW optic[63–67]. This paves the way for the development of optically-inspired magnonic logic devices[68,69], especially for neuromorphic and edge computing components that require nonlinearity[2,3], with high microwave frequency operation at the nanoscale, and, most importantly, low power consumption.

Methods
Micromagnetic simulations

In our research, we employ micromagnetic simulations performed in Mumax3 environment[57] to solve the Landau-Lifshitz equation in the time domain. The system is modeled as a cuboidal layer of Py with dimensions $5.12\,\mu m \times Y\,\mu m \times 10\,\mu m$ (along x, y, z axes respectively). The value Y varies in simulations with different incident SW beam's angle of propagation, namely $Y = \{10.24\,\mu m, 11.33\,\mu m, 12.42\,\mu m, 13.65\,\mu m, 14.88\,\mu m, 17.73\,\mu m$ for angles $\theta = \{30°, 32.5°, 35°, 37.5°, 40°, 45°\}$ respectively. The material parameters of Py used in the simulations are $\alpha = 0.0001$, $M_S = 800$ kA/m, $A_{ex} = 13$ pJ/m, which yield the exchange length of $\lambda_{ex} = 5.69$ nm. We use the discretization grid 5 nm $\times$ 5 nm $\times$ 10 nm (along x, y, z axes respectively), which is shorter than λ_{ex} in the in-plane coordinates of the layer. We place the Py layer in a uniform external magnetic field $B_0 = 300$ mT directed in-plane, opposite to the direction of the y axis. To simulate the infinitely long system along both directions of the x axis and positive direction of the y axis we increase the value of the damping parameter α up to value 0.5 parabolically over the width of 600 nm to prevent reflections at these edges.

The dispersion relation presented in Fig. 1c was obtained as described in Ref. [9]. A small, two-dimensional antenna was placed at the edge of the system. The antenna introduces a locally oscillating external magnetic field with time and space distribution described by *sinc* functions with cut-off parameters $f_{cut} = 100$ GHz and $k_{cut} = 300$ rad/μm. This magnetic field excites omnidirectional SWs in the system thus, the SWs propagate both in the bulk of the system and in the demagnetizing magnetic field dip at the edge. For the dispersion relation calculation, 1000 snapshots of the magnetization configuration were saved with a time step of $0.5/(1.1 f_{cut})$.

To excite the SWs in the scattering simulations we use two antennas, one placed in the bulk of the Py layer and the second at the system's edge. The first antenna has a rectangular-like shape and is rotated by an angle θ thus can be regarded in terms of (x', y') coordinates. It creates the incident SW beam aimed at the edge-localized mode. We used a mathematical formula to create this antenna in the simulations inspired by Ref. [60]

$$B_{ext,y}(t, x', y') = A_{ant}(1 - e^{-0.2\pi ft})R(y')G(x')$$
$$\times [\sin(ky')\sin(2\pi ft) + \cos(ky')\cos(2\pi ft)], \tag{1}$$

where $A_{ant} = 0.01 B_0$ is the amplitude of the dynamic field, $R(y') = H(-y' + \frac{w_a}{2})H(y' + \frac{w_a}{2})$ is a rectangle function, which describes antenna's shape along its y' coordinate ($H(y)$ is Heaviside step function, antenna's width $w_a = 360$ nm), $G(x') = \exp(-\frac{x'^2}{4\sigma_x^2})$ is a Gaussian function defining antenna's shape along the x'-axis ($\sigma_x = 320$ nm), k is the wavevector and f is the frequency of the excited SWs. Such a formula creates a unidirectional SW beam of Gaussian envelope with FWHM= 760 nm. The incident SW beam in all simulations has frequency $f = 45$ GHz and the corresponding wavevector for this SW beam is derived from Kalinikos-
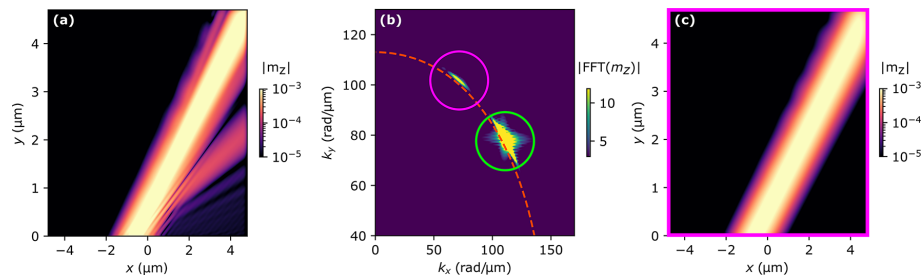
Figure 5. Numerical wavevector filter. (**a**) The $|m_z|$ amplitude space distribution of scattered SWs in SSP for $\theta = 30°$, $\kappa > 0$ and $\nu = 11$ GHz case with visible waves that are the result of secondary scattering on reflected edge mode. (**b**) Fourier transform of the scattered waves presented in (**a**). Two distinctive peaks are evident, one marked with a purple circle corresponds to SSP and the second, a green circle, corresponds to secondary scattering. (**c**) The simulation results after applying the wavevector filtering where only contribution from the wavevector of SSP is taken into consideration (purple circle in (b)).

Slavin formula for SW dispersion relation[70] for each incident SW beam's angle of propagation. We control the angle of the incident SW beam propagation (angle of the wavevector) by changing the rotation of the antenna, θ, with respect to the edge of the system. In these investigations, we limit ourselves to the range of $\theta \in \langle 30°, 45° \rangle$. However, the calculated angles of propagation of the incident and reflected SW beams, Θ_i are different because of the SW anisotropy of propagation. This means that beams' wavevectors and group velocities are not parallel. The second antenna is defined as a point source of Gaussian shape ($\sigma_{\text{edge}} = 15$ nm) placed at the very edge of the system. The purpose of this antenna is to excite the localized edge modes characterized by frequencies in range $\nu \in \langle 11, 15.5 \rangle$ GHz. Depending on the desired wavevector of the edge mode κ we place this antenna either below the point where the incident SW beam reaches the edge (positive κ) or above this point (negative κ).

The numerical simulations consist of three phases. In the first, we obtain a stable static magnetic configuration at the defined external magnetic field by minimizing the energy of the initial magnetic state. In the next phase, we run the dynamic part of the simulation when both antennas are turned on until the system reaches a steady state. The simulation time varies with the system's length along its y-axis, $t = \{240$ ns, 270 ns, 300 ns, 325 ns , 350 ns, 420 ns$\}$ for the incident SW beam angles $\theta = \{30°, 32.5°, 35°, 37.5°, 40°, 45°\}$ respectively. Finally, we save 800 snapshots of the magnetic configuration with $dt = 5$ ps time step. We have also performed simulations of the described system with finer discretization through layer thickness to investigate the convergence of our results. For this purpose, we have used the following discretizations 5 nm $\times$ 5 nm $\times$ 5 nm and 5 nm $\times$ 5nm $\times$ 1 nm. The obtained results differ only slightly (for almost all the cases the difference in lateral shifts are below 1 nm) in the numerical values but dependencies presented in the paper remain qualitatively the same.

Data postprocessing
To process the data obtained in the micromagnetic simulations we use a self-developed code. We start with the spectral analysis of the scattered SWs by calculating the Fourier transform in the time domain using saved magnetic configuration snapshots for each simulation case. From this analysis, we obtain an insight into the frequencies of the processes that undergo in our system and the distribution of complex SW amplitude at a given frequency ($m_z(f) \in \mathbb{C}$), therefore, allowing us to analyze both the amplitude and phase of SWs in each point of the simulated area. The time sampling was chosen to provide such resolution in the frequency domain to analyze the system's response in all anticipated frequencies of $f \pm n\nu$, $n \in \mathbb{N}^+$ configurations, namely $\delta t = 5$ ps time step. In our calculations, we investigate the following frequencies $f = 45$ GHz corresponding to the incident and reflected SW beams, $f - \nu$ corresponding to scattered beam in SSP, and $f + \nu$ corresponding to scattered beam in CP. Even though higher-order nonlinear processes are also present in the spectral analysis we omit them as they are beyond the scope of this paper.

The simulation results for $\kappa > 0$ and low edge mode frequency $\nu = 11$ GHz proved to be problematic in further postprocessing. The reason for that was the unexpected reflection of low-frequency edge mode from the absorbing boundary conditions, where up to 10% of edge mode amplitude was reflected. It caused a secondary scattering in the system and the creation of an additional SW beam of frequency corresponding to SSP but propagating under a different angle, as shown in Fig. 5a $|m_z|$ amplitude for SSP in $\theta = 30°$, $\kappa > 0$ and $\nu = 11$ GHz case. This new beam is a result of a CP with negative values of edge mode frequency and wavevector, as the reflected edge mode propagates in the opposite direction to the excited edge mode, thus resembling SSP in frequency but differing in wavevector of the scattered beam. To limit the effect of secondary scattering in our analysis we use an additional numerical filter that cuts off the contribution of SWs with different wavevectors than predicted by the investigated inelastic scattering processes. For that, we only take the contribution from

the peak and its vicinity in spectral analysis that corresponds to the investigated process, as shown with the purple circle in Fig. 5b. To extract only the contribution for the desired peak and avoid numerical errors in the further steps of postprocessing we multiply the amplitude distribution by an amplitude mask in the shape of a two-dimensional Gaussian curve centered over the peak with a small spread. Then the inverse Fourier transform of the product of amplitude distribution and mask yields the SW amplitude space distribution without any undesired distortions in the system, as shown in Fig. 5c. This procedure was applied to the simulation results with low edge mode frequency, $\nu = 11$ GHz to increase the precision of derivation of beams' trajectories.

Derivation of SW beams trajectories

To derive the trajectories of the investigated SW beams we use distributions of SW intensity in space for a given frequency and wavevector corresponding to incidence, reflection, SSP, and CP. We calculate all of the beams' trajectories in the far field, in terms of geometry used in the simulations, 2 μm away from the edge. We fit the Gaussian function to the cross-sections of the SW $|m_z|$ intensity distributions at fixed y-coordinate. We used 200 cross-sections with an interval 5 nm, as the discretization grid used in the simulations. After fitting the Gaussian function to each cutline we save the position of the curve's center of all the beams. Later, we use these coordinates to perform linear regression to fit line functions to them that we interpret as beams' trajectories. In all simulation cases, the uncertainty of beam trajectory derivation depends on the spread of the beams' center positions. In the simulation, we obtained well-collimated SW beams thus the uncertainty trajectory derivation is within 0.01 nm in all of the simulation cases. The derived trajectories are extended from the far field to the system's edge where the position of the beams' interception with the edge is determined. To calculate the spatial shifts of the scattered beams we take as a point of reference the position where the incident beam reaches the system's edge. Thus the negative value of spatial shifts means that the given beam has its origin left to the incidence spot and the positive value means that the beam shifts to the right of the incidence spot. As the linear regression method calculates linear function fit in the continuous space, the final values of calculated space shifts of SW beams are not constrained by the discretization used in the simulations.

Data availability

References

1. Chumak, A. et al. Advances in magnetics roadmap on spin-wave computing. *IEEE Trans. Magnet.* **58**, 1–72 (2022).
2. Papp, Á., Porod, W. & Csaba, G. Nanoscale neural network using non-linear spin-wave interference. *Nat. Commun.* **12**, 6422. https://doi.org/10.1038/s41467-021-26711-z (2021).
3. Namiki, W. et al. Experimental demonstration of high-performance physical reservoir computing with nonlinear interfered spin wave multidetection. *Adv. Intell. Syst.* **5**, 2300228. https://doi.org/10.1002/aisy.202300228 (2023).
4. Chumak, A. V., Serga, A. A. & Hillebrands, B. Magnon transistor for all-magnon data processing. *Nat. Commun.* **5**, 4700. https://doi.org/10.1038/ncomms5700 (2014).
5. Nakane, R., Hirose, A. & Tanaka, G. Performance enhancement of a spin-wave-based reservoir computing system utilizing different physical conditions. *Phys. Rev. Appl.* **19**, 034047. https://doi.org/10.1103/PhysRevApplied.19.034047 (2023).
6. Lara, A., Metlushko, V. & Aliev, F. G. Observation of propagating edge spin waves modes. *J. Appl. Phys.* **114** (2013).
7. Sebastian, T. *et al.* Nonlinear emission of spin-wave caustics from an edge mode of a microstructured $Co_2Mn_{0.6}Fe_{0.4}Si$ waveguide. *Phys. Rev. Lett.* **110**, 067201 (2013).
8. Hermsdoerfer, S. J. et al. A spin-wave frequency doubler by domain wall oscillation. *Appl. Phys. Lett.* **94**, 223510 (2009).
9. Gruszecki, P., Lyubchanskii, I. L., Guslienko, K. Y. & Krawczyk, M. Local non-linear excitation of sub-100 nm bulk-type spin waves by edge-localized spin waves in magnetic films. *Appl. Phys. Lett.* **118**, 062408 (2021).
10. Yao, X., Jin, Z., Wang, Z., Zeng, Z. & Yan, P. Terahertz magnon frequency comb. *Phys. Rev. B* **108**, 134427. https://doi.org/10.1103/PhysRevB.108.134427 (2023).
11. Wang, Z. et al. Magnonic frequency comb through nonlinear magnon-skyrmion scattering. *Phys. Rev. Lett.* **127**, 037202 (2021).
12. Zhou, Z.-W., Wang, X.-G., Nie, Y.-Z., Xia, Q.-L. & Guo, G.-H. Spin wave frequency comb generated through interaction between propagating spin wave and oscillating domain wall. *J. Magn. Magn. Mater.* **534**, 168046 (2021).
13. Wang, Z., Yuan, H., Cao, Y. & Yan, P. Twisted magnon frequency comb and Penrose superradiance. *Phys. Rev. Lett.* **129**, 107203 (2022).
14. Wang, Z., Zhang, B., Cao, Y. & Yan, P. Probing the Dzyaloshinskii-Moriya interaction via the propagation of spin waves in ferromagnetic thin films. *Phys. Rev. Appl.* **10**, 054018 (2018).
15. Gruszecki, P., Guslienko, K. Y., Lyubchanskii, I. L. & Krawczyk, M. Inelastic spin-wave beam scattering by edge-localized spin waves in a ferromagnetic thin film. *Phys. Rev. Appl.* **17**, 044038 (2022).
16. Gareeva, Z. V. & Guslienko, K. Y. Collective magnetic skyrmion gyrotropic modes in a dot chain. *J. Phys. Commun.* **2**, 035009 (2018).
17. Paikaray, B., Joseph, A., Murapaka, C. & Haldar, A. Tunable microwave properties of a skyrmion in an isolated nanodisk. *J. Magnet. Magnet. Mater.* **529**, 167900. https://doi.org/10.1016/j.jmmm.2021.167900 (2021).
18. Shi, S. et al. Transverse azimuthal dephasing of a vortex spin wave in a hot atomic gas. *Phys. Rev. A* **95**, 033823 (2017).
19. Verba, R. et al. Theory of three-magnon interaction in a vortex-state magnetic nanodot. *Phys. Rev. B* **103**, 014413 (2021).
20. Gao, Z. et al. Interplay between spin wave and magnetic vortex. *Phys. Rev. B* **107**, 214418 (2023).
21. Dadoenkova, N. N., Dadoenkova, Y. S., Lyubchanskii, I. L., Krawczyk, M. & Guslienko, K. Y. Inelastic spin-wave scattering by Bloch domain wall flexure oscillations. *Phys. Status Solidi Rapid Res. Lett.* **13**(5), 1800589. https://doi.org/10.1002/pssr.201800589 (2019).
22. Wojewoda, O. et al. Propagation of spin waves through a Néel domain wall. *Appl. Phys. Lett.* **117**, 022405. https://doi.org/10.1063/5.0013692 (2020).
23. Ordóñez-Romero, C. L. et al. Three-magnon splitting and confluence processes for spin-wave excitations in yttrium iron garnet films: Wave vector selective brillouin light scattering measurements and analysis. *Phys. Rev. B* **79**, 144428 (2009).

24. Zhang, B., Wang, Z., Cao, Y., Yan, P. & Wang, X. Eavesdropping on spin waves inside the domain-wall nanochannel via three-magnon processes. *Phys. Rev. B* **97**, 094421 (2018).

25. Körber, L. et al. Nonlocal stimulation of three-magnon splitting in a magnetic vortex. *Phys. Rev. Lett.* **125**, 207203 (2020).

26. Ge, X., Verba, R., Pirro, P., Chumak, A. V. & Wang, Q. Nanoscaled magnon transistor based on stimulated three-magnon splitting. *Appl. Phys. Lett.* **124** (2024).

27. Lock, E. H. The properties of isofrequency dependences and the laws of geometrical optics. *Physics-Uspekhi* **51**, 375 (2008).

28. Gruszecki, P. & Krawczyk, M. Spin-wave beam propagation in ferromagnetic thin films with graded refractive index: Mirage effect and prospective applications. *Phys. Rev. B* **97**, 094424. https://doi.org/10.1103/PhysRevB.97.094424 (2018).

29. Goos, F. & Hänchen, H. Ein neuer und fundamentaler Versuch zur Totalreflexion. *Ann. Phys.* **436**, 333–346 (1947).

30. Renard, R. H. Total reflection: A new evaluation of the Goos–Hänchen shift. *J. Opt. Soc. Am.* **54**, 1190–1197. https://doi.org/10.1364/JOSA.54.001190 (1964).

31. Snyder, A. W. & Love, J. D. Goos–Hänchen shift. *Appl. Opt.* **15**, 236–238. https://doi.org/10.1364/AO.15.000236 (1976).

32. Bliokh, K. Y. & Aiello, A. Goos–Hänchen and Imbert–Fedorov beam shifts: An overview. *J. Opt.* **15**, 014001 (2013).

33. Wild, W. J. & Giles, C. L. Goos–Hänchen shifts from absorbing media. *Phys. Rev. A* **25**, 2099–2101. https://doi.org/10.1103/PhysRevA.25.2099 (1982).

34. Wang, L.-G., Ikram, M. & Zubairy, M. S. Control of the Goos–Hänchen shift of a light beam via a coherent driving field. *Phys. Rev. A* **77**, 023811. https://doi.org/10.1103/PhysRevA.77.023811 (2008).

35. Wang, L.-G., Zhu, S.-Y. & Zubairy, M. S. Goos–Hänchen shifts of partially coherent light fields. *Phys. Rev. Lett.* **111**, 223901. https://doi.org/10.1103/PhysRevLett.111.223901 (2013).

36. Wang, Y. et al. Targeted sub-attomole cancer biomarker detection based on phase singularity 2d nanomaterial-enhanced plasmonic biosensor. *Nano-Micro Lett.* **13**, 1–11 (2021).

37. Singh, I. & Nayyar, V. Lateral displacement of a light beam at a ferrite interface. *J. Appl. Phys.* **69**, 7820–7824 (1991).

38. Borisov, S., Dadoenkova, N., Lyubchanskii, I. & Lyubchamkii, M. Goos–Hänchen effect for the light reflected from the interface formed by bigyrotropic and nongyrotropic media. *Opt. Spectrosc.* **85**, 225–231 (1998).

39. Dadoenkova, Y. S. et al. Controlling the Goos–Hänchen shift with external electric and magnetic fields in an electro-optic/magneto-electric heterostructure. *J. Appl. Phys.* **119**, 203101 (2016).

40. Dadoenkova, Y. S., Bentivegna, F., Dadoenkova, N., Lyubchanskii, I. & Lee, Y. Influence of misfit strain on the Goos–Hänchen shift upon reflection from a magnetic film on a nonmagnetic substrate. *JOSA B* **33**, 393–404 (2016).

41. Dadoenkova, Y. S., Dadoenkova, N., Kłos, J. W., Krawczyk, M. & Lyubchanskii, I. Goos–Hänchen effect in light transmission through biperiodic photonic-magnonic crystals. *Phys. Rev. A* **96**, 043804 (2017).

42. Tang, T. et al. Weak measurement of magneto-optical Goos–Hänchen effect. *Opt. Exp.* **27**, 17638–17647 (2019).

43. Makarova, A. V. et al. Goos–Hänchen shift spatially resolves magneto-optical Kerr effect enhancement in magnetoplasmonic crystals. *ACS Photon.* **11**, 1619–1626 (2024).

44. Yin, X. & Hesselink, L. Goos–Hänchen shift surface plasmon resonance sensor. *Appl. Phys. Lett.* **89**, 261108. https://doi.org/10.1063/1.2424277 (2006).

45. Parks, A. D. & Spence, S. E. Weak value amplification of an off-resonance Goos–Hänchen shift in a Kretschmann–Raether surface plasmon resonance device. *Appl. Opt.* **54**, 5872–5876. https://doi.org/10.1364/AO.54.005872 (2015).

46. Zeng, S. et al. Plasmonic metasensors based on 2d hybrid atomically thin Perovskite nanomaterials. *Nanomaterials* **10**, 1289. https://doi.org/10.3390/nano10071289 (2020).

47. Chen, X., Lu, X.-J., Ban, Y. & Li, C.-F. Electronic analogy of the Goos–Hänchen effect: A review. *J. Opt.* **15**, 033001 (2013).

48. Bushuev, V. A. & Frank, A. I. Goos–Hänchen effect in neutron optics and the reflection time of neutron waves. *Physics-Uspekhi* **61**, 952 (2018).

49. Wang, Z. The influence of the Goos–Haenchen effect on seismic data processing and AVO in attenuating media. *J. Appl. Geophys.* **122**, 122–133 (2015).

50. Dadoenkova, Y. S. et al. Huge Goos–Hänchen effect for spin waves: A promising tool for study magnetic properties at interfaces. *Appl. Phys. Lett.* **101**, 042404 (2012).

51. Gruszecki, P. et al. Goos–Hänchen effect and bending of spin wave beams in thin magnetic films. *Appl. Phys. Lett.* **105**, 242406 (2014).

52. Gruszecki, P., Mailyan, M., Gorobets, O. & Krawczyk, M. Goos–Hänchen shift of a spin-wave beam transmitted through anisotropic interface between two ferromagnets. *Phys. Rev. B* **95**, 014421 (2017).

53. Stigloher, J. et al. Observation of a Goos–Hänchen-like phase shift for magnetostatic spin waves. *Phys. Rev. Lett.* **121**, 137201 (2018).

54. Wang, Z., Cao, Y. & Yan, P. Goos–Hänchen effect of spin waves at heterochiral interfaces. *Phys. Rev. B* **100**, 064421 (2019).

55. Laliena, V. & Campo, J. Magnonic Goos–Hänchen effect induced by 1d solitons. *Adv. Electron. Mater.* **8**, 2100782 (2022).

56. Dadoenkova, Y., Krawczyk, M. & Lyubchanskii, I. L. Goos–Hänchen shift at Brillouin light scattering by a magnetostatic wave in the Damon–Eshbach configuration. *Opt. Mater. Exp.* **12**, 717–726 (2022).

57. Vansteenkiste, A. et al. The design and verification of MuMax3. *AIP Adv.* **4**, 107133 (2014).

58. Bailleul, M., Olligs, D., Fermon, C. & Demokritov, S. O. Spin waves propagation and confinement in conducting films at the micrometer scale. *Europhys. Lett.* **56**, 741. https://doi.org/10.1209/epl/i2001-00583-2 (2001).

59. McMichael, R. D. & Maranville, B. B. Edge saturation fields and dynamic edge modes in ideal and nonideal magnetic film edges. *Phys. Rev. B* **74**, 024424. https://doi.org/10.1103/PhysRevB.74.024424 (2006).

60. Whitehead, N., Horsley, S., Philbin, T. & Kruglyak, V. Graded index lenses for spin wave steering. *Phys. Rev. B* **100**, 094404 (2019).

61. Sobucki, K., Śmigaj, W., Graczyk, P., Krawczyk, M. & Gruszecki, P. Magnon-optic effects with spin-wave leaky modes: Tunable Goos–Hänchen shift and Wood's anomaly. *Nano Lett.* **23**, 6979–6984. https://doi.org/10.1021/acs.nanolett.3c01592 (2023).

62. Zhen, W. & Deng, D. Giant Goos–Hänchen shift of a reflected spin wave from the ultrathin interface separating two antiferromagnetically coupled ferromagnets. *Opt. Commun.* **474**, 126067 (2020).

63. Gräfe, J. et al. Direct observation of spin-wave focusing by a Fresnel lens. *Phys. Rev. B* **102**, 024420. https://doi.org/10.1103/PhysRevB.102.024420 (2020).

64. Gołebiewski, M., Gruszecki, P., Krawczyk, M. & Serebryannikov, A. E. Spin-wave Talbot effect in a thin ferromagnetic film. *Phys. Rev. B* **102**, 134402. https://doi.org/10.1103/PhysRevB.102.134402 (2020).

65. Gross, F. et al. Building blocks for magnon optics: Emission and conversion of short spin waves. *ACS Nano* **14**, 17184–17193. https://doi.org/10.1021/acsnano.0c07076 (2020).

66. Kiechle, M. et al. Spin-wave optics in YIG realized by ion-beam irradiation. *Small* **19**, 2207293. https://doi.org/10.1002/smll.202207293 (2023).

67. Rivkin, K. A. Spin wave optics. arXiv: 2404.13882 (2024).

68. Gołębiewski, M., Gruszecki, P. & Krawczyk, M. Self-imaging based programmable spin-wave lookup tables. *Adv. Electron. Mater.* **8**, 2200373. https://doi.org/10.1002/aelm.202200373 (2022).

69. Wang, Q., Chumak, A. V. & Pirro, P. Inverse-design magnonic devices. *Nat. Commun.* **12**, 2636. https://doi.org/10.1038/s41467-021-22897-4 (2021).

70. Kalinikos, B. & Slavin, A. Theory of dipole-exchange spin wave spectrum for ferromagnetic films with mixed exchange boundary conditions. *J. Phys. C Solid State Phys.* **19**, 7013 (1986).

Acknowledgements

Author contributions

K.S. performed all micromagnetic simulations presented in this paper, prepared all the figures displayed and wrote the bulk of the manuscript. I.L. was the initiator of the research that is presented in this publication, supervised the work on the manuscript and reviewed the manuscript before submission. M.K. helped with the analysis of the simulation results, reviewed the manuscript before submission, and supervised work. P.G. helped with performing the magnetic simulations, wrote the introduction to the manuscript, reviewed all the figures included in the manuscript, and supervised the work.

Declarations

Competing interests
The authors declare no competing interests.

Additional information
Supplementary Information The online version contains supplementary material available at https://doi.org/10.1038/s41598-025-86879-y.

Correspondence and requests for materials should be addressed to K.S.

Reprints and permissions information is available at www.nature.com/reprints.

Publisher's note Springer Nature remains neutral with regard to jurisdictional claims in published maps and institutional affiliations.

Chapter 6

Additional studies

In this section two additional papers are presented. These works are not included in the main research line showed in Chapter 5. They were done in parallel to the investigation planned before the author's PhD program when the author was invited to collaborate in different research projects.

6.1   Magnon spectrum of Bloch hopfion beyond ferromagnetic resonance

Hopfions are complex magnetic textures that can be regarded as a three-dimensional expression of skyrmions. Because of the complexity of such structures their spectra are rich in eigenmodes which can be measured in ferromagnetic resonance measurements. In this theoretical paper eigenmodes of certain hopfions were investigated by means of numerical micromagnetic simulations. Simulations in the frequency domain provided eigenmode amplitudes and sense of rotation while simulations in the time domain provided spectra of averaged magnetisation response which can be measured in the experiment. The paper provides information how to prepare numerically benchmarks for future experiments of hopfions observation.

The Author performed micromagnetic simulation in the time domain using MuMax3 environment and postprocessed the data. Author has written all of the parts of the manuscript related to the micromagnetic simulations as well as prepared Figures 1, 5, 6.

Magnon spectrum of Bloch hopfion beyond ferromagnetic resonance ᴱᴾ

K. Sobucki,[1] 🆔 M. Krawczyk,[1,a) 🆔 O. Tartakivska,[1,2] 🆔 and P. Graczyk[3] 🆔

AFFILIATIONS

[1] Institute of Spintronics and Quantum Information, Faculty of Physics, Adam Mickiewicz University, Poznań, Poland
[2] Institute of Magnetism, National Academy of Sciences of Ukraine, 36b Vernadskogo Boulevard, Kyiv, Ukraine
[3] Institute of Molecular Physics PAS, Poznań, Poland

Note: This paper is part of the Special Topic on Science and Technology of 3D Magnetic Nanostructures.
a)Author to whom correspondence should be addressed: krawczyk@amu.edu.pl

ABSTRACT

With the development of new nanofabrication technologies and measurement techniques, the interest of researchers is moving toward 3D structures and 3D magnetization textures. Special attention is paid to the topological magnetization textures, particularly hopfions. In this paper, we investigate the magnetization dynamics of the hopfion through the numerical solution of the eigenvalue problem. We show that the spectrum of spin-wave modes of the hopfion is much richer than those attainable in ferromagnetic resonance experiments or time-domain simulations reported so far. We identified four groups of modes that differ in the character of oscillations (clockwise or counter-clockwise rotation sense), the position of an average amplitude localization along the radial direction, and different oscillations in the vertical cross section. The knowledge of the full spin-wave spectrum shall help in hopfion identification, understanding of the interaction between spin waves and hopfion dynamics as well as the development of the potential of hopfion in spintronic and magnonic applications.

I. INTRODUCTION

The resonant spectrum of any object can be seen, from the point of view of its energy states around equilibrium, as its characteristic signature. This holds for different types of systems and forms a ground for various spectroscopic techniques. In the context of the magnetic nanostructures,[1] the spin-wave modes are collective small-amplitude oscillations of the magnetization around its equilibrium orientation. They characterize the magnetic systems, reflect the existing symmetries, and provide information about basic magnetic properties.[2–5]

The spin-wave resonance spectrum in the homogeneous and uniformly magnetized ferromagnetic systems is quite well-known, and it is described by the Kittel formula.[6] In thin films, the ferromagnetic resonance (FMR) spectrum is dependent on the magnetization orientation and may consist of a fundamental mode and perpendicular standing spin waves. In ferromagnetic rods, the spectrum strongly depends on the magnetization orientation. In homogeneously axially magnetized circular nanorods, the azimuthal

and radial modes were identified.[7–9] Interesting spin-wave spectrum exists in planar ferromagnetic nanosystems. It depends on the element shape (e.g., dots, rings, and nanovolcanoes)[2,10–14] and magnetization configurations.[15,16] Nanostructures with topologically protected magnetization textures, like vortexes and skyrmions, are particularly interesting.[17–24] Here, the spectrum consists of the gyrotropic modes, usually at low-frequencies, but at thicker dots, higher-order gyrotropic modes at GHz frequencies can exist as well.[25] There is a family of the azimuthal and radial spin-wave excitations, which reflect a circular symmetry of the system, also, the breathing mode in the skyrmion and the curled modes in the vortex state[25] were identified. Interestingly, in various ferromagnetic nanostructures, the Dzialoshynski–Moriya interactions (DMI), but also dipolar or topological phase, can lift the degeneracy between clockwise and counter-clockwise azimuthal modes.[8,9,21,22,26]

When the system becomes thick enough, the magnetization can also form stable, inhomogeneous configurations in the third dimension, providing further features to the spin-wave spectrum.[27,28] Recently, an interest in the magnetic research community focuses

6.2 Spin wave confinement in hybrid superconductor-ferrimagnet nanostructure

One of the newest ideas in magnonics is to propose novel types of systems where ferrimagnetic elements are combined with superconductors. In this paper a static magnetic field induced by a superconducting stripe is used to lower external magnetic field in which thin ferrimagnetic layer is placed. Such a local decrease of magnetic field provides a condition for spin-wave localisation in the system. The paper presents a semi-analytic model which describes localised spin-wave modes in the ferrimagnetic layer. This model is corroborated by the results of micromagnetic simulations performed in MuMax3 environment. The localisation of spin-wave modes was investigated as a function of external magnetic field magnitude and the width of superconductor in the system.

The Author performed all micromagnetic simulation in MuMax3 environment. The Author has described the simulation and their results in the manuscript and prepared Figures 4., 6.

Spin-wave confinement in a hybrid superconductor-ferrimagnet nanostructure

Julia Kharlan,[1,2] Krzysztof Sobucki ,[1] Krzysztof Szulc ,[1] Sara Memarzadeh,[1] and
Jarosław W. Kłos [1,*]

[1] *ISQI, Faculty of Physics, Adam Mickiewicz University, Poznań, Poland*
[2] *Institute of Magnetism NASU and MESU, Kyiv, Ukraine*

Eddy currents in a superconductor shield the magnetic field in its interior and are responsible for the formation of a magnetic stray field outside of the superconducting structure. The stray field can be controlled by the external magnetic field and affect the magnetization dynamics in the magnetic system placed in its range. In the case of a hybrid system consisting of a superconducting strip placed over a magnetic layer, we theoretically predict the confinement of spin waves in the well of the static stray field. The number of bound states and their frequencies can be controlled by an external magnetic field. We present the results of semianalytical calculations complemented by numerical modeling.

I. INTRODUCTION

The states of superconductivity and ferromagnetism are very rarely observed in a single material. Their intrinsic coexistence (i.e., in one uniform phase for the same electrons) was found for triplet pairing in a proximity to a magnetic quantum critical point (e.g., for UGe_2) [1,2]. The other possibility, known for a long time and more conventional [3,4], is the coexistence of two phases where large and localized moments of 4f electrons (Er, Gd) provide long-range strong ferromagnetism whereas 3d conduction electrons are responsible for superconductivity.

The hybrid systems [5–8], where the superconductor and ferromagnet are part of the same structure and interact with each other, usually offer much more flexibility both in the design and implementation of new features. Superconductor-ferromagnet hybrids can be divided into two categories: both subsystems are in direct contact [9] or separated by a nonmagnetic, nonconducting material. In the latter case, the coupling at a distance results from the fact that both the eddy currents in the superconductor and the magnetic moments in the ferromagnet generate a magnetic field. The coupling provided by the magnetic field can be controlled by the external magnetic field and can be tailored by the geometry, since both the distribution of the eddy currents and the magnetization configuration depend on these factors.

In electromagnetically coupled hybrids, the ferromagnet can modify the properties of the superconductor, e.g., the magnetic screening can increase the value of the critical current density in the superconductor [10], or the presence

of the stray field produced by ferromagnetic nanoelements can affect the nucleation of vortices [11] or pin and guide the vortices in the superconductor [12]. Similarly, the presence of the superconductor can influence the ferromagnet, e.g., by controlling the magnetization dynamics [13,14]. In this research field, we can find reports about induction of magnonic crystals and nonreciprocal spin-wave (SW) transmission in uniform magnetic layers due to the screening of the dynamic demagnetizing field by a superconductor [15,16], magnon-phonon interaction [17,18], the gating of magnons induced by a superconducting current [19,20], enhancement of nonlinear SW dynamics [21], Bragg scattering of SWs on the field produced by the Abrikosov vortex lattice [22,23], or SW generation by moving vortices [24–26]. Undoubtedly, superconductor-ferromagnet hybrids offer many possibilities for controlling the dynamics of SWs. One of the topics not fully explored is the problem of localization of SWs in these systems.

In this study, we conduct a theoretical and numerical investigation of the SW confinement induced in a uniform ferrimagnetic (FM) layer by the stray field of a superconducting (SC) strip. We demonstrate that by adjusting the applied field, we can control the depth of the stray field to modify the number of confined SW modes and their frequencies.

II. MODEL

The considered hybrid system consists of an FM gallium-doped yttrium iron garnet (Ga:YIG) thin film and an SC Nb strip in the Meissner state, electrically isolated from each other by a thin nonmagnetic spacer (see Fig. 1). According to the Meissner effect, an SC strip expels a

---

*Corresponding author: klos@amu.edu.pl

Chapter 7

Summary and Outlook

7.1 Summary and future plans

Magnonics as a subfield of physics holds a great promise of developing a low energy consuming technologies and miniaturisation of devices because of unique properties of SWs. The theoretical foundations of magnonics have been developed in the last century, however the development of a usable, magnonic-based technology is hampered by various factors such as difficulty in manufacturing low-damping magnetic materials [117, 118], a shortage of accurate sensors for SW detection [119, 120], a relatively small number of reliable methods for controlling SW propagation [121, 122].

The scientific work presented in this thesis is in line with the research on new means to control SWs. Namely, two methods for SW propagation control were investigated, by employing magnonic interferometers and by inelastic scattering of SWs on localised modes. While investigating the first method, linear resonance effects have been observed such as Fabry-Perot resonances and excitation of the interferometers leaky-modes. In both of these effects an increase of phase shift of the reflected waves was observed. Especially, when Fabry-Perot resonances conditions were met in magnonic interferometers the significant phase shift was observed. As GHE depends on the phase shift of reflected waves presented linear resonance effects are accompanied by the lateral shift of SWs. It was shown in the investigations on the leaky-modes excitation where the reflected SW beams were spatially shifted when the resonance condition was fulfilled.

The research on inelastic scattering of SW beams on localised modes also presented resonance effects but in non-linear regime. There, when the resonance conditions in the demagnetising field deep were met, a cascade of several non-linear processes created new SWs with altered frequencies that propagated both in the bulk of system and at its edge. Again, these processes enhanced significantly the lateral shift in space what resembles GHE but in the non-linear case.

The investigations presented in this thesis contribute to exploration of new means to control propagation of SWs. The use of magnonic resonators to shift SW phase is investigated by numerical simulations and experiment by other scientific groups which results can be found

in [114, 115]. The examples of research on bound and leaky states in magnonics are published in [123]. While examples non-linear effects for SW propagation control and modulation are [50, 124, 125].

Looking into the future magnonics resonators could be used as elements of artificial neural networks based on SWs. By proper choice of resonator's shape and dimensions the resonator could scatter incoming SWs in desired directions. Such a treatment resembles a node, basic neural network building block, where the azimuthal distribution of scattered SW amplitude may be interpreted as the weights in classical artificial neural networks. On the day of writing this thesis the Author is a part of European Union project, MANNGA 101070347, that aims to propose a realisation of such a system. In this project, among other ideas, nanoresonators with non-uniform magnetisation are investigated which are in line of Author's interests and scientific plans.

An additional area of research considered by the Author is creation and use of spatio-temporal magnetic patterns for control of scattered SWs. The idea behind these investigations is realisation and programming of magnetic patterns that can be assigned to magnonic resonators. These resonators could be used to scatter SWs in a programmable manner that would change in time and space providing a more advanced way to control SW propagation.

7.2   Publication list

- Sobucki, et al. "Goos-Hänchen shift of inelastically scattered spin-wave beams and cascade nonlinear magnon processes."
  Scientific Reports 15.1, 5538, 2025

- Kharlan, Sobucki, et al. "Spin-wave confinement in a hybrid superconductor-ferrimagnet nanostructure."
  Physical Review Applied 21.6, 064007, 2024

- Sobucki, et al. "Magnon-Optic Effects with Spin-Wave Leaky Modes: Tunable Goos-Hänchen Shift and Wood's Anomaly."
  Nano Letters 23.15, 6979-6984, 2023

- Śmigaj, Sobucki, et al. "Modal approach to modeling spin wave scattering."
  Physical Review B 108.1, 014418, 2023

- Sobucki, et al. "Magnon spectrum of Bloch hopfion beyond ferromagnetic resonance."
  APL Materials 10.9, 091103, 2022

- Sobucki, et al. "Control of the Phase of Reflected Spin Waves From Magnonic Gires-Tournois Interferometer of Subwavelength Width."
  IEEE Transactions on Magnetics 58.2, 1-5, 2021

- Sobucki, et al. "Resonant subwavelength control of the phase of spin waves reflected from a Gires-Tournois interferometer."
  Scientific Reports 11.1, 4428, 2021

7.3 Research funding

7.3.1 Grants managed by the author

- PRELUDIUM 21, nr 2022/45/N/ST3/01844,
  Narodowe Centrum Nauki,
  Primary Investigator,
  „Exploiting resonance effects in ferromagnetic nanoresonators towards magnonic spacetime metasurfaces"
  II 2023 – II 2026

7.3.2 Grants in which the author was a contractor

- MANNGA, GA No. 101070347,
  European Union, project Horizon Europe,
  Contractor in project of dr hab. Paweł Gruszecki,
  „Magnonic artificial neural networks and gate arrays (MANNGA)"
  IX 2024 - VII 2025

- NCN SONATA 15, nr 2019/35/D/ST3/03729,
  Narodowe Centrum Nauki,
  Contractor in project of dr hab. Paweł Gruszecki,
  „Novel environment for spin wave propagation: from periodic magnetization textures towards space-time magnonic crystals"
  X 2020 - VIII 2023

7.3.3 Funds obtained from project "Inicjatywa Doskonałości - Uczelnia Badawcza" AMU

- ID-UB call No. 166,
  "08 - Wsparcie publikowania w prestiżowych czasopismach naukowych - Promesa sfinansowania kosztów przez Program ID-UB",
  covering costs of Open Access publication of "Goos–Hänchen shift of inelastically scattered spin-wave beams and cascade nonlinear magnon processes"

- ID-UB call No. 148,
  "06 - Wsparcie udziału naukowców i doktorantów w prestiżowych konferencjach naukowych",
  subsidised conference trip ICM 2024

- ID-UB call No. 127,
  "06 - Wsparcie udziału naukowców i doktorantów w prestiżowych konferencjach naukowych",
  subsidised conference trip Intermag 2024

- ID-UB call No. 071,
  "06 - Wsparcie udziału naukowców i doktorantów w prestiżowych konferencjach naukowych",
  subsidised conference trip MMM22

- ID-UB call No. 070 ,
  "13 - Wsparcie umiędzynarodowienia badań naukowych prowadzonych w Szkole Doktorskiej UAM",
  subsidised internship at Aalto University

- ID-UB call No. 058,
  "06 - Wsparcie udziału naukowców i doktorantów w prestiżowych konferencjach naukowych",
  subsidised conference trip SolSkyMag 2022

- ID-UB call No. 015,
  "06 - Wsparcie udziału naukowców i doktorantów w prestiżowych konferencjach naukowych",
  subsidised conference trip JEMS 2020

7.4   Scientific internship

- Department of Physics and Astronomy, University of Exeter,
  Exeter, United Kingdom,
  financed from PRELUDIUM 21
  II - IV 2025

- Department of Applied Physics, Aalto University,
  Espoo, Finland,
  project "AMU International Compass"
  II - VI 2023

- Interuniversity Microelectronics Centre (IMEC)
  Leuven, Belgium,
  project Erasmus+
  II - VII 2020

7.5   List of attended conferences

1. Symposium on Spintronics and Quantum Information 2025,
   Będlewo, Poland, **oral presentation**,
   titled: "Spin Wave Amplification in Time-Varying Media"
   IV 2025

2. ICM 2024 - 22nd International Conference on Magnetism,
   Bologna, Italy, **poster presentation**,
   titled: "Finite-Element Modal Method for Modelling Dipole-Exchange Spin Wave Scattering in Magnonic Circuits"
   VII 2024

3. 1st Transnational Round Table on Magnonics, High-Frequency Spintronics, and Ultrafast Magnetism,
   Exeter, United Kingdom, **poster presentation**,
   titled: "Controlling Spin-Wave Frequency and Trajectory Through Inelastic Scattering on Localized Modes"
   VI 2024

4. Intermag 2024,
   Rio de Janeiro, Brazil, **oral presentation**,
   titled: "Nonlinear Effects in Inelastic Scattering of Spin-Wave Beams on Localized Modes for Controlling Propagation of Scattered Beams"
   V 2024

5. Symposium on Spintronics and Quantum Information 2024,
   Będlewo, Poland, **oral presentation**,
   titled: "Spin-Wave Beam Inelastic Scattering On Localized Modes For Spin Wave Frequency And Trajectory Control"
   I 2024

6. JEMS 2023,
   Madrid, Spain, **oral presentation**,
   titled: "Inelastic Scattering Of Spin-Wave Beams On Localised Spin Waves And Goos-Hänchen For Scattered Beams"
   VIII 2023

7. Magnonics 2023,
   Le Touquet-Paris-Plage, France, **poster presentation**,
   titled: "Three Magnon Processes In Spin-wave Scattering On Localised Modes For Controllable Frequency And Trajectory Modulation"
   VII 2023

8. Physics of Magnetism 2023,
   Poznań, Poland, **oral presentation**,
   titled: "Inelastic spin wave beam scattering on localised modes for controlling beams'
   trajectory and frequency"
   VI 2023

9. WE.Heraeus Non-linear Magnetism Seminar,
   Bad Honnef, Germany, **poster presentation**,
   titled: "Magnon-optic effects with spin-wave leaky modes in Gires-Tournois interferome-
   ter"
   I 2023

10. Symposium on Spintronics and Quantum Information 2022,
    Poznań, Poland, **oral presentation**,
    titled: „Magnonic counterparts to phenomena known in optics found in spin-wave reflection
    from magnonic Gires-Tournois interferometer"
    XII 2022

11. MMM 2022,
    Minneapolis, United States of America, **oral presentation**,
    titled: "Magnonic interferometer's leaky-mode influence on spin-wave beam reflection"
    XI 2022

12. JEMS 2022,
    Warsaw, Poland, **oral presentation**,
    titled: "Bloch Hopfion Spin-Wave Spectra In Ferromagnetic Medium"
    VII 2022

13. Sol-SkyMag22 Conference,
    San Sebastian, Spain, **oral presentation**,
    titled: "Oblique Incidence Spin Wave Beam Onto Gires-Tournois Interferometer: Excita-
    tion Of Leaky Modes And Goos-Hänchen Effect"
    VI 2022

14. Sol-SkyMag22 Conference,
    San Sebastian, Spain, **poster presentation**,
    titled: "Spin-Wave Spectra Of Hopfion In Ferromagnetic Nanodisc"
    VI 2022

15. WE.Heraeus Non-linear Magnetism Conference,
    online, **poster presentation**,
    titled: "Resonant control of phase of spin wave reflected from subwavelength Gires-
    Tournois interferometer"
    I 2022

16. Physics of Magnetism 2021 Conference,
    online, **oral presentation**,
    titled: "Control of the phase of spin wave reflected from a subwavelength Gires-Tournois interferometer"
    VI 2021

17. Intermag 2021,
    online, **oral presentation**,
    titled: "Control of the phase of reflected spin-waves from magnonic Gires-Tournois interferometer of subwavelength width"
    IV 2021

18. JEMS 2020,
    online, **poster presentation**,
    titled: "Resonant subwavelength control of the phase of spin waves reflected with Gires-Tournois interferometer"
    XII 2020

19. QuTecNOMM'19,
    Poznań, Poland, **oral presentation**,
    titled: "Subwavelength control of the phase of spin waves by ferromagnetic resonators"
    XI 2019

7.6 List of attended doctoral student's schools and workshops

1. Waves in Time Varying Media 2025,
   Madrid, Spain, **poster presentation**,
   titled: "Amplification of spin waves in time-varying media"
   V 2025

2. European School on Magnetism 2023,
   Miraflores de la Sierra, Spain, **poster presentation**,
   titled: "Utilizing Three Magnon Processes to Control Frequency and Trajectory of Spin-Wave Beams Scattered on Localized Modes"
   IX 2023

3. MagIC+ 2023,
   Będlewo, Poland, **oral presentation**,
   titled: "Spin-Wave Scattering On Localized Modes: Harnessing Three Magnon Processes For Frequency And Trajectory Control"
   VII 2023

4. IEEE Summer School 2023,
   Carovigno, Italy, **poster presentation**,
   titled: "Confluence and Stimulated Splitting Processes of Spin Waves Scattered on Localized Modes"
   VI 2023

5. 4th International Advanced School on Magnonics – MAGNETOFON,
   Porto, Portugal, **poster presentation**,
   titled: "Spin Waves Leaky-Modes In Magnonic Gires-Tournois Interferometer"
   VII 2022

6. MagIC+ (online workshop),
   Poznań, Poland, **poster presentation**,
   titled: "Control of the phase of spin wave reflected from a subwavelength Gires-Tournois interferometer"
   VII 2021

7.7   Organisation of conferences

1. Symposium on Spintronics and Quantum Information 2024,
   Będlewo, Poland,
   editing a book of abstracts,
   I 2024

2. Symposium on Spintronics and Quantum Information 2022,
   Poznań, Poland,
   technical help,
   XII 2022

3. 2022 Around-the-Clock Around-the-Globe Magnetics Conference (AtC-AtG),
   online conference under hospices of IEEE Magnetics Society,
   member of the outreach team,
   31 VIII 2022

4. MagIC+
   online workshop as a follow-up to Physics of Magnetism 2021 Conference,
   technical help,
   VII 2021

Bibliography

[1] D. D. Stancil and A. Prabhakar, *Spin waves: theory and applications* (Springer, 2009).

[2] W. Heisenberg, "Über den anschaulichen Inhalt der quantentheoretischen Kinematik und Mechanik", Zeitschrift für Physik **43**, 172–198 (1927).

[3] Bose, "Plancks Gesetz und Lichtquantenhypothese", Zeitschrift für Physik **26**, 178–181 (1924).

[4] E. Fermi, "Sulla quantizzazione del gas perfetto monoatomico", Rendiconti Lincei **145** (1926).

[5] P. A. M. Dirac, "On the theory of quantum mechanics", Proceedings of the Royal Society of London. Series A, Containing Papers of a Mathematical and Physical Character **112**, 661–677 (1926).

[6] W. Gerlach and O. Stern, "Der experimentelle Nachweis der Richtungsquantelung im Magnetfeld", Walther Gerlach (1889–1979) Eine Auswahl aus seinen Schriften und Briefen, 26–29 (1989).

[7] M. Niemeyer, K. Hirsch, V. Zamudio-Bayer, et al., "Spin coupling and orbital angular momentum quenching in free iron clusters", Physical review letters **108**, 057201 (2012).

[8] J. M. Coey, *Magnetism and magnetic materials* (Cambridge university press, 2010).

[9] D. J. Griffiths, "Introduction to electrodynamics, fourth edition", (2013).

[10] T. L. Chow, *Introduction to electromagnetic theory: a modern perspective* (Jones & Bartlett Learning, 2006).

[11] A. G. Gurevich and G. A. Melkov, *Magnetization oscillations and waves* (CRC press, 2020).

[12] R. Moskowitz and E. Della Torre, "Theoretical aspects of demagnetization tensors", IEEE Transactions on Magnetics **2**, 739–744 (1966).

[13] D. Chernyshenko and H. Fangohr, "Computing the demagnetizing tensor for finite difference micromagnetic simulations via numerical integration", Journal of Magnetism and Magnetic Materials **381**, 440–445 (2015).

[14] C. Kittel, *Introduction to solid state physics eighth edition* (John Wiley & Sons, 2021).

[15] W. Heisenberg, "Multi-body problem and resonance in quantum mechanics II", Z Phys **41**, 239 (1927).

[16] G. S. Abo, Y.-K. Hong, J. Park, et al., "Definition of magnetic exchange length", IEEE Transactions on Magnetics **49**, 4937–4939 (2013).

[17] M. Krawczyk, M. Sokolovskyy, J. Klos, and S. Mamica, "On the formulation of the exchange field in the Landau-Lifshitz equation for spin-wave calculation in magnonic crystals", Advances in Condensed Matter Physics **2012**, 764783 (2012).

[18] B. Rana and Y. Otani, "Towards magnonic devices based on voltage-controlled magnetic anisotropy", Communications Physics **2**, 90 (2019).

[19] A. Aharoni, *Introduction to the theory of ferromagnetism*, Vol. 109 (Clarendon Press, 2000).

[20] I. Dzyaloshinsky, "A thermodynamic theory of "weak" ferromagnetism of antiferromagnetics", Journal of physics and chemistry of solids **4**, 241–255 (1958).

[21] T. Moriya, "Anisotropic superexchange interaction and weak ferromagnetism", Physical review **120**, 91 (1960).

[22] A. Fert and P. M. Levy, "Role of anisotropic exchange interactions in determining the properties of spin-glasses", Physical Review Letters **44**, 1538 (1980).

[23] D.-H. Kim, M. Haruta, H.-W. Ko, et al., "Bulk dzyaloshinskii–moriya interaction in amorphous ferrimagnetic alloys", Nature materials **18**, 685–690 (2019).

[24] L. Zhu, L. Zhu, X. Ma, X. Li, and R. A. Buhrman, "Critical role of orbital hybridization in the dzyaloshinskii-moriya interaction of magnetic interfaces", Communications Physics **5**, 151 (2022).

[25] R. M. Bozorth, *Ferromagnetism* (1993).

[26] N. W. Ashcroft, N. D. Mermin, and S. Rodriguez, *Solid state physics*, Vol. 46, 1 (AIP Publishing, 1978), pp. 116–117.

[27] E. C. Stoner and E. Wohlfarth, "A mechanism of magnetic hysteresis in heterogeneous alloys", Philosophical Transactions of the Royal Society of London. Series A, Mathematical and Physical Sciences **240**, 599–642 (1948).

[28] F. Keffer and H. Chow, "Dynamics of the antiferromagnetic spin-flop transition", Physical Review Letters **31**, 1061 (1973).

[29] A. Bogdanov, A. Zhuravlev, and U. Rößler, "Spin-flop transition in uniaxial antiferromagnets: magnetic phases, reorientation effects, and multidomain states", Physical Review B—Condensed Matter and Materials Physics **75**, 094425 (2007).

[30] F. Machado, P. Ribeiro, J. Holanda, et al., "Spin-flop transition in the easy-plane antiferromagnet nickel oxide", Physical Review B **95**, 104418 (2017).

[31] L. Landau and E. Lifshitz, "On the theory of the dispersion of magnetic permeability in ferromagnetic bodies", Phys. Z. Sowjetunion **8**, 101–114 (1935).

[32] C. Kittel, "On the theory of ferromagnetic resonance absorption", Physical review **73**, 155 (1948).

[33] J. H. Griffiths, "Anomalous high-frequency resistance of ferromagnetic metals", Nature **158**, 670–671 (1946).

[34] T. L. Gilbert, "Equation of motion of magnetization", Armour Research Foundation Rep. **11** (1955).

[35] T. L. Gilbert, "A phenomenological theory of damping in ferromagnetic materials", IEEE transactions on magnetics **40**, 3443–3449 (2004).

[36] T. L. Gilbert, "https://ieeexplore.ieee.org/author/37087257290", (access on 05.05.2025).

[37] A. Vansteenkiste, J. Leliaert, M. Dvornik, et al., "The design and verification of MuMax3", AIP Adv. **4**, 107133 (2014).

[38] K. Y. Guslienko and A. N. Slavin, "Magnetostatic Green's functions for the description of spin waves in finite rectangular magnetic dots and stripes", Journal of Magnetism and Magnetic Materials **323**, 2418–2424 (2011).

[39] P. Gruszecki, Y. S. Dadoenkova, N. Dadoenkova, et al., "Influence of magnetic surface anisotropy on spin wave reflection from the edge of ferromagnetic film", Physical Review B **92**, 054427 (2015).

[40] R. W. Damon and J. Eshbach, "Magnetostatic modes of a ferromagnet slab", Journal of Physics and Chemistry of Solids **19**, 308–320 (1961).

[41] U. Bhaskar, G. Talmelli, F. Ciubotaru, C. Adelmann, and T. Devolder, "Backward volume vs Damon–Eshbach: A traveling spin wave spectroscopy comparison", Journal of Applied Physics **127** (2020).

[42] A. B. Ustinov, B. A. Kalinikos, and E. Lähderanta, "Nonlinear phase shifters based on forward volume spin waves", Journal of Applied Physics **113** (2013).

[43] J. Parekh, K. Chang, and H. Tuan, "Propagation characteristics of magnetostatic waves", Circuits, systems and signal processing **4**, 9–39 (1985).

[44] B. Kalinikos and A. Slavin, "Theory of dipole-exchange spin wave spectrum for ferromagnetic films with mixed exchange boundary conditions", Journal of Physics C: Solid State Physics **19**, 7013 (1986).

[45] K. Y. Guslienko, S. O. Demokritov, B. Hillebrands, and A. N. Slavin, "Effective dipolar boundary conditions for dynamic magnetization in thin magnetic stripes", Phys. Rev. B **66**, 132402 (2002).

[46] K. Y. Guslienko and A. Slavin, "Boundary conditions for magnetization in magnetic nanoelements", Physical Review B—Condensed Matter and Materials Physics **72**, 014463 (2005).

[47] T. Holstein and H. Primakoff, "Field dependence of the intrinsic domain magnetization of a ferromagnet", Physical Review **58**, 1098 (1940).

[48] S. Zheng, Z. Wang, Y. Wang, et al., "Tutorial: Nonlinear magnonics", Journal of Applied Physics **134** (2023).

[49] M. A. Slawinski, R. A. Slawinski, R. J. Brown, and J. M. Parkin, "A generalized form of Snell's law in anisotropic media", Geophysics **65**, 632–637 (2000).

[50] P. Gruszecki, K. Y. Guslienko, I. L. Lyubchanskii, and M. Krawczyk, "Inelastic spin-wave beam scattering by edge-localized spin waves in a ferromagnetic thin film", Physical Review Applied **17**, 044038 (2022).

[51] B. E. Saleh and M. C. Teich, *Fundamentals of photonics* (John Wiley & sons, 2019).

[52] H. Yu, B. Kim, S.-g. Jang, K.-H. Kim, and J. J. Yoh, "Performance characterization of a miniaturized exploding foil initiator via modified VISAR interferometer and shock wave analysis", Journal of Applied Physics **121** (2017).

[53] T. V. Vorburger, H.-G. Rhee, T. B. Renegar, J.-F. Song, and A. Zheng, "Comparison of optical and stylus methods for measurement of surface texture", The International Journal of Advanced Manufacturing Technology **33**, 110–118 (2007).

[54] R. Leach and H. Haitjema, "Bandwidth characteristics and comparisons of surface texture measuring instruments", Measurement Science and Technology **21**, 032001 (2010).

[55] P. Pawlus, R. Reizer, M. Wieczorowski, and G. Krolczyk, "Study of surface texture measurement errors", Measurement **210**, 112568 (2023).

[56] R. R. Bommareddi, "Applications of optical interferometer techniques for precision measurements of changes in temperature, growth and refractive index of materials", Technologies **2**, 54–75 (2014).

[57] A. Eshun, B. Gu, O. Varnavski, et al., "Investigations of molecular optical properties using quantum light and Hong–Ou–Mandel interferometry", Journal of the American Chemical Society **143**, 9070–9081 (2021).

[58] A. A. Michelson, "The relative motion of the Earth and the Luminiferous ether", American Journal of Science (1880-1910) **22**, 120 (1881).

[59] L. Zehnder, *Ein neuer Interferenzrefraktor*, 1891.

[60] L. Mach, "Ueber einen Interferenzrefraktor", Zeitschrift für Instrumentenkunde **12**, 89 (1892).

[61] B. P. Abbott, R. Abbott, T. Abbott, et al., "Observation of gravitational waves from a binary black hole merger", Physical review letters **116**, 061102 (2016).

[62] F. Gires and P. Tournois, "Interferometre utilisable pour la compression d'impulsions lumineuses modulees en frequence", C. R. Acad. Sci. Paris. **258**, 6112–6115 (1964).

[63] E. Hecht, *Optics* (Pearson, 2012).

[64] F. Goos and H. Hänchen, "Ein neuer und fundamentaler Versuch zur Totalreflexion", Annalen der Physik **436**, 333–346 (1947).

[65] K. Artmann, "Berechnung der Seitenversetzung des totalreflektierten Strahles", Annalen der Physik **437**, 87–102 (1948).

[66] Y. S. Dadoenkova, N. Dadoenkova, I. Lyubchanskii, et al., "Huge Goos-Hänchen effect for spin waves: A promising tool for study magnetic properties at interfaces", Applied Physics Letters **101** (2012).

[67] N. N. Dadoenkova, Y. S. Dadoenkova, I. L. Lyubchanskii, M. Krawczyk, and K. Y. Guslienko, "Inelastic spin-wave scattering by Bloch domain wall flexure oscillations", physica status solidi (RRL)–Rapid Research Letters **13**, 1800589 (2019).

[68] Y. S. Dadoenkova, M. Krawczyk, and I. L. Lyubchanskii, "Goos-Hänchen shift at Brillouin light scattering by a magnetostatic wave in the Damon-Eshbach configuration", Optical Materials Express **12**, 717–726 (2022).

[69] N. F. Declercq and E. Lamkanfi, "Study by means of liquid side acoustic barrier of the influence of leaky Rayleigh waves on bounded beam reflection", Applied physics letters **93** (2008).

[70] V.-O. de Haan, J. Plomp, T. M. Rekveldt, et al., "Observation of the Goos-Hänchen shift with neutrons", Physical review letters **104**, 010401 (2010).

[71] P. Gruszecki, J. Romero-Vivas, Y. S. Dadoenkova, et al., "Goos-Hänchen effect and bending of spin wave beams in thin magnetic films", Applied Physics Letters **105**, 242406 (2014).

[72] J. Stigloher, T. Taniguchi, H. Körner, et al., "Observation of a Goos-Hänchen-like phase shift for magnetostatic spin waves", Phys. Rev. Lett. **121**, 137201 (2018).

[73] R. W. Wood, "On a remarkable case of uneven distribution of light in a diffraction grating spectrum", The London, Edinburgh, and Dublin Philosophical Magazine and Journal of Science **4**, 396–402 (1902).

[74] R. W. Wood, "XXVII. Diffraction gratings with controlled groove form and abnormal distribution of intensity", The London, Edinburgh, and Dublin Philosophical Magazine and Journal of Science **23**, 310–317 (1912).

[75] R. W. Wood, "Anomalous diffraction gratings", Physical Review **48**, 928 (1935).

[76] L. Rayleigh, "On the dynamical theory of gratings", Proceedings of the Royal Society of London. Series A, Containing Papers of a Mathematical and Physical Character **79**, 399–416 (1907).

[77] U. Fano, "The theory of anomalous diffraction gratings and of quasi-stationary waves on metallic surfaces (Sommerfeld's waves)", JOSA **31**, 213–222 (1941).

[78] S. Enoch and N. Bonod, *Plasmonics: from basics to advanced topics*, Vol. 167 (Springer, 2012).

[79] J. Liu and N. F. Declercq, "Investigation of the origin of acoustic Wood anomaly", The Journal of the Acoustical Society of America **138**, 1168–1179 (2015).

[80] C. Yi, Y. J. Yoo, Y. J. Kim, et al., "Role of Wood's anomaly in the performance of metamaterial absorbers with periodicity comparable to wavelength", Journal of Physics D: Applied Physics **49**, 195103 (2016).

[81] E. Galiffi, Y.-T. Wang, Z. Lim, et al., "Wood anomalies and surface-wave excitation with a time grating", Physical Review Letters **125**, 127403 (2020).

[82] J. Brown William Fuller, "Micromagnetics, Domains, and Resonance", Journal of Applied Physics **30**, S62–S69 (1959).

[83] W. Brown, *Micromagnetics*, Interscience tracts on physics and astronomy (Interscience Publishers, 1963).

[84] G. P. Nikishkov, *Introduction to the finite element method* (2004), pp. 1–70.

[85] R. Lacerda de Orio, *Electromigration modeling and simulation* (Technische Universität Wien, 2010).

[86] K. Banaś, *Wprowadzenie do MES* (Akademia Górniczo-Hutnicza w Krakowie, 2020).

[87] COMSOL Multiphysics 5.2, "www.comsol.com", (access on 10.02.2025).

[88] H. Szambolics, L. Buda-Prejbeanu, J.-C. Toussaint, and O. Fruchart, "Finite element formalism for micromagnetism", COMPEL **27**, 266–276 (2008).

[89] R. J. LeVeque, "Finite difference methods for differential equations", Draft version for use in AMath **585**, 112 (1998).

[90] C. Grossmann, *Numerical treatment of partial differential equations* (Springer, 2007).

[91] R. Fitzpatrick, *Computational physics* (The University of Texas at Austin, 2015).

[92] C. W. Gear, "The numerical integration of ordinary differential equations", Mathematics of Computation **21**, 146–156 (1967).

[93] J. Leliaert, M. Dvornik, J. Mulkers, et al., "Fast micromagnetic simulations on GPU—recent advances made with Mumax3", Journal of Physics D: Applied Physics **51**, 123002 (2018).

[94] W. H. Press, *Numerical recipes 3rd edition: the art of scientific computing* (Cambridge university press, 2007).

[95] A. Rahim, C. Ragusa, B. Jan, and O. Khan, "A mixed mid-point Runge-kutta like scheme for the integration of Landau-Lifshitz equation", Journal of Applied Physics **115** (2014).

[96] TetraX, "https://www.tetrax.software", (access on 10.02.2025).

[97] TetraMAG, "https://github.com/R-Hertel/tetmag", (access on 10.02.2025).

[98] R. Chang, S. Li, M. V. Lubarda, B. Livshitz, and V. Lomakin, "Fastmag: fast micromagnetic simulator for complex magnetic structures (invited)", Journal of Applied Physics **109**, 07D358 (2011).

[99] Nmag, "https://nmag-project.github.io", (access on 10.02.2025).

[100] magpar, "http://www.magpar.net/static/magpar/doc/html/index.html", (access on 10.02.2025).

[101] G. Venkat, H. Fangohr, and A. Prabhakar, "Absorbing boundary layers for spin wave micromagnetics", Journal of Magnetism and Magnetic Materials **450**, Perspectives on magnon spintronics, 34–39 (2018).

[102] A. Vretblad and A. Vretblad, *Fourier analysis and its applications*, Vol. 223 (Springer, 2003).

[103] Q. Wang, B. Heinz, R. Verba, et al., "Spin pinning and spin-wave dispersion in nanoscopic ferromagnetic waveguides", Physical review letters **122**, 247202 (2019).

[104] C. W. Hsu, B. Zhen, A. Stone, J. Joannopoulos, and M. Soljačić, "Bound states in the continuum", Nature Reviews Materials **1**, 16048 (2016).

[105] N. Whitehead, *Making the grade: generating & controlling spin waves with a graded refractive index* (University of Exeter, 2020).

[106] A. V. e. a. Chumak, "Advances in magnetics roadmap on spin-wave computing", IEEE Transactions on Magnetics **58**, 39, 40 (2022).

[107] D. Nikonov and I. Young, "Overview of beyond-CMOS devices and a uniform methodology for their benchmarking", Proceedings of the IEEE **101**, 2498–2533 (2013).

[108] W. L. Barnes, A. Dereux, and T. W. Ebbesen, "Surface plasmon subwavelength optics", nature **424**, 824–830 (2003).

[109] S. Maier, *Plasmonics: fundamentals and applications* (Springer, 2007).

[110] R. D. V. Meade, S. G. Johnson, and J. N. Winn, *Photonic crystals: molding the flow of light* (Princeton University Press, 2008).

[111] W. L. Barnes, "Surface plasmon–polariton length scales: a route to sub-wavelength optics", Journal of optics A: pure and applied optics **8**, S87 (2006).

[112] Á. Papp, W. Porod, and G. Csaba, "Nanoscale neural network using non-linear spin-wave interference", Nature communications **12**, 6422 (2021).

[113]   Y. Au, M. Dvornik, O. Dmytriiev, and V. Kruglyak, "Nanoscale spin wave valve and phase shifter", Appl. Phys. Lett. **100**, 172408 (2012).

[114]   K. Fripp, A. Shytov, and V. Kruglyak, "Spin-wave control using dark modes in chiral magnonic resonators", Physical Review B **104**, 054437 (2021).

[115]   H. Qin, R. B. Holländer, L. Flajšman, et al., "Nanoscale magnonic Fabry-Pérot resonator for low-loss spin-wave manipulation", Nature Communications **12**, 2293 (2021).

[116]   Q. Wang, A. V. Chumak, and P. Pirro, "Inverse-design magnonic devices", Nature communications **12**, 2636 (2021).

[117]   M. A. Schoen, D. Thonig, M. L. Schneider, et al., "Ultra-low magnetic damping of a metallic ferromagnet", Nature Physics **12**, 839–842 (2016).

[118]   L. Soumah, N. Beaulieu, L. Qassym, et al., "Ultra-low damping insulating magnetic thin films get perpendicular", Nature communications **9**, 3355 (2018).

[119]   R. Kryshtal and A. Medved, "Surface acoustic wave in yttrium iron garnet as tunable magnonic crystals for sensors and signal processing applications", Applied Physics Letters **100** (2012).

[120]   M. A. Khan, J. Sun, B. Li, A. Przybysz, and J. Kosel, "Magnetic sensors-a review and recent technologies", Engineering Research Express **3**, 022005 (2021).

[121]   C. Liu, S. Wu, J. Zhang, et al., "Current-controlled propagation of spin waves in antiparallel, coupled domains", Nature Nanotechnology **14**, 691–697 (2019).

[122]   J. Chen, H. Yu, and G. Gubbiotti, "Unidirectional spin-wave propagation and devices", Journal of Physics D: Applied Physics **55**, 123001 (2021).

[123]   T. Tamir and H. Bertoni, "Lateral displacement of optical beams at multilayered and periodic structures", J. Opt. Soc. Am. **61**, 1397–1413 (1971).

[124]   Z.-W. Zhou, X.-G. Wang, Y.-Z. Nie, Q.-L. Xia, and G.-H. Guo, "Spin wave frequency comb generated through interaction between propagating spin wave and oscillating domain wall", J. Magn. Magn. Mater. **534**, 168046 (2021).

[125]   L. Körber, K. Schultheiss, T. Hula, et al., "Nonlocal stimulation of three-magnon splitting in a magnetic vortex", Physical Review Letters **125**, 207203 (2020).